ASSIMILATION OF ALTIMETER DATA IN A QUASI-GEOSTROPHIC MODEL OF THE GULF STREAM SYSTEM: A DYNAMICAL PERSPECTIVE

by

Antonietta Capotondi

S.B., Università di Pisa
(1981)

Submitted in partial fulfillment of the
requirements for the degree of

DOCTOR OF PHILOSOPHY

at the

MASSACHUSETTS INSTITUTE OF TECHNOLOGY

and the

WOODS HOLE OCEANOGRAPHIC INSTITUTION

February 1993

Signature of Author .....
Joint Program in Physical Oceanography
Massachusetts Institute of Technology
Woods Hole Oceanographic Institution
March 5, 1992

Certified by .....
Paola Malanotte Rizzoli
Professor
Thesis Supervisor

Accepted by .....
Lawrence J. Pratt
Chairman, Joint Committee for Physical Oceanography
Massachusetts Institute of Technology
Woods Hole Oceanographic Institution

Abstract

The dynamical aspects involved in the assimilation of altimeter data in a numerical ocean model have been investigated. The model used for this study is a quasi-geostrophic model of the Gulf Stream region. The data that have been assimilated are maps of sea surface height which have been obtained as the superposition of sea surface height variability deduced from the Geosat altimeter measurements and a mean field constructed from historical hydrographic data. The method used for assimilating the data is the nudging technique. Nudging has been implemented in such a way as to achieve a high degree of convergence of the surface model fields toward the observations.

We have analyzed the mechanisms of the model adjustment, and the final statistical equilibrium characteristics of the model simulation when the surface data are assimilated. Since the surface data are the superposition of a mean component and an eddy component, in order to understand the relative role of these two components in determining the characteristics of the final statistical steady state, we have considered two different experiments: in the first experiment only the climatological mean field is assimilated, while in the second experiment the total surface streamfunction field (mean + eddies) has been used.

We have found that the mean component of the surface data determines, to a large extent, the structure of the flow field in the subsurface layers, while the eddy field, as well as the inflow/outflow conditions at the open boundaries, affect its intensity. In particular, if surface eddies are not assimilated only a weak flow develops in the two deeper model layers where no inflow/outflow is prescribed at the boundaries.

Comparisons of the assimilation results with available in situ observations show a considerable improvement in the degree of realism of the climatological model behavior, with respect to the model in which no data are assimilated. In particular, the possibility of building into the model more realistic eddy characteristics, through the assimilation of the surface eddy field, proves very successful in driving components of the mean model circulation that are in good agreement with the available observations.

Acknowledgements

There are many people that I would like to thank for their help in the accomplishment of my thesis work. My first thanks go to my advisor Dr. Paola Malanotte Rizzoli. Paola introduced me to the idea of starting graduate school, convincing me that I was not too old for undertaking this experience. She has provided me scientific guidance and stimulating ideas and she has always been, during my years of graduate school, a continuous source of strength and enthusiasm. My NCAR advisor, Dr. Bill Holland, has assisted me constantly during my thesis work at NCAR, sharing with me the joy for research and understanding. He has taught me most of what I know about numerical modeling, and he has also helped me in developing the right attitude for fully enjoying my work. Both Bill and Paola have been for me excellent advisors and wonderful friends.

I would then like to thank the other members of my thesis committee, Dr. Joe Pedlosky, Dr. Carl Wunsch and Dr. Mindy Hall for their insightful suggestions, illuminating criticisms and stimulating discussions. Joe and Carl have also been the teachers of some of the courses I have attended and, as teachers, they have been of invaluable help in stimulating my creative and critical thinking.

I also would like to thank Dr. Nelson Hogg and Dr. Breck Owens. They have supplied me with some of the in situ data I have used in my thesis and, although not part of my thesis committee, they have always been available for very insightful discussions and explanations.

Special thanks are due to the oceanographic group at the Jet Propulsion Laboratory, especially to Dr. Lee Fu and Dr. Victor Zlotnicki. They have supplied the Geosat data that I have used for my assimilation experiments and have continuously assisted me with their invaluable expertise.

Steve Worley, at the NCAR data support section, has helped me with the computation of the dynamic height fields from the Bauer-Robinson climatology, always showing competence, patience and a good sense of humor.

Dr. Julianna Chow, at the NCAR Oceanographic Group, has been of invaluable help in introducing me to the model I have used and in helping me in the solution of several computational problems.

Dr. Pierre-Yves Le Traon, at CLS-ARGOS in Toulouse, has shared with me his expertise in the processing and analysis of the Geosat data.

Several consultants at the NCAR Scientific Computing Division have assisted me in the process of becoming accustomed to the use of the supercomputer, and have explained to me some of the mysteries of the NCAR graphics.

I would like to give special thanks to the people at the Advanced Study Program at NCAR, who have offered me the possibility of coming to NCAR and benefit of the facilities and of the stimulating atmosphere present in this institution.

Very warm thanks go to all my friends, in Boston, in Boulder and in other parts of the world for helping me to live these years of graduate school not only as an exciting intellectual experience, but also as a fundamental experience of personal growth. In particular I would like to thank my boyfriend Jim Wilczak for sharing my

struggles and desire of accomplishement, for the illuminating scientific discussions on the issues I have been dealing with, and for his precious help in checking my often 'creative' english.

Infine vorrei ringraziare i miei genitori, Angela e Domenico Capotondi, per avermi insegnato, con il loro esempio, che le cose che veramente ci arricchiscono sono quelle che ci conquistiamo con il nostro lavoro e con la nostra dedizione. Nonostante la loro difficolta' ad accettare di avermi lontana, essi mi hanno sempre incoraggiato a rispettare questa mia scelta e a portarla a termine con successo.

This research was carried out with the support of the National Aeronautics Space Administration, through a contract to MIT from the Jet Propulsion Laboratory, # 958208, as a part of the TOPEX-Poseidon investigation.

Table of Contents

Chapter 1

Introduction

Numerical models of the ocean circulation have undergone a considerable development in the last 30 years. In fact, several steps toward a higher degree of realism have been undertaken since the first idealized numerical studies of westward intensification (Bryan, 1963; Veronis, 1966, Holland, 1967). These studies were performed with barotropic models of coarse horizontal resolution in a rectangular domain. A first fundamental improvement in model "realism" has been the increased horizontal and vertical resolution. The higher horizontal resolution has allowed the inclusion of the mesoscale eddy field and of its interactions with the mean flow, processes previously parameterized often in a crude fashion.

A further step in improving the model "realism" has then been the inclusion of a realistic geometry for studying the circulation in specific areas of the world ocean. Models of this type can incorporate the effect of the actual coastline and bottom topography in the area of interest and allow a more straightforward geographical correspondence between the model circulation and the observed ocean circulation.

The present state of the art in ocean modeling is thus represented by eddy resolving models in a realistic domain. Eddy resolving models describe the evolution and statistical equilibrium of a turbulent ocean. Therefore the *General Circulation* of these models includes both characteristics of the mean circulation

and eddy statistics. Comparisons of some aspects of the model climatology with observations have shown the sensitivity of the model behavior to the geometry, frictional parameterizations and boundary conditions. These factors seem to affect, in an interdependent and complicated fashion, the delicate internal processes of eddy-mean flow interactions. For this reason models often fail in reproducing some basic characteristic of the ocean circulation. A typical example of this difficulty is the Gulf Stream area. None of the models presently available, models that incorporate different kinds of numerics and different physical approximations, is able to accurately reproduce all of the observed features of the Gulf Stream jet and its near field, including both mean and eddy characteristics. For example, the location at which the Gulf Stream separates from the coast near Cape Hatteras and its subsequent mean path downstream to the Grand Banks is notoriously difficult to simulate accurately. Reproducing the correct amplitude and structure of the eddy kinetic energy pattern is also very challenging. Correctly determining the mean westward recirculation, presumably an eddy-driven phenomenon, is also exceedingly difficult.

For the above reasons, one can consider the possibility of using data assimilation techniques to improve the model climatology, including characteristics of both the mean field and the eddy statistical properties. Data assimilation is a relatively new topic in oceanography, relative to the long term experience developed in meteorology. In fact, it is only with the advent of the ocean satellite missions that data sets with a large coverage over synoptic time scales have become available to oceanographers. The limitations that ocean models have in their climatological characteristics, as described above, suggests the use of these data sets not only for prediction purposes, as has been the case in meteorology, but also as constraints to the model behavior from a climatological point of view. The data sets obtained from satellite missions contain information only about the ocean surface. Therefore, from

the data point of view, numerical models can be seen as "dynamical extrapolators" of this surface information to areas where data are not available. The goal is to achieve, through this blending of data and models, a better description of the ocean circulation.

A considerable amount of work has already been done to test different assimilation techniques and to determine how effective they are in constraining numerical models. Most of these investigations have been carried out in the context of the so called "twin experiments", in which the data that are assimilated are produced by the model itself, thus allowing easy verification of the degree of success of the data assimilation process. The use of real data represents a further step and poses several new issues that have not yet been fully examined. In particular, due to the present state of ocean models, as described before, we need to understand the dynamical implications involved in the process of combining data and models that have somewhat different statistical characteristics of their climatology.

In this study we start addressing these issues using a quasi-geostrophic (QG) model of the Gulf Stream area. The data we assimilate are maps of sea surface height (SSH) which have been obtained as the superposition of SSH variability deduced from the Geosat altimeter measurements and a mean field constructed from historical hydrographic data. The surface data have been assimilated by using the 'nudging' technique, a technique that has been implemented in such a way as to achieve a high degree of convergence of the model surface field toward the observations.

The first question that we ask is: "How does the model respond to the surface data constraint? That is, what are the physical processes responsible for the model adjustment and for the final equilibrium state, when surface data are assimilated?" By answering this question we hope to obtain a physical

understanding of the assimilation process, so that our findings can be generalized to other assimilation experiments, and ways of improving the assimilation procedure can be devised.

The second question concerns the success of the assimilation experiment in improving the model climatology, namely "How effective are surface data in constraining the global model behavior? How realistic do the model fields become when surface data are assimilated?" In order to answer these questions we compare the results of the assimilation experiments with several sets of observations available in the Gulf Stream area, including aspects of the mean circulation and eddy climatology as well as measurements collected in a time period partially overlapping the Geosat mission. The latter consist of current meter data that have been obtained in the context of the SYNOP (Synoptic Ocean Prediction) experiment, at different locations and at different depths. The availability of such diverse data sets allows for the verification of both the improvement of the model climatology and also the "realism" of the instantaneous subsurface signature of the assimilated eddy field.

The emphasis of the present study is in understanding the model response to the prescription of a surface streamfunction boundary condition, or, equivalently, of a surface pressure boundary condition. For this reason we assume a complete and uniformly accurate knowledge of the surface streamfunction fields. In the language of estimation theory this study might then be defined as a study "in control": "To which extent can a surface pressure boundary condition control the dynamical system under consideration? And why?"

The novel results of this study are the following:

- The analysis of the model behavior when no data are assimilated represents the first study in which the climatological characteristics of a limited-area, QG model of the Gulf Stream region, including a realistic coastline and open

boundaries are compared with observations. This analysis does not include an exhaustive sensitivity study to the different model parameters. A study of this type is underway (Holland and Schmitz, personal communication). We analyze, here, the climatological behavior of a particular model realization, obtained with a particular choice of the different model parameters, initial and boundary conditions.

- We have described how the model adjusts when surface data are assimilated, the model adjustment time being determined by the time scale of potential vorticity evolution. We have shown that the pattern of the circulation in the model subsurface layers can be related to the characteristics of the surface mean field that is assimilated. The dynamical mechanism into play is the modification of the geostrophic contour distributions produced by the model nonlinearities. The intensity of the flow in the subsurface layers depends upon the strength of the eddy forcing as well as upon the inflow/outflow conditions specified at the open boundaries.

- We have shown that assimilation of surface data can improve considerably some aspects of the model climatology, including characteristics of the mean circulation as well as characteristics of the eddy field. A comparison with in situ current meter time series shows that the model eddy signals remain coherent with the current meter measurements down to approximately 1500m depth. Below this depth the model eddy signal becomes weaker and the coherence drops. The model mean circulation, on the other hand, appears to be in better agreement with the observations at depth. In fact, away from the surface, the constraint of the climatological mean field that is assimilated weakens and the eddy driving effect becomes relatively more important. In particular, the eddy field present in the model during the

assimilation experiment is able to drive a recirculation flow, south of the model Gulf Stream, in good agreement with the observations.

The presentation is organized as follows: In Chapter 2 we introduce the Geosat data that are assimilated. We describe the interpolation procedure used to map the data onto a regular space-time grid, and discuss the characteristics of the final interpolated data sets. In Chapter 3 we present the quasi-geostrophic model used for this study. We also describe how the missing mean component of the surface data has been computed from climatological hydrographic data in a way consistent with the specification of initial and boundary conditions. The *General Circulation* of our model ocean, when no data are assimilated, is analyzed in Chapter 4. This numerical experiment, that we define as the "control run", represents a reference case for understanding how effectively the model behavior is altered by the surface data constraint. To that end the control run is performed by using the same boundary conditions, initial conditions, forcing and frictional parameters that are adopted for the assimilation experiments.

In Chapter 5 we consider the assimilation experiments. This chapter consists of two parts: in the first one we develop a theoretical framework for understanding the assimilation results. The dynamical implications of the surface data constraint are examined by a simple analytical example. In the second part we describe two assimilation experiments that have been performed and we interpret their results in the context of our theoretical framework. Since the surface data that are assimilated consist of a mean part and a time dependent part, we would like to identify the relative contribution of these two components in determining the final results. For this reason we have considered two different experiments: in the first one only the mean field is assimilated, whereas in the second experiment both components (mean + eddies) are used.

After having developed, in Chapter 5, a dynamical understanding of the processes involved in the assimilation procedure we move, in Chapter 6, to the comparison of the results with the available observations. In this context we try to critically assess how successful the surface data constraint is in producing a more realistic model behavior and we also try to identify and explain its limitations. Finally, in Chapter 7, we conclude with a summary of the results obtained and with a discussion of the major findings that have emerged from this study.

Chapter 2

Geosat data

2.1 Introduction

In this chapter we introduce the altimeter data that are used for the assimilation study. The data set consists of measurements of sea surface height collected during the Geosat mission, covering the period November 1986 - December 1988. The Geosat satellite operated on a near-repeat orbit, with a repeat cycle of 17.05 days. The separation between parallel tracks is about 110 km in the area of interest.

Here we describe the basic characteristics of the data set, the statistical interpolation procedure used to map the data on a regular space-time grid and, in particular, we discuss the capability of the resulting data set to properly capture important features of the mesoscale eddy field in the Gulf Stream area. We will use current meter time series taken during a period of time partially overlapping the Geosat mission to assess the degree of realism of the interpolated data set.

2.2 The data set

The Geosat data set has been supplied by the oceanographic group at the Jet Propulsion Laboratory. The oceanic Geophysical Data Record (GDR), produced at the NOAA National Service (Cheney et al., 1987) has been processed at the

Jet Propulsion Laboratory according to the following steps (Zlotnicki et al., 1989, Zlotnicki, 1990):

1) First, data outliers have been removed and the data have been resampled along the satellite's track to a fixed set of latitudes, corresponding to an along-track separation of about 7 km. This procedure is necessary for computing, at each point along a track, a temporal mean which will then be subtracted from each individual repeat.

2) Environmental corrections have been applied. They include the effects, on the altimeter's travel time, of free electrons in the ionosphere and water vapour in the troposphere, computed according to the distributions of free electrons and water vapour predicted by the FNOC (Fleet Numerical Ocean Center) model, as supplied by Cheney et al.(1987). The effects of static response to atmospheric pressure (inverted barometer) have been removed based on the FNOC pressure fields. Estimates of the predictable sea level changes, attributable to tides, have been removed by using the Schwiderski (1980) model.

3) An approximate estimate of the radial position of the satellite has been removed using the Naval Astronautics Group's (NAG) orbit, supplied by Cheney et al. (1987). After this step individual repeats along the same ground track can be offset by a few meters, due the an inaccurate knowledge of the satellite orbit radius. This residual orbit radius error is known to be numerically the largest error of all. For Geosat it is quoted to be as large as 2-3 m rms. Since this error is confined to spatial scales of the order of the radius of the earth several algorithms have been developed for removing long wavelengths from the measurements by subtracting a best-fit curve which minimizes the cross-over differences (Fu and Vasquez,

1988, Tai, 1988). In our case the residual orbit error has been corrected by subtracting a second order polynomial over 2000 km. As discussed by Gaspar and Wunsch (1989) this procedure can also remove signals associated with real oceanic fluctuations at these same spatial scales. However, only the along-track component of these long wavelength signals is affected by the orbit correction procedure. An analysis of sea level oscillations in the tropical Pacific (Perigaud, 1990), for example, shows the presence of equatorial waves with zonal wavelengths of the order of 1000 km after the Geosat data set has been processed using a procedure similar to the one described above for the orbit error correction. The typical length scales of the ocean variability tend to decrease with latitude (Stammer and Böning, 1992). At mid-latitudes, analysis of along-track wavenumber spectra in the North Atlantic (Le Traon et al., 1990, Stammer and Böning, 1992) show the tendency, for the spectral energy, to plateauing at wavelengths longer than a few hundred kilometers. Therefore we expect that, in the area we are considering, most of the energy is confined at scales shorter than the ones affected by the orbit error correction.

4) The temporal mean, relative to the years 1987 - 1988, has been subtracted. The temporal mean has been defined, at each point along the track, if at least 70% of all possible measurements were available for that point. The step of mean removal is necessary in order to eliminate the uncertainties associated with the present knowledge of the geoid, uncertainties which are comparable with the signal we want to measure. Therefore only the temporal changes in the sea surface height can readily be obtained from altimetry. The definition of an absolute sea surface topography, which is necessary for this work, will require the determination of a mean sea surface height field from other sources. This will be discussed in the next chapter. We should notice that

the process of mean removal can affect the final estimate of the variability. In fact creating a mean from samples at 17-day intervals will alias motion at periods of 34 days or shorter into longer periods. However, as shown by Wunsch (1989b), due to the presence of several repeats over the area of interest within a 17-day period, aliasing does not seem to be a dominant issue.

2.3 Statistical interpolation of the data

For the assimilation experiment described in this study we have decided to use a data set interpolated onto the model grid at equally spaced intervals of time so that the data can be assimilated at each grid point and at each time step. The alternative approach would have been the assimilation along the satellite tracks at the times of the satellite passages, so that the model would have been the dynamical interpolator among data values. There are several reasons for our choice.

First of all, it is not clear, from a dynamical viewpoint, what is the best way of implementing a data assimilation scheme for an irregular data distribution. In fact, as shown by Holland and Malanotte-Rizzoli (1989) in the context of twin experiments, the effectiveness of the assimilation procedure in driving the model ocean toward the control run depends not only on the space-time resolution of the data, but also on the technical choices made in the actual implementation. For example they found that assimilation of the quantity $\frac{\partial^2 \psi}{\partial \xi^2}$, where ψ is the surface streamfunction and ξ is the along-track coordinate gives better results than assimilation of the relative vorticity $\zeta = \frac{\partial^2 \psi}{\partial x^2} + \frac{\partial^2 \psi}{\partial y^2}$. The reasons for this result are not clear yet.

The success of the assimilation procedure, in their experiments, was also dependent upon the typical model space and time scales and on the sampling characteristics of the assimilated data set. A spectral analysis that I have performed on their results showed, for example, that continuous assimilation of data characterized by a coarse time sampling resulted in a severe damping of the missing frequencies in the assimilated model as well. When a strong nudging was applied the model frequency spectra became very similar to the frequency spectra of the assimilated data. The damping of the model signals affected especially the fast barotropic waves, whose frequencies were poorly resolved by the coarsely sampled data.

In a twin experiment the typical model scales coincide with the ones of the 'real world'. However, this is not necessarily true when real data are considered. In fact, as we will see in chapter 4, the model frequency and wavenumber spectra differ from the ones derived from observations, with the degree of difference dependent on the geographical location considered. In particular the spatial scales seem to be longer in the model than in the data. In the ideal case, in which the model spectral characteristics were in 'good' agreement with the observations, an assimilation scheme in which data are inserted only along the tracks at the times when they are available would allow the model more freedom for developing those scales which are not resolved by the data. These scales could be updated by the assimilation process through nonlinear processes. However, since a perfect agreement is lacking, it is unclear to what extent the model can reconstruct the unresolved scales in the correct way and at the correct locations.

A final consideration comes from the fact that the model mean streamfunction field is not completely 'realistic', as we will discuss in next chapter. By assimilating data at each grid point the model will be driven, everywhere, toward

the local estimate of the surface mean state. On the other hand, assimilating data only along the satellite tracks would allow some portions of the model domain to drift back to the model mean rather than to the 'observed' mean state, a much more complicated and difficult scenario to understand. For all these reasons we think that an experiment in which complete surface information is supplied at all times is the first logical and necessary step for trying to understand the way the model dynamics is affected by the data assimilation process, which is the major goal of this work. Our results can represent a reference case for future studies in which alternative assimilation schemes are implemented.

So we will assume that the maps of sea surface height created by the statistical interpolation procedure are the time dependent component of 'the observations' and we will try to understand how the scales which they contain affect the model behavior. In section 2.4 we will discuss the degree of 'realism' of the interpolated data by comparison with the current meter time series mentioned earlier. In Chapter 6 we will compare the same current meter data with the results of the assimilation experiment at different depths, in order to assess how "realistically" the surface information is extrapolated downward. The degree of agreement between current meter measurements and surface geostrophic velocities from our interpolated maps defines the best result that can be expected in the comparisons performed in Chapter 6.

The algorithm used for the statistical interpolation is the 'successive corrections' method, formerly used in meteorology (Tripoli and Krishnamurti, 1975). The name, first introduced by Cressman (1959), refers to the iterative nature of the algorithm. In fact four iterations are performed using spatial covariance functions with decreasing radii in order to capture smaller and smaller scales. The procedure is similar to the one outlined by Roemmich (1983) in his estimation of

hydrographic quantities in the Florida Strait. The spatial covariance functions are Cressman functions, $(R^2 - r^2)/(R^2 + r^2)$, where r is the distance between the data point and the analyzed point and R is the correlation distance. R ranges successively from 2° to 1.5° , 1.25° and 1° through the different iterations. Thirty-four days of altimeter data centered on the time of the analysis are introduced with an e-folding scale of 5 days for each of the analyses, performed every 2 days. The description of the algorithm and the considerations which led to the parameter choices are given in Appendix A.

The final interpolated data set consists of a series of sea surface height maps, at 2 day intervals, spanning the period November 1986 - May 1988. During the last seven months of the Geosat mission, from June 1988 to December 1988, the data coverage degrades considerably. In fact, not only are the descending tracks missing in most of the domain, but also the ascending tracks are very often absent, leading to large areas without altimetric information. Therefore the data after May 1988 have not been used.

The time interval of two days has been chosen because we want to assimilate data continuously in time. Time scales shorter than a few days do not seem to be relevant in the model dynamics, so that we can interpolate linearly between our bi-daily maps to obtain data to assimilate at every time step (one hour) of our model run. The choice of the two day time interval does not imply that the Geosat data actually contain information at periods as short as four days. The exact spectral content of altimetric measurements is still a topic of research (Wunsch, 1989b), due to the very irregular space-time distribution of the satellite data. However, even if each track is revisited by the satellite not more often than every 17 days, oceanic information can be gained from neighboring tracks within the satellite subcycle

(three days), so that we can expect a better time resolution than the one dictated by the 17 days repeat period.

As an example of a typical interpolated map, we show, in Fig. 2.1a, the eddy streamfunction field corresponding to the day 6 January 1987. The spatial distribution of the data used for creating that map is shown in Fig. 2.1b. This distribution corresponds to the data available in the area in a time window of 34 days centered on the day of the analysis. Most of the data are concentrated along the ascending tracks. In fact, as mentioned before, most of the descending tracks are missing in this area due to a malfunctioning of the altimeter. Note that the distribution of the eddy field is suggestive of the mean position of the Gulf Stream.

The associated geostrophic velocities are shown in Fig. 2.1c for the $10° \times 10°$ square centered at 60°W, 37°N. This area lies in the range of latitudes where the variability is most intense. We can see several energetic cyclonic eddies, with velocities up to about 120 cm/s.

2.4 Comparison with current meter data

The current meter data which are used for the comparison were collected in the context of the SYNOP (Synoptic Ocean Prediction) experiment at the SYNOP East array, centered at about 55°W (Hogg, personal communication). The SYNOP East array was deployed from September 1987 to August 1989. Each of the moorings included a minimum of two current meters, located around 500 m and 4000 m. Some of the moorings were equipped with current meters at the additional depths of about 250 m, 1000 m and 1500 m. The location of the moorings and the depths of the relative current meters are given in Table 2.1. The position of the moorings in the Gulf Stream region, as supplied by Hogg, is shown in Fig. 2.2.

The data consist of daily averages of zonal and meridional velocity components. The temporal mean has been removed, for comparison with the time dependent part of the altimetric fields. Similar time series for the zonal and meridional surface geostrophic velocities were computed from the bi-daily eddy streamfunction fields obtained from the statistical interpolation of Geosat data, starting from September 1987.

In Figs. 2.3 and 2.4 we show, as typical examples, the comparison of the time series at two different locations, at the same longitude of 54.67°W. The first location (Fig. 2.3) is the one at 40.87°N, the second (Fig. 2.4) is at 37°N. The depth of the current meters used for the comparison is 247 m at both moorings. Figs. 2.3a and 2.4a represent the zonal velocity, Figs. 2.3b and 2.4b the meridional velocity. In all figures the solid line represents the current meter time series, while the dotted line represents the evolution of the geostrophic velocities. Day 0 in the abscissa corresponds to 1 September 1987.

In both examples the comparison shows striking similarities in the general behavior of the two time series. In particular, the most energetic, low-frequency events present in the current meter records can be observed also in the geostrophic velocities. This result is even more remarkable considering that at least 50% of Geosat data is missing in this area with respect to the expected data coverage for a perfect altimeter operation. Also we are here comparing surface geostrophic velocities with total velocities measured at some depth below the surface. In the time series at 37°N peak velocities obtained with the Geosat data are often smaller than the ones observed in the current meter data. At both locations we can often observe a phase shift. Also higher frequencies are generally filtered in the surface velocity time series. These characteristics can be considered a consequence of the space-time interpolation of the altimeter data.

Figs. 2.5 to 2.9 show the comparisons between the five available current meter spectra at ~250 m depth and geostrophic velocity spectra at the same locations. In the same figures we also show coherences and phases between the current meter time series and the geostrophic velocity time series. All the spectra have been computed considering time series of the same durations, so that they can be easily compared. A running average over 9 frequency bins has been performed on the periodograms, in order to increase statistical reliability. This procedure leads to approximately 17 degrees of freedom, which is the value used in the estimate of the corresponding confidence interval. In these figures the first panels (a) show the spectra of the zonal velocities, while the second panels (b) refer to the meridional velocities. In all cases the spectra obtained from the geostrophic velocities (dashed line) are quite similar, both in shape and energy level, to the ones obtained from the current meter measurements (solid line). However, the geostrophic velocity spectra tend to decrease faster, at higher frequencies, than the corresponding current meter spectra. This result can probably be explained in terms of the temporal smoothing associated with the interpolation procedure. However, the presence of ageostrophic motion associated with high frequency meandering processes (Johns, Watts and Rossby, 1989) could also be partially responsible for the lower energy level observed in the Geosat spectra. Most of the differences lie within the 95% confidence interval, which is shown in all figures.

Since we are here considering surface estimates of geostrophic velocities and measurements at about 250 m depth, comparisons of both time series and spectra can only be approximate. We have therefore computed coherences and phases in order to better quantify the degree of agreement between the Geosat data and the current meter measurements. The coherence is a measure of the correlation between the different frequency components contained in the two time series, while the phase quantifies how 'in phase' these frequency components are. Coherences

and phases will also be computed between the current meter records and the results of the assimilation experiment. The present analysis thus represents the frame of reference for assessing how successful the assimilation experiments will be.

In Figs. 2.5 to 2.9 panels (c) show the coherences of zonal velocities (solid line) and meridional velocities (dotted line), while panels (d) show the phase differences, the solid lines referring to the zonal velocities and the dotted lines to the meridional velocities. The results for both velocity components show a high coherence, much above the significance level (dashed line), for periods longer than about thirty days. At higher frequencies the coherence drops to values which are not statistically significant. Periods longer than about 30 days have generally very small phase shifts. The reason for the loss of coherence at periods shorter than 30 days is not clear. The coarse time sampling of the altimetric measurements at each location (the repeat period is 17.05 days) as well as the dominance of ageostrophic effects at these frequencies could represent possible explanations. In Chapter 6, where the results of the assimilation experiments will be compared with the current meter measurements at depths, only the coherence at periods longer than approximately 30 days will be considered for assessing the success of the assimilation.

2.5 Eddy kinetic energy distribution in the interpolated maps

The eddy kinetic energy level and distribution is one of the quantities that models are often not able to reproduce correctly (Schmitz and Holland, 1982, Schmitz and Thompson, 1992). One of the aspects we want to analyze in this work is the way the model extrapolates the eddy intensity of the surface data to the subsurface layers. Therefore we are interested in assimilating surface data with the 'correct' energy level. The eddy kinetic energy distribution calculated

geostrophically from our statistically interpolated fields is shown in Fig. 2.10a. It has been compared both with the 'classical' map of surface eddy kinetic energy constructed by Richardson from surface drifter data (Richardson, 1983b) and with the eddy kinetic energy distribution computed by Le Traon et al. (1990) from Geosat data themselves. Richardson's estimate of surface eddy kinetic energy, obtained from data averaged over $2° \times 2°$ squares, is reproduced in Fig. 2.10b.

The general pattern of eddy kinetic energy distribution is very similar in all three cases: the area of highest values is centered around the position of the mean Gulf Stream and follows the Stream path around the Grand Banks. The eddy energy decreases away from the stream to values of about 200 cm^2s^{-2}, which are found both in the gyre interior, south of the stream, and along the continental shelf area to the north. The maximum of about 1000 cm^2s^{-2}, found by Richardson (1983b) in the Newfoundland basin, is also present in our results.

The main discrepancy between Fig. 2.10a and the corresponding maps prepared by the other authors is in the reduced peak values, in the area between 60°W and 70°W. In fact in this area Richardson (1983b) finds values greater than 2000 cm^2s^{-2} with isolated maxima higher than 3000 cm^2s^{-2}. In the results of Le Traon et al. (1990) the area with values greater than 2000 cm^2s^{-2} is even larger than in Richardson's (1983b). The values we find, on the other hand, are slightly smaller than 2000 cm^2s^{-2}, with an isolated maximum of about 2400 cm^2s^{-2} at 64°W, 38°N. The reason for our smaller values is clearly in the smoothing effect produced by the statistical interpolation, which filters out small scales, especially the spatial ones contained by the data in the along-track direction. This is illustrated in Fig. 2.11, where two of the original profiles of sea surface height (solid line), along the tracks shown in Fig. 2.11c, are compared with the ones obtained by reprojecting the interpolated data, on the same days, along the same tracks. The abscissa in the

figures gives the increasing latitude along the ascending tracks. We can see that the finer scales have been removed and the peak values reduced.

The consequences of the interpolation procedure on the characteristics of the wavenumber spectra are illustrated in Fig. 2.12, where we compare the wavenumber spectra in the along-track direction obtained from the original data (solid lines) with the corresponding spectra obtained from the interpolated data (dotted lines). 18 repeats, at intervals of 34 days, have been used for the evaluation of the spectra in Fig. 2.12. The two panels correspond to the same two tracks shown in Fig. 2.11c, panel (a) corresponding to track A and panel (b) to track B. The 18 profiles of sea surface height used for the computation of the mean spectra can be considered as statistically independent. We have also performed a running average over 3 wavenumber bins in the periodogram. This leads to approximately 90 degrees of freedom, which is the value used to compute the confidence interval shown in the figures. The spectra from the interpolated data are practically coincident with the spectra from the original data at wavelengths longer than approximately 240 km, while at shorter wavelengths the energy level is considerably reduced.

The procedure adopted by Le Traon et al. (1990) was to compute the geostrophic velocities, and the associated kinetic energy, directly from the along-track slopes, assuming isotropy. They then averaged the kinetic energy values in 2° squares and performed an optimal interpolation to map them. The reduced gradients in the sea surface height profiles in the along-track direction, resulting from the statistical interpolation procedure, can therefore explain the differences between our results and the results of Le Traon et al. (1990).

We should notice, however, that the maximum values of eddy kinetic energy seem to be very sensitive to the particular procedure used to average the data in space and time. In fact the map of eddy kinetic energy which is obtained from

the drifter data, when they are processed in the same way as the Geosat data (Le Traon et al., 1990), shows reduced peak values, which are very similar to the ones we obtain. We can conclude, therefore, that the eddy kinetic energy distribution associated with the interpolated data that we are going to assimilate into the model can be considered in reasonably good agreement with the other available estimates of this quantity.

Before concluding this section we consider a more direct comparison between the eddy kinetic energy profile derived from the interpolated Geosat maps at 55°W, and the profile obtained from the surface drifters at the same longitude. The comparison is shown in Fig. 2.13. In this figure the dashed line represents the eddy kinetic energy derived from Geosat, averaged over two degrees of longitude, while the dots represent the estimates of eddy kinetic energy computed from the drifters data over $2° \times 2°$ squares. Fig. 2.13 shows that the maximum value is reached at approximately the same latitude in both cases, but this peak value is about 40% lower in the estimate from Geosat. Also, in the profile from the Geosat data the eddy kinetic energy decreases much faster, both north and south of the maximum, than in the profile from the drifter data. Similar comparisons will be carried out in Chapter 6 between the results of the assimilation experiment and estimates of subsurface eddy kinetic energy obtained from SOFAR floats (Owens, 1991). The comparison in Fig. 2.13 thus represents the proper frame of reference for assessing the success of the assimilation in producing the "correct" eddy kinetic energy levels in the subsurface model layers. It tells us that if the model eddy kinetic energy is underestimated in the assimilation results with respect to the estimates derived from the float data, this can be considered as a consequence of the assimilated eddy field and not the expression of a failure of the assimilation procedure.

APPENDIX A

The 'successive correction' algorithm is an iterative algorithm. Covariance functions with decreasing radii are used in the different iterations in order to capture smaller and smaller scales. At each iteration corrections to the previous estimate are computed at each grid point according to the following formula:

$$F_x^a(v+1) = F_x^a(v) + \frac{\sum_{i=1}^n w_{xi}(v)(F_i^0 - F_i^a(v))}{\sum_{i=1}^n w_{xi}(v)} \qquad (A.1)$$

where $F_x^a(v)$ is the interpolated (analyzed) value at position x, iteration v; F_i^0 is an observed value at position i; and $F_i^a(v)$ is the estimate of the field at position i for the vth iteration. The weights, $w_{xi}(v)$, involve separate space and time factors:

$$w_{xi}(v) = \begin{cases} \exp[-(t_x - t_i)^2/1.44T^2] \times (R_v^2 - r_{xi}^2)/(R_v^2 + r_{xi}^2) & R > r \\ 0 & r \geq R \end{cases} \qquad (A.2)$$

where t_i is the time at observation point i, r_{xi} is the spatial distance between interpolation point x and observation point i, and T and R_v are correlation time and space scales, respectively. T was chosen to be 5 days, a time much shorter than the 34 days search window. This value for the Gaussian e-folding scale was intended to include altimeter data points from tracks west (-3 days) and east (+3 days) of any particular track, while preserving ocean signals in the mesoscale band and longer. The spatial radii R_v are 2°, 1.5° , 1.25° and 1° for each of the four iterations, respectively. These values were determined by trial and error in order to capture scales as small as possible while still producing smooth maps.

The successive correction algorithm is not an optimal algorithm, since the weights w_{xi} in (A.1) are not chosen so to minimize the expectation value of the interpolation error (Bretherton et al., 1976). The reason for the choice of a suboptimal algorithm is mainly associated with computational efficiency. Due to the need of inverting large matrices, the optimal interpolation schemes involve a large computational load, especially when the analyzed fields are computed very

frequently in time. Also, the assumptions underlying the determination of the optimal weights (isotropy and homogeneity of the statistics, knowledge of the error statistics, etc.) are often not met in the actual implementation of the algorithm, thus reducing its optimal character.

The successive correction scheme does not supply, automatically, error maps for the interpolated fields. Interpolation error maps should be consider together with the interpolated fields, in order to be able to assess the relative reliability of different estimated values. One can compute error fields for the successive correction algorithm, as outlined by Wunsch (1989a). However, this would introduce a computational load comparable with the one of the optimal interpolation algorithm itself. Since we are not using an assimilation scheme which can rigorously account for the data error distribution, we delay, for the moment, the computation of the error maps.

Mooring # EXP	BUOY	Lat (N)	Lon (W)	Water Depth (m)	Duration From 9/87 Day	Duration To 8/89 Day	Current Meter Nominal Depths (m)				
Setting # 1											
1	857	41 36.2	54 39.0	4877	20	24	269	522			4018
2	858	40 51.4	53 41.6	5090	21	23	244	497			3992
3	859	40 51.7	54 40.0	5062	21	24	247	500	1008	1516	3995
4	860	40 52.4	55 40.2	5091	22	25		485			3996
5	861	40 08.0	54 40.2	5193	23	23		499	1007	1510	3997
6	862	39 23.0	53 38.9	5252	24	22		485			3997
7	863	39 24.0	54 34.8	5258	25	21		499	1006	1510	3996
8	864	39 23.8	55 40.4	5259	27	20		484			3995
9	865	38 34.9	54 40.3	5331	27	19		500	1007	1511	3997
10	866	37 52.3	53 40.0	5386	28	17	246	500			3995
11	867	37 48.1	54 39.9	5375	29	16	252	505	1012	1520	3999
12	868	37 00.2	54 40.2	5404	29	15	247	500			3996
13	869	37 48.0	55 39.9	5339	30	13		497			4008

Table 2.1 Mooring information for the SYNOP East Array as supplied by Nelson Hogg. The first column is the experiment mooring number. The second column is the Buoy Group's consecutive mooring number. The depths were computed by using program NOYFB.

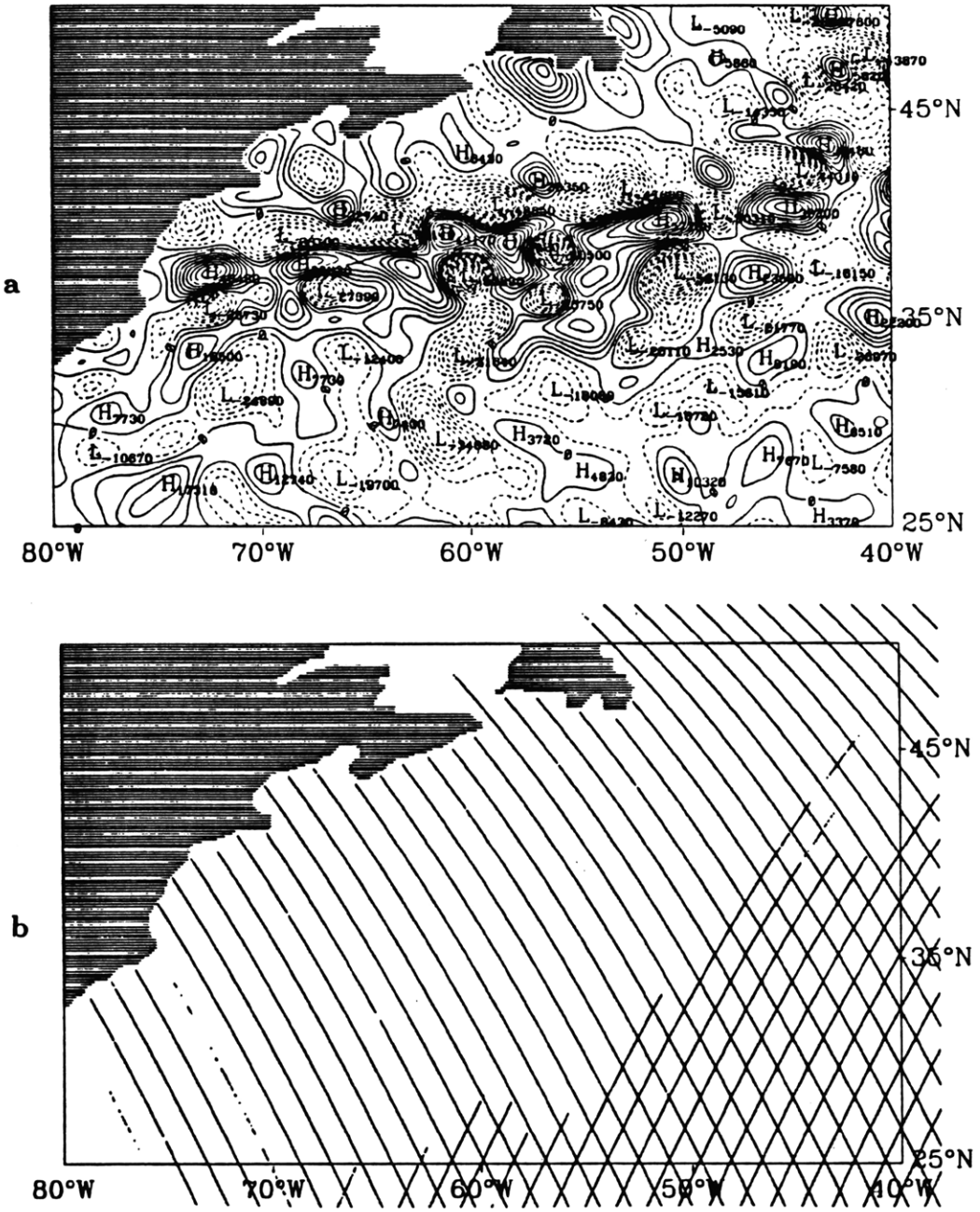

Fig. 2.1 (a) Example of eddy streamfunction field obtained by space-time interpolation of the Geosat data. It corresponds to the day 6 January 1987. (b) Spatial distribution of the Geosat data used for creating the eddy field in Fig. 2.1a. The data are relative to a time period of 34 days, centered at 6 January 1987.

c

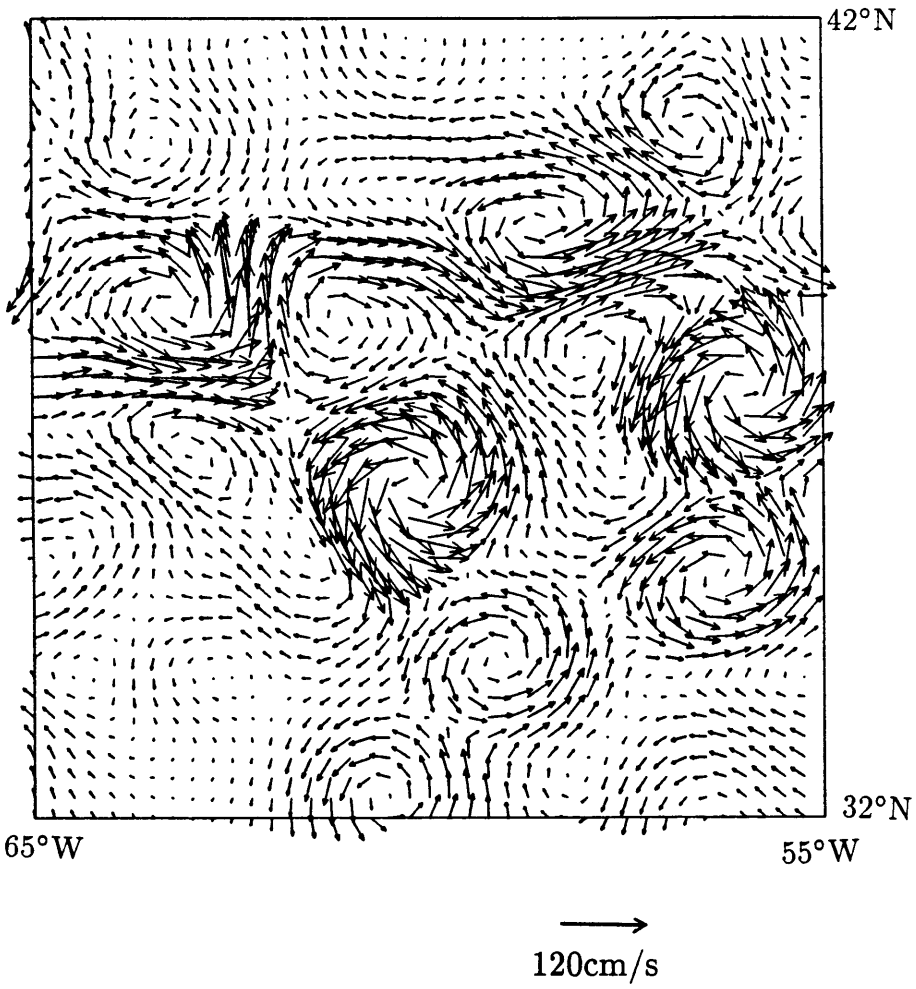

Fig. 2.1 (continued) (c) Eddy velocities derived from the streamfunction field in Fig. 2.1a. in the $10° \times 10°$ square centered at 60°W, 37°N. Maximum velocities are about 120cm s^{-1}.

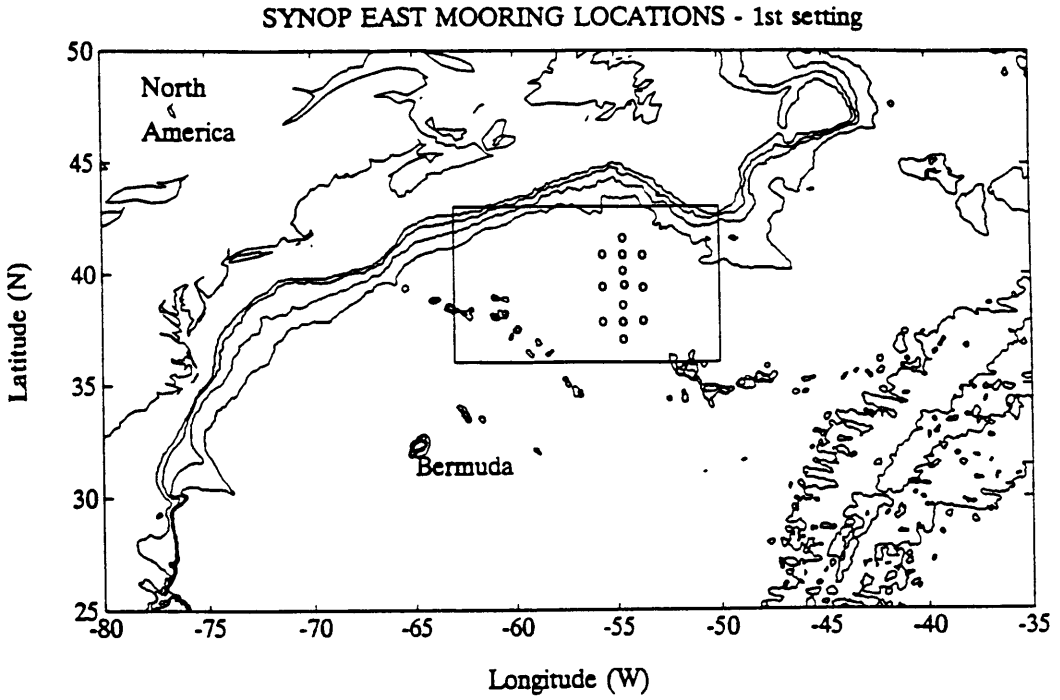

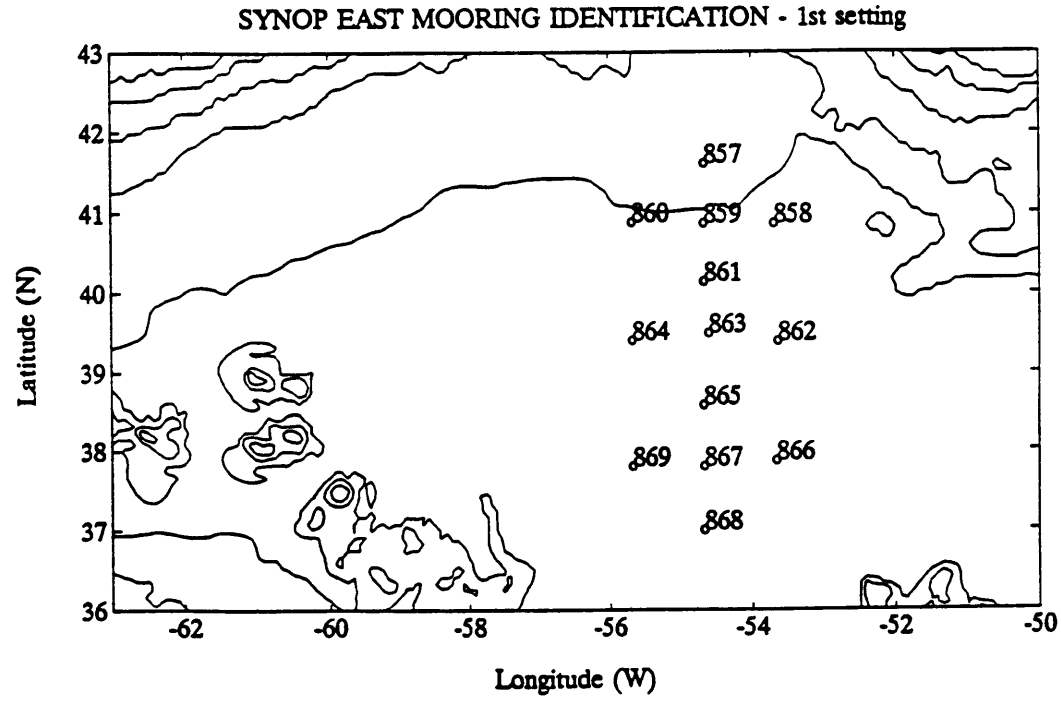

Fig. 2.2 Position of the moorings at the SYNOP east array within the Gulf Stream area. The figure has been supplied by Nelson Hogg.

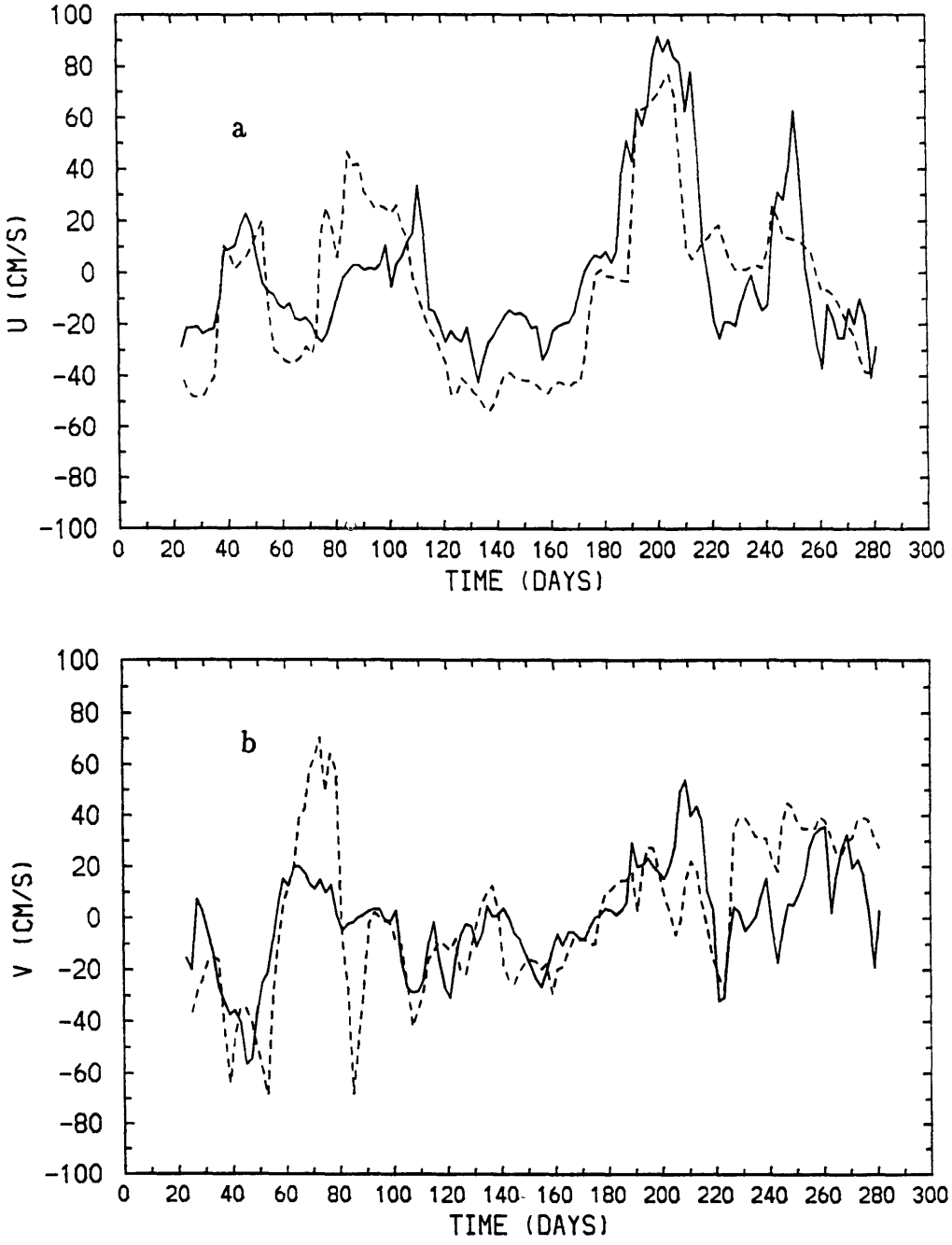

Fig. 2.3 Comparison of velocity time series at 40.87°N, 54.67°W. The solid line represents current meter measurements at 247m depth. The dashed line represents the time evolution of the surface geostrophic velocity derived from the interpolated Geosat maps, available at 2 day intervals. (a) Zonal velocity components. (b) Meridional velocity components.

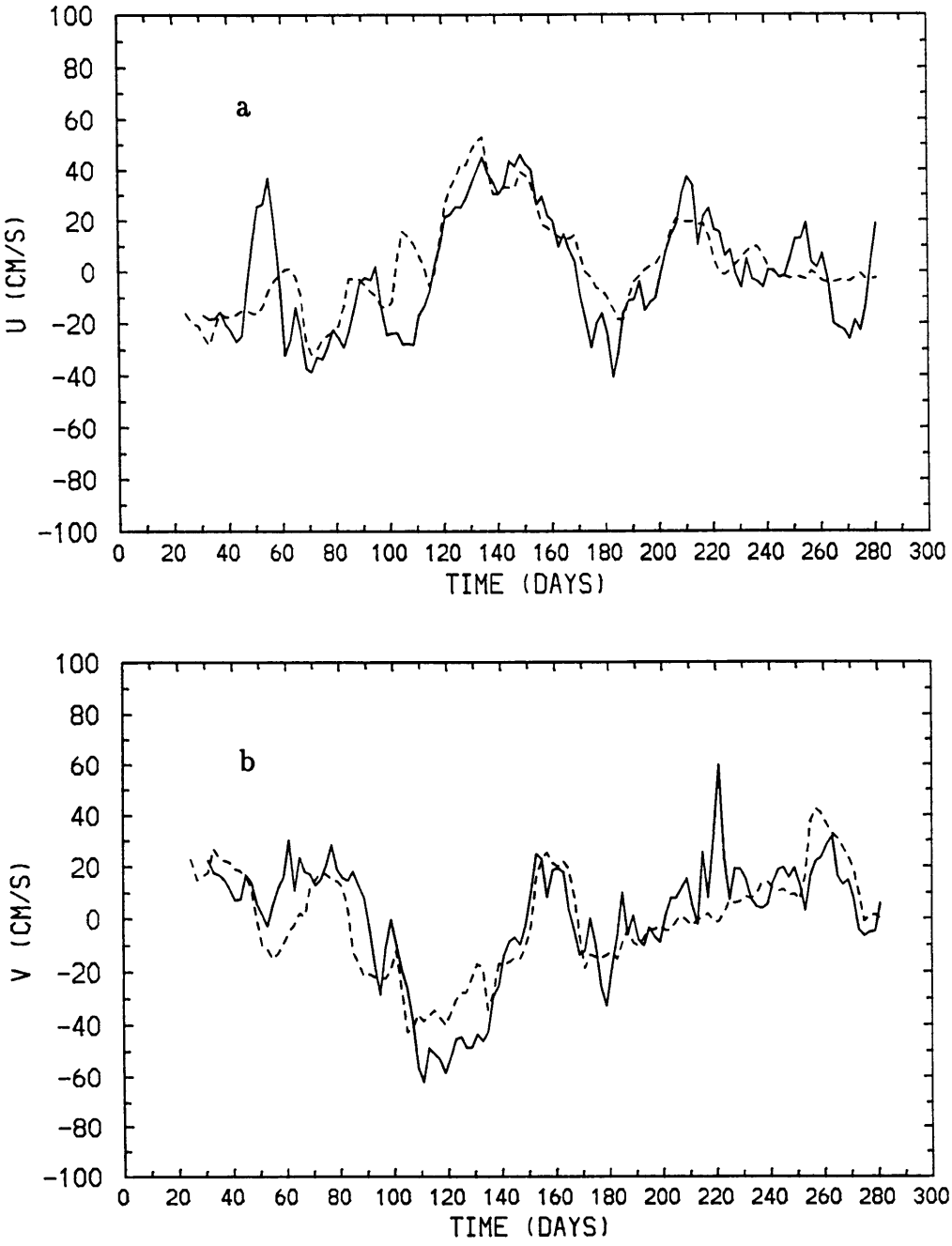

Fig. 2.4 Same as in Fig. 2.3, but at 37°N, 54.67°W.

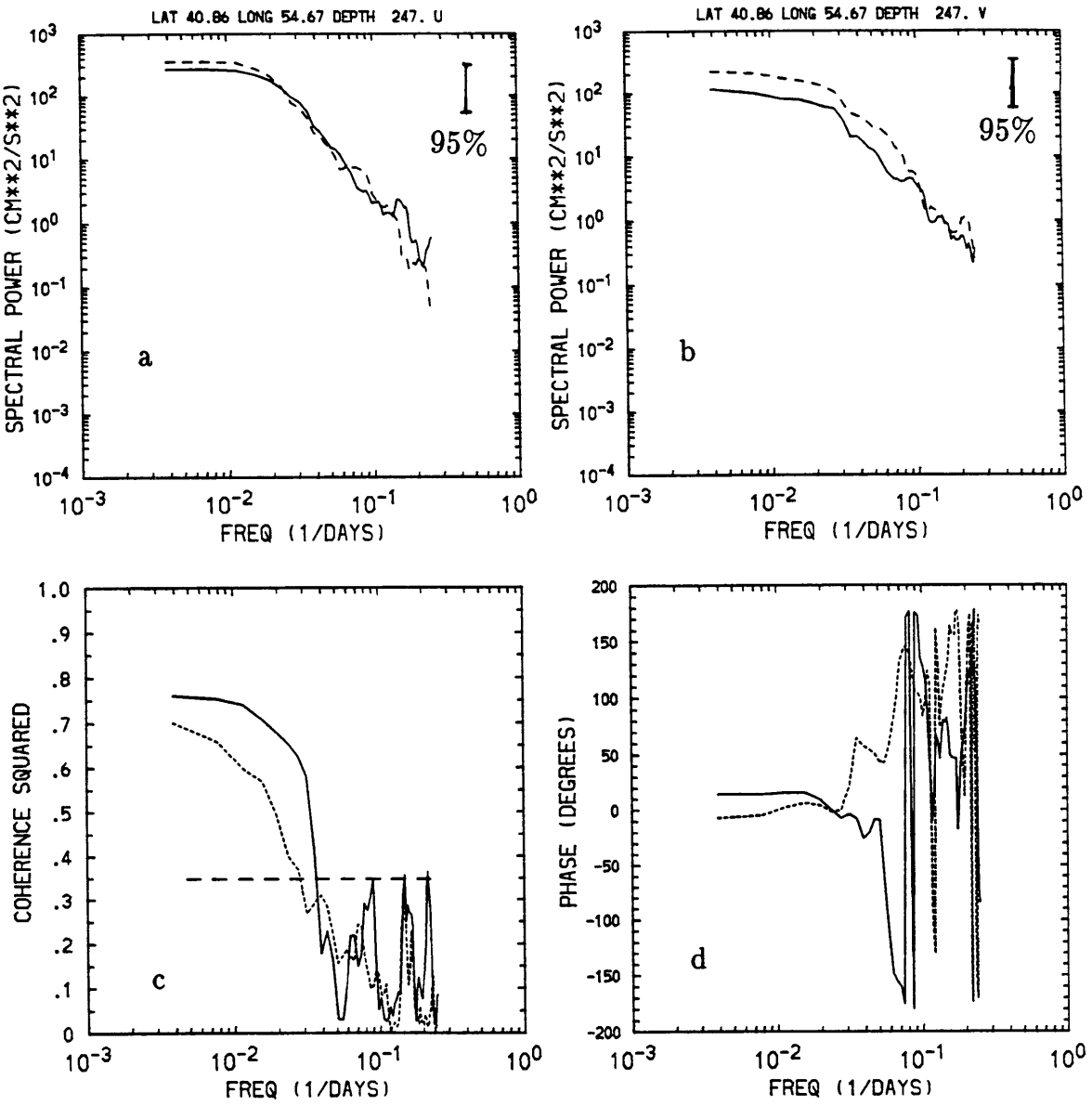

Fig. 2.5 (a) Comparison of zonal velocity spectra at 40.87°N, 54.67°W. The solid line represents the spectrum from the current meter measurements at 247m depth. The dashed line represents the spectrum of zonal geostrophic velocities derived from the interpolated Geosat data. (b) Comparison of meridional velocity spectra at 40.87°N, 54.67°W. (c) Coherence squared between current meter time series and geostrophic velocity time series at 40.87°N, 54.67°W. The solid line refers to the zonal velocity component, the dotted line to the meridional velocity component. (d) Phase difference between current meter time series and geostrophic velocity time series at 40.87°N, 54.67°W.

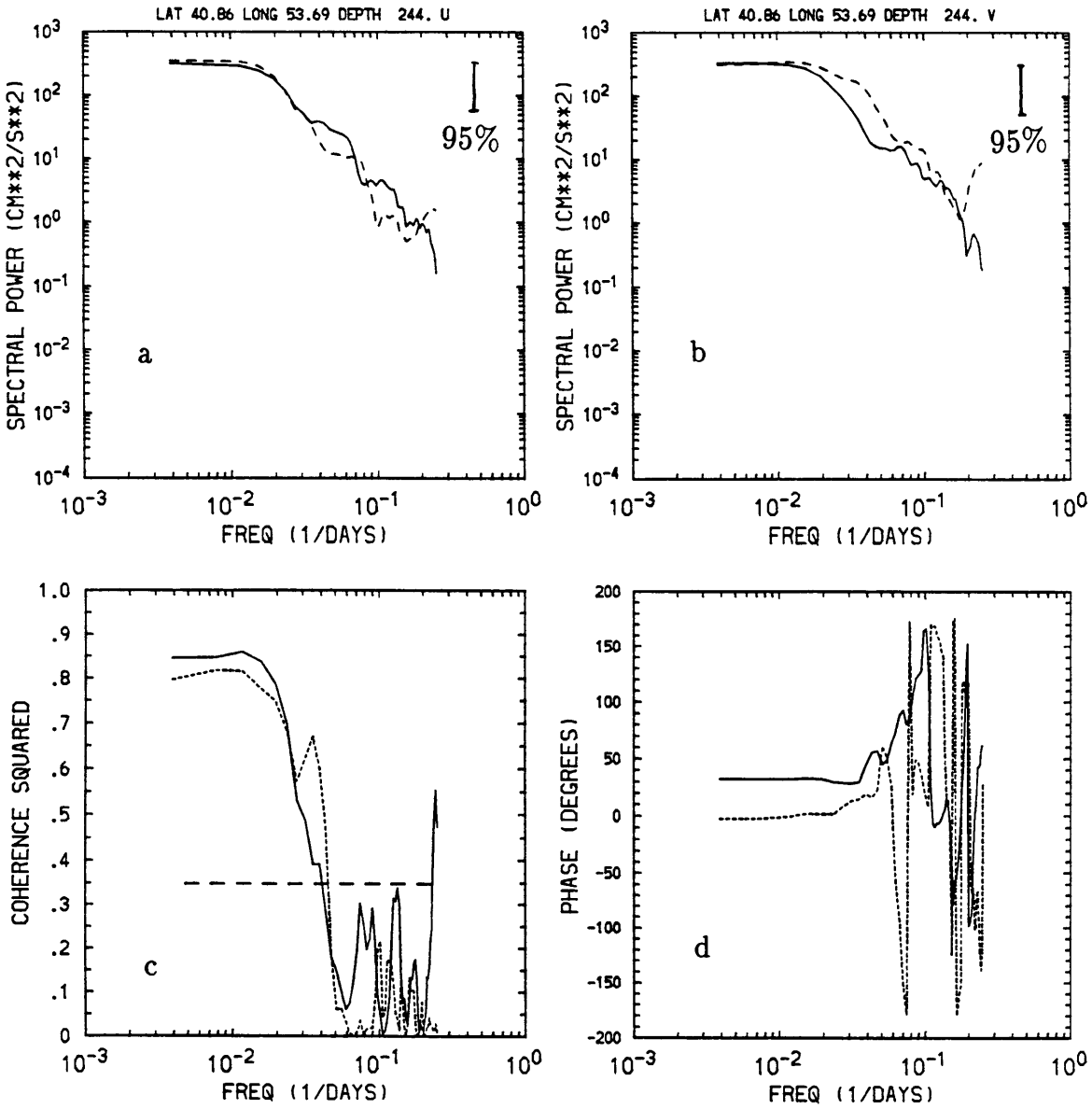

Fig. 2.6 Same as Fig. 2.5, but at 40.86°N, 53.69°W.

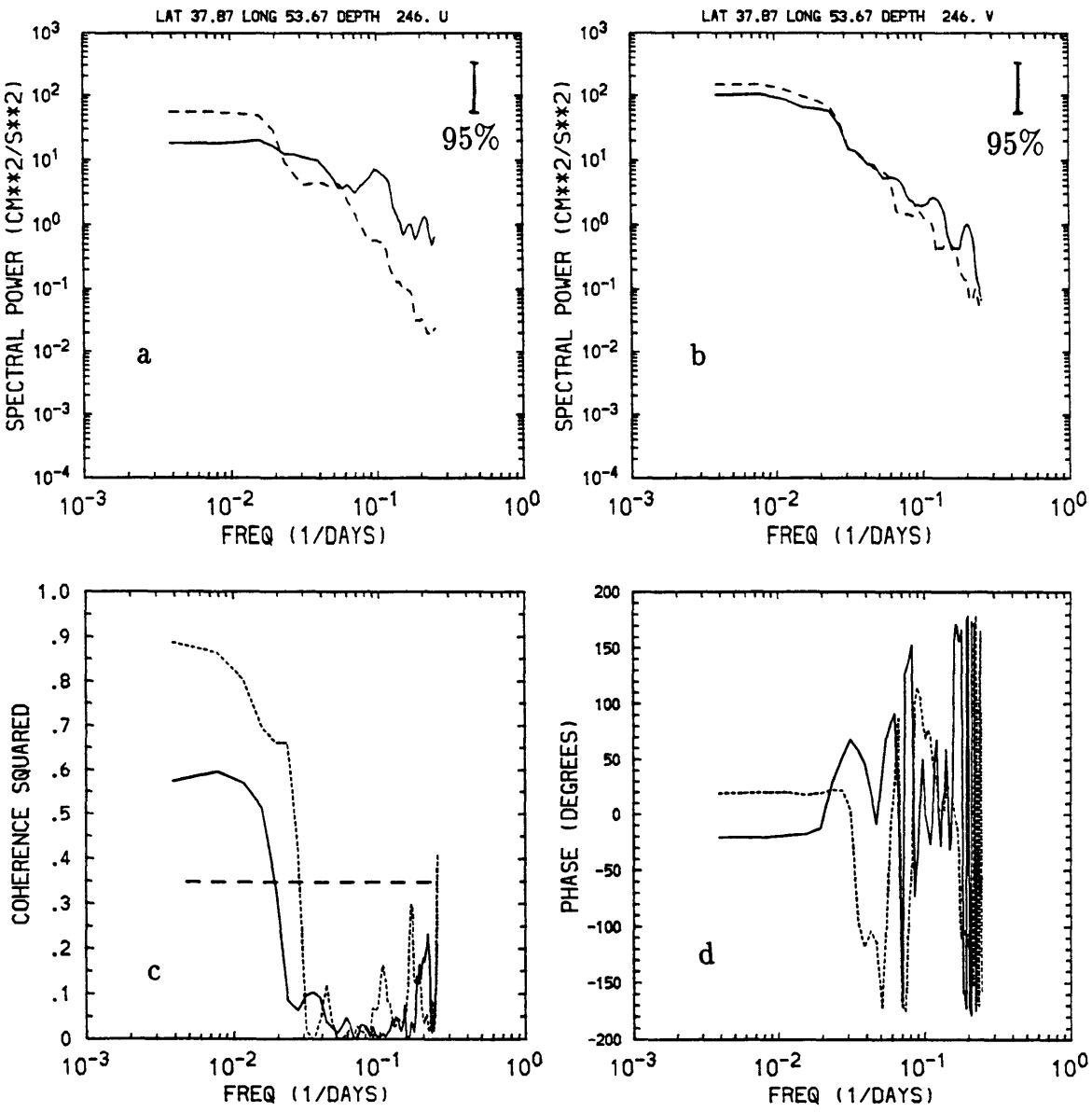

Fig. 2.7 Same as Fig. 2.5, but at 37.87°N, 53.67°W.

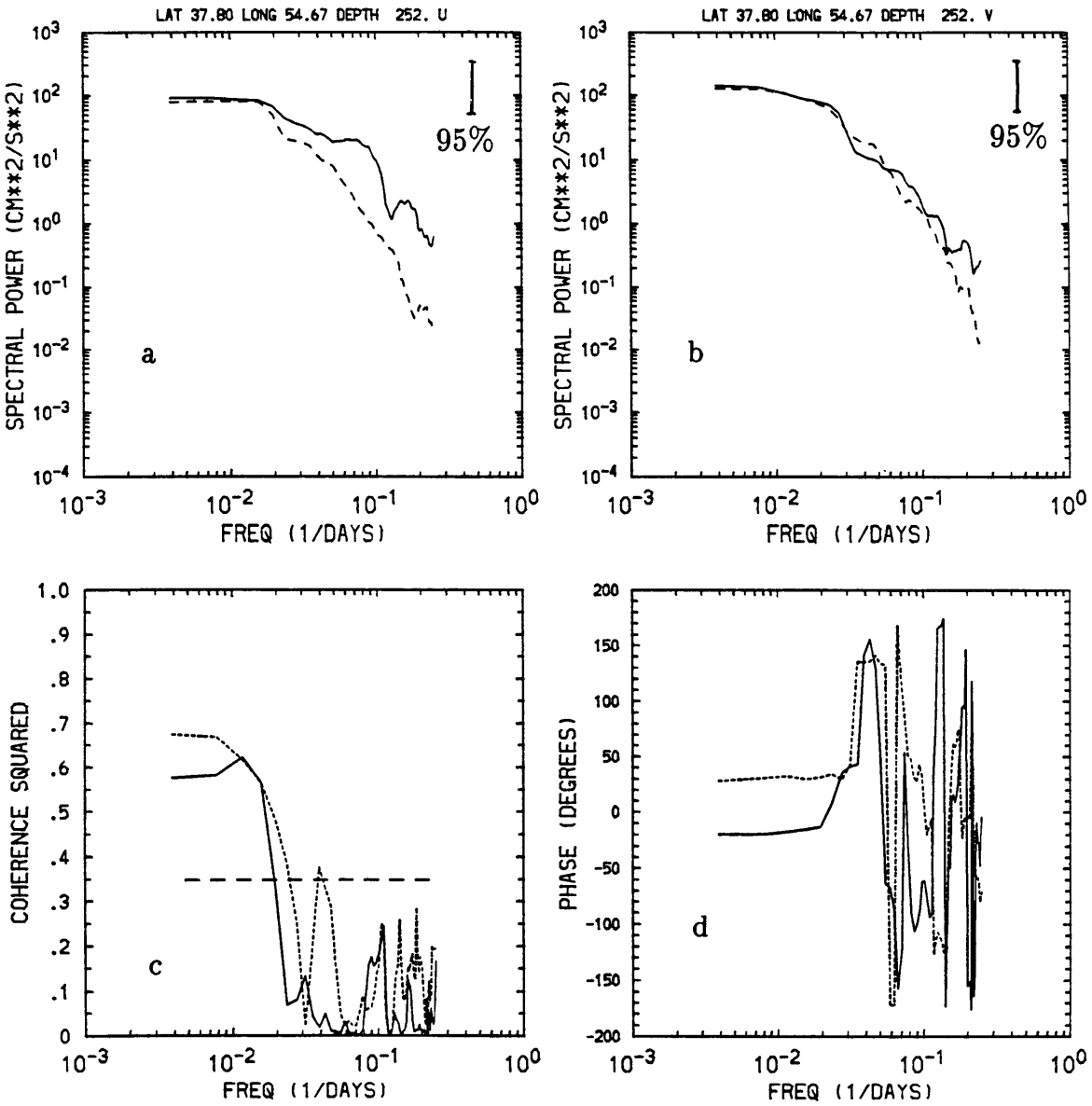

Fig. 2.8 Same as Fig. 2.5, but at 37.80°N, 54.67°W.

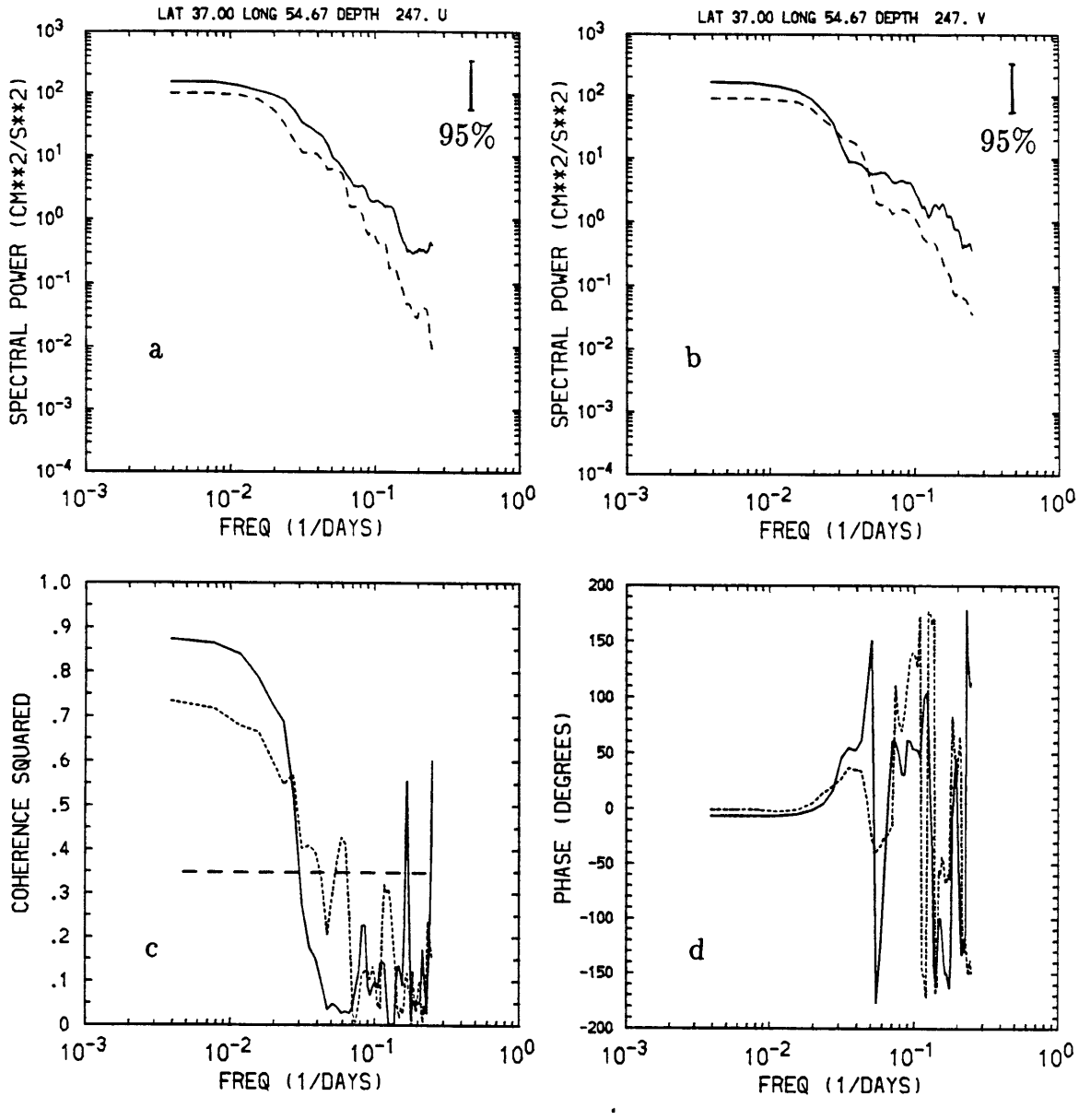

Fig. 2.9 Same as Fig. 2.5, but at 37.00°N, 54.67°W.

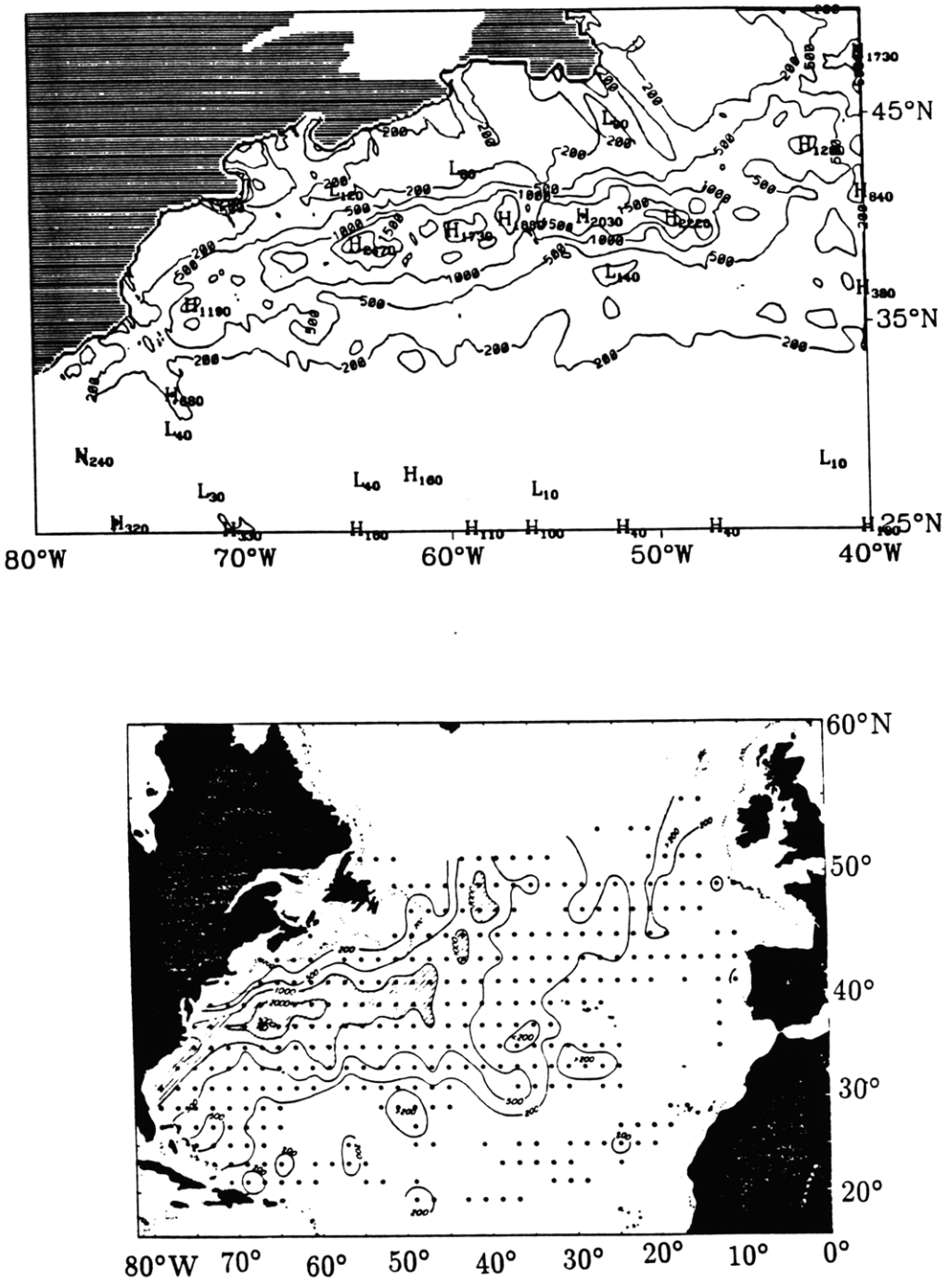

Fig. 2.10 (a) Eddy kinetic energy distribution derived from the interpolated Geosat data. (b) Surface eddy kinetic energy distribution computed by Richardson from drifter data, based on values in 2° × 2° boxes. The dots show location of boxes containing more than 20 observations. Reproduced from Richardson (1985). Units are cm^2/s^2.

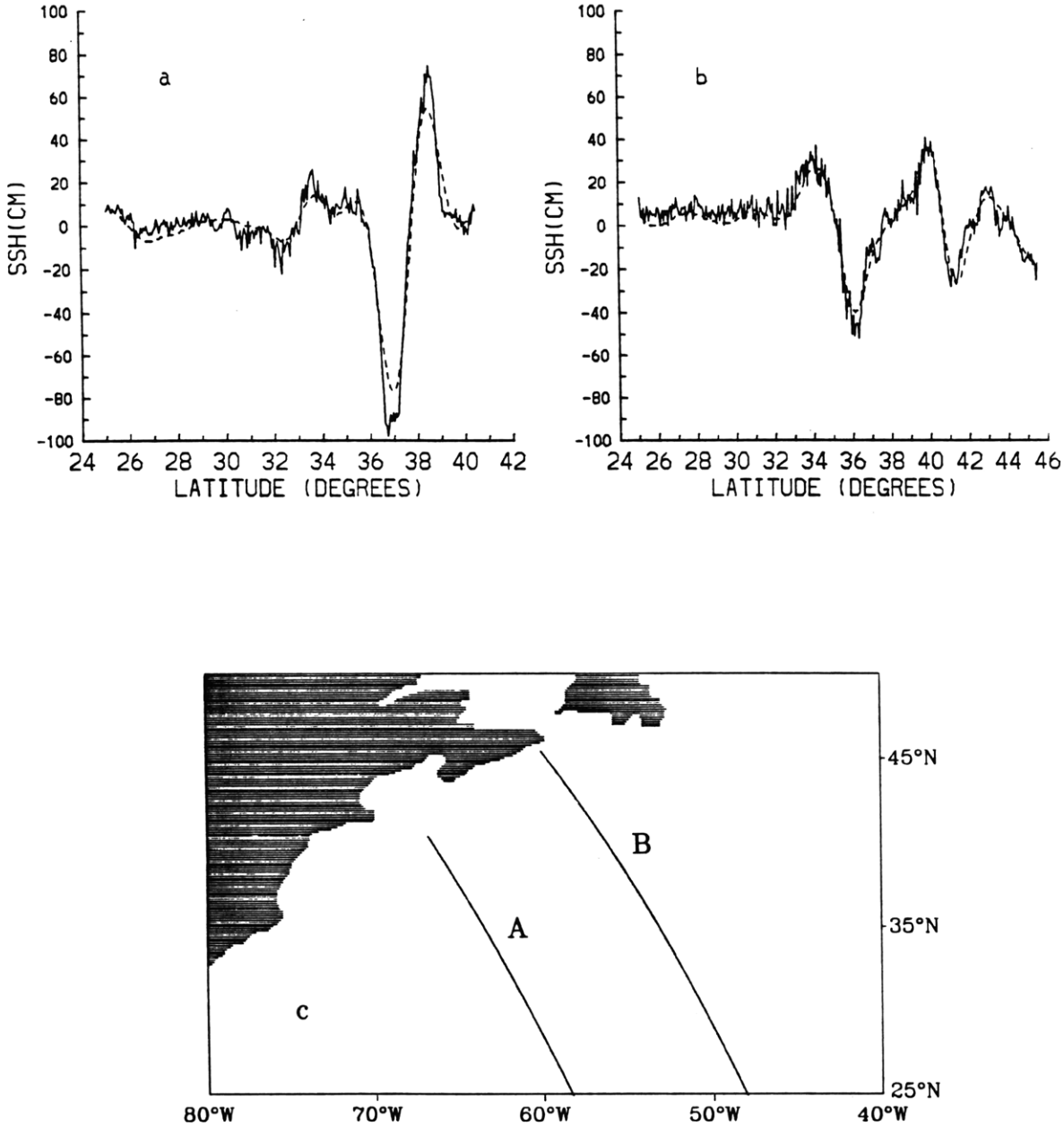

Fig. 2.11 Comparison between along-track sea surface height profiles before (solid line) and after (dashed line) the interpolation. (a) Profiles along the track indicated with "A" in panel (c). (b) Profiles along the track indicated with "B" in panel (c). (c) Representation of the Geosat ground tracks considered for this comparison.

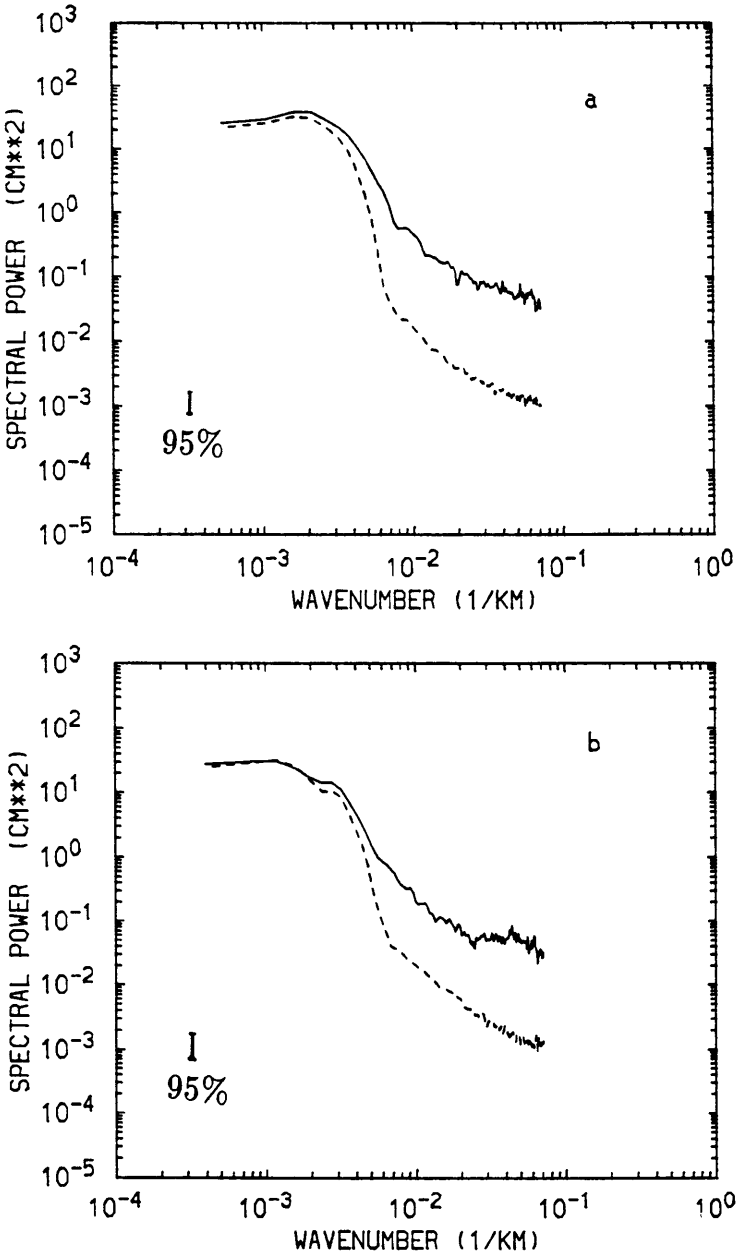

Fig. 2.12 Comparison between along-track wavenumber spectra before (solid line) and after (dashed line) the interpolation. (a) Average wavenumber spectra computed from 18 sea surface height profiles, at 34 day interval, along the Geosat track indicated with "A" in Fig. 2.11c. (b) Average wavenumber spectra computed from 18 sea surface height profiles, at 34 day interval, along the Geosat track indicated with "B" in Fig. 2.11c.

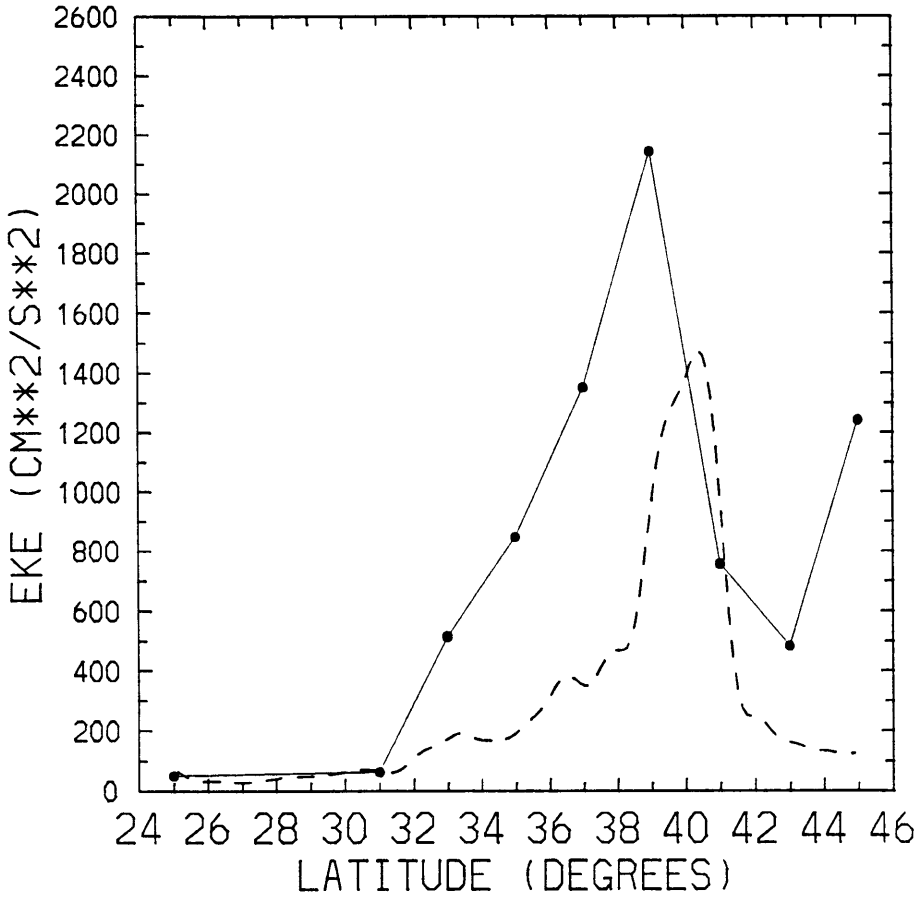

Fig. 2.13 Comparison of meridional eddy kinetic energy profiles along 55°W. The dashed line indicates the profile derived from the interpolated Geosat data. The dots connected by the thin solid line are estimates computed by Richardson (1983a) from surface drifter data.

Chapter 3

The model

3.1 Introduction

In this chapter we describe the basic characteristics of the model used for this study. This includes the governing equations, which define the model physics, and the numerical implementation of these equations in the Gulf Stream region, in a domain characterized by an irregular coastline and open boundaries. The specification of the boundary conditions at these open boundaries requires particular care. The choice we have made for the boundary values is consistent with the characteristics of the fields which are assimilated in the assimilation experiments. In the study that we are going to describe in the following chapters we will consider the model behavior in the 'free evolution' mode, in which no data are assimilated, as well as the model behavior when the surface fields are constrained to follow the 'observations'.

3.2 Governing equations

The model is based upon the closed-basin quasi-geostrophic (QG) model first discussed by Holland (1978) and now used in many basic studies of eddy-resolved ocean circulation.

The quasi-geostrophic model formulation with N arbitrary layers is a straightforward extension of the two–layer case described by Holland (1978). The governing equations are the vorticity and interface height perturbation equations, and the thermal wind relation:

$$\frac{\partial}{\partial t}\nabla^2\psi_k = J(f+\nabla^2\psi_k,\psi_k)+\frac{f_o}{H_k}\left(w_{k-\frac{1}{2}}-w_{k+\frac{1}{2}}\right)+F_k+T_k : k=1 \text{ to } N \quad (3.2.1a)$$

$$\frac{\partial}{\partial t}h_{k+\frac{1}{2}} = J\left(h_{k+\frac{1}{2}},\psi_{k+\frac{1}{2}}\right)+w_{k+\frac{1}{2}} : k=1 \text{ to } N-1 \quad (3.2.1b)$$

$$h_{k+\frac{1}{2}} = \frac{f_o}{g'_{k+\frac{1}{2}}}(\psi_{k+1}-\psi_k) \quad (3.2.1c)$$

Here whole number subscripts (k) denote the vertical layers (k increasing downward) in which the quasigeostrophic streamfunction is defined (nominally at the center of each of the layers) while fractional subscripts ($k+1/2$) denote the interfaces between layers where vertical velocity and interface height perturbation are defined. The variables are the quasigeostrophic streamfunction (ψ_k) with horizontal velocity components ($u=-\psi_y$, $v=\psi_x$), the interface height perturbation ($h_{k+1/2}$), positive upward, and the vertical velocity ($w_{k+1/2}$) also positive upward. The horizontal coordinates are x (eastward) and y (northward), the Coriolis parameter is $f = f_o + \beta y$, and the mean layer thicknesses are H_k. The values of f_o and β are defined at the central latitude of the model domain (37.5°N). The basic background vertical stratification is written in terms of the reduced gravity $g' = g\Delta\rho_{k+1/2}/\rho_o$, where $\Delta\rho_{k+1/2}$ is the (positive) density difference between layers $k+1$ and k. Frictional effects, written symbolically in Eq. (3.2.1a) as F_k, are parameterized as lateral friction of the biharmonic kind (Holland, 1978), in which

$F_k = -A_4\nabla^6\psi_k$. In addition, F_k includes a bottom friction, $-\varepsilon\nabla^2\psi_N$, when $k = N$ (the bottom layer). The term T_k represents the forcing. T_k is different from zero only for $k = 1$. T_1 is the wind forcing, equal to curl τ/H_1. It produces an Ekman pumping stretching tendency in the upper layer that is equivalent to a body force acting on the upper layer. At the sea surface, $w_{1/2} = 0$ and at a flat sea bottom $w_{N+1/2} = 0$. The advective velocities at the interfaces, needed in Eq. (3.1b), are calculated from a weighted average of the velocities in the layers, i.e., $\psi_{k+1/2} = (\alpha_{k+1/2})\psi_k + (1 - \alpha_{k+1/2})\psi_{k+1}$, where $\alpha_{k+1/2} = H_k/(H_k + H_{k+1})$.

The model has five layers in the vertical, with layer thicknesses of 300, 450, 750, 1300 and 2200 m respectively, from top to bottom. The horizontal resolution is 1/8° of latitude and longitude, a resolution necessary for resolving the turbulent processes occurring in the model. The model domain is shown in Fig. 3.1. It covers the region 25°N - 30°N, 40°W - 80°W and it includes a realistic coastline.

We should notice that in this model we cannot have outcropping, because of the QG approximation, we also do not have any interfacial friction between layers. Therefore eddies are the only agent that can drive the deep layers.

As is well known, the QG approximation is valid only with relatively small amplitude variation in bottom topography. The accuracy of the model simulation in the case of finite topography, such as that existing in some parts of the region under consideration, is not known. The major topographic features in this area include the New England Seamounts, the Bermuda Rise, the Corner Rise as well as the continental shelf. Preliminary experiments in which topography was included showed that one of the major difficulties was to model the influence exerted on the flow by the sloping continental shelf, especially in the area of the Grand Banks, where the path of the stream turns northward following the bathymetry. We have chosen to exclude from this study the uncertainties associated with the

topographic issue, by considering the constant depth case. This neglect of important bathymetric influences can be regarded as an imperfection in the model geometry whose consequences on the model climatology can hopefully be partially corrected by data assimilation.

The regional nature of the model and the fact that it is needed to study an actual piece of the real ocean requires that the lateral open boundary conditions as well as surface-forcing conditions be carefully considered. As the QG model is not very useful for examining local thermohaline forcing, those aspects of the physical problem will not be considered here. For that purpose a PE model will be needed. The surface forcing is therefore given only by the wind stress. The annual mean climatological winds from Hellerman and Rosenstein (1983) have been used. Fig. 3.1 shows the corresponding wind stress curl, which is the forcing term in the QG equations. In this figure the solid lines correspond to positive values, the dashed lines to negative values. The line of zero wind stress curl defines the separation between the region to the north where positive vorticity is supplied to the ocean and the region to the south where the wind is a source of negative vorticity. At intermediate latitudes the variation of the wind stress curl is mainly meridional, as assumed in many idealized studies of ocean circulation. However, the general pattern shows a structure which is much more complex than the simple sinusoidal variation with latitude adopted in those studies.

The streamfunction distributions at the lateral boundaries have been derived from climatological data, as described in the next section. They are therefore time independent. Inflows and outflows are confined to the upper three layers (the upper 1500 m), while layers 4 and 5 are bounded by solid walls. The inflow is specified at the western boundary. The total transport entering the domain corresponds to the observed value of about 52 Sverdrups (52×10^3 m^3/s) which has been measured off

Cape Fear by Richardson, Schmitz and Niiler (1969). This is approximately at the location at which 80°W longitude crosses the North American coast. Thus the Gulf Stream enters the domain as a western boundary current, somewhat southwest of Cape Hatteras.

At the eastern boundary, where most of the outflow occurs, radiation boundary conditions, together with relaxation toward the given streamfunction distribution, are specified. They are implemented by solving the equation:

$$\frac{\partial \psi_b}{\partial t} + u\frac{\partial \psi_b}{\partial x} = -R_b(\psi_b - \psi^*) \qquad (u > 0) \qquad (3.2.2)$$

Here ψ_b is the streamfunction at the boundary, ψ^* is the climatological streamfunction distribution toward which the boundary values are relaxed, u is the outgoing fluid velocity close to the boundary and R_b is the relaxation constant. The radiation condition is used to prevent the reflection of waves from the boundary back into the model domain. The use of a relaxation condition is adopted in order to give the outflow some flexibility of meandering, according to the interior dynamics, around the outport defined by the eastern boundary values. These technical issues associated with the treatment of open boundaries are an active area of research in regional ocean modeling and are by no means settled. The implementation of the radiation boundary conditions is particularly critical, due to the large range of phase speeds in the model wave fields. It is in fact unknown how effective a simple wave equation like the LHS of (3.2.2) can be in 'radiating out' all the intervening waves. A possible way of overcoming this uncertainty, in the context of the assimilation experiment, could be the use of time dependent boundary conditions. They would automatically supply the correct evolution for waves entering or exiting the domain. The altimeter data could be used for this purpose in the first model layer. For the lower layers, however, we do not have any corresponding time dependent information, unless we devise a way of projecting

the values at the boundaries in depth. We have not explored this possibility in the present study.

A complete definition of the boundary conditions requires the specification of the vorticity $\nabla^2\psi_k$ and of the Laplacian of the vorticity $\nabla^4\psi_k$ at both open and closed boundaries. The latter quantity, $\nabla^4\psi_k$, is necessary for the computation of the biharmonic friction term at the interior points. At the closed boundary, along the irregular coastline, the vorticity is determined by requiring that the tangential velocity is zero at the boundary (no-slip condition). In the area of the inflow at the western boundary, the vorticity is computed assuming that the jet enters the domain at a 45° angle. Along the rest of the open boundaries vorticity is set to zero. The value of $\nabla^4\psi_k$ at all boundaries has been extrapolated from the interior values.

3.3 Determination of initial and boundary conditions

The choice of the initial and boundary conditions used in all our numerical experiments has been dictated by the criteria used for the assimilation experiment. Before proceeding to a detailed description of the exact computational steps we summarize here the general criteria adopted. Assimilation of surface data in a nonlinear model requires the knowledge of the total (mean + variability) surface fields. The altimeter measurements can only provide accurate estimates of the sea surface height variability, so that we need to determine a mean sea surface height from other sources of information. This mean field has been obtained with the dynamic method from climatological data of temperature and salinity. The corresponding values at the boundaries of the model domain are used as boundary conditions for the first layer. However, we need to determine boundary values

also for layers 2 and 3. In fact, the inflow at the western boundary is distributed over the first three layers of the model on the basis of the measurements at Cape Fear mentioned in the previous section. Therefore we need to prescribe appropriate inflow/outflow conditions in each of these layers. In order to meet these requirements we have computed climatological flow fields also for layers 2 and 3. They supply both initial and boundary conditions for these two layers. The use of initial conditions obtained from a dynamic computation is adopted in order to build into the model a 'realistic' baroclinic structure that reduces the model adjustment time during the assimilation experiment.

3.3.1 Choice of the climatological data

The data of temperature and salinity used for our computation are the ones analyzed by Bauer and Robinson and presented in Version VIII of their Atlas (Bauer and Robinson, 1985). Versions of these data have been analyzed and presented in several Atlases by Bauer and Robinson (Bauer, 1985; Robinson, 1979). The 1986 version of the MOOD data has been used to build the Generalized Digital Environmental Model (GDEM) (Davis et al., 1986). We have preferred the Bauer-Robinson data set with respect to the one prepared by Levitus because the latter gives an extremely smooth version of the temperature and salinity fields. The Levitus climatology (Levitus, 1982) was in fact obtained by first averaging the data over 1° x 1° squares and then applying an objective mapping procedure in order to smooth the fields. The objective mapping algorithm is the same 'successive corrections' algorithm which is described in Appendix A, at the end of Chapter 2. It has been applied using covariance functions having radii of 1541 km, 1211 km, 881 km and 771 km at each of the four iterations. Scales shorter than 1200 km are reduced more than 50% in the resulting fields. In Fig. 3.2 we compare the surface

dynamic height field obtained from the Robinson climatology (Fig. 3.2a) with the one obtained from the Levitus climatology (Fig. 3.2b). In both cases the reference level is 1500 m. We can see that the range of dynamic height values is approximately the same in the two maps. The two patterns give also a similar perception of the large scale surface flow. However, the field in Fig. 3.2a contains more information on smaller scales with respect to the one from Levitus. It resolves, for example, the high pressure cell, east of the Grand Banks, which seems to have been observed by several investigators (Mann, 1967; Clarke et al., 1980). A comparison between the surface dynamic topography derived from the GDEM climatology and the one obtained from the Levitus climatology (Teague et al., 1990) leads to similar results. The jet is much narrower and dynamic heights are generally larger in GDEM than in Levitus. As our main purpose here is to obtain a mean field to be used in conjunction with the Geosat data, whose duration is only two years, the most sensible choice seems to be the climatology with the least degree of smoothing and broadening. Therefore we have chosen Bauer-Robinson data set for the computation of the mean field.

For completeness we have considered a third data set which could be used for determining a surface mean field as well as initial and boundary conditions in the first three layers. This data set is the one processed and presented in Atlas form by Fukumori et al. (1991). In this case the original data were from the hydrographic trans-Atlantic sections which took place in the period 1981-1985. Maps of dynamic height at a series of standard depths, relative to 3000db were constructed by Fukumori by using an optimal interpolation procedure. In Fig. 3.2c we show the surface dynamic height field (0 db/3000 db) in the area of the model domain. Values are higher than the ones in Fig. 3.2a and Fig. 3.2b, due to the shorter duration of the period in which the data were collected and to the deeper reference level chosen for the computation. The map shows a broadening of the

dynamic height contours defining the Gulf Stream toward the western boundary, where they should become closer in order to describe the jet entering the domain south of Cape Hatteras. Contours tend also to broaden and cover the area of the Grand Banks where a signature of the flow associated with the subpolar gyre would, on the contrary, be expected. These features are a result of the interpolation procedure used, at locations far from the available data, as shown by the associated error field (Fig. 61 of the Atlas by Fukumori et al., 1991). Therefore the use of these data would be possible only if the associated interpolation error could be carefully considered. Obviously, also the fields in Fig. 3.2a and Fig. 3.2b cannot be expected to be uniformily accurate. However, their characteristics are in better agreement with our perception of the mean circulation in this area, so that the inclusion of an error field does not seem as critical in their case.

3.3.2 Determination of the climatological fields in practice

The exact procedure applied in order to obtain the streamfunction fields for the upper three layers from Robinson's data can be summarized as follows: first a dynamic height computation is performed from the reference level of 1125 m, which corresponds to the middle of layer 3. Apart from the shallowest part of the continental shelf this level is above all the other topographic features present in this area, so that dynamic height values can be determined in most of the domain. The integration has been carried out up to the depths of 525 and 150 m, which correspond to the middle of layers 2 and 1, respectively. The Bauer-Robinson data set do not contain information in the area of the northern recirculation gyre, so that this component of the flow is missing in the dynamic height fields. The jet entering at the western boundary is also not resolved by the data used. We have determined it by requiring mass conservation from the interior geostrophic flow. The flow in the

subpolar gyre is much more difficult to infer and any definition of it would be purely arbitrary. Therefore we have decided to concentrate our analysis on the Gulf Stream and subtropical gyre. We will see that the neglect of the northern recirculation flow will lead to some unrealistic features in that part of the model domain. However, even if unrealistic, these features will help in illustrating the mechanisms of model adjustment when a surface data constraint is imposed.

Dynamic heights (d) can be immediately translated into streamfunction values (ψ), since they are both related to the pressure fields:

$$\psi(x,y) = \frac{g}{f} d(x,y) \qquad (3.3.2.1)$$

where f is the local Coriolis parameter and g the acceleration of gravity. The resulting streamfunction fields obtained for the first two layers are relative to the flow in the third layer. The reference flow in the third layer, which coincides with the barotropic component in the three upper layers, is basically unknown. In order to proceed we have made the assumption that the pattern of the circulation in layer 3 is the same as the one in layer 2. This assumption is arbitrary and must be taken as a work hypothesis. The intensity of the flow in layer 3 has been determined by requiring that the total transport at the western boundary inflow, distributed in layers 1, 2 and 3, reproduces the observed value of 52 Sv. In this way, even if the computation has been carried out from the reference level of 1125 m, the additional information relative to the total inflow at the western boundary allows some sort of 'tuning' of these fields. The inflows in layers 1, 2 and 3 are 25 Sv, 19 Sv and 7 Sv, respectively. The final result for the climatological streamfunction fields in the upper three layers of the model is shown in Fig. 3.3. These fields will be used as initial conditions for the corresponding layers in the assimilation experiment as well as in the experiment without assimilation. Only the field for the first layer, however, will be used in conjunction with Geosat data to obtain maps of total

streamfunction which will be assimilated into the model. The model subsurface layers will be free to evolve from the initial conditions and eventually develop a different mean circulation as a result of the interactions with the assimilated eddy field.

How does this surface (150 m depth) field compare with equivalent estimates of the surface Gulf Stream? Richardson (1985) computed a mean zonal velocity section at 55°W from a combined data set including surface drifters, SOFAR floats at 700 m and 2000 m depth and deep (4000 m) current meters. His construction gives a picture of the average Eulerian Gulf Stream. Therefore it seems to be the appropriate term of comparison for our mean field which has been obtained as a time average of a long-term data set. Average synoptic sections obtained following the meandering jet as it moves as a whole (Hall and Bryden, 1985; Leaman et al., 1989; Hogg, 1992) are certainly closer to a description of the real jet, but they carry a type of information which is not comparable with ours. In Fig. 3.4 we show the meridional profile of surface zonal velocity which has been derived from the streamfunction field in Fig. 3.3a (dashed line). The zonal velocity has been averaged over 10° longitude, from 50°W to 60°W, as were Richardson's data, in order to make the comparison more consistent. In the same figure the dots connected by the thin solid line represent Richardson's estimates, at each degree of latitude, with their standard errors. Since our values are relative to a depth of 150 m (the middle point of the model upper layer) we have interpolated linearly between the estimates obtained by Richardson at the surface and at 700 m. In both cases the eastward flowing jets extend approximately from 36°N to 43°N, corresponding to a width of about 800 km. The peak value of 25 cm/s obtained by Richardson at 39.5°N, is higher than the maximum of our estimate, which is approximately 18 cm/s at about 40.5°N. This discrepancy is consistent with the much longer duration of the

Bauer-Robinson data set with respect to the 2 year duration of the measurements used by Richardson for his construction.

If we compare the upper layer 'mean field' (Fig 3.3a) with the eddy map in Fig. 2.1a of the previous chapter we see a remarkable correspondence between the position of the mean Gulf Stream and the distribution of the eddy intensity. A similar agreement can be found in the comparison between Fig. 3.3a and the eddy kinetic energy distribution derived from the Geosat maps in Fig. 2.10a. Features of the mean path, like the large curve around the Grand Banks and the subsequent splitting in two separate branches, are clearly suggested by the eddy field itself. So, even if the choice of a climatological field as the missing mean component of Geosat data is called into question due to the different duration of the two data sets, the remarkable agreement that we obtain between the two final fields tells us that the choice is consistent and sensible.

3.3.3 Initial potential vorticity fields

Within the quasi-geostrophic framework the potential vorticity of layer k is defined (Pedlosky, 1979):

$$q_k = \nabla^2\psi_k + f_0 + \beta y + \frac{f_0}{H_k}(h_{k+1/2} - h_{k-1/2}) \qquad (3.3.3.1)$$

The potential vorticity is thus the superposition of three terms: the relative vorticity ($\nabla^2\psi_k$), the planetary vorticity ($f_0 + \beta y$), and the stretching term ($\frac{f_0}{H_k}h_{k+1/2} - \frac{f_0}{H_k}h_{k-1/2}$). Here f_0 represents the value of the Coriolis parameter at the central latitude of the model domain (37.5°N), which is assumed as the origin of the y-coordinate. Therefore the term βy is negative in the southern half of the domain and positive in the northern half. The stretching term is associated with the deviation of the layer thickness from its rest value H_k. According to

the notation introduced in section 3.2, $h_{k-1/2}$ is the displacement of the upper interface of layer k, positive upward, while $h_{k+1/2}$ is the dispacement of the lower interface. Therefore the stretching term is positive when the layer thickness decreases. The potential vorticity fields in the three upper layers, corresponding to the climatological streamfunction distributions in Fig. 3.3 and no flow in layers 4 and 5, are shown in Fig. 3.5. They are described here for future comparison with the potential vorticity distributions corresponding to the statistical steady state of the numerical experiments. In all three layers the major contributions to the potential vorticity is given by the planetary vorticity and stretching terms. The relative vorticity is negligible everywhere except in the area of the jet entering at the western boundary.

In the upper layer stretching is associated with the depression of the lower interface, due to the shear between the flow in the first and second layers. Therefore the stretching term is negative, but increasing with latitude. The planetary vorticity is also an increasing function of latitude, and so is the total potential vorticity. In layer 3 the major contribution to stretching is associated with the displacement of its upper interface, which is below the rest level. This 'squeezing' of layer 3, which corresponds to a positive contribution to the potential vorticity, decreases with latitude. Since the planetary term increases with latitude an area of maximum potential vorticity values is achieved between 35°N and 40°N.

We will find that these initial potential vorticity fields are different from the ones corresponding to the model statistical steady state, both in the control run and in the assimilation experiments. In other words they do not seem to represent equilibrium distributions for the model. In all the experiments we consider in this study the potential vorticity fields will evolve from the initial distributions in Fig. 3.5 to final equilibrium distributions characterized by large areas of reduced

gradients. Whether this is associated with inaccuracies in the initial fields or is the consequence of limitations in the quasi-geostrophic potential vorticity dynamics is not clear. In particular the question of how realistic is the tendency, observed in QG models, to develop areas of homogenized potential vorticity is still a topic of research.

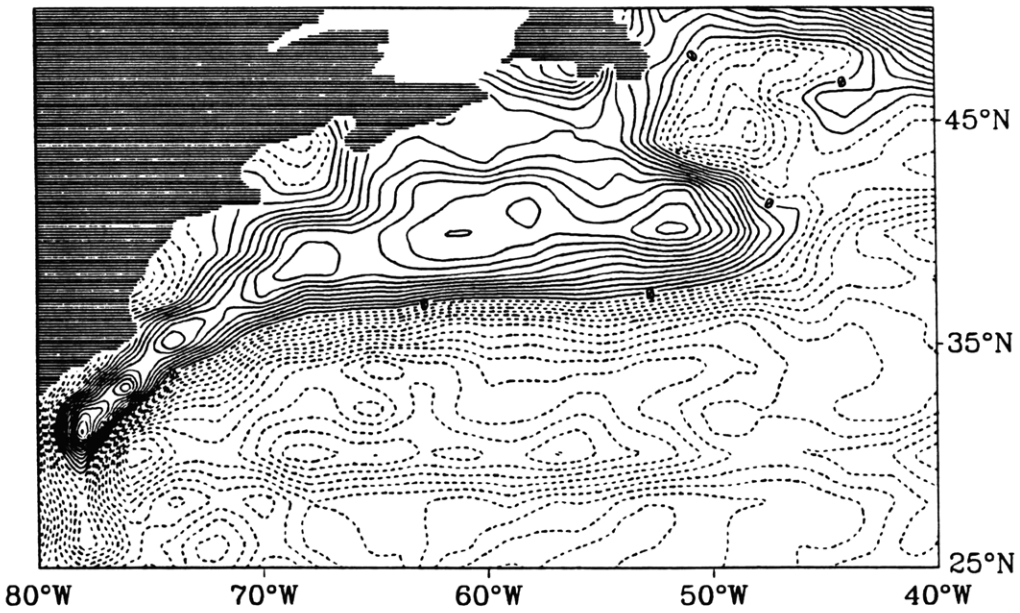

Fig. 3.1 Distribution of wind stress curl from the annual climatological data processed by Hellerman and Rosenstein, shown in the area of the model domain. This wind stress distribution is used as forcing for the model.

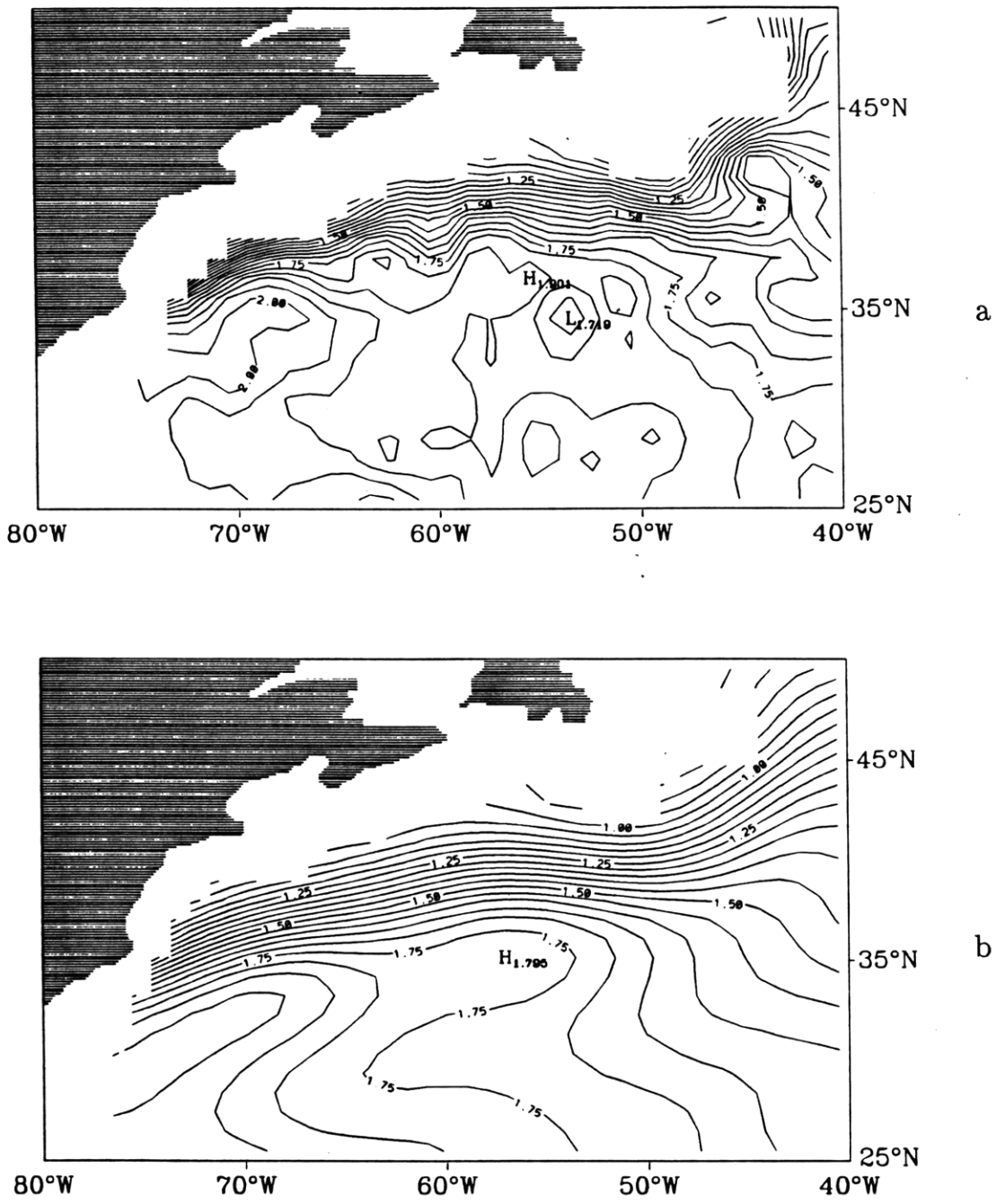

Fig. 3.2 (a) Surface dynamic height field (in dynamic meters) computed from Bauer-Robinson climatology relative to 1500db. (b) Surface dynamic height field (in dynamic meters) computed from Levitus climatology relative to 1500db.

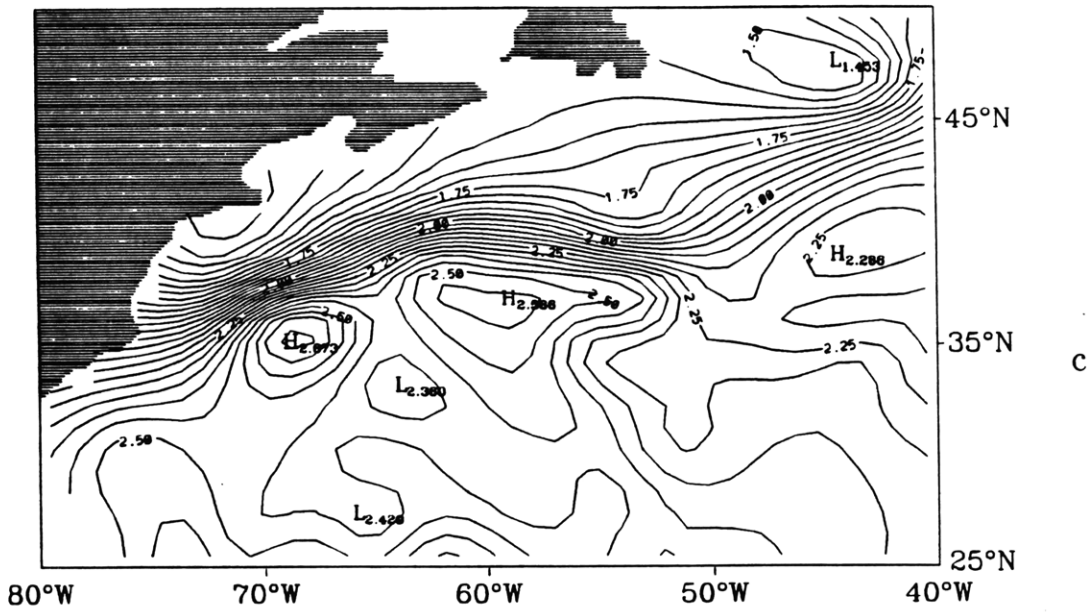

Fig. 3.2 (continued) (c) Surface dynamic height field computed by Fukumori et al. (1991) from the hydrographic trans-Atlantic sections which took place in the period 1981-1985. The map of dynamic height has been obtained by optimal interpolation. The reference level is 3000db.

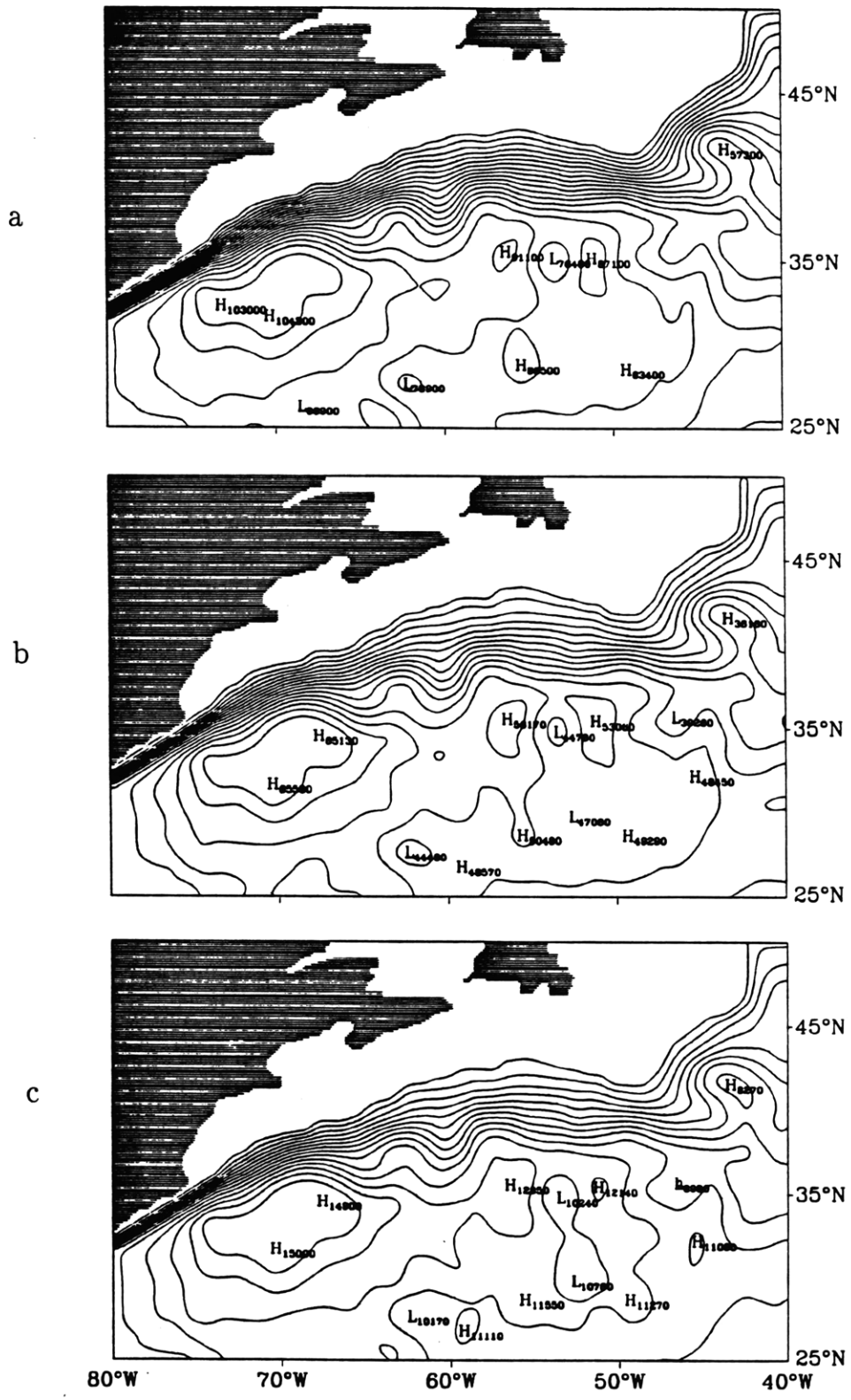

Fig. 3.3 Streamfunction distributions derived from the Bauer-Robinson climatology for the model layers 1 (a), 2 (b) and 3 (c). Contour intervals are 5000 m^2s^{-1} for layer 1, 4000 m^2s^{-1} for layer 2 and 1000 m^2s^{-1} for layer 3.

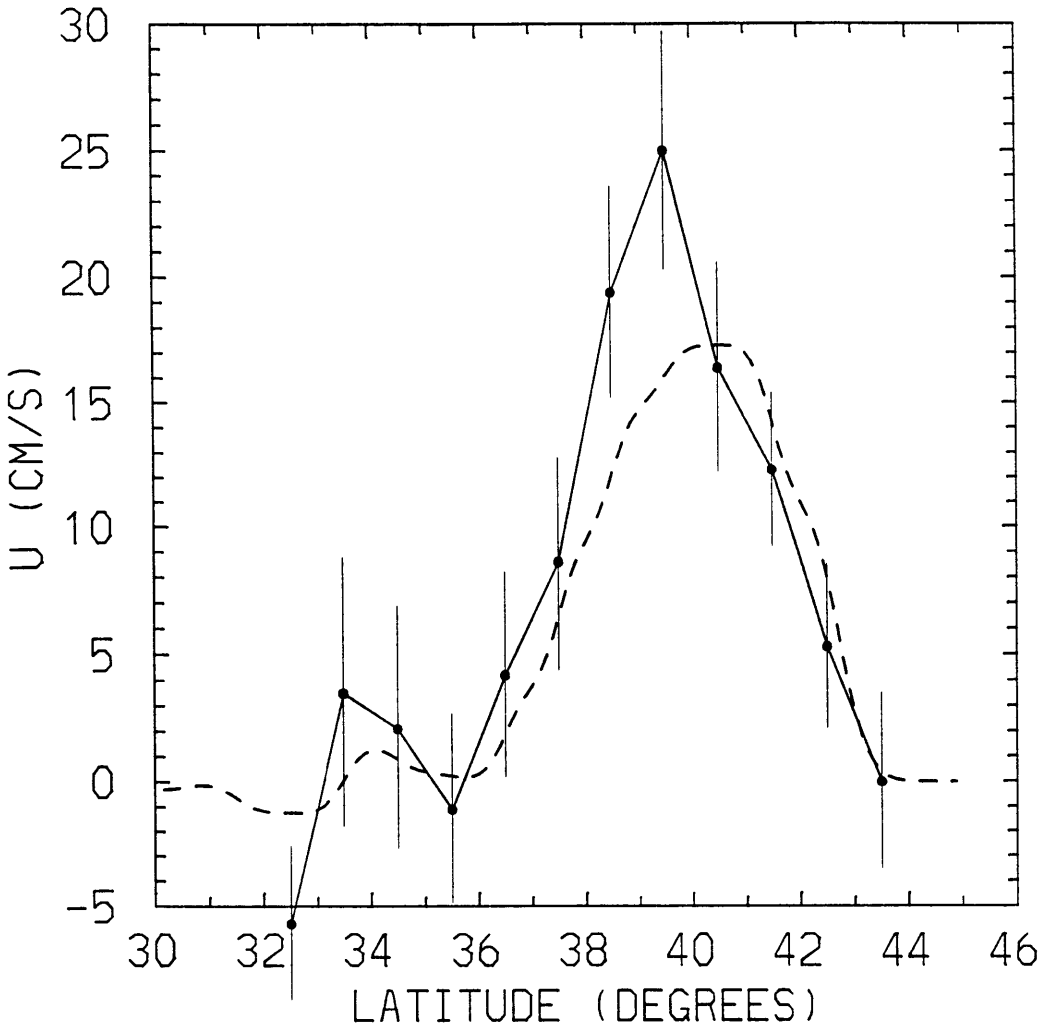

Fig. 3.4 Comparison of mean zonal velocity sections around 55°W. The dashed line indicates the profile derived from the climatological streamfunction field in Fig. 3.3a. The dots joined by the thin solid line are values derived from the estimates computed by Richardson (1985) using data from surface drifters and SOFAR floats. Richardson's estimates at the surface and at 700m have been linearly interpolated to the depth of 150m, which represents the middle of the model upper layer. The vertical bars indicate the standar errors of the mean.

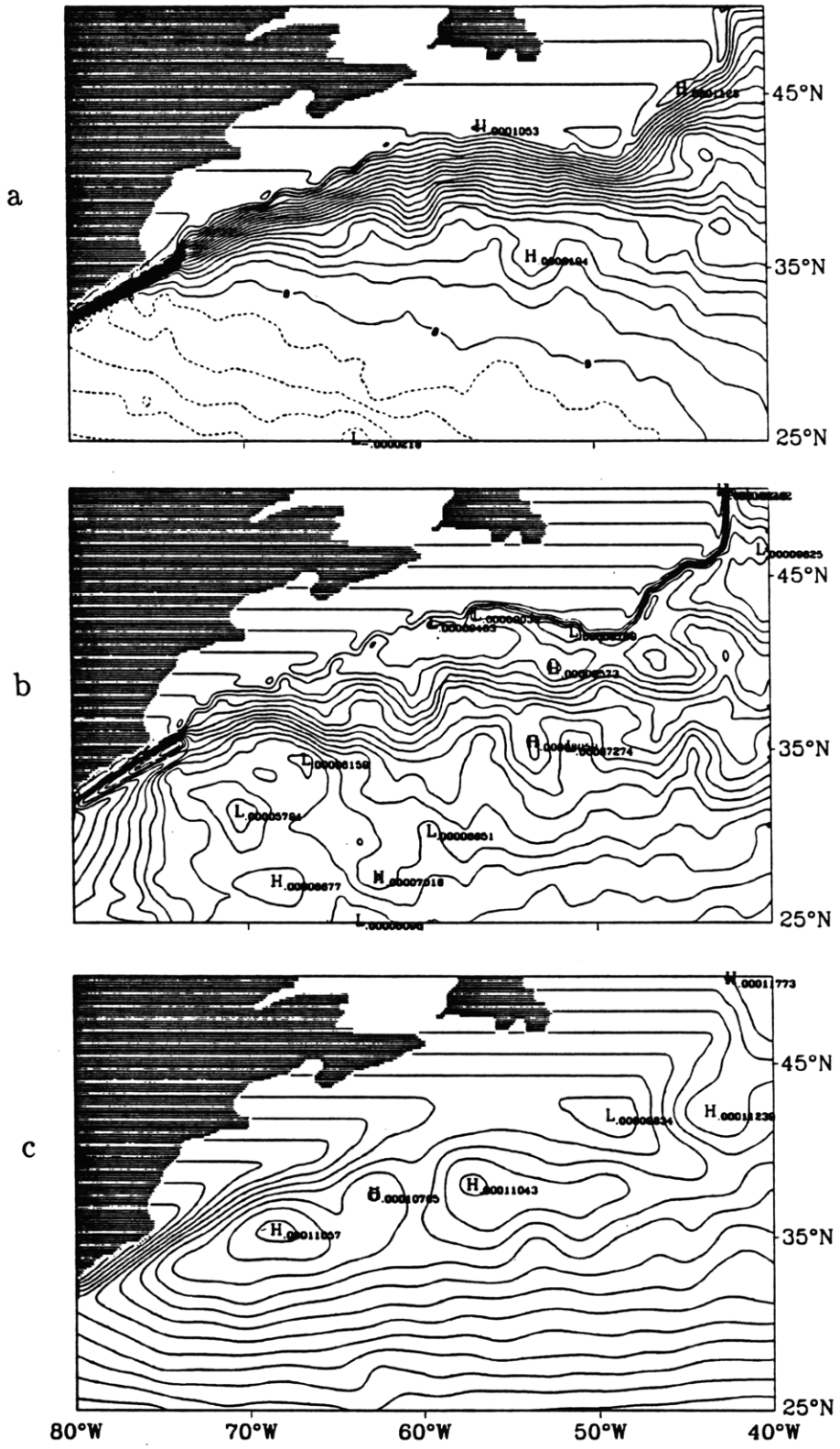

Fig. 3.5 Potential vorticity fields in layer 1 (a), 2 (b) and 3 (c), corresponding to the initial conditions of all the numerical experiments described in this study. The initial conditions are given by the streamfunction fields in Fig. 3.3 in the three upper model layers and no flow in layers 4 and 5.

Chapter 4

The control run

4.1 Introduction

The 'control run' is a model simulation in which no data are assimilated at the surface. In fact we want first to define the climatological characteristics of the model when no surface data constraints are imposed. The results will represent a basis of comparison for assessing the impact of the surface data insertion on the global model behavior. In order to make the comparison more straightforward the numerical simulation is started from the same initial conditions that will be used for the assimilation experiment. The boundary conditions as well as the friction parameters are also the same in both experiments. The two model runs are therefore completely equivalent except for the data assimilation procedure which is applied only in one case. It is important to emphasize that, since the model behavior is dependent on the boundary conditions and friction coefficients used, we could have 'tuned' those values in order to make the results as 'realistic' as possible. However, we are not interested, here, in achieving the best possible model behavior, but in comparing the climatology of the model with and without assimilation. Therefore we use the exact same boundary conditions and viscosities in the two experiments.

The numerical simulation has been carried out for 20 years, in order to allow the model fields to reach a statistical equilibrium. The latter has been diagnosed by inspection of the total kinetic energy evolution in each of the five model layers,

based on the criterion that the total kinetic energy level must remain constant in statistical steady state conditions. We have thus verified that the increase in total kinetic energy level, characteristic of the model spin-up phase, was no longer occurring, and the energy level had reached its final mean level. The climatology of the model, for the given boundary conditions and surface wind forcing, has been determined from the results corresponding to the last four years of the model simulation. The aspects of the model climatology in which we are interested are the ones that can be compared with available observations. Therefore we have considered the mean streamfunction, the total transport, the eddy kinetic eddy energy intensity and distribution and the spectral characteristics of the model eddy field. Because of its dynamical significance we will present also the mean potential vorticity fields. These aspects are described and discussed in the following sections.

The analysis described in this chapter represents the first study in which the climatological characteristics of a limited-area, QG model of the Gulf Stream region, including a realistic coastline and open boundaries, are compared with observations. In fact the studies of model-data intercomparison in this region, involving QG models, that are available in the literature, have been performed with models configured in a rectangular domain and forced with idealized wind fields (Holland and Schmitz, 1985; Schmitz and Holland, 1982; Schmitz and Holland, 1986). Those studies represent the first attempts to relate the model behavior to real observations. They have shown the possibility of realistically reproducing some of the observed features of the ocean circulation, through a careful tuning of the model parameters. However, they have also shown the sensitivity of the model behavior to these parameters, including horizontal and vertical resolution, intensity of the wind forcing, frictional parameterizations etc. The inclusion of a realistic geometry, as in the present case, introduces additional degrees of complexity, such as the effect of irregular coastlines and the treatment of open boundaries. The

mechanisms through which all these factors affect the model behavior is still a topic of research. An extensive sensitivity study is beyond the scope of the present work. In this chapter our goal is to obtain a clear and complete description of one particular model realization, as explained before. We will try to understand the present results on the basis of previous sensitivity and process studies existing in the literature.

4.2 The mean streamfunction fields

The mean streamfunction fields for each of the 5 layers are shown in Fig. 4.1. In the upper three layers the jet entering the model domain at the western boundary slightly overshoots Cape Hatteras, before leaving the coast. After separation the stream path becomes mainly zonal. The inertial jet flows eastward along a latitude which roughly coincides, in the central part of the domain, with the line of zero wind stress curl (Fig. 3.1). In the area of the separation from the coast, however, both the stream and part of its southern recirculation lie in the region of positive Ekman pumping. These characteristics are in agreement with the results obtained by Rhines and Schopps (1991) in their investigation of the effect of progressively tilting the line of zero wind stress curl. In the case of wind patterns that are perfectly symmetric with respect to the middle latitude of a rectangular domain the boundary jet leaves the coast at this central latitude and then flows eastward exactly along the line of zero wind stress curl (see, for example, Holland, 1978). This simple symmetric response is lost when the symmetry of the wind pattern is altered. In particular, when the wind pattern is tilted in the NE-SW direction, Rhines and Schopps show that the mean circulation obtained from the numerical simulation leaves the western boundary at a latitude poleward of the zero pumping line. In their results part of the subtropical gyre lies in the upward-pumping area.

This is also true for the Sverdrup transport that can be derived from the Ekman pumping distribution. So the coincidence between the path of the inertial jet and the position of the zero wind stress curl line is lost.

In our model simulation the flow patterns in the upper three layers are controlled also by the inflow and outflow conditions specified at the open boundaries. What can be said about the relative importance of wind forcing with respect to 'boundary forcing' in shaping the mean circulation in these layers? At steady state the QG equations for layers 1, 2 and 3 are

$$J(\psi_1, \nabla^2\psi_1 + F_{12}(\psi_2 - \psi_1)) + \beta\psi_{1x} = T_1 + F_1 \qquad (4.2.1a)$$

$$J(\psi_2, \nabla^2\psi_2 + F_{21}(\psi_1 - \psi_2) + F_{23}(\psi_3 - \psi_2)) + \beta\psi_{2x} = F_2 \qquad (4.2.1b)$$

$$J(\psi_3, \nabla^2\psi_3 + F_{32}(\psi_2 - \psi_3) + F_{34}(\psi_4 - \psi_3)) + \beta\psi_{3x} = F_3 \qquad (4.2.1c)$$

Here ψ_1, ψ_2 and ψ_3 represent the streamfunctions in layers 1, 2 and 3, respectively, $F_{ij} = \frac{f_0^2}{g'_{ij}H_i}$, T_1 is the wind forcing and the terms F_i are the frictional terms for the scales not resolved by the model. Let us first decompose the variables into time mean and eddy components:

$$\psi_i = \bar{\psi}_i + \psi'_i \qquad (4.2.2a)$$

$$q_i = \bar{q}_i + q'_i \qquad (4.2.2b)$$

The time averaged equations are:

$$J(\bar{\psi}_1, \nabla^2\bar{\psi}_1 + F_{12}\bar{\psi}_2) + \beta\bar{\psi}_{1x} = \bar{T}_1 + \bar{F}_1 - \overline{J(\psi'_1, q'_1)} \qquad (4.2.3a)$$

$$J(\bar{\psi}_2, \nabla^2\bar{\psi}_2 + F_{21}\bar{\psi}_1 + F_{23}\bar{\psi}_3) + \beta\bar{\psi}_{2x} = \bar{F}_2 - \overline{J(\psi'_2, q'_2)} \qquad (4.2.3b)$$

$$J(\bar{\psi}_3, \nabla^2\bar{\psi}_3 + F_{32}\bar{\psi}_2 + F_{34}\bar{\psi}_4) + \beta\bar{\psi}_{3x} = \bar{F}_3 - \overline{J(\psi'_3, q'_3)} \qquad (4.2.3c)$$

The reason for the decomposition into mean and eddy components is that the space, time and velocity scales typical of the mean quantities are different with

respect to the ones characteristics of the eddy field, so that eddy advection could be important even when mean advection is not. This eddy advection term, which appears on the RHS of (4.2.3), represents the explicit eddy 'viscosity', which can also act as a forcing term for the mean flow (Holland and Rhines, 1980; Marshall, 1984). If both nonlinear terms and dissipation can be considered as second order effects, away from the western boundary, the set of equations (4.2.3) reduces to:

$$\beta\bar{\psi}_{1x} = \bar{T}_1 \tag{4.2.4a}$$

$$\beta\bar{\psi}_{2x} = 0 \tag{4.2.4b}$$

$$\beta\bar{\psi}_{3x} = 0 \tag{4.2.4c}$$

The flow field within the model domain can be obtained by integrating Eq.s (4.2.4) from the eastern boundary:

$$\bar{\psi}_1(x,y) = \int_x^{x_E} \frac{\bar{T}_1(x',y')}{\beta} dx' + \bar{\psi}_{1E}(y) \tag{4.2.5a}$$

$$\bar{\psi}_2(x,y) = \bar{\psi}_{2E}(y) \tag{4.2.5b}$$

$$\bar{\psi}_3(x,y) = \bar{\psi}_{3E}(y) \tag{4.2.5c}$$

In the case of a closed domain, in which the streamfunction values $\bar{\psi}_{iE}$ at the eastern boundary are constant, we recover the well known result that, in the absence of nonlinearities, flow is possible only in the upper layer and it is given by the Sverdrup transport (Rhines and Young, 1982). When, on the contrary, the eastern boundary is an open boundary, the integration into the interior is carried out from a distribution of boundary values which is representative of the flow in the eastern part of the ocean not included in the model domain. In this case flow is possible in all layers. In the upper layer (eq. 4.2.5a) the circulation is the result of the boundary distribution $\bar{\psi}_{1E}(y)$ and of the input of vorticity from the wind, which can allow the development of a meridional component of the flow. In layers 2 and 3

the circulation implied by (4.2.5b) and (4.2.5c) is purely zonal. So, in the absence of nonlinearities, the flow in the lower layers, even if different from zero, does not 'feel' the presence of the wind driven circulation above.

If the wind were turned off, on the basis of eqs. (4.2.5) we would expect a purely zonal flow in all three layers. The only source of vorticity which could allow fluid particles to move meridionally is associated with eddy driving effects. If these effects are small the streamlines emanating from the eastern boundary cross the model domain along latitude circles. At the western boundary, where nonlinearities and/or friction can be expected to become important, the matching with the western boundary values can be achieved through the formation of a western boundary layer.

An auxiliary experiment performed with the wind stress turned off shows, in fact, a predominantly zonal flow in the eastern half of the domain and the development of a boundary layer along the irregular coastline. The corresponding streamfunction fields in all five layers are shown in Fig. 4.2. The characteristics of the stream separation from the coast remain similar in the absence of wind forcing: the jet entering at the western boundary follows the coastline, overshoots at Cape Hatteras and then turns eastward into the interior at about the same latitude as in the wind driven case. The two inertial recirculation gyres are present also in the purely 'boundary forced' experiment. However, they are much weaker, especially the cyclonic one, on the northern side of the stream. The flow is weaker everywhere and so is the eddy field. The broad recirculation in the interior is present only when wind forcing is acting and therefore it is essentially wind driven, even if eddy forcing might also play a role.

Layers 4 and 5 do not have any inflow/outflow condition prescribed at the boundaries. Therefore the flow present in these layers can only be eddy driven. As shown by Holland and Rhines (1980) the major driving mechanism for the deep

gyres is the eddy flux of interface height, known also as eddy form drag. Notice the tendency for the formation of a series of counterrotating gyres on either sides of the central, more energetic, gyre pair. This tendency has been observed in several idealized experiments in a box ocean (Holland and Rhines, 1980)

As discussed in the previous chapter, the streamfunction distribution specified at the northern boundary is constant. In fact, due to the impossibility of using the dynamic method in a shallow area, we were not able to construct the shallow flow crossing the northern boundary. We specifically decided not to include a hypothetical subpolar gyre input at our northern boundary. The way the model responds to the corresponding boundary conditions used in this simulation is through a broadening of the jet, with little subpolar gyre flow. The excess of transport carried by this portion of the stream, with respect to the prescribed boundary values, is probably responsible for the tight recirculation gyre which forms at the northeastern corner of the domain, although eddy-driving may also play a role. This feature is clearly unrealistic and suggests a re-evaluation of our boundary conditions there. For example the prescription of boundary values that allow the excess flow to exit the domain are expected to eliminate the formation of the Fofonoff-type gyre. Radiation boundary conditions appears also to be desirable. We will discuss this issue more in detail later.

4.2.1 Comparison with the initial conditions

The mean streamfunction fields in the upper three layers at statistical steady state (Fig 4.1a - 4.1c) show several differences with respect to the initial conditions used in this simulation (Fig. 3.3). This tells us that the mean flow consistent with the model dynamics, for the given choice of boundary conditions, wind forcing and friction parameters, is different from the mean flow derived from climatological

data. The major discrepancies are the separation of the model Gulf Stream from the coast as well as the stream path, which tends to be much more zonal in the model and displaced further south. Fig. 4.3 shows the comparison between the meridional profiles of mean zonal velocity at 55°W in the model (dashed line) and in the initial fields. These values have been averaged over 10° of longitude, as in Fig. 3.4. This comparison illustrates how the model fields have drifted away from the initial conditions, by developing a narrower eastward flowing jet which is displaced about three degrees of latitude south of the initial one. In layers 1 and 2 the maximum eastward velocity is almost the same, while in the third layer the eastward flow has become more intense.

There can be several reasons for these discrepancies. First of all the outflow conditions specified at the eastern boundary appears to have a large influence in determining the Stream path, as seen in the previous section. The lack of any inflow associated with the subpolar gyre can also affect the position of the Stream. In fact, as shown by Holland in a series of sensitivity studies with this type of models (Holland, personal communication) the specification of an inflow at the northern and eastern boundaries can be used to tune the position of the eastward flowing jet. The inclusion of a deep western boundary current has proved useful in improving the characteristics of the Stream separation from the coast in a 2-layer, primitive equation model with a domain similar to ours (Thompson and Schmitz, 1989). In that case, however, the vertical discretization is probably too coarse for deriving general conclusions. The lack of a variable bathymetry might represent another important factor in determining the pattern of the mean model circulation. Preliminary experiments that included bottom topography showed the possibility of achieving a more realistic Stream separation from the coast. Finally, we have also to mention possible inaccuracies in the wind field. The climatological winds used in the present study (Hellerman and Rosenstein, 1983) has been derived from the

historical data set of surface marine observations, primarily from ships. Therefore the effect of inhomogeneous data distribution, associated with the ship routes, the possible bias introduced by the visual character of the observations as well as the processes of data averaging and smoothing can be expected to introduce errors in the final estimates of the wind field. A clear assessment of these errors is lacking. However, the Hellerman-Rosenstein winds appear consistent with long-term in situ observations over the North-Atlantic, so that they seem to have some reliability in this area. The wind variability is another aspect that is missing in this study. However, in the region we are considering, instability processes are very likely to be the most efficient source of time dependent motion.

All the factors that we have listed above (eastern and northern open boundary conditions, variable bottom topography, wind inaccuracies and variability) can be very effective in shaping the mean model circulation. However, a complete description of their interdependent effects and a clear understanding of the processes involved is still lacking, not only in the context of QG models, but in ocean modeling in general. In particular issues like the mechanisms for the Stream separation (Cessi, 1990), the effect of different wind patterns (Rhines and Shopps, 1991) as well as the influence of different space-time averaging of the winds (Large, Holland and Evans, 1991; Large, Milliff and Holland, personal communication) are still active topics of research.

Another difference between the final streamfunction fields and the initial ones is given by the two tight recirculation gyres which develop during the free model evolution and which seem to be partially responsible for the rapid depletion of the eastward flowing jet and for its limited penetration scale. Experiments performed by Marshall and Marshall (1992) with a reduced gravity model suggest that the characteristics of the inertial recirculation and the consequent penetration

scale of the jet can be affected by the boundary condition used to describe the jet entering at the western boundary. The rationale behind their results is that the profile chosen for the jet at the western boundary establishes a relationship between streamfunction and potential vorticity, with a given value of the parameter $\alpha = \frac{dq}{d\psi}$. Depending on the sign of α, either Fofonoff-like solutions ($\alpha > 0$) or modon-like solutions ($\alpha < 0$) can be excited in a resonant fashion. In the first case the jet can cross the whole domain, while in the second case a tight recirculation close to the western boundary is expected. The characteristics of the recirculation in our solution are consistent with these results even if the context of the present model simulation is more complex than the simple idealized experiment of Marshall and Marshall. The possibility of improving the degree of realism of the model recirculation by a proper tuning of the inflow condition at the western boundary should be carefully considered in future studies.

4.2.2 Total transport

The total transport streamfunction is computed by adding the transports in each layer:

$$\psi_T = \sum_{i=1}^{5} H_i \psi_i \qquad (4.2.2.1)$$

The result for this model simulation is shown in Fig. 4.4a. The units for ψ_T in this figure are $10^6 m^3/s$, so that the corresponding transports between any pair of contours are in Sverdrups. The contour interval is 15 Sverdrups. The jet entering the domain south of Cape Hatteras increases its transport rapidly from the initial value of 52 Sv prescribed at the western boundary to a maximum of about 400 Sv around 72°W, which is the longitude corresponding to the most intense inertial recirculation flow in the model. East of this longitude the stream transport decreases rapidly. Not more than 30 Sv are left at 55°W, and only 15 - 20 Sv are carried

by the stream east of 50°W. This along-stream variation in total transport can be compared and contrasted with the observational estimates reported by Richardson (1985) and reproduced here in Fig. 4.4b. In this figure he compares the along-stream variation of 'synoptic' transport as given by Worthington (1976) with the variation of the long-term mean transport obtained from space-time averages of velocities. Although the two curves differ in their maximum values, the transport variations are qualitatively similar in both cases. In particular in both estimates the maximum transport is attained around 65°W, further east than in the model. The maximum value, which is reported by Worthington, is about 150 Sv, much smaller than the maximum transport of 400 Sv estimated in the model. However, the model jet transport decreases rapidly farther east where its values are lower than the observed ones. This comparison confirms the considerations made before about the characteristics of the recirculation in this numerical simulation, which seems to be much too intense and too limited in its zonal extent with respect to that suggested by observations.

4.3 Potential vorticity fields

Potential vorticity represents the central dynamical quantity in QG models. In fact the QG equations presented in Chapter 3 are statements of quasi-conservation of this quantity. In the context of the assimilation experiment (Chapter 5) the evolution of the potential vorticity fields will supply the most stringent criterion for monitoring the convergence of the system toward a statistical steady state. The quasi-geostrophic potential vorticity has been defined in Chapter 3 (section 3.3.3). In this section we consider the climatological distributions of potential vorticity when the model is allowed to run freely, without any data constraints applied at the surface. The characteristics of these fields can be

rationalized in terms of the time averaged equations (4.2.3), which can be rewritten in a more compact form for the generic layer k:

$$J(\bar{\psi}_k, \bar{q}_k) = \bar{T}_k \delta_{k1} + \bar{F}_k - \overline{J(\psi'_k, q'_k)} \tag{4.3.1}$$

The dominant processes leading to the final distributions are the advection by the mean flow ($J(\bar{\psi}_k, \bar{q}_k)$), the input of vorticity by the wind in the first layer ($\bar{T}_1$), the dissipation by biharmonic friction ($\bar{F}_k$) and the divergence of the eddy flux of eddy potential vorticity ($\overline{J(\psi'_k, q'_k)}$). This last term represents the end result (the time averaged effect) of the eddy processes. These processes produce a distortion of the potential vorticity contours, which become more and more convoluted with finer and finer structure, a phenomenon known as enstrophy cascade (Rhines, 1979). At the scales comparable with the model resolution enstrophy is finally dissipated by biharmonic friction. This process results in mixing of potential vorticity by the turbulent eddy field, leading to an irreversible deformation of the potential vorticity contours. Marshall (1984) shows that the divergent part of the eddy potential vorticity flux is directed down the $\bar{q}$-gradients in order to balance the dissipation of eddy enstrophy by the biharmonic friction. As a consequence, the eddy advection term in (4.3.1) will tend to flatten the $\bar{q}$-gradients if mean advection and forcing are not efficient enough in restoring them. The tendency for the development of large plateaus of potential vorticity in the intermidiate layers of QG models has in fact been observed in several studies, starting with the numerical experiments of Holland (personal communication) and leading to the theory of homogenization of potential vorticity by Rhines and Young (1982). According to some observational studies (McDowell, Rhines and Keffer, 1982; Keffer, 1985) areas of homogenized potential vorticity are also found in data. However, these studies used data sets with a coarse resolution, so that their validity is still controversial.

The results obtained in this particular model simulation show characteristics of potential vorticity evolution in agreement with the previous numerical studies. In Fig. 4.5 we show the mean potential vorticity contours (dashed lines) superimposed on the mean streamfunction contours (solid lines). Notice that the contour intervals used for the first layer (10000 m^2/s for the streamfunction and $5\times10^{-6}s^{-1}$ for the potential vorticity) are different from the ones used for the other four layers (5000 m^2/s for the streamfunction and $2.5\times10^{-6}s^{-1}$ for the potential vorticity).

In the first layer (Fig. 4.5a), where the mean flow is strong and forcing is present, large gradients of mean potential vorticity can be observed, the largest gradients being associated with the eastward flowing jet. Due to the zonal character of the stream the $\bar{q}$-contours are essentially zonal in this area, with gradients much larger than the planetary vorticity gradients. We can notice, in Fig. 4.5a, a general tendency for the $\bar{q}$-contours to follow the $\bar{\psi}$-contours. However, in some parts of the domain a significant component of the flow crosses the $\bar{q}$-contours. This occurs mainly in the area of the inertial recirculation, west of 60°W, with characteristics very similar to the ones described by Marshall (1984) for the case of a QG barotropic model. Due to the highly non-linear nature of the flow in this area the mechanism which allows the $\bar{\psi}$-contours to cross the $\bar{q}$-contours is the divergence of the eddy flux of potential vorticity.

In layers 2 and 3 (Fig. 4.5b and 4.5c), where forcing is no longer present and the mean flow is weaker, the potential vorticity gradients are largely reduced due to the turbulent eddy mixing processes. This is evident especially in layer 3, where we can notice both the effect of the advection by the mean flow, which tends to wrap the $\bar{q}$-contours around following the shape of the gyres, and the effect of the eddy mixing, which tends to erode the $\bar{q}$-gradients and to create plateaus in the potential vorticity distribution. In layer 3 the area where this irreversible deformation of

the $\bar{q}$-contours occurs appears slightly smaller and displaced toward the north-west with respect to layer 2. In the southern part of the domain, on the other hand, the zonal contours associated with the planetary vorticity gradients appear. Finally, in layers 4 and 5, where the flow is much weaker, the potential vorticity gradients are dominated by the βy term. A slight distortion of these contours is evident only in the area of the inertial recirculation gyres, which represent the only significant flow in these layers.

Fig. 4.6 and Fig. 4.7 present sections of potential vorticity at two different longitudes, 70°W and 55°W. The contributions of the planetary vorticity (thin solid line), stretching (dashed line) and relative vorticity (dotted line) to the total potential vorticity profiles (thick solid line) are shown. Only layers 1, 3 and 5 are shown for brevity. At both longitudes the dominant contributions are given by the planetary vorticity and stretching terms. The latter is particularly large in layer 1, while the planetary term is dominant in layer 5. In layer 3 the two contributions are comparable and almost compensating in the central latitude range, leading to a plateauing (homogenized region) in the total potential vorticity profiles. Relative vorticity is almost indistinguishable from zero everywhere, except in the area of the jet. The contribution of the relative vorticity is relatively larger at 70°W, where smaller scales and sharper gradients in the flow fields can be found. However, even at this longitude, this contribution is not as large as the one associated with the stretching term.

4.4 The eddy field

In this section we analyze the climatology of the model eddy field. Since we are considering here the model in which no data have been assimilated, the eddy field is produced by the natural baroclinic and barotropic instabilities that

occur in the model. As an example, Fig. 4.8 shows a typical instantaneous state on a particular day toward the end of the integration. Only the first, third, and fifth layer streamfunctions are shown for brevity. The far field is dominated by intense eddies of barotropic nature, whose characteristic length scales appear to be much larger than the ones typical of the ocean variability (Le Traon et al., 1990). According to Holland (personal communication) such unrealistic eddies are often found in QG experiments with constant depth. The comparison of Fig. 4.8 with the instantaneous eddy field derived from Geosat data (Fig. 2.1a) illustrates visually these differences. In the next chapter we will describe an experiment in which the Geosat data are assimilated into the model. The modifications induced by that procedure in the model behavior will depend on the differences between the 'observed' eddy field and the eddy field developed by the model in its free evolution. We would like to understand the dynamical meaning of the flow that develops in the subsurface layers when the surface field is 'nudged' toward the 'observations', so that we can interpret the results of the assimilation experiment in that perspective. To that end we define, in this section, some of the characteristics of the model eddy field in relation to 'observed' characteristics. The aspects of the eddy climatology that we analyze are the eddy kinetic energy level and distribution as well as the space and time scales typical of the eddy field in different areas of the unconstrained model.

4.4.1 Eddy kinetic energy

The most energetic part of the flow, including the strong westward flow associated with the inertial recirculation gyres, seems to be confined in all five layers to the western half of the domain. Therefore we may expect that also the instability processes, leading to eddy production, will mainly take place in this area. Fig. 4.9

shows, in fact, the eddy kinetic energy distribution within the model domain. A large pool of high eddy kinetic energy, up to values of 6000 cm^2/sec^2 in layer 1, is found in the western part of the domain. A tongue of maximum values extends a bit north of Cape Hatteras and then mainly eastward, centered upon 37°N. The tongue of high values is oriented along the stream path. This is especially evident in layer 1. The eddy kinetic energy levels in all layers maintain relatively high values in much of the domain, due to the presence of large barotropic eddies.

By comparison with the 'classical' picture of surface eddy kinetic energy distribution produced by Richardson (Fig. 2.10b), it is immediately evident that the corresponding map obtained from the model simulation (Fig. 4.9a) is far from realistic both in pattern and intensity. The discrepancy in pattern is obviously associated with the mean position of the model jet which, as mentioned before, leaves the coast a little past Cape Hatteras and remains at a latitude which is too far south with respect to the position of the real Gulf Stream, as illustrated by the climatological field in Fig. 4.1a.

The eddy kinetic energy in the model simulation is at least 50% higher than in Richardson's map. Also at depth the level is far too high when compared with the abyssal eddy kinetic energy picture constructed by Schmitz (1984). These unrealistically high eddy kinetic energy values can be probably explained with intense instability processes taking place in the western half of the domain. In this area, in fact, the model jet is very narrow and energetic, thus favoring barotropic instability processes. We also have, in the same area, intense westward flows associated with the inertial recirculation gyres, where baroclinic instability is very likely to occur (Pedlosky, 1979). The basin-like character of the eddy kinetic energy distribution, especially at depths, can be attributed to the presence of the barotropic eddies mentioned before. In the next section we will see, in fact, that the barotropic

disturbances present in the model eddy field tend to organize themselves in the form of basin modes.

A careful tuning of the frictional parameters may have allowed us to achieve a more realistic energy level. Also if we had included realistic bottom relief, the barotropic eddies might have been reduced in amplitude. However, as stated before, we have decided to avoid any tuning of the model alone, in order to illustrate the effect of data assimilation on the model behavior when the same parameter choices are adopted.

4.4.2 Time scales

The distribution of eddy kinetic energy described in the previous section suggests the existence of different dynamical regimes in different parts of the domain. Eddy generation seems to be confined to the western half of the region where the flow can be expected to be strongly nonlinear and instability processes are more likely to occur. In the far field, on the other hand, we can anticipate a more linear regime. Also, from Fig. 4.8, we can expect a strong barotropic signal in the time dependent motion in this area. The geographical variation of the frequency spectra reflects these differences in dynamics, as illustrated by Fig. 4.10. In this figure we show frequency spectra for the streamfunction at four locations. The different curves in each panel refer to the different layers: the solid line corresponds to layer 1, the long-dashed line to layer 2, the short-dashed line to layer 3, the dot-dashed line to layer 4 and the dotted line to layer 5. The time series used to compute the spectra were obtained from the data corresponding to the last two years of the model simulation, sampled daily. Fig. 4.10a shows the streamfunction spectra at 65°W, 37°N, a point located in the centre of the eastward flowing jet. In all layers the energy level is high and relatively constant at low frequencies and then

it decreases rapidly at frequencies greater than about 3 x 10^{-2}days^{-1} (~30 days). The energy level decreases with depth at almost all frequencies with the exception of the band between 14 and 50 days, where the decay from the surface to the bottom layers seems minor. In this band isolated peaks can be observed at approximately 14 days, 20 days and 30-35 days.

If we move to 55°W at the same latitude (Fig. 4.10b) the energy level generally decreases. The smallest variations are observed, again, in the band 14 - 50 days, where the intensity seems to be also independent of depth. However, outside this band, the energy level is now much lower than at 65°W and is a strong function of depth. In layers 4 and 5, in particular, the intensity decays much faster both at higher and lower frequencies.

Fig. 4.10c and 4.10d show the changes in spectral shape at locations away from the jet, in the far field. The spectra in Fig. 4.10c refer to the point 55°W, 43°N, while the spectra in Fig. 4.10d are from the point 55°W, 30°N. At these locations, away from the more nonlinear regions, the dominant signal is given by the peaks in the band 14 - 50 days. The amplitude of these frequencies has remained approximately the same as in the spectra from the locations within the jet. At all the other frequencies, on the other hand, the energy has dropped several orders of magnitude. At these 'far field' positions the spectra corresponding to the different layers are almost indistinguishable from each other, supporting the idea of a barotropic nature of these oscillations.

The spectral description that seems to emerge from this analysis is the following: the barotropic oscillations in the model tend to organize themselves in basin mode structures, whose amplitude is almost the same everywhere. The frequencies of these oscillations are in the interval between approximately 14 and 50 days. In regions where nonlinear interactions are weak this is the dominant signal

in the time dependent motion. In areas where the flow is more energetic, on the other hand, baroclinic instability mechanisms are more likely to occur and nonlinear interactions play a more important role. In this case the spectral peaks associated with the basin modes are partially hidden by the energy level associated with the nonlinear interaction, characterized by an almost monotonic energy growth toward the low frequencies.

How 'realistic' are the model frequency spectra? In order to answer this question we compare, in Fig. 4.11, velocity spectra from the model with velocity spectra from current meter time series. The current meter measurements used for this comparison are the ones described in Chapter 1 (Hogg, personal communication). Here we consider only the time series from the mooring at 40.86°N, 54.67°W, at the depths of 247 m, 1008 m and 3995 m. The position of this mooring is within the range of excursion of the meandering Gulf Stream. The velocity time series from the model are computed geostrophically from the streamfunction fields in the different layers and then interpolated linearly to the depths of the current meters. The point chosen for the comparison in the model is 55°W, 37.5°N, a point which lies within the model Gulf Stream. Therefore the spectra we compare can be considered representative of dynamically equivalent regions. Large discrepancies can be observed in the band 14 - 50 days, especially in the meridional velocity spectra at 1000 and 4000m depth. The energy bulge present in the model spectra at these frequencies, which we have identified with perhaps artificial basin modes, is indeed not found in the current meter spectra. Discrepancies are also observed in the high frequency tail of the spectra: the energy level decreases in the data while it tends to flatten in the model. At 3995m the low frequency energy in the model zonal velocity spectra is almost an order of magnitude lower than in the current meter data, a difference that exceeds the estimated confidence interval.

4.4.3 Length scales

The visual comparison between Fig. 4.8 and Fig. 2.1a shows that the eddies produced by the natural instabilities of the model seem to have larger scales than the ones in the eddy field obtained from the Geosat data. In this section we make this observation more quantitative by comparing the wavenumber spectra obtained from the Geosat data along the satellite tracks with similar spectra obtained from the model. Because of their high resolution in the along-track direction, the Geosat data can supply an accurate spatial sampling of the mesoscale eddy field in the ocean. They have in fact been used by Le Traon et al. (1990) for the definition of the spatial scales typical of different areas of the North Atlantic.

Here we consider the two ascending subtracks shown in Fig. 4.12c. They are labeled with the letters A and B. For each of them we have selected, from the Geosat data set, 18 profiles of sea surface height, at intervals of 34 days. We have constructed a similar data set from the model by interpolating the upper layer streamfunction fields to the same points along the subtracks. The streamfunction values have then been converted to sea surface height values. We have considered fields at 34 days interval also for the model. The average wavenumber spectra for the two subtracks are shown in Fig. 4.12a and Fig. 4.12b. In these figures the solid line identifies the spectra from the Geosat data, while the dashed line is used for the spectra from the model. The wavenumber spectra from Geosat data do not change noticeably from one subtrack to the other, while the model spectra show a relatively large decrease in energy level from subtrack A to subtrack B. This reflects the rapid decrease in eddy kinetic energy toward the east, that we have observed in the maps of eddy kinetic energy (Fig. 4.9). The Geosat data, on the other hand, suggest a much slower variation of the eddy kinetic energy as a function of longitude.

In both cases the energy level in the model spectra is much larger than the one in Geosat spectra at low wavenumbers, but it decreases much faster at high wavenumbers. The dotted line in Fig. 4.12a and Fig. 4.12b represents the spectra obtained when only the component of sea surface height associated with the model baroclinic modes is considered. The high energy level present in the dashed line spectra at wavelengths longer than about 500 km drops considerably in the spectra relative to the baroclinic part of the time dependent motion, suggesting that the unrealistically large scales observed in Fig. 4.8 are mainly associated with the barotropic eddies. If we adopt, as an integral measure of the spatial scales, the inverse of the mean wavenumber:

$$< k >^{-1} = \frac{\int E(k)dk}{\int kE(k)dk} \qquad (4.4.3.1)$$

we obtain values of 276 km and 294 km for the Geosat data along the subtracks A and B, respectively. For the model, on the other hand, we obtain a value of ~770 km along subtrack A and a value as large as 1091 km along subtrack B. For comparison, the value of $< k >^{-1}$ obtained by Le Traon et al. (1990) in this area, by averaging wavenumber spectra along both ascending and available descending tracks in squares of 10° latitude times 10° longitude is 380 km, a value only slightly larger than the ones we find along the subtracks considered. These figures clearly quantify the differences in spatial scales between the model and the Geosat data which we have anticipated by visual comparison.

4.5 Summary and conclusions

In this chapter we have tried to define the basic characteristics of the model behavior when no data are assimilated at the surface. Among all the possible model realizations, which can be obtained as a result of different parameter choices, we have considered that particular realization which is obtained when initial conditions,

boundary conditions as well as frictional parameters are chosen to be exactly the same as the ones considered appropriate for the assimilation experiment. In this way we will be able to clearly identify the changes that can be induced in the model behavior by nudging the surface fields to follow 'the observations'. The results we obtain are in agreement with previous studies of QG dynamics in idealized domains and can be explained within the dynamical framework developed from those studies. However, when considering available observations, discrepancies appear between the model behavior and the perception of the ocean circulation that can be derived from the measurements in this area. These discrepancies, which, in different ways and to different extents, are common to any ocean model, are mainly associated with the path of the model stream and with the distribution and intensity of the eddy kinetic energy. From a spectral point of view the model reveals a high degree of complexity and richness in its spatial and temporal scales. However, the typical model length scales seem to be larger than the ones associated with the mesoscale eddy field in the ocean. A better agreement with observations seems to exist in frequency domain. In fact frequency spectra from velocity time series in the model show remarkable similarities with the spectra computed from current meter measurements, both in shape and energy level. However, the model reveals a tendency to develop basin mode structures of a barotropic nature for which no evidence has been found in the available data.

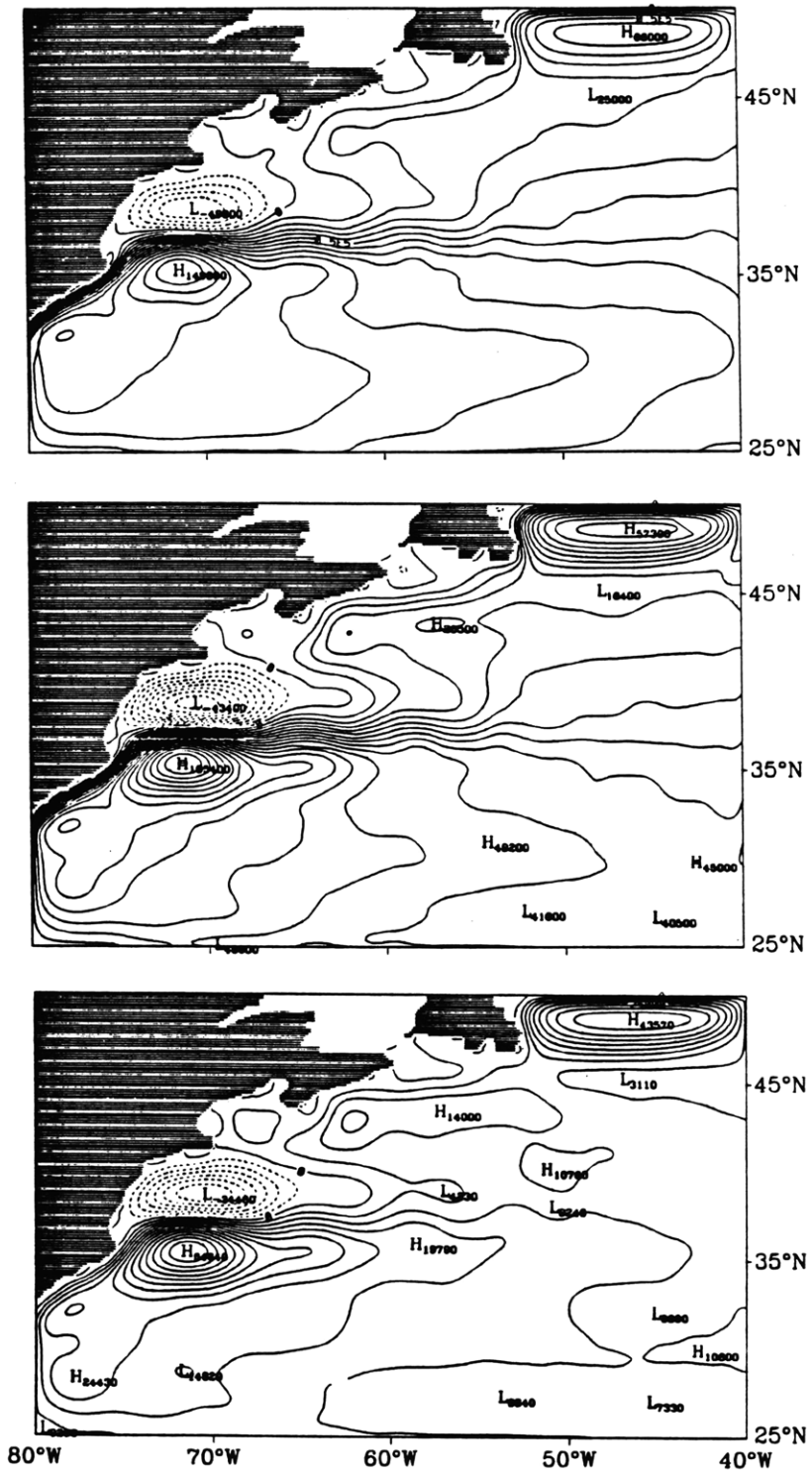

Fig. 4.1 Mean streamfunction fields in the five model layers obtained in the case in which no data are assimilated at the surface. The model is forced with Hellerman annual winds as well as inflow/outflow at the open boundaries. The time average is performed over a four year period. (a) Layer 1. Contour interval is $10000 m^2/s$. (b) Layer 2. Contour interval is $5000 m^2/s$. (c) Layer 3. Contour interval is $5000 m^2/s$.

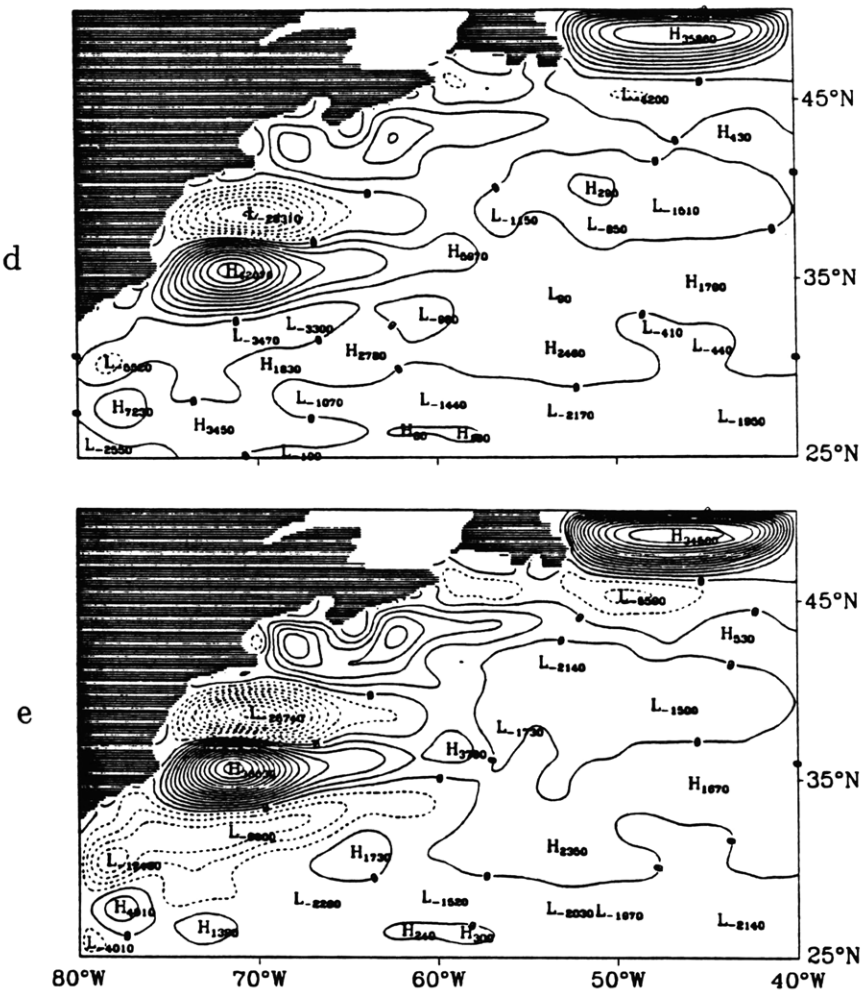

Fig. 4.1 (continued) (d) Layer 4. Contour interval is $4000 m^2/s$. (e) Layer 5. Contour interval is $2500 m^2/s$.

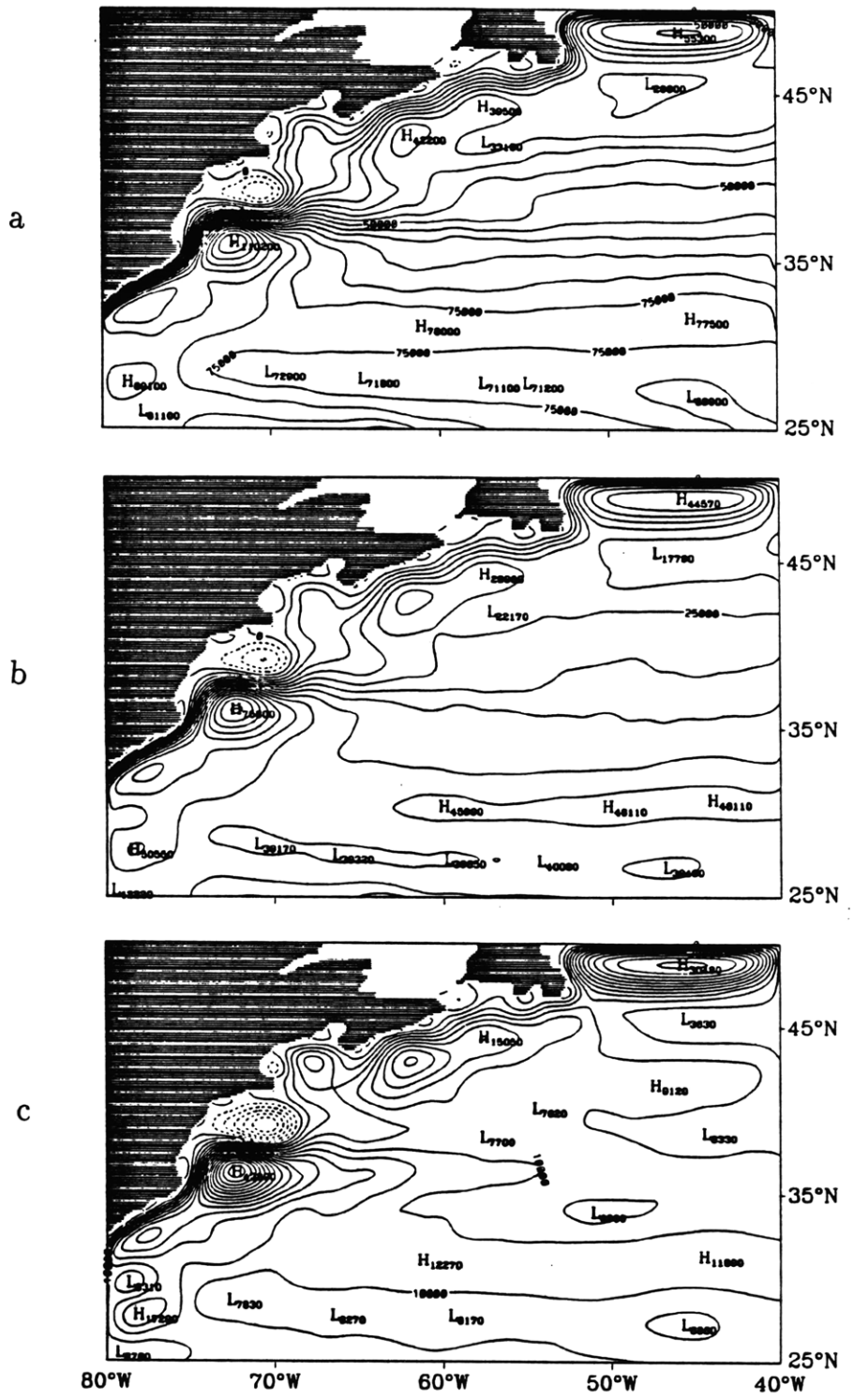

Fig. 4.2 Mean streamfunction fields in the five model layers obtained in the case in which no data are assimilated at the surface. In this case the model is forced only with inflow/outflow at the open boundaries. The time average is performed over a four year period. (a) Layer 1. Contour interval is $5000\text{m}^2/\text{s}$. (b) Layer 2. Contour interval is $5000\text{m}^2/\text{s}$. (c) Layer 3. Contour interval is $2500\text{m}^2/\text{s}$.

d

e

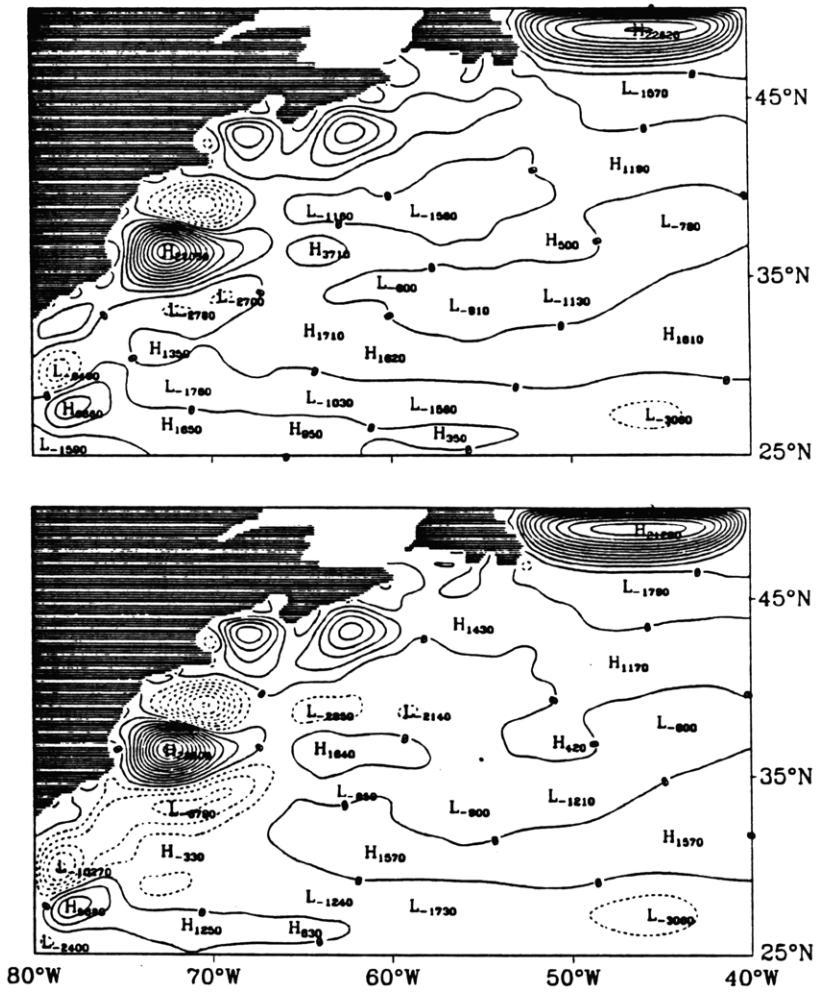

Fig. 4.2 (continued) (d) Layer 4. Contour interval is $2500 m^2/s$. (e) Layer 5. Contour interval is $2000 m^2/s$.

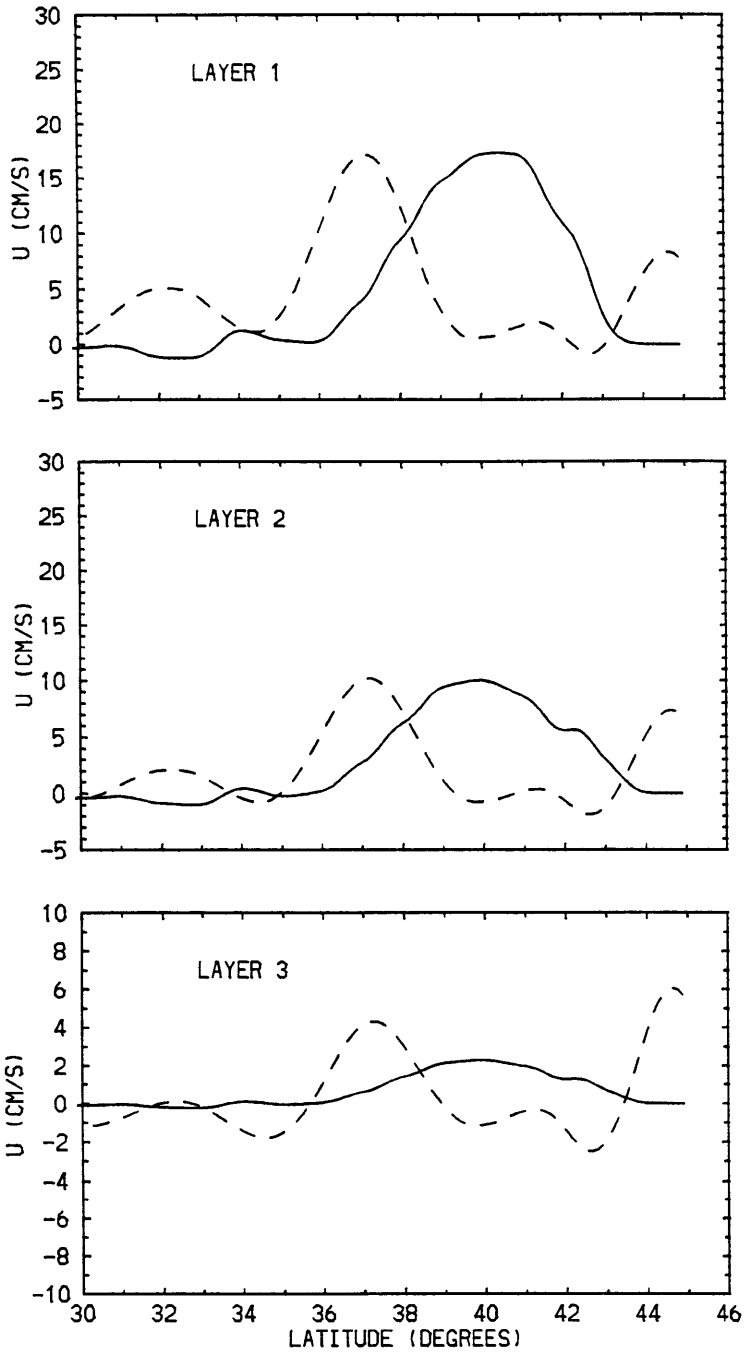

Fig. 4.3 Comparison of meridional profiles of mean zonal velocity around 55°W in the three upper model layers. The solid line indicates the zonal velocity profiles derived from the climatological fields in Fig. 3.3. The dashed line indicates the profiles from the control run.

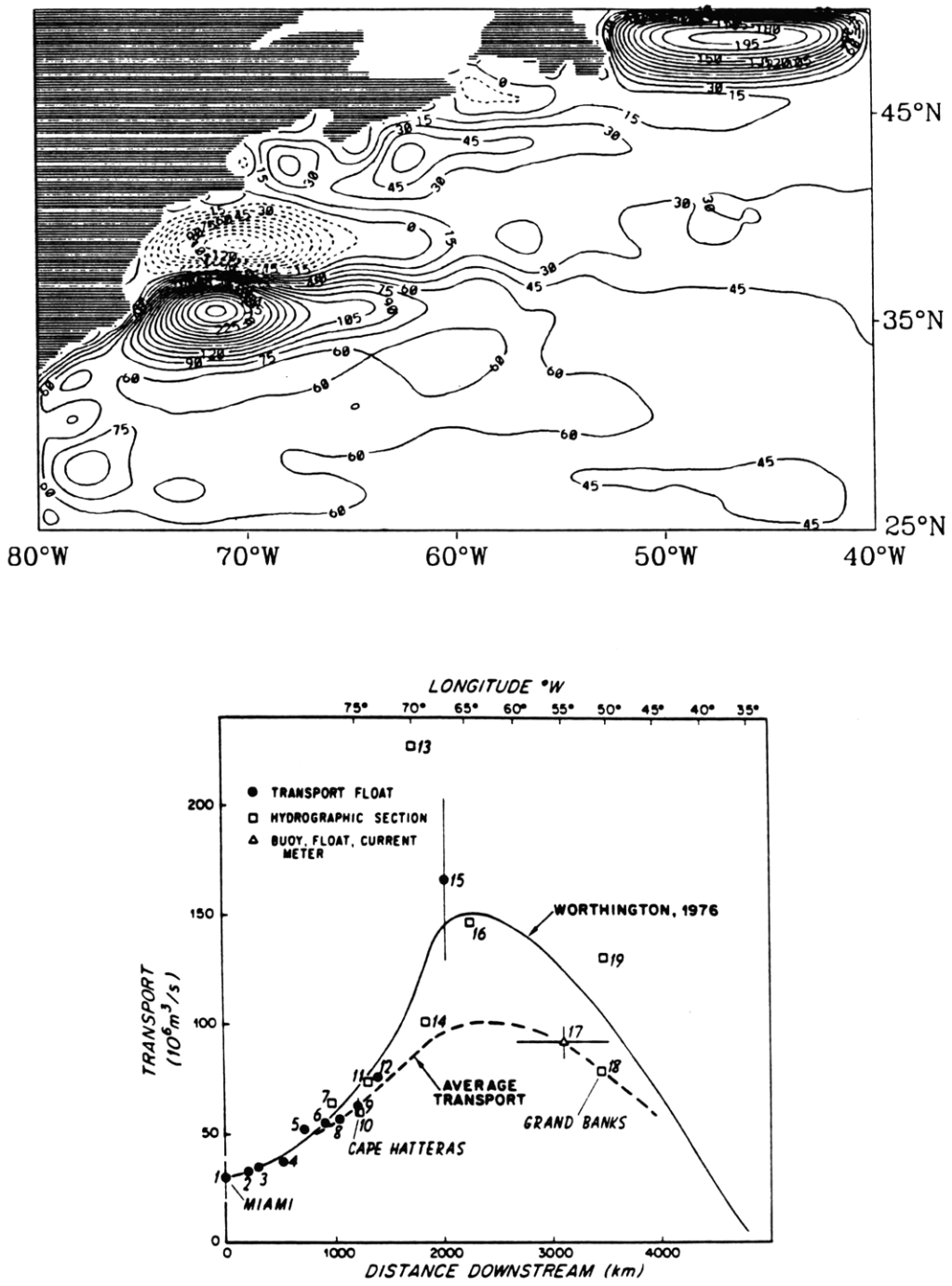

Fig. 4.4 (a) Mean barotropic streamfunction from the control run. The time average is computed over 4 years. Units are $10^6 m^3/s$ (1 Sv). Contour interval is 15 Sv. (b) Variation of the Gulf Stream transport as a function of distance downstream from Miami, reproduced from Richardson (1985). The solid curve represents the variation of synoptic transport as given by Worthington (1976). The dashed curve shows the variation of time-averaged transport.

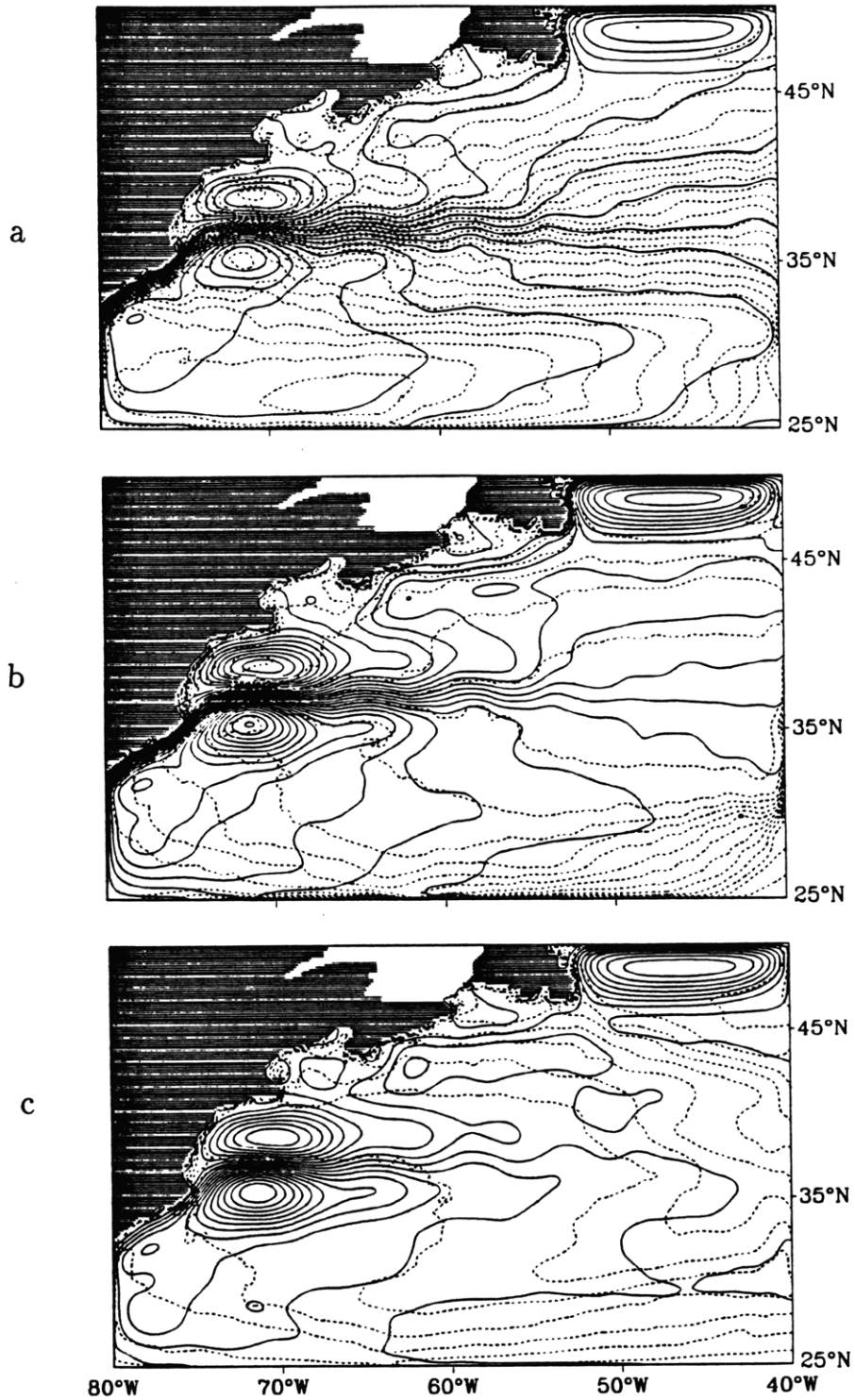

Fig. 4.5 Comparison between mean streamfunction contours and mean potential vorticity contours for the control run in the 5 model layers. (a) Layer 1. Streamfunction contour interval is 10000 m^2/s. Potential vorticity contour interval is $5\times10^{-6}s^{-1}$. (b) Layer 2. Streamfunction contour interval is 5000 m^2/s. Potential vorticity contour interval is $2.5\times10^{-6}s^{-1}$. (c) Layer 3. Streamfunction contour interval and potential vorticity contour interval as in layer 2.

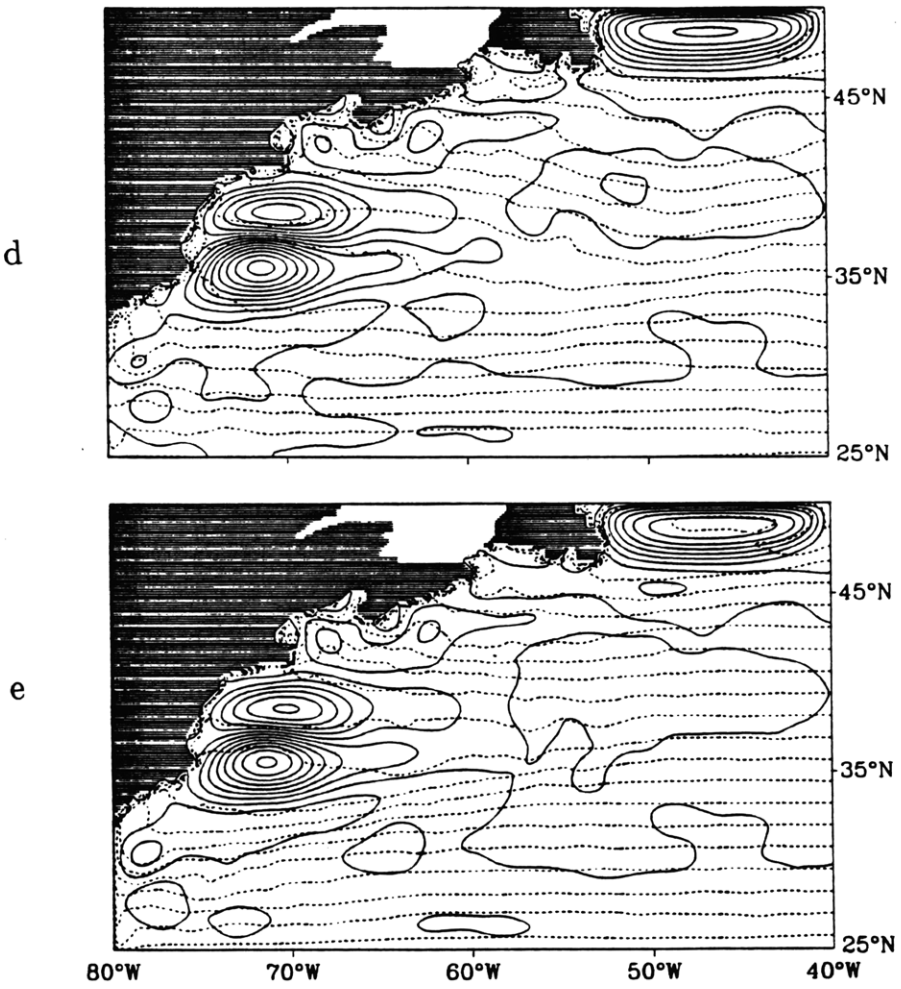

Fig. 4.5 (continued) (d) Layer 4. Streamfunction contour interval and potential vorticity contour interval as in layer 2. (e) Layer 5. Streamfunction contour interval and potential vorticity contour interval as in layer 2.

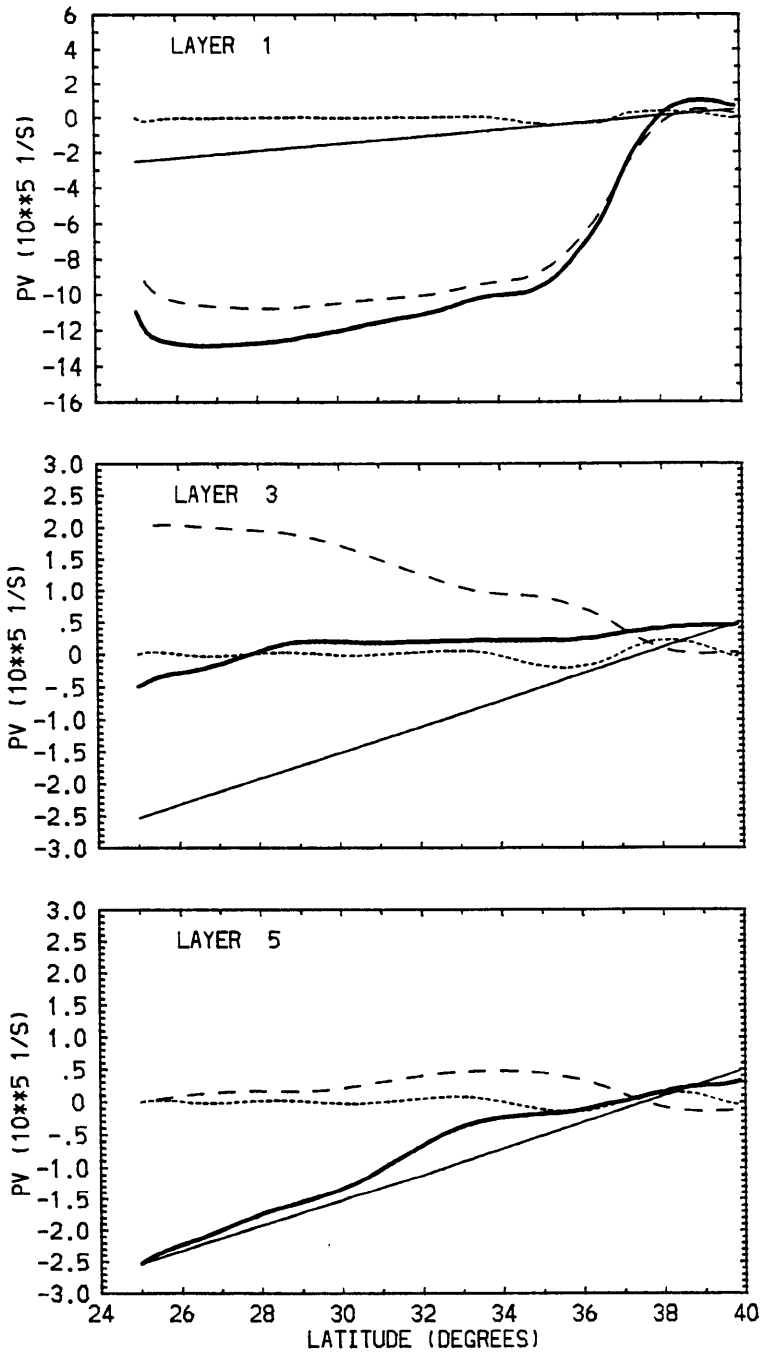

Fig. 4.6 Meridional profiles of potential vorticity components around 70°W in layer 1 (top), layer 3 (middle) and layer 5 (bottom). The thin solid line represents the planetary term, the dashed line the stretching term, the dotted line the relative vorticity and the thick solid line the total potential vorticity.

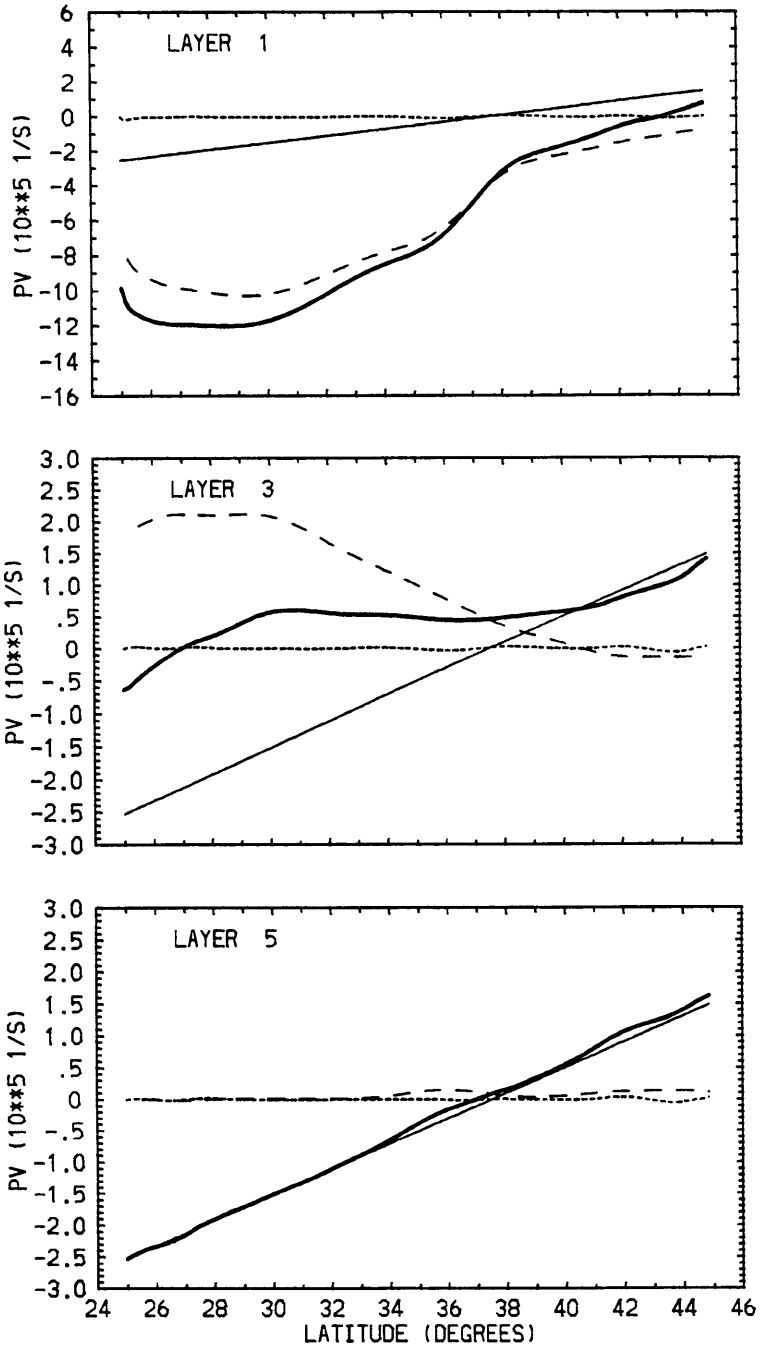

Fig. 4.7 Meridional profiles of potential vorticity components around 55°W in layer 1 (top), layer 3 (middle) and layer 5 (bottom). The thin solid line represents the planetary term, the dashed line the stretching term, the dotted line the relative vorticity and the thick solid line the total potential vorticity.

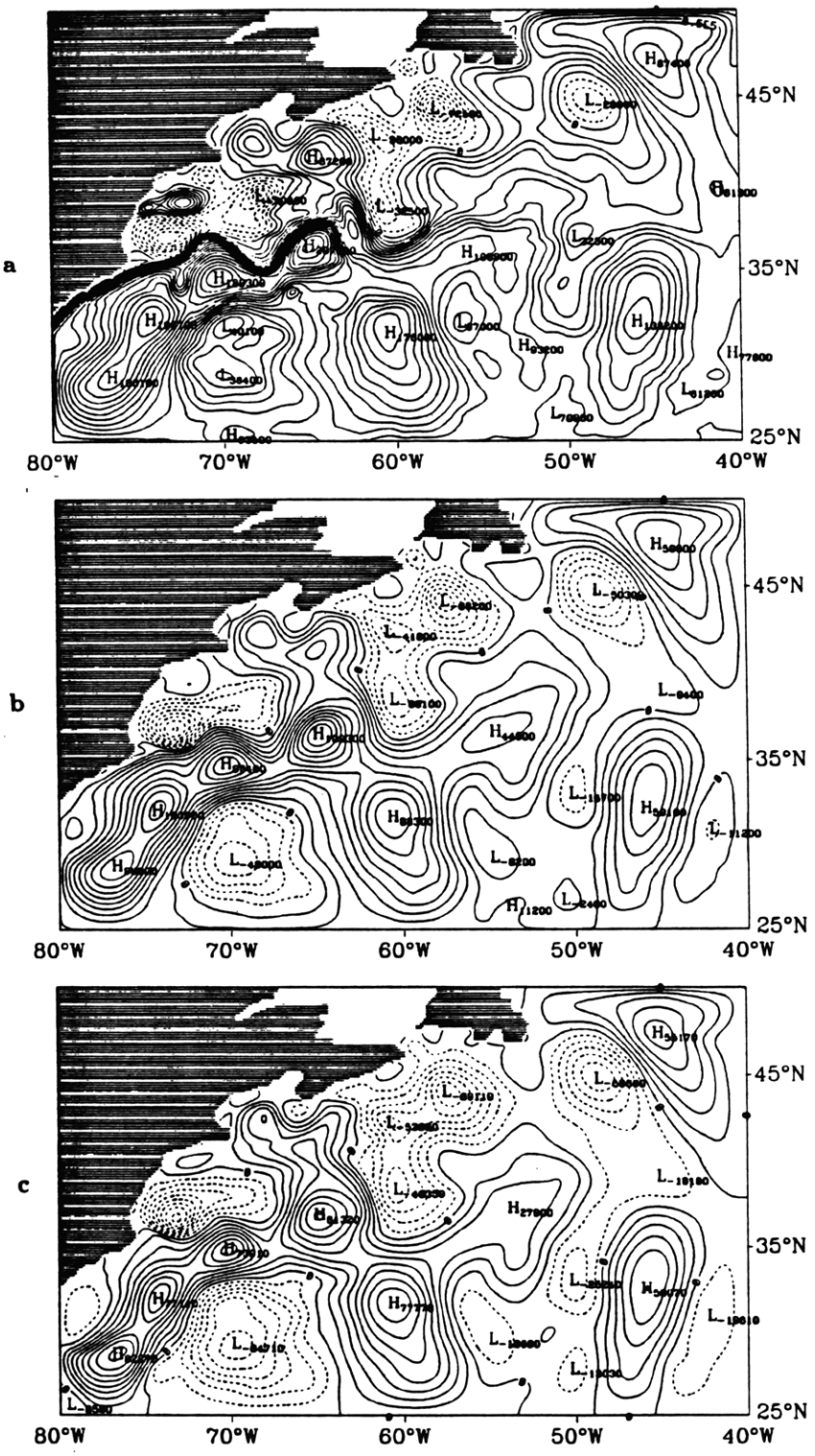

Fig. 4.8 Instantaneous streamfunction fields on a day toward the end of the 20 years integration. Only layer 1 (top), layer 3 (middle) and 5 (bottom) are shown.

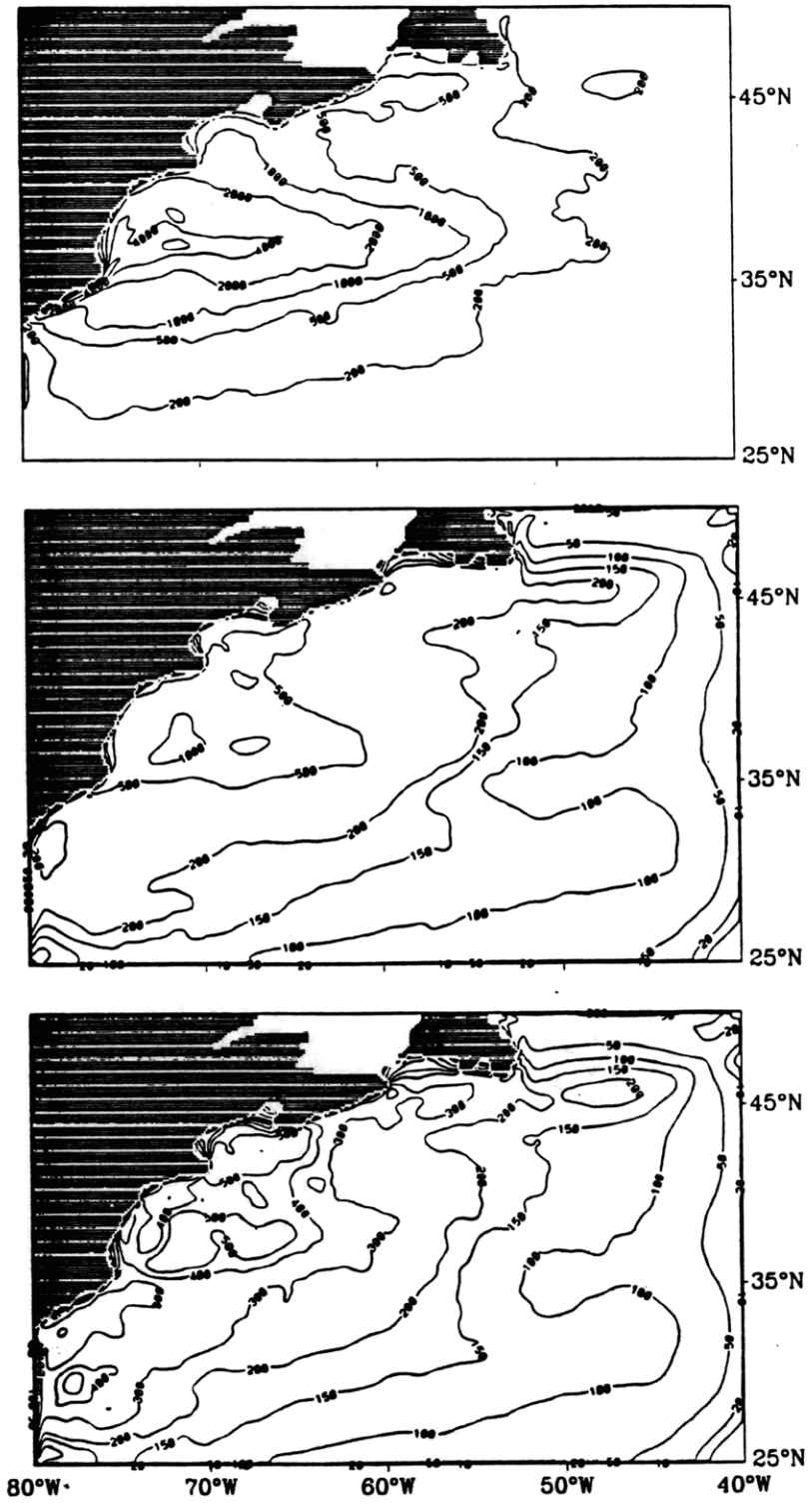

Fig. 4.9 Eddy kinetic energy distributions in layer 1 (top), layer 3 (middle) and layer 5 (bottom). Units are cm^2/s^2.

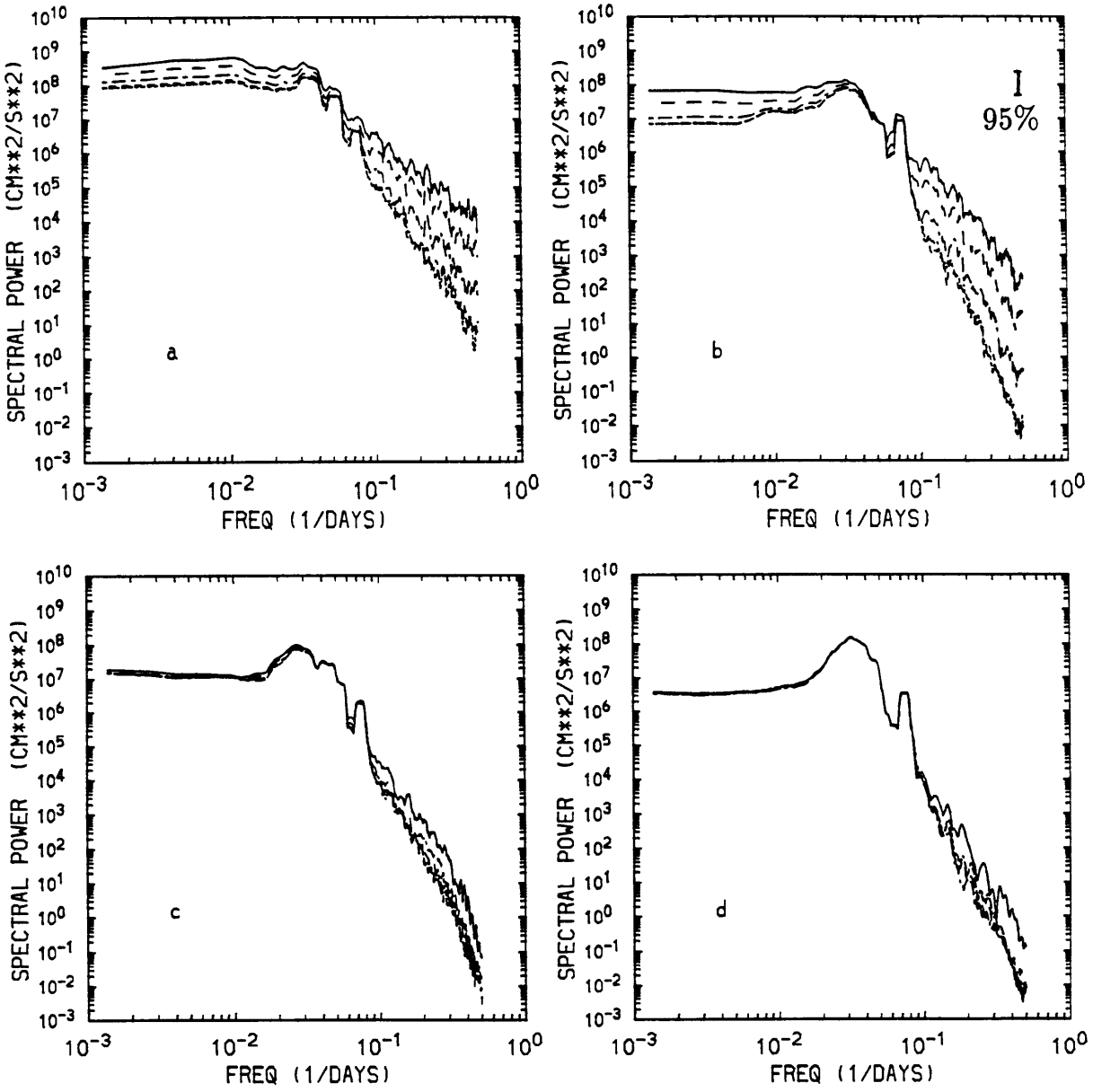

Fig. 4.10 Variation of model frequency spectra with location. The different curves in each panel refer to the five model layers. The solid line represents layer 1, the long-dashed line layer 2, the short-dashed line layer 3, the dot-dashed line layer 4 and the dotted line layer 5. (a) 65°W, 37°N. (b) 55°W, 37°N. (c)55°W, 43°N. (d)55°W, 30°N.

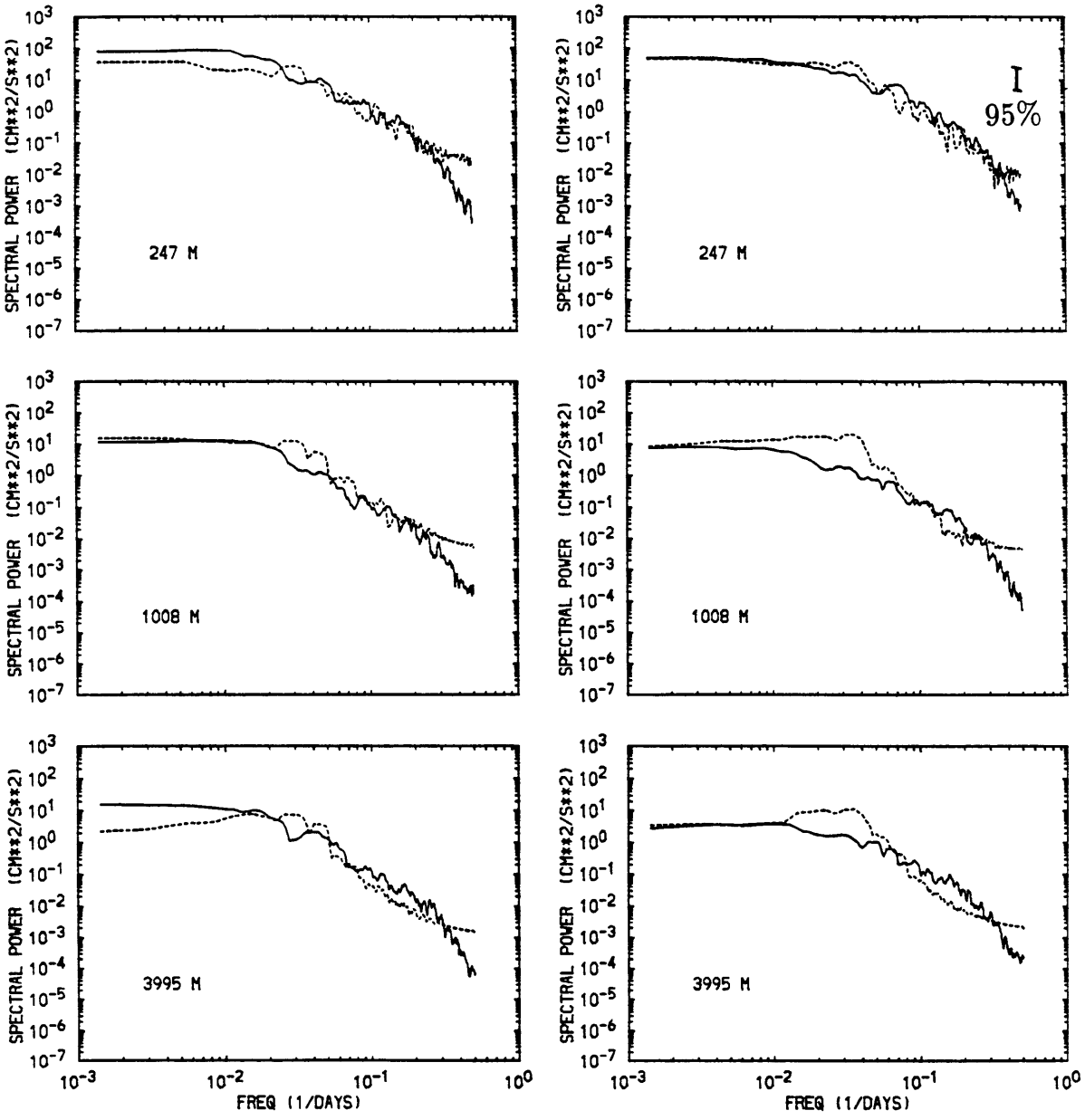

Fig. 4.11 Comparison between frequency spectra from current meter measurements at 10.86°N, 54.67°W (solid line) and geostrophic velocity spectra from the control run (dotted line). The time series from the model have been computed at the point 55°W, 37.5°N. They have been linearly interpolated from the layer depths to the current meter depths. The left panels correspond to the zonal velocity at 247m (top), 1008m (middle) and 3995m (bottom), while the right panels refer to the meridional velocity.

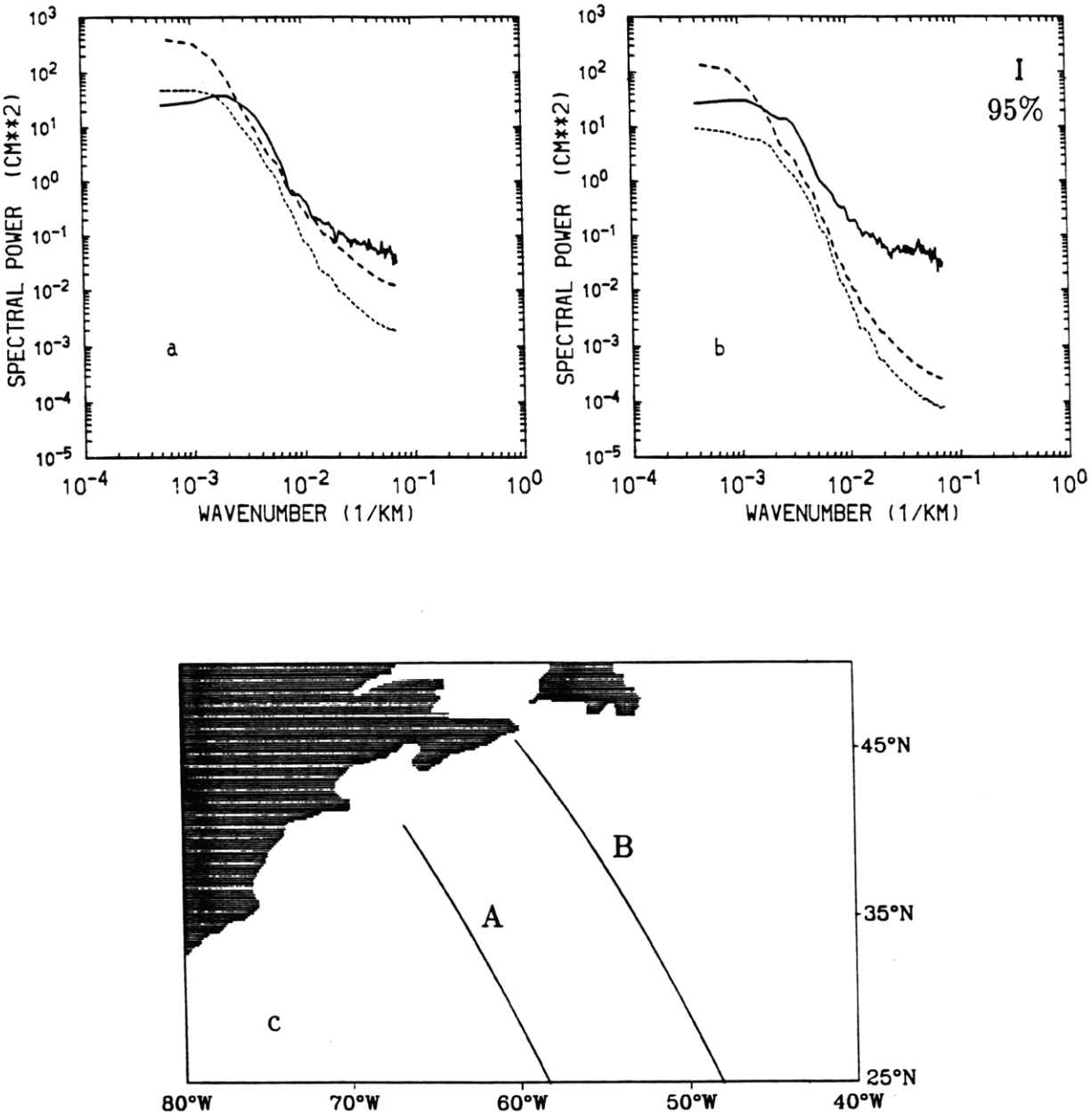

Fig. 4.12 Comparison between mean wavenumber spectra from Geosat data and equivalent spectra from the control run. All spectra have been computed as an average over 18 profiles of sea surface height, at 34 days intervals, along the Geosat subtracks shown in panel (c). The wavenumber corresponds to the along-track direction. The solid line describes the spectra from Geosat data, while the dashed line represents the spectra from the model. The dotted line is obtained from the baroclinic component of the model SSH. (a) Spectra relative to subtrack A in panel (c). (b) Spectra relative to subtrack B in panel (c). (c) Layout of the 2 subtracks considered for this comparison.

Chapter 5

Assimilation of surface data: Dynamical considerations and results

5.1 Introduction

In chapter 4 we have shown how the model, when allowed to evolve freely, drifts away from the climatological streamfunction fields used as initial conditions by developing a mean circulation different from the climatological one. Moreover, we have shown how the eddy field produced by the intrinsic model instabilities differs, in pattern, intensity and in some of its spectral characteristics, from the eddy fields derived from the Geosat data. In this chapter we consider the model behavior when surface 'observations' are assimilated. These surface 'observations' are obtained as the superposition of the upper layer climatological field (Fig. 3.3a) and of the Geosat-derived eddy maps. Therefore they are not directly observed, but rather are obtained from observations of temperature and salinity and from measurements of sea surface height along the Geosat tracks. However, we consider them to be an adequate representation of the surface fields and in the context of the present study we will refer to them as the 'observations' or the 'data'. Because of the method and parameterizations chosen in the assimilation of the surface data the model upper layer is tightly constrained to follow the observations.

Two questions that we would like to answer in this chapter are: first, how is the global model behavior altered when its surface fields are 'forced' to follow the observations?; and second, what are the dynamical mechanisms responsible for the changes which occur in the model subsurface layers? In order to answer these questions we devote a large part of this chapter to the development of a dynamical framework for understanding the effect of the surface data constraint associated with the assimilation procedure. These dynamical ideas are illustrated with the aid of an analytical example. We then try to interpret the results of the assimilation experiments within this framework. The aspects of the model behavior which we concentrate upon in this chapter are the mean streamfunction and the mean potential vorticity fields. Since the surface 'observations' are composed, by construction, of a mean part and an eddy part, we are interested in investigating the relative influence of the two components on the assimilation results. To that end we present here two experiments: in the first one we assimilate the mean field only; in the second experiment we add the eddy component and assimilate the total surface fields. The differences between the results of the two experiments will help to identify the relative contribution of mean field and eddies in determining the characteristics of the time averaged flow in the subsurface layers.

The presentation is organized as follows: in section 5.2 we introduce some concepts of optimal data assimilation, that have been developed in the context of optimal estimation theory. These theoretical ideas represent the proper conceptual framework for any data assimilation scheme. Since their implementation presents several problems, of both practical and conceptual type, most of the assimilation techniques currently used are suboptimal approximations of the optimal theory. The nudging method, which is the method used here for assimilating the data, is one of these suboptimal methods. We describe the nudging technique in section 5.3. In section 5.4 we develop a dynamical framework which can be applied for

interpreting the results of the assimilation experiments; in section 5.5 we describe the assimilation of the mean field only, while in section 5.6 we present the experiment in which both mean field and eddies are assimilated. Finally, in section 5.7 we discuss the results obtained.

5.2 Optimal data assimilation theory

The theory of how to optimally combine data and models is well known (Gelb, 1974) and can be summarized in few simple concepts. Following the notation in Gill and Malanotte-Rizzoli (1991) we define $\boldsymbol{x}_f(t)$ to be the state vector corresponding to the model forecast at time t, $\boldsymbol{x}_t(t)$ the true state of the system and $\boldsymbol{x}_o(t)$ the observation vector. In a QG model, for example, $\boldsymbol{x}_f(t)$ will contain the streamfunction values in each layer and at each horizontal grid point. Such a set of values can completely identify the state of the system at any given time. The evolution of $\boldsymbol{x}_f$ that is obtained as the result of the numerical model integration can be written in the form:

$$\boldsymbol{x}_f(t) = \boldsymbol{A}[\boldsymbol{x}_f(t-1), \boldsymbol{Bq}(t)] \tag{5.2.1}$$

With $\boldsymbol{Bq}$ we indicate the external information, such as forcing and boundary conditions, that is required to completely specify the system evolution. The observation vector $\boldsymbol{x}_o(t)$ can be expressed in terms of the state vector corresponding to the true state of the system in the form:

$$\boldsymbol{x}_o(t) = \boldsymbol{H}[\boldsymbol{x}_t(t)] + \boldsymbol{n}(t) \tag{5.2.2}$$

where the matrix $\boldsymbol{H}$ represents the operator that maps the state vector space into the observation space. If, for example, the observations are measurements of sea surface height the operator $\boldsymbol{H}$ will select only the surface model grid points in the state vector and will convert the streamfunction values into sea surface height values. $\boldsymbol{n}(t)$ represents the observational noise.

The best way of combining the information derived from the dynamical model with the available observations is to determine the state vector $\boldsymbol{x}(t)$ that minimizes, in a global sense, the "distance" between model predictions and observations. This distance is defined according to a metrics that properly accounts for the model and data errors. The function to minimize is of the form:

$$J = \sum_{t=0}^{T} [\boldsymbol{x}_0(t) - \boldsymbol{H}(\boldsymbol{x}_f(t))]^T \boldsymbol{R}(t)^{-1} [\boldsymbol{x}_0(t) - \boldsymbol{H}(\boldsymbol{x}_f(t))] \tag{5.2.3}$$

and it is referred to in the literature as the cost function. $\boldsymbol{R}(t)$ can be the covariance of $\boldsymbol{n}(t)$ or any other useful weight matrix. The problem thus formulated is one of constrained optimization. There are several possible methods of solution. A variational approach leads to the so-called Pontryagin minimum principle or adjoint method. A sequential estimation approach, on the other hand, leads to methods known as the Kalman filter or smoother. In the first case (filter) only the past observations, including the time t of the analysis, are considered; in the case of the smoother, on the other hand, both past and future observations are used for the estimate at time t.

Here we summarize, for future reference with the nudging method, the Kalman filter formalism. Such a formalism has been originally developed for a linear model, even if ways of extending it to weakly nonlinear systems can be devised (Budgell, 1986). As before $\boldsymbol{x}_f$ indicates the state vector corresponding to the model forecast, $\boldsymbol{x}_t$ is true state of the system and $\boldsymbol{x}_o$ the observation vector. $\boldsymbol{A}$ is the operator associated with the linear model evolution. The Kalman filter proceeds in two steps. The first step is the model forecast:

$$\boldsymbol{x}_f(t) = \boldsymbol{A}(t)\boldsymbol{x}_a(t-1) \tag{5.2.4}$$

where $\boldsymbol{x}_a$ is the analysis vector. The second step consists in the optimal blending of the model forecast and the data:

$$\boldsymbol{x}_a(t) = \boldsymbol{x}_f(t) + \boldsymbol{K}(t)(\boldsymbol{x}_o(t) - \boldsymbol{H}(t)\boldsymbol{x}_f(t)) \tag{5.2.5}$$

The analysis vector $\boldsymbol{x}_a$ is thus the superposition of the model forecast and of a weighted difference between the observations and the mapping of the model forecast into the observation space. The matrix $\boldsymbol{H}$ is the same matrix defined before. $\boldsymbol{K}$ is known as the Kalman gain. Its expression is derived by requiring that the expected error $\boldsymbol{P}_a(t)$, associated with the estimate $\boldsymbol{x}_a(t)$, is minimum. This error is given by:

$$\boldsymbol{P}_a(t) = [\boldsymbol{I} - \boldsymbol{K}(t)\boldsymbol{H}(t)]\boldsymbol{P}_f(t) \tag{5.2.6}$$

$\boldsymbol{I}$ is the identity matrix and $\boldsymbol{P}_f$ is the forecast error:

$$\boldsymbol{P}_f(t) = \boldsymbol{A}(t-1)\boldsymbol{P}_a(t-1)\boldsymbol{A}^T(t-1) + \boldsymbol{Q}(t-1) \tag{5.2.7}$$

The forecast error is thus the sum of the foreward integration of the analysis error and of the model error covariance $\boldsymbol{Q}$, evaluated at the previous time step. The expression (5.2.6) tells us that the error associated with the estimate $\boldsymbol{x}_a$ is smaller than the model forecast error unless $\boldsymbol{H}$=0 (no data available). The expression for the Kalman gain is:

$$\boldsymbol{K}(t) = \boldsymbol{P}_f(t)\boldsymbol{H}^T(t)[\boldsymbol{H}(t)\boldsymbol{P}_f(t)\boldsymbol{H}^T(t) + \boldsymbol{R}(t)]^{-1} \tag{5.2.8}$$

or, in terms of $P_a(t)$:

$$\boldsymbol{K}(t) = \boldsymbol{P}_a(t)\boldsymbol{H}^T(t)\boldsymbol{R}^{-1}(t) \tag{5.2.9}$$

where $\boldsymbol{R}$ is the observation error covariance matrix. Equation (5.2.8) shows that $\boldsymbol{K}$=0 if either $\boldsymbol{P}_f = 0$ (perfect forecast) or $\boldsymbol{H} = 0$. Otherwise, from (5.2.9), $\boldsymbol{K}$ is inversely proportional to the accuracy of the observations. The Kalman filter approach can thus properly account for the error structure of both model and data. Also, the presence of the model error covariance matrix $\boldsymbol{Q}$ will allow the information contained in the data to affect all the correlated model variables.

In practice, however, the application of the Kalman filter presents several problems. First of all the need for a continuous updating of the model forecast

error, as in equation (5.2.7), introduces a very large computational load. The possibility of using a suboptimal, steady filter, has been investigated by Fukumori et al. (1992) with a linear, primitive equations model of the North Atlantic, in a coarse resolution version. Another problem in the implementation of the Kalman filter is the definition of the model error covariances, that are basically unknown. Therefore the actual implementation of this method requires "educated guesses" that may degrade its optimal character. For these reasons it is desirable to consider the feasibility of suboptimal methods that are easier to implement and have lower computational costs. For applications such as data assimilation in large scale, high resolution models, these methods may represent the only affordable ones, at least in the near future. In this study we thus investigate the performance of the nudging technique, which is one of the suboptimal versions of the Kalman filter, for the assimilation of altimeter data. The emphasis here is in trying to understand the dynamical implications of this method. An analysis of the type performed in this work is still lacking in the literature, but it is essential for developing a physical understanding of the model response to the assimilation procedure. The nudging method is described in the next section.

5.3 The nudging method

The nudging technique, originally introduced by Anthes (1974), is still applied in meteorology for operational prediction purposes (Krisnamurti et al., 1991). In oceanography it has been used in several studies of assimilation of surface data, both in QG and in primitive equation models (Verron and Holland, 1989; Holland and Malanotte-Rizzoli, 1989; Haines et al., 1991). A detailed review of the method is given in Ghil and Malanotte-Rizzoli (1991). Here we outline the basic characteristics of the nudging technique and describe our specific application.

'Nudging' consists in modifying the prognostic model equations by adding a Newtonian relaxation term toward the observations, in the form:

$$\frac{\partial \alpha_i}{\partial t} = \text{`}Physics\text{'} - R(x,y,t)(\alpha_i - \alpha_i^{obs}) \tag{5.3.1}$$

Here α_i indicates any of the prognostic model variables, and '*Physics*' includes all the physical terms, in the model, responsible for the time evolution of the quantity α_i. The relaxation coefficient R has the dimension of the inverse of a time, the relaxation time scale. We can see from (5.3.1) that, by making R sufficiently large, the relaxation term can become the dominant one in the evolution equation, leading to an exponential convergence of α_i toward α_{obs} with a time scale of R^{-1}. R is, in general, a function of space and time. In fact, when the observations are not available at each grid point and at each time step, R will be different from zero only in limited areas around the data points and for finite intervals around the times when observations arrive. Moreover, if the data have different accuracies their influence can be made dependent upon their reliability by weighting the relaxation coefficient with the data errors. So, in general, we can have the following expression for the relaxation coefficient:

$$R(x,y,t) = \frac{R_0}{\sigma(x,y,t)/\sigma_{min}} e^{-\frac{(x-x_0)^2}{\delta_x^2}} e^{-\frac{(y-y_0)^2}{\delta_y^2}} e^{-\frac{(t-t_0)^2}{\tau^2}} \tag{5.3.2}$$

Here (x_0, y_0) and t_0 are location and time of a given observation; δ_x, δ_y and τ are decorrelation scales in the x-direction, y-direction and time, respectively; $\sigma(x,y,t)$ represents the space-time distribution of the data errors and σ_{min} its minimum value. Equation (5.3.2) is the general expression for R used in Malanotte-Rizzoli and Young (1991). According to (5.3.2) the relaxation coefficient will decrease from its maximum value R_0 away from the locations where data are available and from the times when data arrive and when σ exceeds its minimum value σ_{min}. In the present study the 'observations' have been determined at each grid point and

at time intervals short enough to allow a continous assimilation. Although these data cannot be expected to be uniformily accurate, they supply a perception of the surface ocean circulation that appears to be much closer to reality than the one obtained from the free model run. In that regard we consider the data as "perfect" and neglect, at this stage, the inclusion of data errors in our assimilation experiments. Consequently we can choose R to be a constant.

The implementation of 'nudging' in the QG model we are using is straightforward. The upper layer model equation is altered by adding the relaxation term in the form:

$$\frac{\partial \nabla^2 \psi_1}{\partial t} = `Physics' - R(\nabla^2 \psi_1 - \nabla^2 \psi_{obs}) \tag{5.3.3}$$

The equations for the lower layers are left unchanged. Here $`Physics'$ includes the rate of change of vortex stretching, the advection of potential vorticity by the surface flow, the steady wind forcing and the biharmonic friction term. We have decided to implement nudging by relaxing the upper layer relative vorticity toward the relative vorticity of the 'observations'. A question can arise about this choice. In fact, since the prognostic variable in the QG equations is the potential vorticity, that should be the variable used in the nudging term. However, we only have available, from altimetry, measurements of sea surface height, which do not contain any information about the upper layer stretching term. Therefore we cannot determine, from the available observations, upper layer potential vorticity fields, $\bar{q}_{obs}$, to use in the nudging term. Results obtained in the context of twin experiments (Verron and Holland, 1989; Holland and Malanotte Rizzoli, 1989) have shown that the use of relative vorticity as the nudged variable can be very successful in driving the model streamfunction fields toward the reference fields. Similar positive results can be obtained when the streamfunction itself is used in the nudging term, with a proper rescaling of the coefficient R (Verron, 1992). This implies that either $\nabla^2 \psi$ or ψ, or

any combination of them can be appropriate choices for the nudging term. Similar conclusions emerge from analytical considerations using linear quasi-geostrophic equations. A theoretical rationalization of these results can be derived from the Kalman filter formalism. In fact, the choice of either ψ or $\nabla^2\psi$ as the "observations" to be used in the nudging term will simply correspond to different expressions for the matrix H in (5.2.5), while retaining the same information content. The main motivation for choosing the relative vorticity for our experiments is simply associated with the fact that this has been the "traditional" choice, already used in most of the previous assimilation studies with the nudging method.

The use of the relative vorticity as relaxation variable implies a double differentiation of ψ_{obs}. Since the data can be expected, in general, to be noisy, a double differentiation of ψ_{obs} does not seem to be desirable. However, this does not represent a real problem in practice. In fact, in the process of solution of the model equations, the relative vorticity fields, including $\nabla^2\psi_{obs}$ are inverted back, a smoothing operation, to obtain the updated streamfunction fields. The numerical round-off errors do not affect the reversibility of this operation in any noticeble way.

From the physical point of view nudging can be considered a way of correcting the upper layer vorticity, without affecting, directly, the potential vorticities in the lower layers. The choice of leaving the potential vorticity unchanged in the lower layers, while modifying the upper layer fields, implies a physical choice about the way the surface information is projected downward. This choice relies on the relative 'slow' and 'passive' nature of the potential vorticity evolution, as observed in several simulations with QG models. On this basis Haines (1991) has demonstrated, in the context of twin experiments, why nudging is more successful in predicting the subsurface flow with respect to methods in which the

upper layer streamfunction is directly updated (Berry and Marshall, 1989) with consequent modifications of the potential vorticity in the second layer.

The value chosen for the nudging coefficient is

$$R = (0.5\text{day})^{-1} \tag{5.3.4}$$

corresponding to a relaxation time scale of 1/2 day. This value is close to the upper limit dictated by numerical stability considerations and thus constitutes a "strong" nudging. The value of 1/2 day has proven effective in driving the surface streamfunction fields toward the 'observations' in previous studies (Holland, personal communications). It can be shown, in fact, that the time scale of 1/2 day is shorter than the time scales associated with the terms in '*Physics*'. In that regard it is instructive to perform a scale analysis of the upper layer model equation. Define

$$(x, y) = L(x', y') \tag{5.3.5a}$$

$$t = Tt' \tag{5.3.5b}$$

$$\psi = UL\psi' \tag{5.3.5c}$$

$$\tau = \tau_0\tau' \tag{5.3.5d}$$

where L is a typical horizontal length scale, T a typical time scale, U a velocity scale and τ_0 the magnitude of the wind stress. The primed variables are nondimensional. By introducing these expressions in (5.3.3), we can rewrite the equation, after dropping the primes, in the form:

$$\frac{1}{T}\frac{\partial}{\partial t}[\nabla^2\psi_1 + L^2F_{12}(\psi_2 - \psi_1)] =$$

$$-\frac{1}{T_R}\frac{\partial\psi_1}{\partial x} - \frac{1}{T_A}J(\psi_1, \nabla^2\psi_1 + L^2F_{12}(\psi_2 - \psi_1))$$

$$+\frac{1}{T_W}curl\tau + \frac{1}{T_D}\nabla^6\psi_1 - R(\nabla^2\psi_1 - \nabla^2\psi_{obs}) \tag{5.3.6}$$

where

$$T_R = (\beta L)^{-1} \tag{5.3.7a}$$

$$T_A = \frac{L}{U} \tag{5.3.7b}$$

$$T_W = (\frac{\tau_0/\rho_0}{H_1 U})^{-1} \tag{5.3.7c}$$

$$T_D = \frac{L^4}{A} \tag{5.3.7d}$$

Equation (5.3.6) tells us that advection of planetary vorticity occurs on time scales of the order of T_R; the larger the variation of the Coriolis parameter over the typical scale of motion, the shorter the corresponding time scale. T_A is the advective time scale, associated with the strength of the nonlinear term. T_W is the time scale associated with the input of vorticity from the wind, while T_D is the time scale of frictional dissipation by biharmonic friction.

Assuming $L \sim$ 100 km, $U \sim$ 20 cm/s, $\tau_0 \sim$ 1 dyne/cm^2, β ~2 x 10^{-11}m^{-1}s^{-1}, and with A =2 x 10^{10} m^4/s we obtain the following estimates for the time scales defined above:

$$T_R \sim 5.8\text{days}$$

$$T_A \sim 5.8\text{days}$$

$$T_W \sim 7\text{days}$$

$$T_D \sim 158\text{years}$$

The relaxation time scale chosen is about an order of magnitude shorter than the time scales associated with the terms in '*Physics*', so that the nudging term can be expected to be the dominant one in equation (5.3.3).

In terms of the Kalman filter formalism, introduced in the previous section, our implementation of nudging corresponds to a given choice of the Kalman gain matrix $\boldsymbol{K}$, observation matrix $\boldsymbol{H}$ and data error covariance $\boldsymbol{R}$. In particular the large

value of the nudging coefficient is equivalent to the assumption of perfect data, so that $\boldsymbol{R}$ can be considered zero in this case. From equation (5.2.8) we can see that these choices also define, implicitly, the characteristics of the model forecast error $\boldsymbol{P}_f$.

5.4 A dynamical framework

In this section we develop some theoretical considerations and establish a dynamical framework for interpreting the results of the assimilation experiments. The starting point are the QG equations for the evolution of potential vorticity. Since we are interested in separating the effect of the time averaged flow from the effect of the eddies in controlling the model dynamics we split the variables in the usual form:

$$\psi_k = \bar{\psi}_k + \psi'_k \tag{5.4.1a}$$

$$q_k = \bar{q}_k + q'_k \tag{5.4.1b}$$

Subscripts indicate the layer. As usual, the temporal mean is supposed to be computed over a time interval much longer than the eddy time scales. The time averaged equation for the generic layer k is:

$$\frac{\partial \bar{q}_k}{\partial t} + J(\bar{\psi}_k, \bar{q}_k) = T_k \delta_{1k} + \bar{F}_k - \overline{J(\psi'_k, q'_k)} \tag{5.4.2}$$

This equation describes the slow variation of the mean potential vorticity in the presence of mean advection, external forcing, dissipation by biharmonic friction and eddy advection of eddy potential vorticity. In the subsurface layers, where no external forcing is present and biharmonic friction is negligible at the relevant scales of motion, the evolution of $\bar{q}_k$ is determined by the relative strength of mean flow advection and eddy flux divergence:

$$\frac{\partial \bar{q}_k}{\partial t} + J(\bar{\psi}_k, \bar{q}_k) \simeq -\overline{J(\psi'_k, q'_k)} \tag{5.4.3}$$

If the eddies are vanishingly weak, and the mean flow $\bar{\psi}_k$ is different from zero the evolution of $\bar{q}_k$ is determined by mean flow advection. If a steady state can be reached equation (5.4.3) says that mean potential vorticity contours and mean streamlines will coincide. This is a state in which a functional relationship exists between the time averaged streamfunction and the time averaged potential vorticity:

$$\bar{\psi}_k = \mathcal{F}(\bar{q}_k) \tag{5.4.4}$$

How does the presence of a finite eddy flux divergence change this scenario?

Rhines and Young (1982) parameterize the eddy term as a weak Laplacian diffusion. In their theory mean flow advection of $\bar{q}$ is the leading order process, so that, at first approximation, (5.4.4) holds. Eddy diffusion then comes into play by determining a slow erosion of the $\bar{q}_k$-gradients and producing homogenization of $\bar{q}_k$ inside closed contours.

The results of the numerical simulation described in the previous chapter support the hypothesis that mean flow advection represents the leading order process in determining the large scale structure of the flow in the subsurface layers. In fact the comparison between mean streamfunction fields and mean potential vorticity fields in Fig. 4.4b and 4.4c clearly shows the effect of the mean flow advection in shaping the distribution of potential vorticity in layers 2 and 3. The potential vorticity contours tend to follow the streamlines. In these layers we have also noticed the presence of large areas of reduced gradients, in partial agreement with the theory of Rhines and Young. However, the evolution of the eddy field in the control run appears as a very turbulent and chaotic process and the erosion of the $\bar{q}_k$-contours is more effective where the eddy field is more energetic. Therefore, in the context of the control run, 'homogenization' of potential vorticity seems more properly described in terms of turbulent mixing than in terms of a weak diffusion.

Let us consider, now, how these dynamical considerations can be applied to the experiments in which surface data are assimilated. Because of the short time scale used in the nudging term the upper layer fields can be expected to become very similar to the observations when nudging is imposed on the model. Therefore we will assume, in this analysis, that ψ_1 is a given function:

$$\psi_1 = \psi_{obs} \tag{5.4.5}$$

where, by construction, the observations are composed of a time averaged component plus an eddy component:

$$\psi_{obs} = \bar{\psi}_{obs} + \psi'_{obs} \tag{5.4.6}$$

The set of time averaged equations for the five model layers become:

$$\bar{\psi}_1 = \bar{\psi}_{obs} \tag{5.4.7a}$$

$$\frac{\partial \bar{q}_2}{\partial t} + J(\bar{\psi}_2, \bar{q}_2) = \bar{F}_2 - \overline{J(\psi'_2, q'_2)} \tag{5.4.7b}$$

$$\frac{\partial \bar{q}_3}{\partial t} + J(\bar{\psi}_3, \bar{q}_3) = \bar{F}_3 - \overline{J(\psi'_3, q'_3)} \tag{5.4.7c}$$

$$\frac{\partial \bar{q}_4}{\partial t} + J(\bar{\psi}_4, \bar{q}_4) = \bar{F}_4 - \overline{J(\psi'_4, q'_4)} \tag{5.4.7d}$$

$$\frac{\partial \bar{q}_5}{\partial t} + J(\bar{\psi}_5, \bar{q}_5) = \bar{F}_5 - \overline{J(\psi'_5, q'_5)} \tag{5.4.7e}$$

where

$$\bar{q}_k = \nabla^2 \bar{\psi}_k + \beta y + F_{k,k-1}(\bar{\psi}_{k-1} - \bar{\psi}_k) + F_{k,k+1}(\bar{\psi}_{k+1} - \bar{\psi}_k) \tag{5.4.8a}$$

$$q'_k = \nabla^2 \psi'_k + \beta y + F_{k,k-1}(\psi'_{k-1} - \psi'_k) + F_{k,k+1}(\psi'_{k+1} - \psi'_k) \tag{5.4.8b}$$

and

$$\psi'_1 = \psi'_{obs} \tag{5.4.9}$$

Therefore $\bar{\psi}_{obs}$ enters in the expression for $\bar{q}_2$ and ψ'_{obs} enters in the expression for q'_2. The problem reduces to a 4-layer problem. We start by assuming that, at

first order, the eddy flux divergence can be neglected. This is certainly a very good approximation when considering the experiment in which only the mean field is assimilated. In that experiment, in fact, we relax the surface field toward a steady field, so that the model variability is heavily damped. In the experiment in which the Geosat-derived maps are assimilated together with the mean field the eddy intensity is no longer negligible. However, on the basis of the results of the control run, it seems sensible to assume that the divergence of the eddy flux represents a second order effect also in that case. As before, biharmonic friction can be considered negligible at the relevant scales of motion. Therefore, at steady state, we can rewrite the system (5.4.7) in the form:

$$\bar{\psi}_1 = \bar{\psi}_{obs} \tag{5.4.10a}$$

$$J(\bar{\psi}_2, \bar{q}_2) \sim 0 \tag{5.4.10b}$$

$$J(\bar{\psi}_3, \bar{q}_3) \sim 0 \tag{5.4.10c}$$

$$J(\bar{\psi}_4, \bar{q}_4) \sim 0 \tag{5.4.10d}$$

$$J(\bar{\psi}_5, \bar{q}_5) \sim 0 \tag{5.4.10e}$$

The set of equations (5.4.10) defines a generalization of the Fofonoff problem (Fofonoff, 1954) to a baroclinic, 4-layer 'ocean', with a prescribed surface topography and inflow/outflow conditions at the boundaries.

Marshall and Nurser (1986) showed how to construct analytical solutions to the baroclinic generalization of a Fofonoff problem in an idealized rectangular ocean bounded by solid walls. In the context of our experiments the particular solution of equations (5.4.10) that satisfies the given lateral and surface boundary conditions cannot be determined analytically, due to the irregular model geometry and to the specification of a "surface topography" and boundary conditions which are not analytically defined. Therefore it is instructive to consider a simple analytical

example in order to illustrate how an inertial solution to a problem of the type (5.4.10) can be achieved. First, however, we rewrite the system (5.4.10) in a simplified form. In Chapter 4 we have seen, from the results of the control run, that relative vorticity is negligible with respect to planetary vorticity and stretching in most of the model domain. The contribution of relative vorticity is very small also in the potential vorticity fields associated with the initial conditions derived from climatological data (Chapter 3). More generally relative vorticity can be expected to be negligible with respect to the planetary term when the fluid velocity U is much smaller than the phase speed of long barotropic waves

$$U \ll \beta L^2 \tag{5.4.11}$$

When the scale of motion L is much larger than the Rossby deformation radii $F_{ij}^{-1/2}$

$$L^2 \gg F_{ij}^{-1} \tag{5.4.12}$$

relative vorticity is negligible also with respect to vortex stretching. In our case U ~10 cm/s, L ~300 km, $F_{ij}^{-1/2} \sim$ 30 km, so that both (5.4.11) and (5.4.12) are satisfied. If the relative vorticity is neglected, equations (5.4.10) for the four lower layers become:

$$J(\bar{\psi}_2, \beta y + F_{21}\bar{\psi}_{obs} + F_{23}\bar{\psi}_3) \sim 0 \tag{5.4.13a}$$

$$J(\bar{\psi}_3, \beta y + F_{32}\bar{\psi}_2 + F_{34}\bar{\psi}_4) \sim 0 \tag{5.4.13b}$$

$$J(\bar{\psi}_4, \beta y + F_{43}\bar{\psi}_3 + F_{45}\bar{\psi}_5) \sim 0 \tag{5.4.13c}$$

$$J(\bar{\psi}_5, \beta y + F_{54}\bar{\psi}_4) \sim 0 \tag{5.4.13d}$$

In equation (5.4.13a) we have made the substitution $\bar{\psi}_1 = \bar{\psi}_{obs}$. We have also simplified the expressions of the stretching terms by considering only the components of the interface heights which can be advected by the flow in each layer.

5.4.1 An analytical example

Consider a 2-layer model in a rectangular domain, as shown in Fig. 5.1. The model has flat bottom, specified boundary conditions and prescribed surface flow. Since, in this case, we do not have any layer 3, equation (5.4.13a) becomes:

$$J(\bar{\psi}_2, \beta y + F_{21}\bar{\psi}_{obs}) \sim 0 \tag{5.4.1.1}$$

The quantity we define

$$\hat{q}_2 = \beta y + F_{21}\bar{\psi}_{obs} \tag{5.4.1.2}$$

is a known function. Therefore the problem (5.4.1.1) is a linear problem, in which the $\hat{q}_2$-contours define the streamlines. A general solution of (5.4.1.1) will be of the form

$$\bar{\psi}_2 = A_2(\hat{q}_2) \tag{5.4.1.3}$$

We consider here the case in which $\bar{\psi}_{obs}$ is given by the anticyclonic flow shown in Fig. 5.1a, and described by the expression

$$\bar{\psi}_{obs} = \begin{cases} \frac{\psi_0}{R^2}(R^2 - x^2 - y^2), & r < R \\ 0 & r \geq R \end{cases} \tag{5.4.1.4}$$

The surface velocity field is confined inside the disk $r \leq R$, with intensity increasing from zero at the centre to the maximum value $2\frac{\psi_0}{R}$ at the periphery of the disk. The presence of this surface flow distorts the interface between layer 1 and layer 2, producing a circular depression in the interface. The problem thus formulated is similar to the example studied by Rhines and Young (1982) in the context of the wind-driven circulation. In that case the barotropic streamfunction was known, since it could be computed from the prescribed wind stress curl distribution.

From (5.4.1.2) and (5.4.1.4) the function $\hat{q}_2$ is given by:

$$\hat{q}_2 = \begin{cases} \frac{F_{21}\psi_0}{R^2}(R^2 + y_{02}^2 - x^2 - (y - y_{02})^2) & r < R \\ \beta y & r \geq R \end{cases} \tag{5.4.1.5}$$

where the quantity y_{02} is given by:

$$y_{02} = \frac{1}{2}\frac{\beta R^2}{F_{21}\psi_0} \tag{5.4.1.6}$$

The $\hat{q}_2$-contours are straight lines outside the disk of radius R and arcs of circle inside the disk. As in the problem discussed by Rhines and Young closed contours can be found if $y_{02} < R$. This condition is satisfied if

$$\mid U_{max} \mid > \frac{\beta}{F_{21}} \tag{5.4.1.7}$$

where $\mid U_{max} \mid = 2\psi_0/R$ is the maximum surface velocity. Therefore, in order to have closed contours, the surface velocity must exceed the phase speed of the long baroclinic Rossby waves supported by the present model, c_{ph}, where $\mid c_{ph} \mid = \frac{\beta}{F_{21}}$. In fact, in the system we are considering, where only one layer can evolve freely, these waves are the only agent which can propagate the information about the boundary values into the interior. However, if the flow is sufficiently strong to oppose the Rossby wave propagation, areas isolated from the boundaries can be created. The condition (5.4.1.7) also coincides with the requirement that the basic state potential vorticity gradient changes sign in the lower layer (in the case U represented a zonal flow) and can thus be interpreted as a necessary condition for instability.

Contours of $\hat{q}_2$ are shown in Fig. 5.1b for the case $y_{02} = \frac{1}{2}R$ which occurs when $\psi_0 = \frac{\beta R}{F_{21}}$. The value of $\bar{\psi}_2$ on the open contours is determined by the boundary values. Therefore, if no inflow or outflow is prescribed at the boundaries, motion is possible only inside the closed contours as discussed by Rhines and Young. Inside closed contours the flow is undefined at this order. This is a case of 'steady state resonance' in which any flow is, in principle, possible. A weak forcing can produce an arbitrary large response which can be limited only by friction. The selection of a particular solution in these areas will be obtained, therefore, as a balance between forcing and dissipation. In the absence of any external forcing, as in our case, the

only source of energy for the motion within the closed contours is given by the eddy flux divergence term. As shown by Holland and Rhines (1980) the component of this flux which is more effective in driving the deep gyres is the flux of interface height, corresponding to vertical propagation of horizontal momentum. Therefore, following Rhines and Young (1982), we parameterize this flux as a down-gradient flux of interface height displacement

$$\overline{J(\psi_2', q_2')} \sim -\nabla \cdot (\kappa \nabla F_{21}(\bar{\psi}_1 - \bar{\psi}_2)) \tag{5.4.1.8}$$

where κ is the diffusion coefficient, in general a function of position. In order to simplify the analysis and obtain an explicit solution we consider κ to be a constant. Since the second layer is the bottom layer the main source of dissipation is given by bottom friction:

$$D_2 = -\epsilon \nabla^2 \bar{\psi}_2 \tag{5.4.1.9}$$

The steady state equation for layer 2 becomes:

$$J(\bar{\psi}_2, \bar{q}_2) = -\kappa \nabla^2 (F_{21}(\bar{\psi}_2 - \bar{\psi}_1)) - \epsilon \nabla^2 \bar{\psi}_2 \tag{5.4.1.10}$$

As in the study of Rhines and Young a solution inside the closed contours can be determined by considering integral constraints over the area within a closed streamline. By integrating (5.4.1.10) over such an area we have:

$$(\kappa F_{21} + \epsilon) \oint \nabla \bar{\psi}_2 \cdot \hat{n} dl = \kappa F_{21} \oint \nabla \bar{\psi}_{obs} \cdot \hat{n} dl \tag{5.4.1.11}$$

The line intagrals are computed along the bounding streamline. Using the fact that $\bar{\psi}_2 = A_2(\hat{q}_2)$, so that

$$\nabla \bar{\psi}_2 = A_2' \nabla \hat{q}_2 \tag{5.4.1.12}$$

and noticing that

$$\oint \beta \hat{y} \cdot \hat{n} dl = 0$$

where $\hat{y}$ is the unit vector in the y-direction, we obtain

$$A_2' = \frac{\kappa}{\kappa F_{21} + \epsilon} \tag{5.4.1.13}$$

Thus $\bar{\psi}_2$ is a linear function of $\hat{q}_2$ inside closed contours. We should notice here that the intensity of the flow in layer 2 depends on the forcing and dissipation parameters κ and ϵ, and it is an increasing function of κ only if ϵ is different from zero. If no explicit dissipation were present A_2' would attain its maximum value, which only depends upon the model density structure:

$$A_2' = \frac{1}{F_{21}} \tag{5.4.1.14}$$

The same result would hold also with a spatially varying diffusion coefficient κ.

In fact, if the only non-conservative process is the downgradient flux of potential vorticity by the eddies the only possible end state will be the one with uniform potential vorticity inside closed contours.

The boundary conditions that we prescribe in the second layer are a uniform eastward flow both at the western and eastern boundaries:

$$\bar{\psi}_2 = -U_2 y \qquad \text{at} \quad x = -L, L$$

The general solution for $\bar{\psi}_2$ over the whole domain can be written in the form:

$$\bar{\psi}_2 = A_2 \hat{q}_2 + C_2 \tag{5.4.1.15}$$

where:

$$A_2 = \begin{cases} -\frac{U_2}{\beta} & \text{open contours } (\hat{q}_2 < \beta R) \\ \frac{\kappa}{\kappa F_{21} + \epsilon} & \text{closed contours } (\hat{q}_2 > \beta R) \end{cases} \tag{5.4.1.16}$$

and C_2 is a constant chosen so that $\bar{\psi}_2$ is continous at the edge of the closed contours:

$$C_2 = \begin{cases} 0 & (\hat{q}_2 < \beta R) \\ -R\beta(\frac{U_2}{\beta} + \frac{\kappa}{\kappa F_{21} + \epsilon}) & (\hat{q}_2 > \beta R) \end{cases} \tag{5.4.1.17}$$

In this particular case the streamfunction in layer 2 is a linear function of the potential vorticity also in the area of open contours, due to the particular choice of boundary conditions. This simple example illustrates how different flow regimes, with different relationships between streamfunction and potential vorticity, can be achieved.

The potential vorticity $\bar{q}_2$ is given by:

$$\bar{q}_2 = \hat{q}_2 - F_{21}\bar{\psi}_2$$

$$= \hat{q}_2(1 - A_2F_{21}) - F_{21}C_2 \qquad (5.4.1.18)$$

In general $\bar{q}_2$ is a linear function of $\hat{q}_2$, the linear relationship being determined by the value of A_2. Inside the closed contours, if bottom friction is absent ($\epsilon = 0$), (5.4.1.18) predicts $\bar{q}_2$ to be a constant given by:

$$\bar{q}_2 = \beta R(1 + U_2\frac{F_{21}}{\beta}) \qquad (5.4.1.19)$$

The expression (5.4.1.19) tells us that the constant value of $\bar{q}_2$ coincides with the value of potential vorticity at the northern rim of the gyre, as determined by the planetary term βR and by the sloping of the interface associated with the uniform eastward flow U_2, which is prescribed by the boundary values. The extent to which the constant $\bar{q}_2$ value depends upon the velocity along the open contours is measured by the ratio between the velocity U_2 and the phase speed of long Rossby waves, c_{ph}, where $\mid c_{ph} \mid = \frac{\beta}{F_{21}}$. If the flow outside the closed contours becomes vanishingly small the constant value of $\bar{q}_2$ tends to coincide with the value of the planetary vorticity at the northern rim of the gyre, $\bar{q}_2 = \beta R$.

From (5.4.1.2) we can see that the extent to which $\bar{\psi}_{obs}$ constrains the pattern of the flow in the lower layer is strongly dependent on the density structure of our 2-layer system, as expressed by $F_{21} = \frac{f_0^2}{g'_{12}H_2}$. If F_{21} is very small, either because the second layer is very deep or because the density difference between

the two layers is very large, the $\hat{q}_2$-contours cannot diverge noticeably from the βy-contours.

In order to make this analysis more complete we consider, now, a 3-layer case. From (5.4.13) the governing equations for layers 2 and 3 at the leading order are:

$$J(\bar{\psi}_2, \beta y + F_{21}\bar{\psi}_{obs} + F_{23}\bar{\psi}_3) \sim 0 \qquad (5.4.1.20a)$$

$$J(\bar{\psi}_3, \beta y + F_{32}\bar{\psi}_2) \sim 0 \qquad (5.4.1.20b)$$

In the second layer the streamline distribution is now determined not only by the prescribed surface topography, but also by the topography of the lower interface, which is a function of the flow in layer 3. However, the intensity of the flow can be expected to decrease with depth, so that, at first order, the displacement of the lower interface in layer 2 can be considered much smaller than the displacement of the upper interface. In these conditions the solution in the second layer can be obtained as before, and it is given by (5.4.1.15). Since we are mainly interested, here, in understanding how the surface mean field can affect the structure of the subsurface flows, we simplify the analysis by considering the case in which the boundaries are closed in all layers, so that no inflow or outflow is prescribed. In this case A_2 and C_2 are given by:

$$A_2 = \begin{cases} 0 & \text{open contours } (\hat{q}_2 < \beta R) \\ \frac{1}{F_{21}+F_{23}} & \text{closed contours } (\hat{q}_2 > \beta R) \end{cases} \qquad (5.4.1.21a)$$

and

$$C_2 = -\beta R A_2 \qquad (5.4.1.21b)$$

The value of A_2 inside closed contours is obtained by assuming that the eddy flux of interface height is the only non-conservative term. Now, in fact, the second layer is no longer the bottom layer, so that bottom friction is no longer present. The corresponding potential vorticity distribution is constant inside the closed contours

and coincides with the value of the planetary component at the northern rim of the gyre, $\bar{q}_2 = \beta R$. We should recall, however, that in the model used for the assimilation experiments we have biharmonic friction as a dissipative term.

Consider, now, the flow that can be expected in layer 3. From (5.4.1.20b) we have

$$\bar{\psi}_3 = A_3(\hat{q}_3) \tag{5.4.1.22}$$

where

$$\begin{aligned} \hat{q}_3 &= \beta y + F_{32}A_2\hat{q}_2 + F_{32}C_2 \\ &= \tilde{\beta} y + \tilde{F}\bar{\psi}_{obs} - F_{32}\beta R A_2 \end{aligned} \tag{5.4.1.23}$$

where

$$\tilde{\beta} = (1 + F_{32}A_2)\beta \tag{5.4.1.24}$$

and

$$\tilde{F} = A_2 F_{32} F_{21} \tag{5.4.1.25}$$

A_2 is given in (5.4.1.21a) and it is a function of position. The $\hat{q}_3$-contours, as well as the $\bar{\psi}_3$-contours can thus be related to the surface topography $\bar{\psi}_{obs}$. The influence of the surface flow in shaping the mean circulation in layer 3 is measured by $\tilde{F} = A_2 F_{32} F_{21}$. Outside the closed $\hat{q}_2$-contours A_2 is zero, so that no surface information can be felt in layer 3. Inside the closed $\hat{q}_2$-contours $\tilde{F}$ is given by:

$$\tilde{F} = \frac{F_{32}F_{21}}{F_{21} + F_{23}} \tag{5.4.1.26}$$

If $H_2 = H_3 = \tilde{H}$ we have that $F_{23} = F_{32} = \frac{f_0^2}{g'_{23}\tilde{H}}$. Therefore (5.4.1.26) can be rewritten in the form:

$$\frac{1}{\tilde{F}} = \frac{1}{F_{21}} + \frac{1}{F_{23}} \tag{5.4.1.27}$$

so that the magnitude of $\tilde{F}$ is smaller then either F_{21} or F_{23} and it is given by:

$$\tilde{F} = \frac{f_0^2}{\tilde{H}\tilde{g}} \tag{5.4.1.28}$$

where $\tilde{g} = g'_{12} + g'_{23}$ is the reduced gravity associated with the total density difference between layer 3 and layer 1. If, more generally, H_3 is different from H_2, $\tilde{F}$ can be written:

$$\tilde{F} = \frac{f_0^2}{g'_{23} H_3} \frac{1}{1 + \frac{\rho_2 - \rho_1}{\rho_3 - \rho_2}} \tag{5.4.1.29}$$

We can distinguish two limiting cases:

a) $(\rho_3 - \rho_2) \gg (\rho_2 - \rho_1)$. In this case $\tilde{F} \sim F_{32}$, so that the penetration of the surface information is only determined by the 'rigidity' of layer 3. If layer 3 is very deep and/or its density is much larger than the density of the layer above the influence of $\bar{\psi}_{obs}$ in determining the distribution of the $\hat{q}_3$-contours can be expected to be negligible with respect to the planetary term.

b) $(\rho_3 - \rho_2) \ll (\rho_2 - \rho_1)$. In this case $\tilde{F} \sim \frac{f_0^2}{g'_{21} H_3}$. The influence of the surface information still depends upon the thickness of layer 3, but now it depends upon the largest density difference, which is the one between layer 1 and layer 2.

From this simple analysis we see that the penetration of the mean surface information is tightly linked to the stratification characteristics of the area under consideration.

We now solve for the flow in layer 3. The explicit expression of $\hat{q}_3$ can be written:

$$\hat{q}_3 = \begin{cases} \frac{\tilde{F}\psi_0}{R^2}(R^2 + y_{03}^2 - x^2 - (y - y_{03})^2) - \beta R \frac{F_{32}}{F_{21} + F_{23}} & \hat{q}_3 > \beta R \\ \beta y & \hat{q}_3 \leq \beta R \end{cases} \tag{5.4.1.28}$$

where

$$\begin{aligned} y_{03} &= \frac{1}{2} \frac{\tilde{\beta} R^2}{\tilde{F}\psi_0} \\ &= (1 + \frac{1}{F_{32} A_2}) y_{02} \end{aligned} \tag{5.4.1.29}$$

Outside the area of closed $\hat{q}_2$-contours, where A_2 is zero, the $\hat{q}_3$-contours are latitude circles. In the area of closed $\hat{q}_2$-contours A_2 is positive. Therefore $y_{03} > y_{02}$. As

in the case considered by Rhines and Young (1982) the area of closed geostrophic contours becomes smaller and displaced northward with depth. Some contours are shown in Fig. 5.1c. As before, the flow along the open contours is prescribed by the boundary conditions. If the boundaries are closed, as in the case we consider here no flow is possible along these contours. Inside the closed contours the amplitude of the flow can be determined, as before, by considering forcing and dissipation processes. We assume, here, that layer 3 is the last moving layer over a motionless abyss, and the only non-conservative term is the eddy flux of interface height. Using the same integral constraint applied in the 2-layer case we find:

$$\bar{\psi}_3 = A_3(\hat{q}_3 - \beta R) \tag{5.4.1.30}$$

where

$$A_3 = \frac{1}{F_{32} + F_{34}} \tag{5.4.1.31}$$

The constant term in (5.4.1.30) assures continuity of the solution at the border of the closed $\hat{q}_3$-contours.

The potential vorticity in layer 3 is:

$$\begin{aligned} \bar{q}_3 &= \hat{q}_3 - (F_{32} + F_{34})\bar{\psi}_3 \\ &= \beta R \end{aligned} \tag{5.4.1.32}$$

The potential vorticity is a constant equal to the value at the northern rim of the gyre. Therefore, when no flow outside the closed contours is present, the constant value of potential vorticity inside the closed contours is independent of depth and equal to βR.

Before concluding this section we consider a continuously stratified case in order to develop a better intuition for the shape of the "bowl" in which the surface information can be felt. With continuous stratification the quasi-geostrophic

potential vorticity can be written in the form:

$$q = \psi_{xx} + \psi_{yy} + \left(\frac{f_0^2}{N^2}\psi_z\right)_z + \beta y \qquad (5.4.1.33)$$

where $N = N(z)$ is the Brunt-Väisälä frequency. In the previous examples we have seen that in the absence of inflow/outflow at the lateral boundaries motion is possible only inside closed geostrophic contours. The existence of such contours depends upon the strength of the surface flow as well as on the stratification characteristics. Let us define $D(x,y)$ the depth bounding the "bowl" of closed contours and let us assume that the potential vorticity is constant within this bowl. So we have:

$$\left(\frac{f_0^2}{N^2}\psi_z\right)_z + \beta y = \beta R \qquad (5.4.1.34)$$

Again, we have neglected the relative vorticity. The constant value of the potential vorticity inside the bowl has been chosen equal to the value of the βy-term at the northern rim of the gyre, in analogy with the results of the previous examples. The boundary conditions are:

$$\psi, \psi_z = 0 \qquad \text{at} \quad z = -D \qquad (5.4.1.35)$$

$$\psi = \psi_{obs} \qquad \text{at} \quad z = 0 \qquad (5.4.1.36)$$

The condition (5.4.1.35) assures continuity of the streamfunction and vanishing vertical velocity at the boundary of the bowl. Condition (5.4.1.36) prescribes the surface mean flow.

Consider, for simplicity, the case with N constant, corresponding to a density field increasing linearly with depth. In this case (5.4.1.34) can be easily integrated from $D(x,y)$, where the boundary conditions (5.4.1.35) are applied. The result is:

$$\psi(x,y,z) = \frac{N^2}{2f_0^2}\beta(R-y)(z+D)^2 \qquad (5.4.1.37)$$

which expresses the streamfunction in terms of the unknown function $D(x,y)$. By applying the condition (5.4.1.36) we can determine $D(x,y)$ in terms of the prescribed surface field ψ_{obs}:

$$D(x,y) = \left[\frac{2f_0^2}{\beta N^2}\frac{\psi_{obs}}{(R-y)}\right]^{1/2} \tag{5.4.1.38}$$

If we consider ψ_{obs} given by (5.4.1.4), the line along which $D(x,y)$ achieves its maximum values is at $x = 0$:

$$D(0,y) = \frac{f_0}{N}\left[\frac{\mid U_{max} \mid}{\beta}\left(1+\frac{y}{R}\right)\right]^{1/2} \tag{5.4.1.39}$$

The penetration depth thus increases with the intensity of the surface velocity $\mid U_{max} \mid$ and decreases with increasing stratification. Let us now try to see the effect of relaxing the assumption that the constant value of potential vorticity is independent of depth. We have seen before that, if an inflow is specified at the open boundaries, the flow in the area connected with the boundaries can affect the uniform value of the potential vorticity inside the closed contours, in a way that is controlled by the specification of the boundary conditions. We assume, therefore, a "small" depth-dependent perturbation to the constant value, that we write in the form:

$$\beta R(1+\epsilon z) \tag{5.4.1.40}$$

where ϵ is a small parameter. If we go through the same procedure outlined before and expand $D(x,y)$ in powers of ϵ we have:

$$D(x,y) = D_0(x,y) + \epsilon D_1(x,y) + ... \tag{5.4.1.41}$$

we obtain

$$D(x,y) = D_0 + \frac{1}{6}\epsilon\frac{D_0^2}{(R-y)} \tag{5.4.1.42}$$

where D_0 is the value obtained for ϵ equal to zero, given by (5.4.1.38). If the value of potential vorticity increases with depth ($\epsilon > 0$) the depth reached by the surface

information also increases. The opposite occurs when the value of potential vorticity is a decreasing function of depth.

From this analytical example we can make the following points:

a) Due to nonlinear effects the prescription of a surface flow $\bar{\psi}_{obs}$ can constrain the flow structure in the subsurface layers. The extent to which the surface information can penetrate at depth is very strongly affected by the vertical density profile.

b) In the 2-layer case the structure of the flow in the second layer is completely determined by the structure of the surface flow. However, the intensity of the flow is dictated by the boundary values on the open contours and by the characteristics of forcing and dissipation processes inside the closed contours.

c) In a model with more than two layers the exact structure of the flow will depend in a more complex fashion on the surface constraint, as well as on boundary conditions, forcing and dissipation processes in each layers. However, the gross features of this structure are still determined by the prescribed surface flow.

d) If closed contours are present, in a given layer, as a consequence of the prescription of the surface field, different flow regimes can be found: the functional relationship between streamfunction and potential vorticity is dictated by the boundary values in the area of the open contours and by the characteristics of forcing and dissipation inside closed contours.

e) If the eddy flux of interface height is the only non-conservative mechanism present, the intensity of the flow inside closed contours will not depend on the intensity of the eddy field, but only upon the model density structure.

The corresponding potential vorticity fields are constant. However, if some explicit dissipation is present in each layer, as in the assimilation experiments which we are going to discuss, the amplitude of the solution will depend on the relative strength of forcing and dissipation.

f) If no-flow conditions are specified at the boundaries motion is possible only inside closed contours, as in Rhines and Young (1982) theory. The driving agent for this flow is the eddy flux divergence term.

We now go back to the specific problem under consideration. By applying the insights gained from this analytical study we try to infer, approximately, the structure of the flow which can be expected in layers 2 and 3 when the climatological field $\bar{\psi}_{obs}$ is imposed at the surface.

5.4.2 Streamfunction patterns in layers 2 and 3 during the assimilation experiments

In the experiment in which only the mean field $\bar{\psi}_{obs}$ is imposed at the surface the eddies are very weak. As the mean flow in layers 4 and 5 can only be eddy-driven, the two bottom layers are practically motionless in this experiment. In the following sections we will compare the mean streamfunction fields from the assimilation experiment in which only $\bar{\psi}_{obs}$ is assimilated with the results of the experiment in which also the surface eddy field ψ'_{obs} is imposed. Due to the absence of any relevant flow in layers 4 and 5 during the first experiment, only the mean streamfunction distributions in layers 2 and 3 can be meaningfully compared. Thus we concentrate our attention, here, on these two layers. In the following the climatological fields for layers 2 and 3, corresponding to Fig. 3.3b and Fig. 3.3c, will be referred to as $\bar{\psi}_{2obs}$ and $\bar{\psi}_{3obs}$, respectively. At the initial time the ratio between the variances of

$\bar{\psi}_{3obs}$ and $\bar{\psi}_{obs}$ is

$$\frac{\sqrt{\sum_{i,j} \bar{\psi}^2_{3obsi,j}}}{\sqrt{\sum_{i,j} \bar{\psi}^2_{obsi,j}}} \sim 13\% \qquad (5.4.2.1)$$

Therefore, at this time, the function

$$\hat{q}_2 = \beta y + F_{21}\bar{\psi}_{obs} \qquad (5.4.2.2)$$

defines, to a good approximation, the $\bar{\psi}_2$ distribution. Contours of $\hat{q}_2$ are shown in Fig. 5.2a. As in the analytical example discussed in the previous section some of the $\hat{q}_2$-contours in Fig. 5.2a are closed and do not reach the boundaries, while some others are connected with the boundaries. In the 'subpolar' area, where $\bar{\psi}_{obs}$=0, the $\hat{q}_2$-contours coincide with the βy-contours and are given by zonal lines. In this area these contours suggest a westward flow emanating from the eastward flowing jet. In fact, as the surface topography is flat in this area, fluid particles must move along latitude circles in order to conserve their potential vorticity. A no-flow condition must be satisfied at the coastline, so that some higher order physics is required, there, to close the circulation. Therefore we might anticipate the formation of a boundary jet along the coastline where relative vorticity will no longer be negligible. Away from the subpolar region, the circulation which is suggested in layer 2 by the $\hat{q}_2$-contours does not show evident discrepancies with $\bar{\psi}_{2obs}$ (Fig. 3.3b). Therefore we use $\bar{\psi}_{2obs}$ in (5.4.13b) in order to obtain an approximation for the structure of the flow field in layer 3. At the initial time layer 4 is at rest. In the experiment in which only $\bar{\psi}_{obs}$ is assimilated the two bottom layers can be considered motionless. Therefore the lower interface does not enter into play in determining the circulation pattern in layer 3. The latter can thus be described, within the approximations made, by the function $\hat{q}_3$ given by:

$$\hat{q}_3 = \beta y + F_{32}\bar{\psi}_{2obs} \qquad (5.4.2.3)$$

The contours of $\hat{q}_3$ are shown in Fig. 5.2b. Also in this case the absence of a subpolar flow in $\bar{\psi}_{2obs}$ leads to zonal contours of $\hat{q}_3$, which imply a westward flow in

this area of layer 3. Again, some higher order physics must enter into play close to the solid boundary in order to satisfy the no-flow condition.

If we compare the flow pattern in layer 3, as given by the $\hat{q}_3$-contours, with the flow pattern in layer 2 we can notice how the recirculation gyre in layer 3 appears tighter and more elongated in the NE-SW direction with respect to the recirculation in layer 2. The contours south of about 30°N join both the eastern and western boundaries in Fig. 5.2b. At these latitudes the streamfunction values specified at the western boundary are constant and they have only minor variations along the eastern boundary. Therefore only a weak flow can be expected south of 30°N. This variation with depth of the shape of the recirculation area represents the model analogue of the results of the analytical example, where the area of closed geostrophic contours becomes smaller and displaced northward with depth.

The flow pattern expected in layer 3 shows differences with respect to the field $\bar{\psi}_{3obs}$ used as initial condition in this layer. We recall that $\bar{\psi}_{3obs}$ has not been determined by a direct dynamic height computation, but it has been inferred from the assumption that the flow in layer 3 has the same structure as the flow in layer 2. Therefore our initial assumption about the structure of the flow in layer 3 was not consistent with the model dynamics and vertical discretization. We thus need to discuss the possible consequences of this assumption on the results of the assimilation experiments. We will see that the initial conditions in layers 2 and 3 do not affect the final streamfunction distributions in these two layers, since the model fields evolve rapidly from these initial conditions toward the states compatible with the model physics and geometry. Since the field $\bar{\psi}_{3obs}$ has been used as the barotropic component in the three upper layers (see chapter 3) the only implications for the results of the assimilation experiments are associated with the error in the barotropic component of the surface field, which is continously assimilated. However, as seen

before, the variance of $\bar{\psi}_{3obs}$ is only 13% of the variance of $\bar{\psi}_{obs}$, so that the error in the estimate of the barotropic component of the surface field cannot be expected to affect significantly the basic conclusions of this study.

5.4.3 Potential vorticity evolution

Rhines and Young (1982) have shown that, when a problem like the one described by equations (5.4.10) can be linearized, as in our analytical example (equation (5.4.1.1)) a simple equation can be derived for the evolution of the potential vorticity field. For simplicity let us consider a 2-layer model first. In this case the time averaged streamfunction in the deep layer can be expressed in the form:

$$\bar{\psi}_2 = \frac{\hat{q}_2 - \bar{q}_2}{F_{21}} \tag{5.4.3.1}$$

with $\hat{q}_2$ given in (5.4.1.2). Substituting this expression for $\bar{\psi}_2$ in a time averaged equation of the form of (5.4.7b) we obtain an evolution equation for $\bar{q}_2$ in the form:

$$\frac{\partial \bar{q}_2}{\partial t} + J(\Theta, \bar{q}_2) = \text{`}Dissipation\text{'} \tag{5.4.3.2}$$

where

$$\Theta = \frac{\hat{q}_2}{F_{21}} \tag{5.4.3.3}$$

defines a known advective field. In the expression for $\bar{\psi}_2$ only the component depending on $\hat{q}_2$ can actually advect $\bar{q}_2$. The evolution of potential vorticity defined by (5.4.3.3) is therefore the evolution typical of a passive tracer.

If we apply similar considerations to the initial evolution of the model fields during the assimilation experiments, as described in the previous section, we can obtain the following expressions for the streamfunction fields advecting the potential vorticity in layers 2 and 3:

$$\Theta_2 = \frac{\hat{q}_2}{F_{21} + F_{23}} \tag{5.4.3.4a}$$

$$\Theta_3 = \frac{\hat{q}_3}{F_{32} + F_{34}} \qquad (5.4.3.4b)$$

Here $\hat{q}_2$ and $\hat{q}_3$ are given by (5.4.2.2) and (5.4.2.3), respectively. The corresponding velocity fields $\boldsymbol{V}_k$, computed according to

$$\boldsymbol{V}_k = \boldsymbol{k} \times \nabla\Theta_k \qquad k = 2, 3 \qquad (5.4.3.5)$$

are shown in Fig. 5.3a and Fig. 5.3b, for layer 2 and 3, respectively. In Fig. 5.3a the longest vector corresponds to a velocity of about 40 cm/s, while in layer 3 the maximum velocity is about 18 cm/s. In both layers the most energetic advection occurs in the area of the jet. In layer 2 the velocities in the stream are much larger than everywhere else in the domain. In layer 3, on the contrary, the strength of the advection by the jet becomes more comparable with the advection occurring in the recirculation area. Several recirculation gyres can be noticed, especially in layer 3. In this layer $\boldsymbol{V}_3$ is predominantly zonal and directed westward in the area south of about 30°N. Also, as anticipated, a weak westward velocity is present, in both layers, in the area of the subpolar flow.

5.4.4 Influence of the eddy field on the mean flow

Consider, again, equations (5.4.7). The discrepancy between $\bar{q}$-contours and $\bar{\psi}$-contours determines a non-vanishing advection of mean potential vorticity by the mean flow. At steady state, in the subsurface layers, this advection must be balanced by the eddy advection of eddy potential vorticity. Therefore the discrepancy between $\bar{q}$-contours and $\bar{\psi}$-contours gives a measure of the strength of the eddy flux divergence term. It also expresses the deviation of the model behavior from a free-mode behavior.

A way of formally diagnosing this deviation is through the use of scatter diagrams. These diagrams have been used largely for testing the existence of a

functional relationship between streamfunction and potential vorticity in different applications (Bretherton and Haidvogel (1976), McWilliams and Zabusky (1982), McWilliams (1983), Illari and Marshall (1983)). In this study we will compute scatter diagrams following the approach suggested by Reid et al. (1986). Consider the straight line AB in Fig. 5.4a. This line joins two points along a closed streamline. At point M $\bar{\psi}$ reaches its maximum value. A hypothetical scatter diagram is sketched in Fig. 5.4b. The points A′, M′ and B′ in this diagram correspond to the points A, M and B in physical space. The net flux of $\bar{q}$ across the segment AB, due to the geostrophic flow $\bar{\psi}$ is:

$$F_q = \int_A^B \frac{\partial \bar{\psi}}{\partial x} \bar{q} dx \qquad (5.4.4.1)$$

where F_q is assumed positive when directed northward across the line AB. We can rewrite (5.4.4.1) in the form:

$$F_q = \int_{A'}^{M'} \bar{q} d\bar{\psi} - \int_{B'}^{M'} \bar{q} d\bar{\psi} \qquad (5.4.4.2)$$

where now the integrals are considered in $(\bar{\psi}, \bar{q})$ space. The difference between the two integrals in (5.4.4.2) is the area enclosed in A′M′B′. Therefore F_q, which is a measure of the deviation from a free-mode behavior, can be related to the dispersion of the points in the scatter diagram. In order for the scatter diagram to supply an estimate of F_q which is independent of the characteristics of the line in physical space, a suitable normalization is required. Suppose, for example, that $\bar{\psi}$ and $\bar{q}$ have a simple sinusoidal behavior, with a phase shift ϕ:

$$\bar{\psi} = \psi_0 \sin kx \qquad (5.4.4.2a)$$

$$\bar{q} = q_0 \sin(kx + \phi) \qquad (5.4.4.2b)$$

In this case the flux F_q can be computed and it is proportional to $\sin\phi$. The representation of the two sinusoidal functions $\bar{\psi}$ and $\bar{q}$ in $(\bar{\psi}, \bar{q})$ space is an ellipse,

like a simple Lissajous' figure. When the amplitudes of the two functions are equal the major axis of the ellipse is inclined at 45°. The ratio of the minor to major axis is proportional to $\tan\phi$. Therefore, for small ϕ, it supplies an estimate of the flux F_q. The width-to-length ratio of the loop in $(\bar{\psi}, \bar{q})$ space thus appears to be a sensible measure of the departure from the free-mode behavior. The $\bar{\psi}$ and $\bar{q}$ values need to be scaled with their total variations $\Delta\bar{\psi}$ and $\Delta\bar{q}$ so that the major axis of the loop is inclined at about 45°. We will apply these criteria in the computation of the scatter diagrams from the results of the assimilation experiments.

5.5 Assimilation of the mean field

The assimilation experiment has been started using the fields in Fig. 3.3 as initial conditions for layers 1, 2 and 3, while layers 4 and 5 were initially at rest. These are the same initial conditions used for the control run, and the same initial conditions which will be used in the assimilation experiment in which the surface eddy fields will be assimilated together with the mean field. The nudging term has been added to the equation for the first layer (see equation 5.3.3) in the form:

$$-R(\nabla^2\psi_1 - \nabla^2\bar{\psi}_{obs}) \tag{5.5.1}$$

where $\bar{\psi}_{obs}$ is the climatological field in Fig. 3.3a. The relaxation coefficient is $R = (0.5\text{day})^{-1}$. At each time step ψ_1 is relaxed toward the steady field $\bar{\psi}_{obs}$ with a very short relaxation time scale. Therefore any time dependent motion that the model might try to develop will be strongly damped. From the considerations developed in the previous section eddies can be expected to be the forcing agent for the flow inside the closed geostrophic contours in the subsurface layers. In particular they are the only source of vorticity for the motion in layers 4 and 5, where no inflows or outflows are specified at the boundaries. Therefore, if the eddy

field has vanishing intensity only a very weak time averaged flow can be expected in the two deepest layers.

The numerical simulation has been carried out for twenty years, in order to allow all the transient processes to decay. We have monitored the time evolution of the total kinetic energy in each of the five layers in order to ensure that statistical steady state (in this case almost coincident with an absolute steady state) has been reached. The 'climatology' of this numerical experiment has been computed by averaging the model fields over the last four years of the simulation, as for the control run. The basic characteristics of this 'climatology' are described and discussed in the following sections.

5.5.1 The streamfunction fields

Fig. 5.5 shows the time averaged circulation in all the five model layers. In the first layer the flow field is essentially the same as $\bar{\psi}_{obs}$. As anticipated, the nudging term represents the dominant contribution for the evolution of the relative vorticity in equation (5.3.1), so that the upper layer streamfunction becomes almost identical to $\bar{\psi}_{obs}$. A closer comparison between the two surface fields shows that the major differences occur in the area of the jet separation from the coast, northeast of Cape Hatteras, and in the area of the Grand Banks, where one of the branches of the stream turns northward. At both locations the streamlines in the $\bar{\psi}_1$ field tend to 'open' toward the coast. This deviation of $\bar{\psi}_1$, with respect to $\bar{\psi}_{obs}$, is produced by the circulation which develops in the 'subpolar' area of the subsurface layers, as we will see in a moment. The maximum differences between $\bar{\psi}_1$ and $\bar{\psi}_{obs}$ in both places are of the order of 15%.

Consider, now, the circulation in the second layer. If the dynamical framework developed in section 5.4 captures the essential physics of this model simulation, the flow pattern obtained in layer 2 should be well described by the distribution of the $\hat{q}_2$-contours in Fig. 5.2a. Comparison between Fig. 5.5b and Fig. 5.2a shows, indeed, striking similarities. The structure of the subtropical recirculation gyre obtained in this numerical simulation is rendered in great detail by the $\hat{q}_2$-contours. The three anticyclonic cells which can be observed in Fig. 5.2a around 70°W, 58°W and 42°W do appear as features of the time averaged circulation in layer 2. The same is true for the cyclonic cell which is predicted by the $\hat{q}_2$-contours inside the curve of the stream around the Grand Banks. Also, as anticipated, a westward flow can be observed in the subpolar area. As the stream emerges from Cape Hatteras and flows eastward as a free jet, fluid particles detach from the stream and move westward. As expected, a thin jet forms along the coastline in order to close the circulation. This coastal jet, whose intensity tends to increase with latitude, develops instabilities. As it tries to follow the irregular and sinuous coastline, meanders develop and ring-like structures are shed, which remain trapped between the jet and the boundary. The presence of this coastal jet, not predicted by the simplified derivation of $\bar{q}_2$, has the effect of somehow distorting the whole flow field, so that a precise agreement between $\bar{\psi}_2$ and $\hat{q}_2$ cannot be found. The presence of the flow in layer 3, which has not been considered in the derivation of $\hat{q}_2$, is an additional reason for discrepancies. However, the basic characteristics of the flow in the second layer are predicted by the structure of $\hat{q}_2$, supporting the hypothesis of the inertial nature of the circulation.

Similar considerations can be applied to layer 3 (Fig. 5.5c). In this case the streamline distribution should be compared with the distribution of the $\hat{q}_3$-contours in Fig. 5.2b. Also in this case the shape of the subtropical recirculation gyre, the presence of smaller scale anticyclonic cells, the development of a westward

flow in the subpolar area as well as the consequent formation of the coastal jet are features predicted by the $\hat{q}_3$-contours. The most energetic component of the circulation is found north of 30°N, a latitude which defines the southern border of the recirculation at this depth. In this layer most of the recirculation is bounded by closed streamlines which do not reach the boundaries. Therefore in layer 3 eddy driving can be expected to be relatively more important than in layer 2 in determining the strength of the circulation.

In Fig. 5.5d and Fig. 5.5e we show, for completeness, the time averaged streamfunction fields in layers 4 and 5, respectively. In both layers, as expected, the flow is vanishingly small almost everywhere. The only noticeable component of the circulation is found in the proximity of the northern boundary, where eddies produced by instabilities of the boundary jet have relatively larger amplitudes. Maps of eddy kinetic energy show, in fact, values lower than a few cm^2/s^2 in most of the domain. However, values as high as 100 cm^2/s^2 are observed in some limited areas close to the northern boundary, and are clearly associated with instabilities of the jet. This appears to be the only area where eddies can drive any flow in the two deepest layers.

5.5.2 The potential vorticity fields

The time averaged potential vorticity fields are shown in Fig. 5.6. In layer 1 the potential vorticity distribution has remained very similar to the initial distribution (Fig. 3.5). The major differences occur in the 'subpolar area', where the stretching effect produced by the flow in the second layer determines a distortion of the βy-contours present in the initial field.

In layers 2 and 3 the potential vorticity distributions clearly show the advective control of $\bar{q}$. In both layers the $\bar{q}$-contours reproduce, in fact, the shape of the recirculation gyre, with large areas of reduced gradients inside the closed contours. In this experiment, where the intensity of the eddy field is extremely weak, we establish the conditions hypothesized in the theory of Rhines and Young (1982). As predicted by that theory, advection of potential vorticity by the mean flow is able to establish, first, uniform values of q along streamlines. At this point the eddy flux term enters into play and smooths the gradients between adjacent streamlines. Plateaus of 'homogenized' q are thus created inside the closed contours, while the $\bar{q}$-gradients are expelled toward the rim of the gyres.

How effective is the advective control of the $\bar{q}$ distribution in this numerical experiment? Or, in other words, how close is the model behavior to a 'free mode' behavior? In Fig. 5.7 we compare the mean streamfunction field in layer 2 (Fig. 5.7a) with the potential vorticity field in the same layer (Fig.5.7b). The agreement between the two sets of contours is almost perfect. In order to make this statement more quantitative, and for future comparison with the case in which ψ'_{obs} is also assimilated, we show, in Fig. 5.7c, a scatter diagram of $\bar{q}_2$ versus $\bar{\psi}_2$. The points used for this diagram are the ones along the segment AB in Fig. 5.7a and Fig. 5.7b. At points A and B $\bar{\psi}_2$ has the same value. The streamfunction and potential vorticity values used for the scatter diagram have been normalized with their total variations $\Delta\bar{\psi}_2$ and $\Delta\bar{q}_2$, as described in section 5.4.4. Moving eastward from point A along the line in physical space the streamfunction values first increase, while the potential vorticity decreases. A maximum value of $\bar{\psi}_2$ is reached at point M, which corresponds to a minimum in $\bar{q}_2$. The segment AM maps on the line A'M' in $(\bar{\psi}_2, \bar{q}_2)$ space, with points widely separated because of the large $\bar{\psi}_2$-gradients. After point M the streamfunction values decrease again, while the potential vorticity values increase. In $(\bar{\psi}_2, \bar{q}_2)$ space this corresponds to the branch M'B', which has

points more densily spaced, because of the slower variation of the fields. Apart from the first few points which, in physical space, are within the jet, the two branches of the scatter diagram are practically coincident. Therefore the area enclosed by them is practically indistinguishable from zero, and so is the flux $J(\bar{\psi}_2, \bar{q}_2)$ across the segment AB. The scatter diagram in Fig. 5.7c describes a linear relationship between $\bar{q}_2$ and $\bar{\psi}_2$, in agreement with the hypothesis that led Fofonoff to find the solutions that bear his name (Fofonoff, 1954). However, in the present case, we have $\frac{\partial \bar{q}_2}{\partial \bar{\psi}_2} < 0$. In a barotropic ocean, like the one considered by Fofonoff, $\frac{\partial q}{\partial \psi}$ must be positive, so that inertial boundary layers can be supported. However, as demonstrated by Marshall and Nurser (1986), this constraint can be released in a baroclinic ocean, where dynamical effects associated with vortex stretching are also present.

Fig. 5.8 shows the same analysis for layer 3. In this figure the $\bar{\psi}_3$-contours (Fig. 5.8a) are compared with the $\bar{q}_3$-contours (Fig. 5.8b) Also in this case the agreement between the two sets of contours is very good. The segment CD in Fig. 5.8a represents the sequence of points, joining streamlines with the same value of $\bar{\psi}_3$, used to compute the scatter diagram in Fig. 5.8c. Point C is within the boundary current, so that the first few points in the scatter diagram show the relatively large variations of $\bar{\psi}_3$ and $\bar{q}_3$ in the area of the jet. After these points we enter the large potential vorticity plateau, where $\bar{q}_3$ is practically constant all the way to point D. The only contribution to a flux $J(\bar{\psi}_3, \bar{q}_3)$ across the segment CD comes, therefore, from the area of the boundary current.

5.6 Assimilation of mean + eddies

In this experiment the upper layer streamfunction ψ_1 is relaxed toward the total 'observed' streamfunction ψ_{obs}, where

$$\psi_{obs}(t) = \bar{\psi}_{obs} + \psi'_{obs}(t) \tag{5.6.1}$$

As before, $\bar{\psi}_{obs}$ is the climatological field in Fig. 3.3a and $\psi'_{obs}(t)$ is the sequence of eddy maps constructed from the Geosat data. As described in Chapter 2 the total duration of the ψ'_{obs} data set is 570 days. Also this experiment has been started from the fields in Fig. 3.3 as initial conditions for layers 1, 2 and 3 and with no flow in layers 4 and 5.

Since we are now imposing a time dependent constraint at the surface, we need to define sensible criteria for assessing when the model has adjusted to the observations. The evolution of the total kinetic energy during the first 570 days of the experiment shows that, in each of the five layers, the energy increases from the initial value to a 'steady' level during the first 10-20 days of the simulation. After this short transient the level of total kinetic energy remains practically constant in each layer. The potential vorticity distributions, on the other hand, show a continuous evolution. Starting from the initial conditions in Fig. 3.5, potential vorticity is redistributed by advection processes. These processes now include not only mean flow advection, as in the previous experiment, but also eddy advection. While the mean flow tries to establish constant values of potential vorticity along streamlines, the turbulent eddy field acts as an efficient mixing agent which tends to smooth out the q gradients. The evolution of the potential vorticity fields is the result of the competition between these two processes and a statistical steady state will be reached when mean flow advection balances the eddy mixing effect. In Fig. 5.9a and Fig. 5.9b we show instanteneous potential vorticity maps in layers 2 and

3, respectively. Notice the convoluted distribution of the q contours, which is due to eddy advection and is a manifestation of the enstrophy cascade.

Eddy mixing can be expected to depend only on the statistical characteristics of the eddy field and not on the details of its instantaneous realizations. In order to allow these processes to evolve until statistical equilibrium is reached we have extended this experiment beyond the 570 days duration of our data set by assimilating the same data in a sequence of runs each of which is started from the final fields of the previous one. The total experiment consists of 20 of these assimilation segments, totaling 11400 days or about 31.6 years of spinup time. The convergence of the potential vorticity fields toward an equilibrium distribution is illustrated in Fig. 5.10, where we show meridional profiles of mean potential vorticity in the four subsurface layers. The different curves in each diagram refer to the averages over each of the 570 days assimilation segments, 'A' corresponding to the first segment, 'B' to the second and so on. These profiles have been computed as averages over 10° of longitude centered at 55°W. In layers 2 and 3 we can see the convergence of these different profiles to a meridional distribution showing, in its central part, a large plateau where the potential vorticity has been homogenized, due to the very effective eddy mixing. We can also notice how the value of q tends to decrease, from segment to segment, at the northern end of these meridional profiles, due to advection of low potential vorticity anomalies by the mean flow.

After the 31.6 years of spinup time variations can still be observed, from segment to segment, in the mean streamfunction fields. The rms differences between the streamfunctions corresponding to the last two segments are only a few percent in the upper three layers, but they can be as large as 40% in layers 4 and 5, where they are mainly associated with slight changes in the position of the gyres present in the deep mean fields. Since the mean flow in these two layers is purely eddy driven,

the difficulty in achieving a complete steady state after the 31.6 years of spinup time can be a consequence of the relatively short duration of the Geosat time series with respect to the typical eddy time scales. Therefore the time averaged fields in layers 4 and 5 will define the basic characteristics of the mean flow in these layers for the available eddy statistics.

The 'climatology' of this model has been computed by considering a time average over the last segment. In the following we describe the characteristics of the mean streamfunction and mean potential vorticity fields. In particular we discuss the differences with the results of the previous experiment in order to identify the contribution of the surface eddies in determining the time averaged model circulation.

5.6.1 Mean streamfunction fields

The 'climatological' streamfunction fields for this experiment are shown in Fig. 5.11. We can immediately notice the striking similarity of the flow patterns in the three upper layers with the results of the previous experiment (Fig. 5.5). The surface layer is strongly constrained by the nudging procedure, so that $\bar{\psi}_1$ cannot deviate much from $\bar{\psi}_{obs}$. However, also the circulation in layers 2 and 3, although not directly constrained, has basically the same structure as in the experiment where only $\bar{\psi}_{obs}$ was assimilated. In both layers the shape of the recirculation gyres, with all their smaller scale features, has remained essentially unchanged. Some differences can be observed in the 'subpolar' area. In Fig. 5.11b and Fig.5.11c we can still notice the tendency, for fluid particles, to leave the jet and move westward, but now no well defined boundary jet develops along the coastline. The presence of the eddy field is now able to supply a potential vorticity input which allows the

mean flow to move northward also in the interior of the 'subpolar' area, without the need of invoking the higher order physics of a boundary layer.

Due to the presence of an energetic eddy field motion is now possible also in layers 4 and 5. The most energetic component of the flow is found in the western half of the domain, and represents the deep expression of the inertial recirculation for this numerical experiment. The streamfunction fields in these two layers are rich in small scale features. As observed before, this could be a consequence of the short duration of the Geosat time series. Notice, in particular, the tendency for the formation of elongated zonal gyres. The presence of these gyres could be an artifact of the neglect of bottom topography (Holland, personal communication). In fact, in the absence of any topographic steering, 'free' flow tends to develop along βy-contours. We will see in the next chapter that evidence of zonal jets has indeed been found in observations of the deep flow in this area.

Although the structure of the circulation in layers 2 and 3 has not been noticeably affected by the assimilation of the eddy field, the intensity of the flow has indeed been altered. This is evident especially in layer 3. In this layer, in fact, the extent of the area inside closed geostrophic contours, where eddy forcing can be more effective, is larger than in layer 2. In order to illustrate the differences in the flow strength, differences which are induced when surface eddies are assimilated, we show in Fig. 5.12 meridional profiles of mean zonal velocity along 55°W in all the five model layers. The profiles have been averaged over 10° of longitude. In each figure the solid line represents the zonal velocity obtained in the experiment in which only $\bar{\psi}_{obs}$ is assimilated, while the dashed line corresponds to the case in which the total ψ_{obs} is imposed at the surface. In all the layers the presence of the surface eddy field enhances the amplitude of the zonal velocity. In layers 4 and 5, in particular, the flow is practically zero in the absence of eddies. Notice, in Fig.

5.12a and Fig. 5.12b, the strong correlation between the solid and dashed velocity profiles. The position of the eastward jet and of the westward return flow has not been altered by the assimilation of the eddy field. Only the intensity of the zonal velocity has been increased.

5.6.2 Mean potential vorticity fields

The time averaged potential vorticity fields for the five layers are shown in Fig. 5.13. The upper layer distribution is, again, practically unchanged with respect to the initial distribution, as it was in the previous experiment. In layers 4 and 5, which are now in motion, larger deviations from the zonal contours of the planetary vorticity gradients can be observed. The second and third layers are not directly constrained by the nudging procedure and, in both experiments, they carry relatively significant components of the flow. Therefore the differences introduced in their potential vorticity distributions by the presence of the surface eddy field are of particular interest. The maps in Fig. 5.13b and Fig. 5.13c no longer show any closed contours reproducing the exact shape of the recirculation gyres, as in Fig. 5.6b and Fig. 5.6c. Only tongues of low potential vorticity anomalies can be noticed on the southern flanks of the recirculation gyres. As before, the mean flow tries to create uniform distributions of potential vorticity along streamlines, but now the energetic eddy mixing prevents the completion of this process. In Fig. 5.14 and Fig. 5.15 we compare the $\bar{\psi}$-contours with the $\bar{q}$-contours in layers 2 and 3, respectively. Although the potential vorticity distributions show clearly the effect of mean flow advection, the almost exact correspondence observed in Fig. 5.7 and 5.8 is now lost. This is clearly illustrated in the scatter diagrams in Fig. 5.14c and Fig. 5.15c. The points used for these diagrams are the ones along the straight lines shown in Fig. 5.14a and 5.15a, respectively. These lines join points with the same values of

$\bar{\psi}$, which have been chosen to be the same as the ones used in the computation of the scatter diagrams in Fig. 5.7c and 5.8c. The area enclosed by the loops in Fig. 5.14c and 5.15c is now much larger than what was found in the absence of an eddy field. The width-to-length ratio is now about 0.6, while before it was practically zero. So in this experiment the presence of a finite eddy flux divergence allows the $\bar{\psi}$-contours to deviate from the $\bar{q}$-contours, the eddy flux of eddy potential vorticity balancing the flux of $\bar{q}$ by the time averaged flow $\bar{\psi}$.

Before concluding this section we want to discuss in more detail the characteristics of the potential vorticity evolution, as illustrated in Fig. 5.10b and Fig. 5.10c. To that end we show, in Fig. 5.16 and Fig. 5.17, the evolution of the different potential vorticity components along 55°W in layer 2 and 3, respectively. The profiles in Fig. 5.16a correspond to time averages over the first 570 days of the experiment in layer 2. The thin solid curve refers to the planetary vorticity, the dashed curve to the vortex stretching term, the dotted curve to the relative vorticity and the thick solid curve is the total potential vorticity. The thick solid curve in this diagram corresponds to curve 'A' in Fig. 5.10b. In Fig. 5.16b we show equivalent profiles averaged over the last 570 days of the experiment. In this case the thick solid curve, the meridional profile of total potential vorticity, corresponds to curve 'T' in Fig. 5.10b. While the relative vorticity remains practically unchanged and very small during the course of the whole experiment, vortex stretching shows the largest variations. In particular, in the central part of these profiles, its negative slope becomes, at the end of the experiment, comparable to the positive gradient of the planetary vorticity term. The two components can therefore balance, leading to a plateauing in the total potential vorticity profiles. Similar considerations can be applied to layer 3, whose profiles of potential vorticity components, for the first and the last segments of this assimilation experiment, are shown in Fig. 5.17a and 5.17b, respectively. The turbulent eddy mixing thus results in a time averaged increase of

interface height displacements which is, in turn, associated with an increased shear between the flow in adjacent layers. In this experiment, as in the case analyzed by Holland and Rhines (1980), eddy form drag represents, therefore, the dominant mechanism through which eddies drive the mean flow.

5.7 Conclusions

In this section we have tried to understand the modifications induced in the model fields by the assimilation of surface data whose climatological characteristics are different from the climatology of the unconstrained model. In particular we have analyzed the relative effect, on the model behavior, of the two components of the surface observations, the mean component and the eddy component. If the relaxation time in the nudging term is much shorter than the typical model time scales, the surface fields become practically coincident with the observations, and can be considered as given. In these conditions we have shown that the structure of the subsurface circulation is mainly determined by the characteristics of the surface mean field. This structure is the result of the model nonlinearities and can be interpreted in the framework of 'baroclinic Fofonoff modes', in a domain with a prescribed surface topography (the surface mean field which is assimilated at the surface) and inflow-outflow conditions specified at the open boundaries. We have shown, with the aid of an analytical example, how such a solution can be achieved. The geometry of the geostrophic contours in each layer can be related to the pattern of the climatological field which is imposed at the surface. Some of these contours join the boundaries, while others are closed and isolated from the boundaries. On the first type of contours the intensity of the flow is determined by the boundary values. Inside the closed contours, on the other hand, the amplitude of the flow can

be expected to be the result of a balance between forcing and dissipation. Therefore different flow regimes can be present.

The results of the assimilation experiments confirm this dynamical framework. The structure of the flow remains basically the same, whether or not the eddy field is assimilated at the surface thus confirming that the surface mean field ψ_{obs} defines, indeed, the pattern of the mean streamlines in the subsurface layers. Consequently, this defines also the paths along which mean flow advection of potential vorticity will take place. However, the evolution of the potential vorticity fields appears to depend also upon the intensity of the eddy field. The characteristics of the mean potential vorticity distributions at statistical steady state are determined, in fact, by the relative strength of mean flow advection and eddy advection. If the eddies are very weak, as in our first experiment, mean flow advection dominates during the adjustment phase. First, uniform values of potential vorticity are established along mean streamlines. The weak eddy mixing comes then into play by "slowly" eroding the gradients between adjacent streamlines and expelling them toward the rim of the gyre. If, on the other hand, eddy advection is comparable, in strength, with mean flow advection, potential vorticity will be stirred and mixed by the eddies before the establishment of uniform values along mean streamlines is completely achieved. Therefore, only tongues of anomalous potential vorticity values can be observed in the final time average distributions, as a result of mean flow advection. In both experiments the end effect of eddy mixing is to partially smooth the potential vorticity gradients. This is essentially achieved through eddy flux of eddy interface height, which results in the modification of the mean interface displacements. The variation of the stretching term, thus modified by the eddies, can partially cancel the planetary vorticity gradients, leading to large areas of constant potential vorticity.

The most remarkable difference introduced by the presence of an energetic eddy field is the more efficient downward transfer of momentum. The intensity of the mean flow in the subsurface layers is, in fact, enhanced when eddies are assimilated. This is particularly evident in layers 4 and 5 where the mean flow can only be eddy driven. In fact, hardly any noticeable flow is found, in these layers, in the absence of an energetic eddy field.

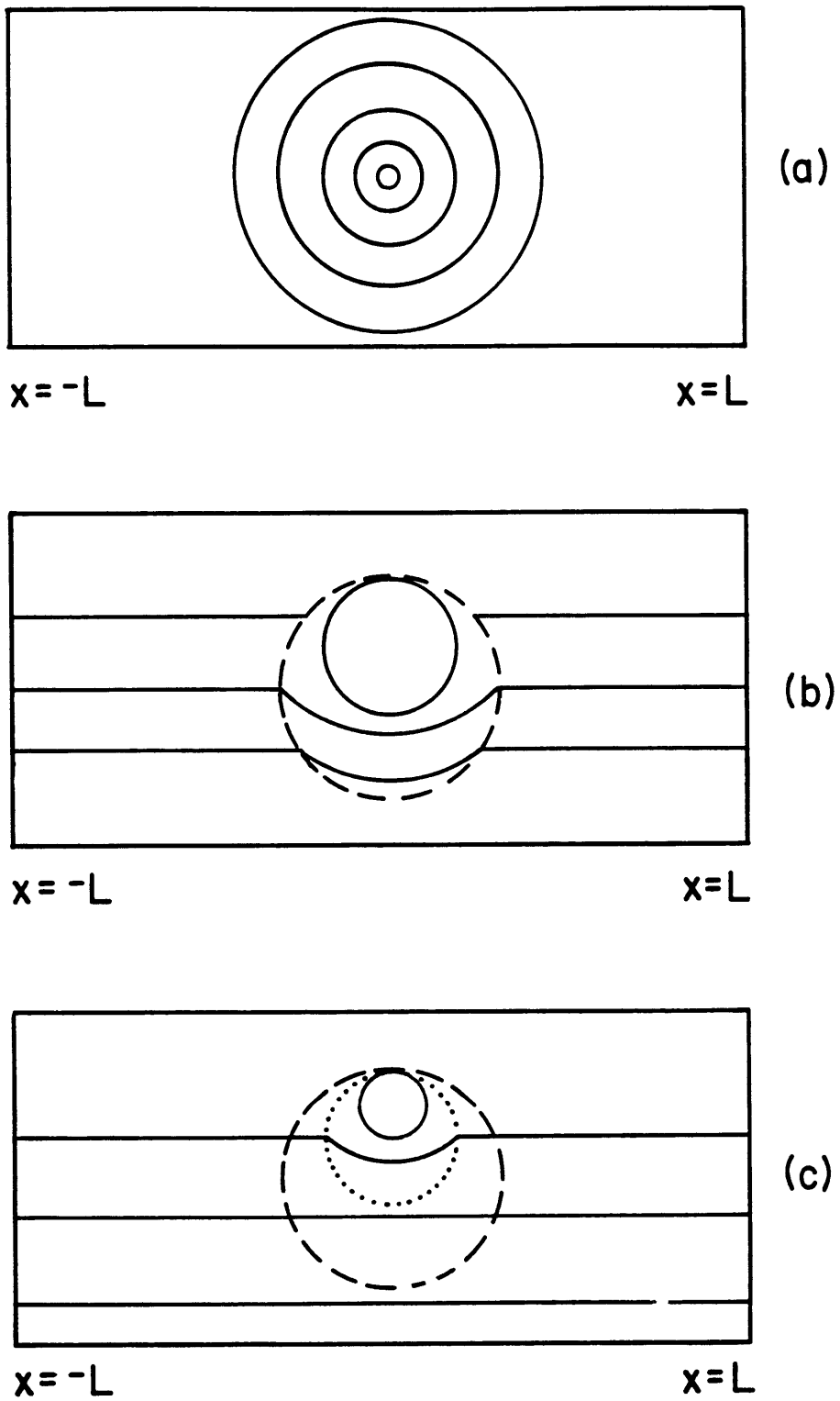

Fig. 5.1 (a) Surface streamfunction $\bar{\psi}_{obs}$ for the analytical example. $\bar{\psi}_{obs}$ describes an anticyclonic flow inside the disk of radius R. (b) Geometry of the geostrophic contours in the second layer. The dashed line indicates the disk inside which the surface flow is confined. (c) Geometry of the geostrophic contours in layer 3. All the lateral boundaries are assumed to be closed. The dashed line encloses the disk of radius R; the dotted line defines the area of closed geostrophic contours in layer 2.

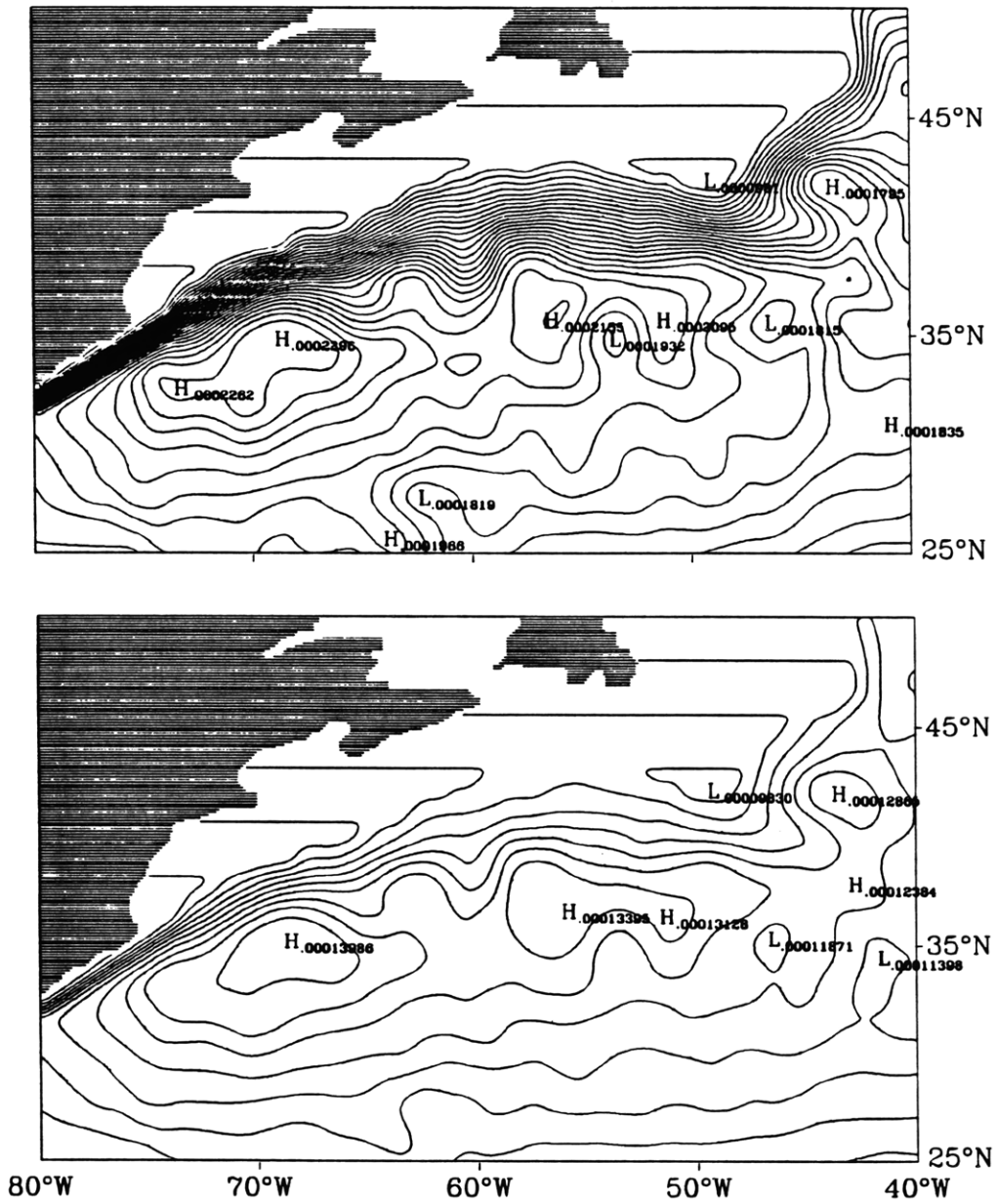

Fig. 5.2 (a) Contours of the function $\hat{q}_2 = \beta y + F_{21}\bar{\psi}_{obs}$ for the assimilation experiments. $\bar{\psi}_{obs}$ is the surface climatological streamfunction field that is assimilated. The $\hat{q}_2$-contours supply, approximately, the pattern of the flow field in layer 2 during the assimilation experiments. (b) Contours of the function $\hat{q}_3 = \beta y + F_{32}\bar{\psi}_{2obs}$. $\bar{\psi}_{2obs}$ is the climatological streamfunction field computed for layer 2 from the Bauer-Robinson data. This field is considered here as a good approximation for the time average streamfunction distribution in layer 2. The $\hat{q}_3$-contours represent the approximate streamfunction distribution in layer 3.

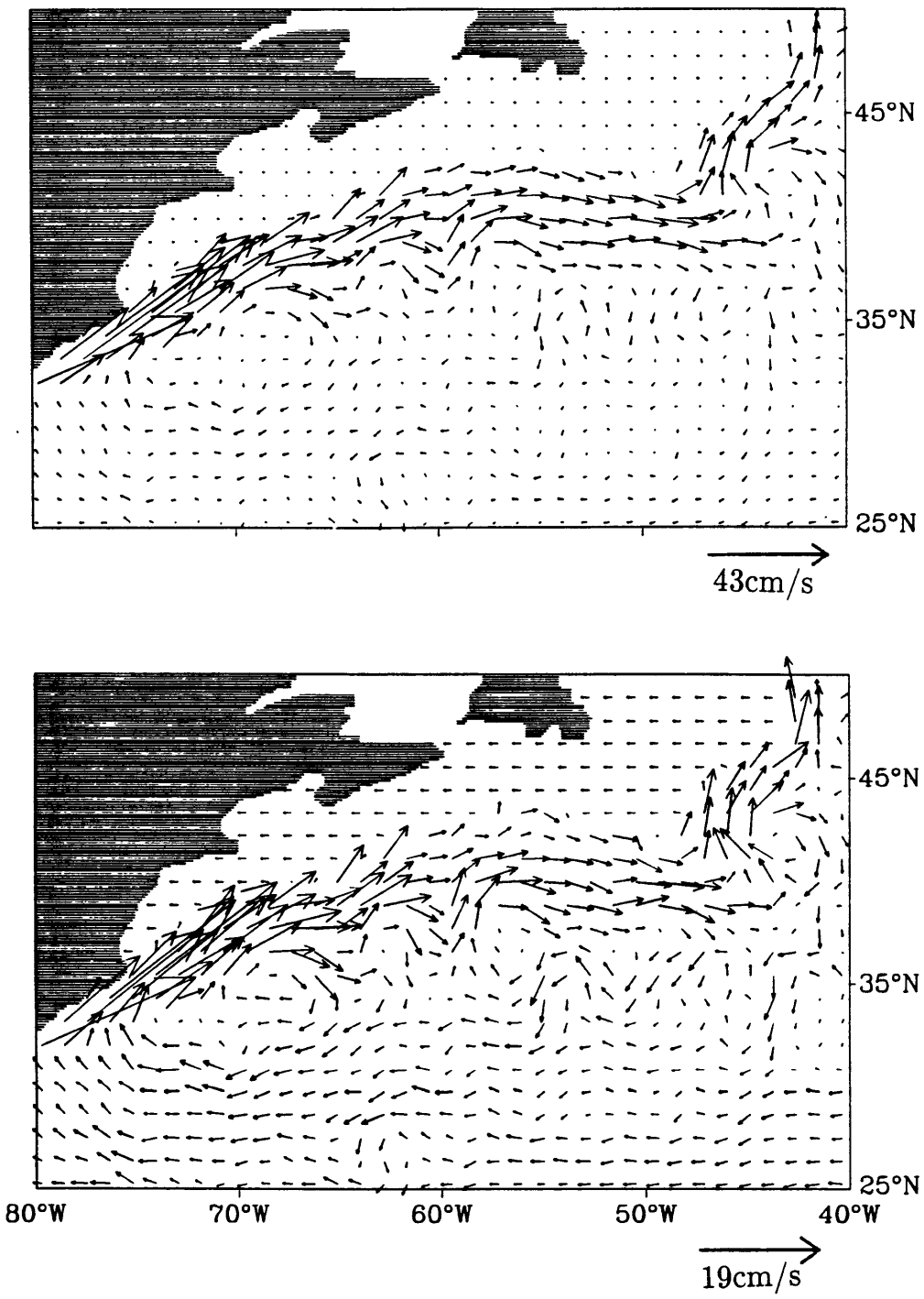

Fig. 5.3 Distribution of the potential vorticity advective velocity. (a) Layer 2. (b) Layer 3.

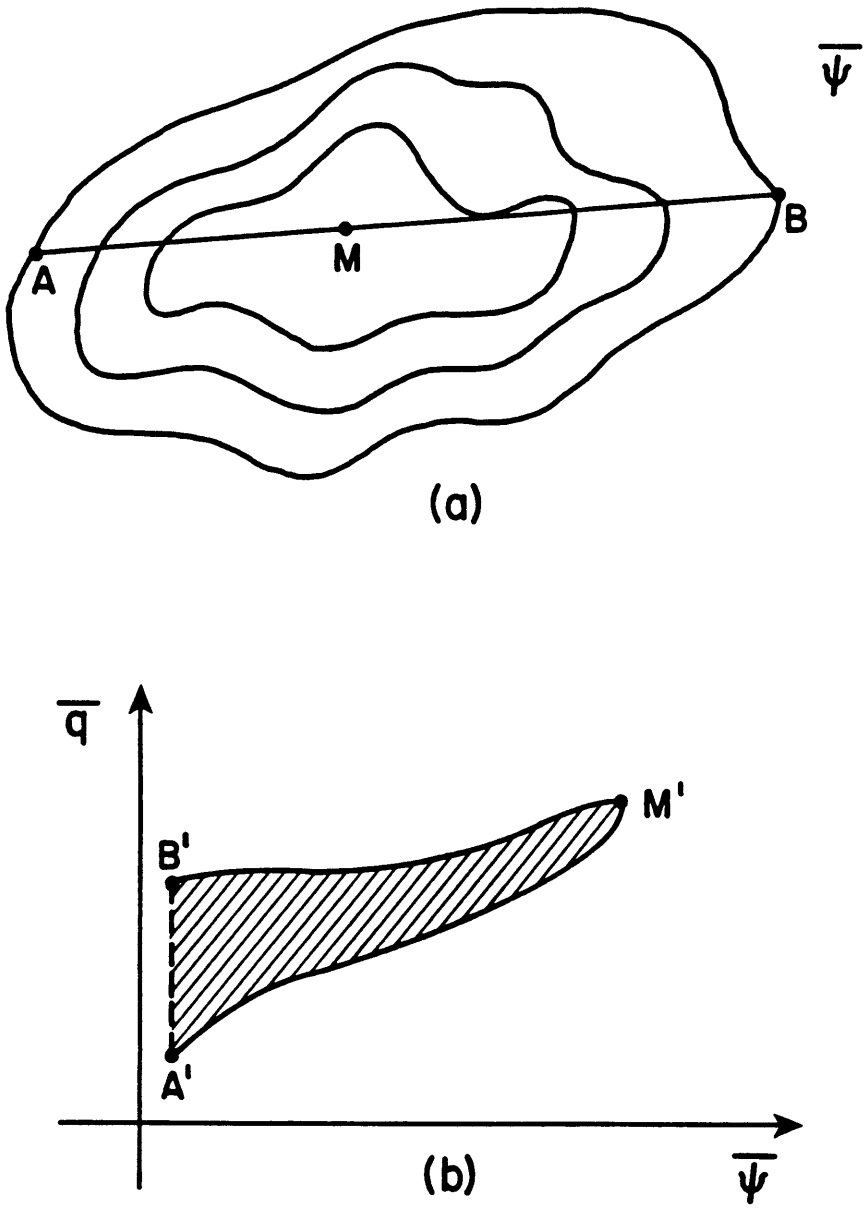

Fig. 5.4 Illustration of the use of scatter diagrams for testing the validity of the equation $J(\bar{\psi}, \bar{q}) \sim 0$. (a) Hypothetical streamline pattern. The dashed line joining the points A and B, where the streamfunction has the same values, represents the set of points used for constructing the scatter diagram. Point M corresponds to the streamfunction maximum. (b) Hypothetical scatter diagram. Points A′, B′ and M' correspond to the points A, B, and M in physical space. The width-to-length ratio of the loop in $(\bar{\psi}, \bar{q})$ space can supply a sensible measure of the departure from the free-mode behavior $J(\bar{\psi}, \bar{q}) = 0$.

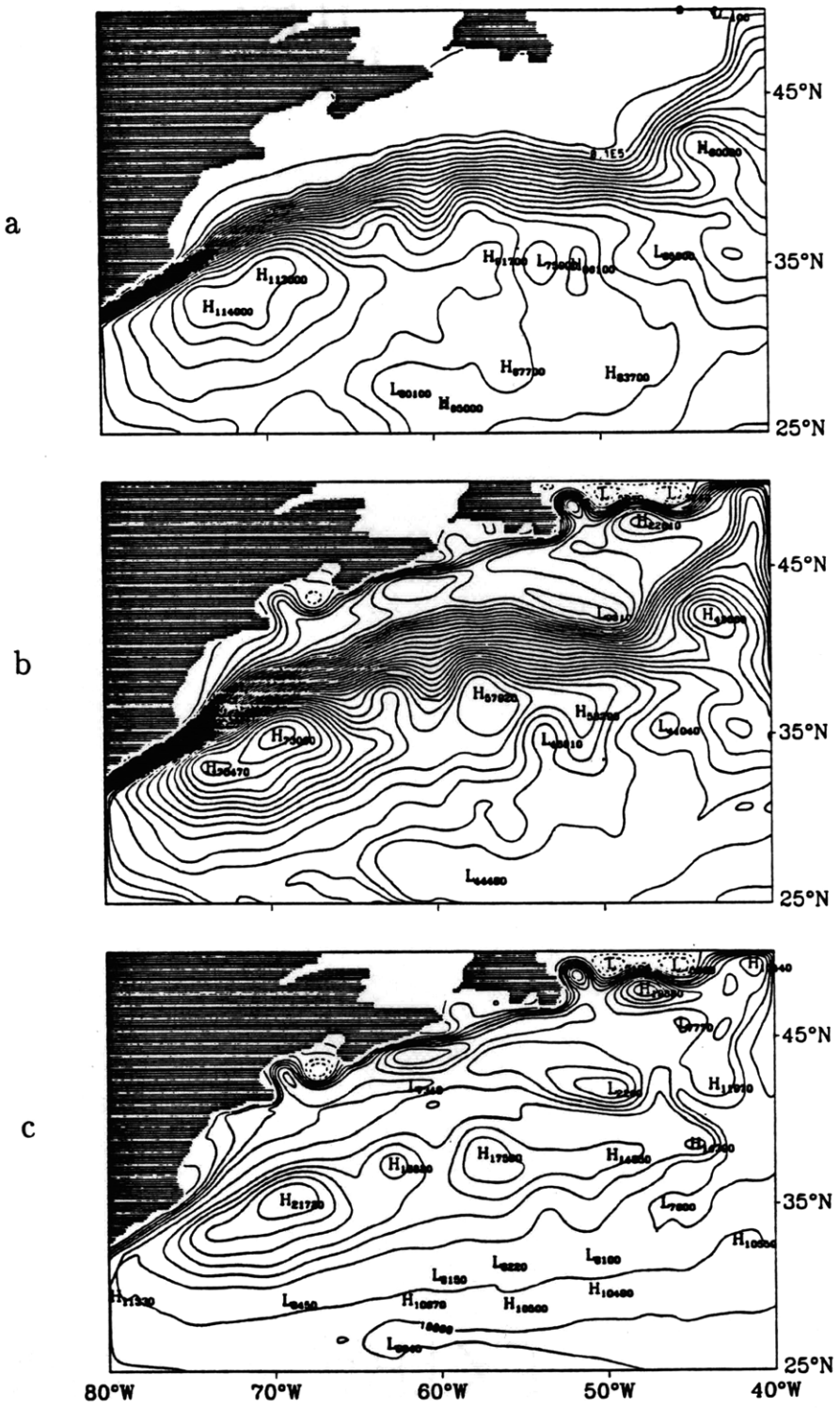

Fig. 5.5 Time average streamfunction field obtained in the experiment in which only the mean field $\bar{\psi}_{obs}$ is assimilated at the surface. (a) Layer 1. Contour interval is $5000\text{m}^2/\text{s}$. (b) Layer 2. Contour interval is $2000\text{m}^2/\text{s}$. (c) Layer 3. Contour interval is $2000\text{m}^2/\text{s}$.

d

e

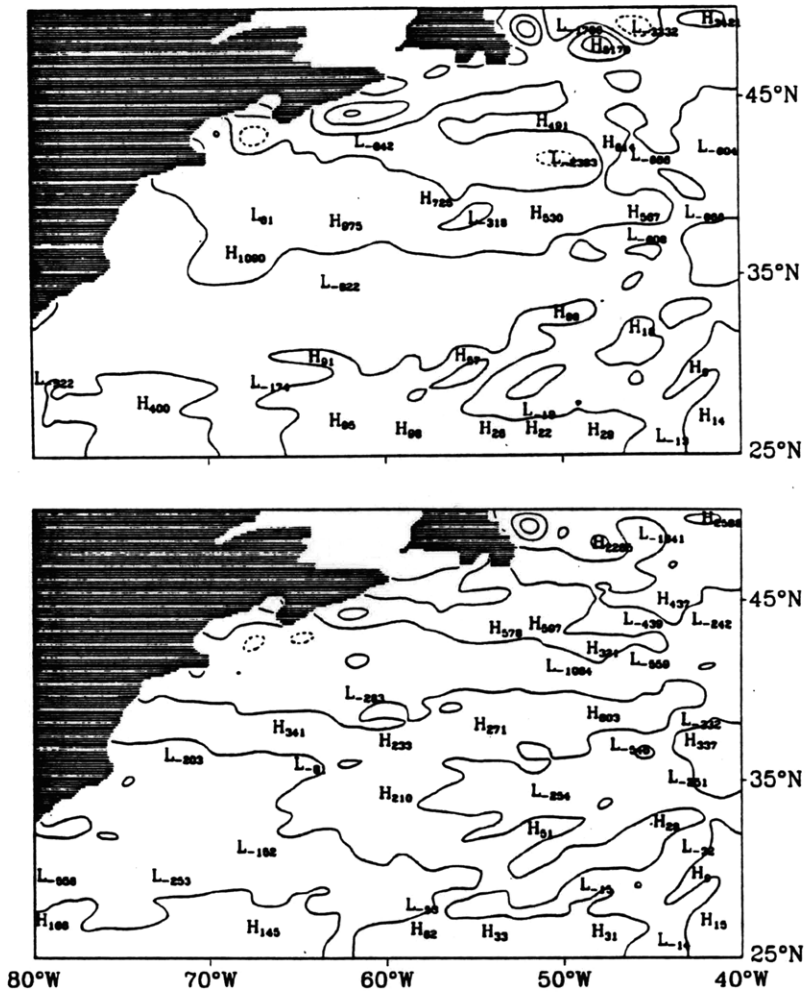

Fig. 5.5 (continued) (d) Layer 4. Contour interval is 2000m^2/s. (e) Layer 5. Contour interval is 2000m^2/s.

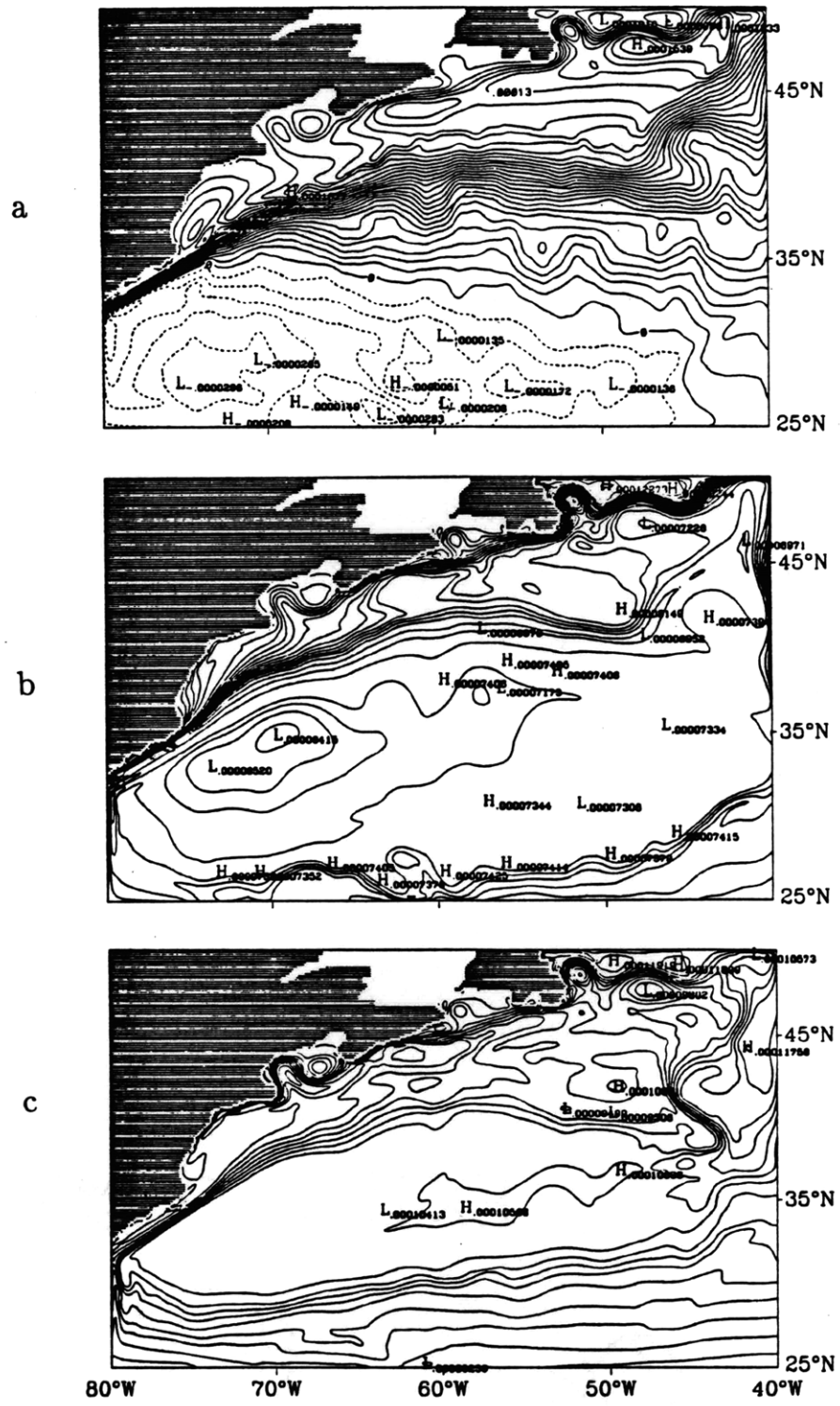

Fig. 5.6 Time average potential vorticity fields for the experiment in which only $\bar{\psi}_{obs}$ is assimilated at the surface. (a) Layer 1. Contour interval is $5 \times 10^{-6}\text{s}^{-1}$. (b) Layer 2. Contour interval is $2.5 \times 10^{-6}\text{s}^{-1}$. (c) Layer 3. Contour interval is $2.5 \times 10^{-6}\text{s}^{-1}$.

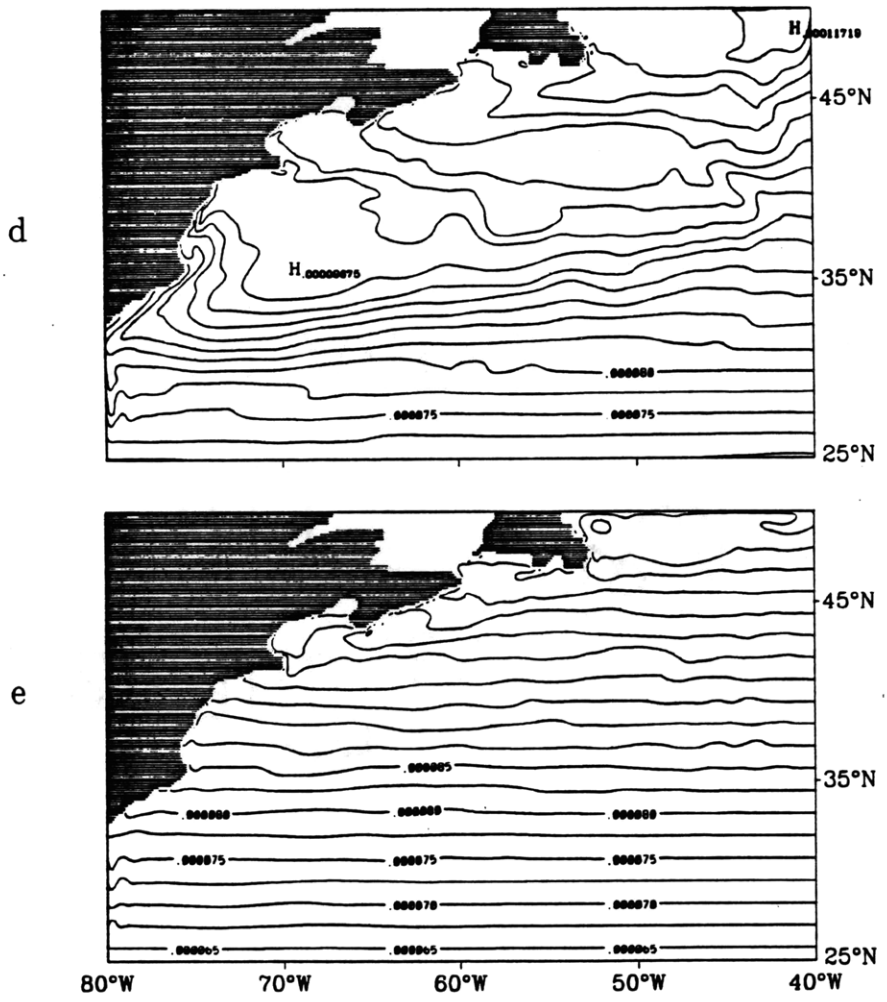

Fig. 5.6 (continued) (d) Layer 4. Contour interval is $2.5 \times 10^{-6}s^{-1}$. (e) Layer 5. Contour interval is $2.5 \times 10^{-6}s^{-1}$.

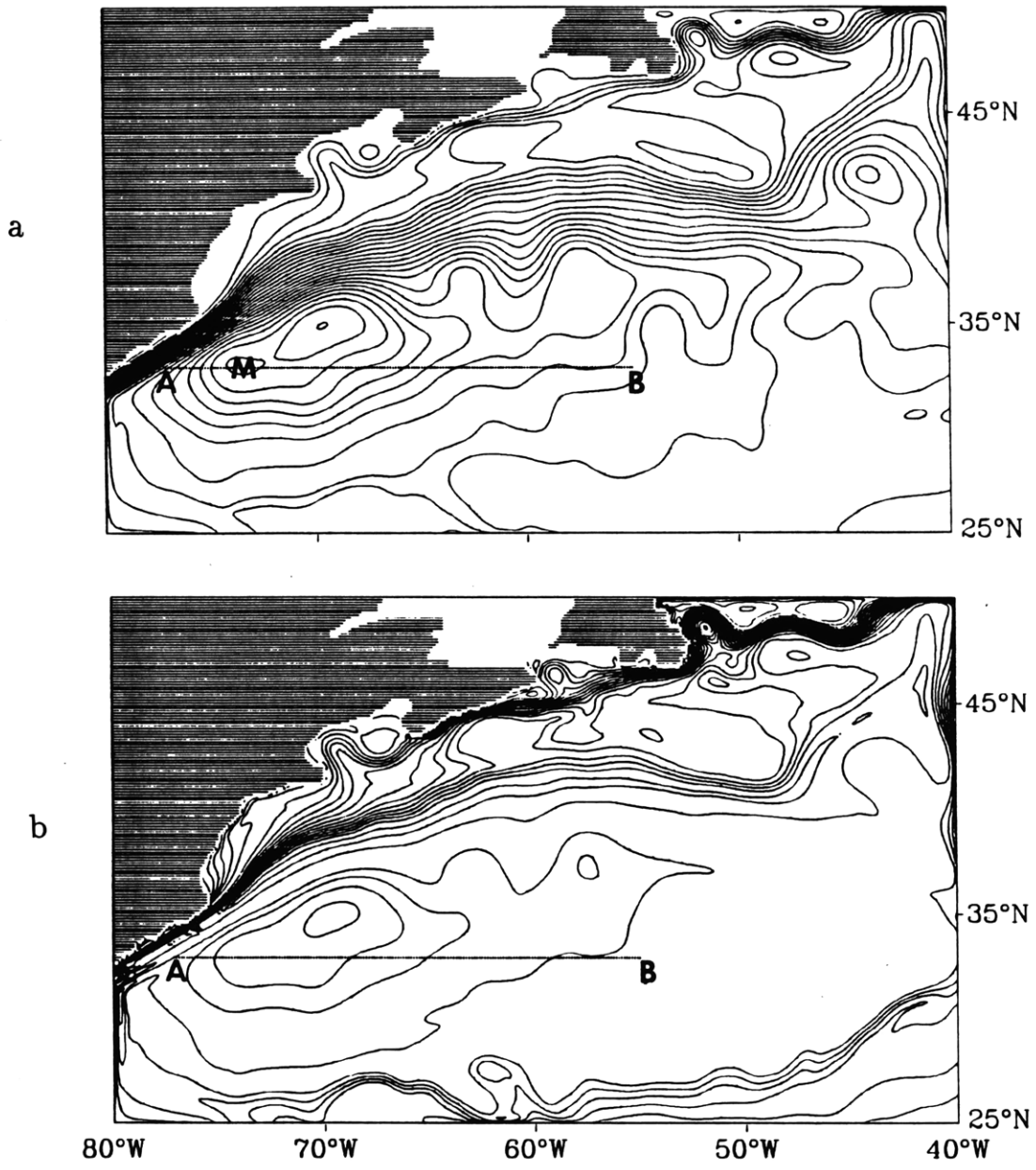

Fig. 5.7 Verification of the degree of agreement between streamfunction and potential vorticity contours in layer 2. (a)Streamfunction contours. Contour interval is $3000 m^2/s$. At the points A and B the streamfunction has the same value. Point M corresponds to the streamfunction maximum. The segment AB contains the points used for the scatter diagram. (b) Potential vorticity contours. Contour interval is $2.5 \times 10^{-6} s^{-1}$.

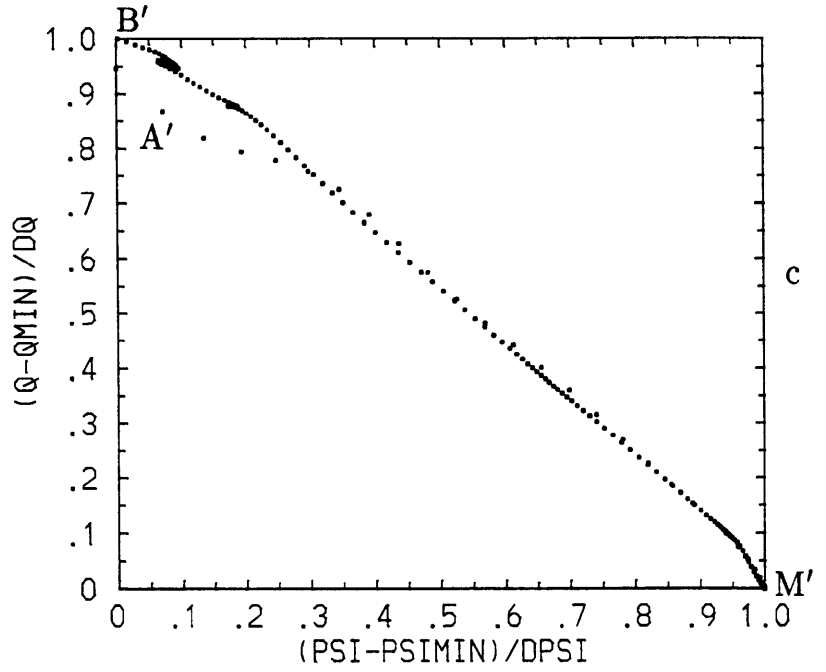

Fig. 5.7 (continued) (c) Scatter diagram for the points contained in the segment AB. The points A′, B′ and M′ are the representation in $(\bar{\psi}_2, \bar{q}_2)$ space of the points A, B and M in Fig. 5.7a.

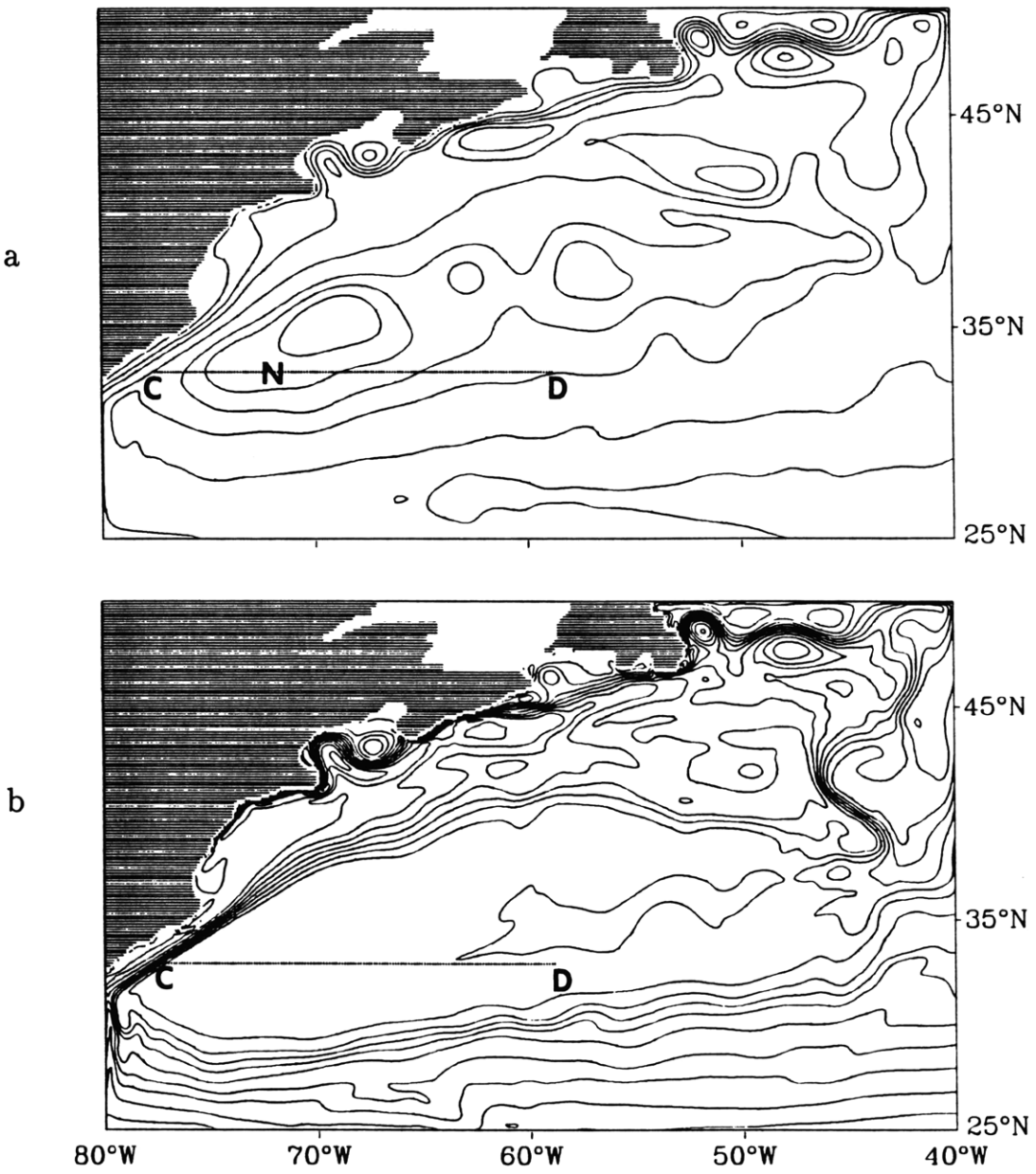

Fig. 5.8 Verification of the degree of agreement between streamfunction and potential vorticity contours in layer 3. (a)Streamfunction contours. Contour interval is $3000 m^2/s$. At the points C and D the streamfunction has the same value. Point N corresponds to the streamfunction maximum. The segment CD contains the points used for the scatter diagram. (b) Potential vorticity contours. Contour interval is $2.5 \times 10^{-6} s^{-1}$.

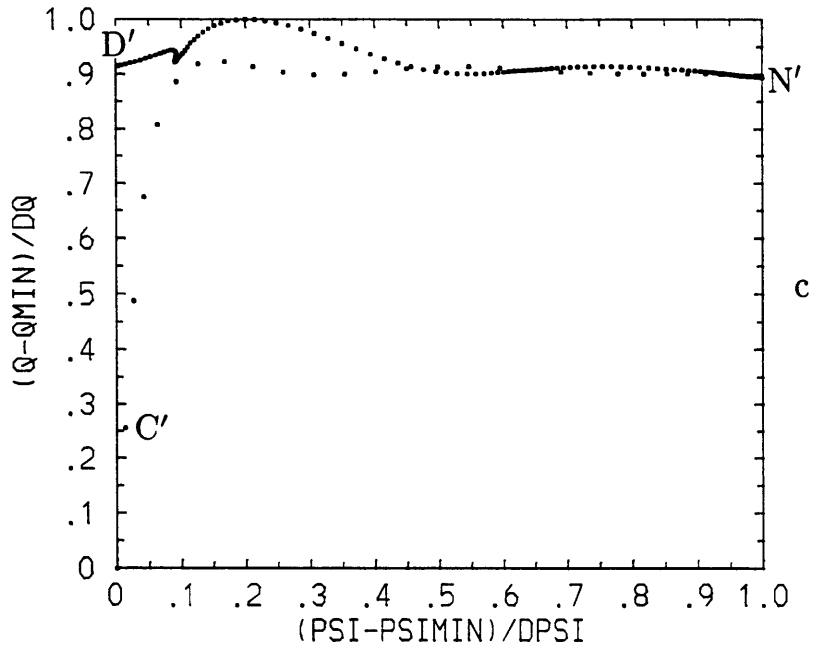

Fig. 5.8 (continued) (c) Scatter diagram for the points contained in the segment CD. The points C′, D′ and N′ are the representation in $(\bar{\psi}_2, \bar{q}_2)$ space of the points C, D and N in Fig. 5.8a.

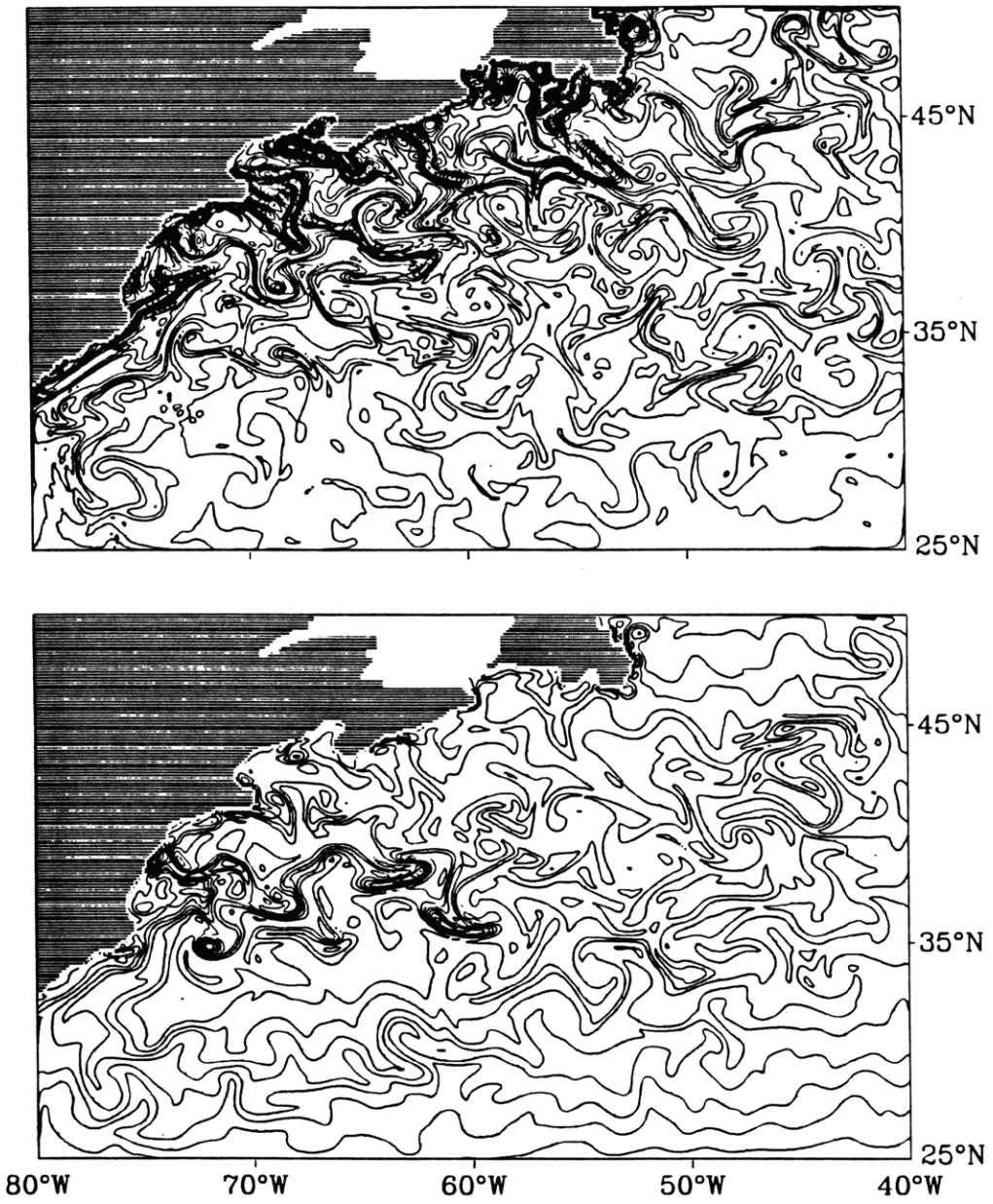

Fig. 5.9 Instanteneous potential vorticity fields in layer 2 (top) and 3 (bottom) at day 96 from the beginning of the assimilation experiment. In this experiment the total surface streamfunction field $\psi_{obs} = \bar{\psi}_{obs} + \psi'_{obs}$ is assimilated. Contour interval is $4 \times 10^{-6}\text{s}^{-1}$ in layer 2 and $3 \times 10^{-6}\text{s}^{-1}$ in layer 3.

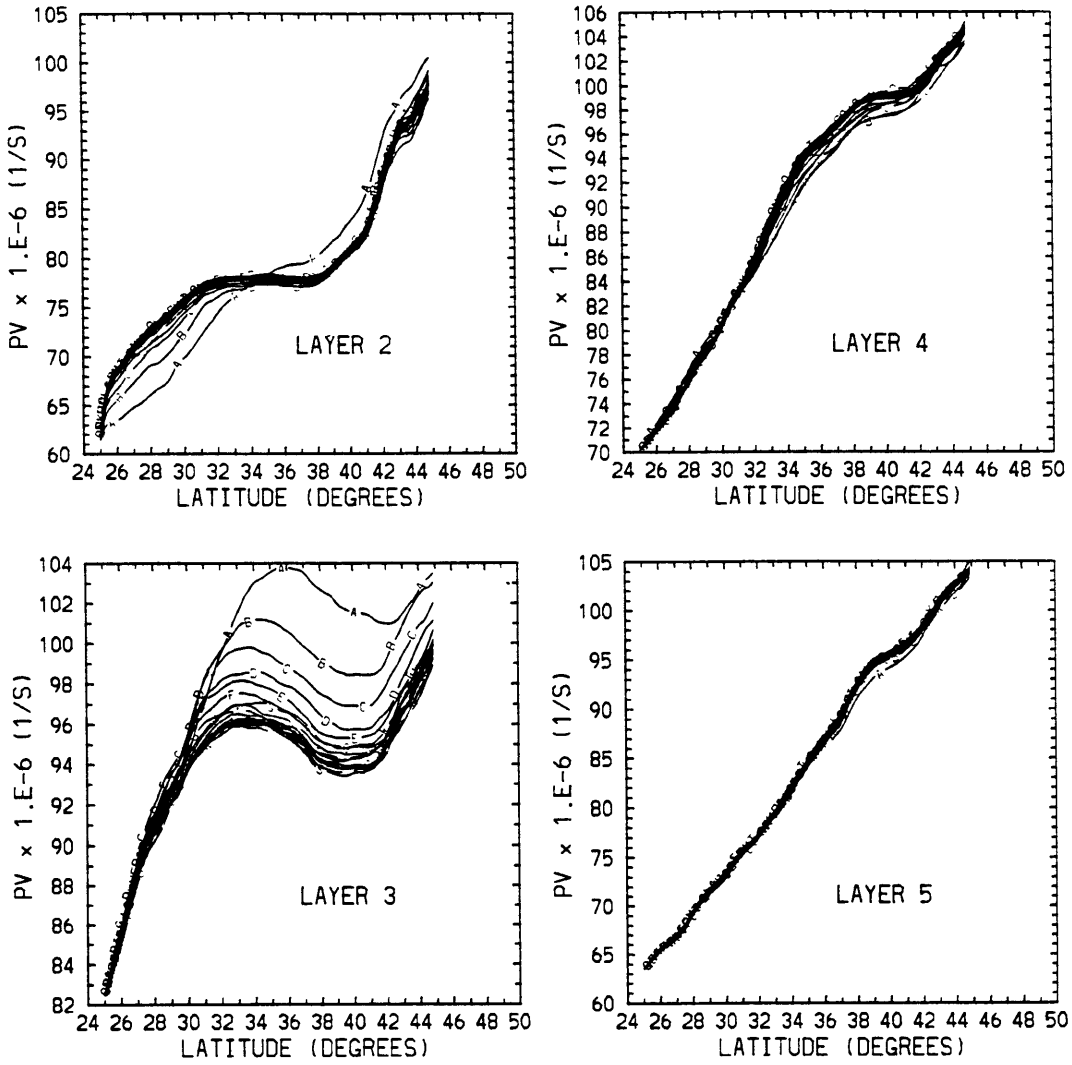

Fig. 5.10 Meridional profiles of mean potential vorticity at 55°W in the four model subsurface layers during the experiment in which the total surface streamfunction is assimilated. The sequence of surface eddy streamfunction fields $\psi'_{obs}(t)$, covering a period of 570 days, is repeated periodically 20 times, in order to allow the adjustment of the subsurface potential vorticity fields. The curves in each panel refer to the averages over each of the 570 days assimilation segments, 'A' corresponding to the first segment, 'B' to he second and so on.

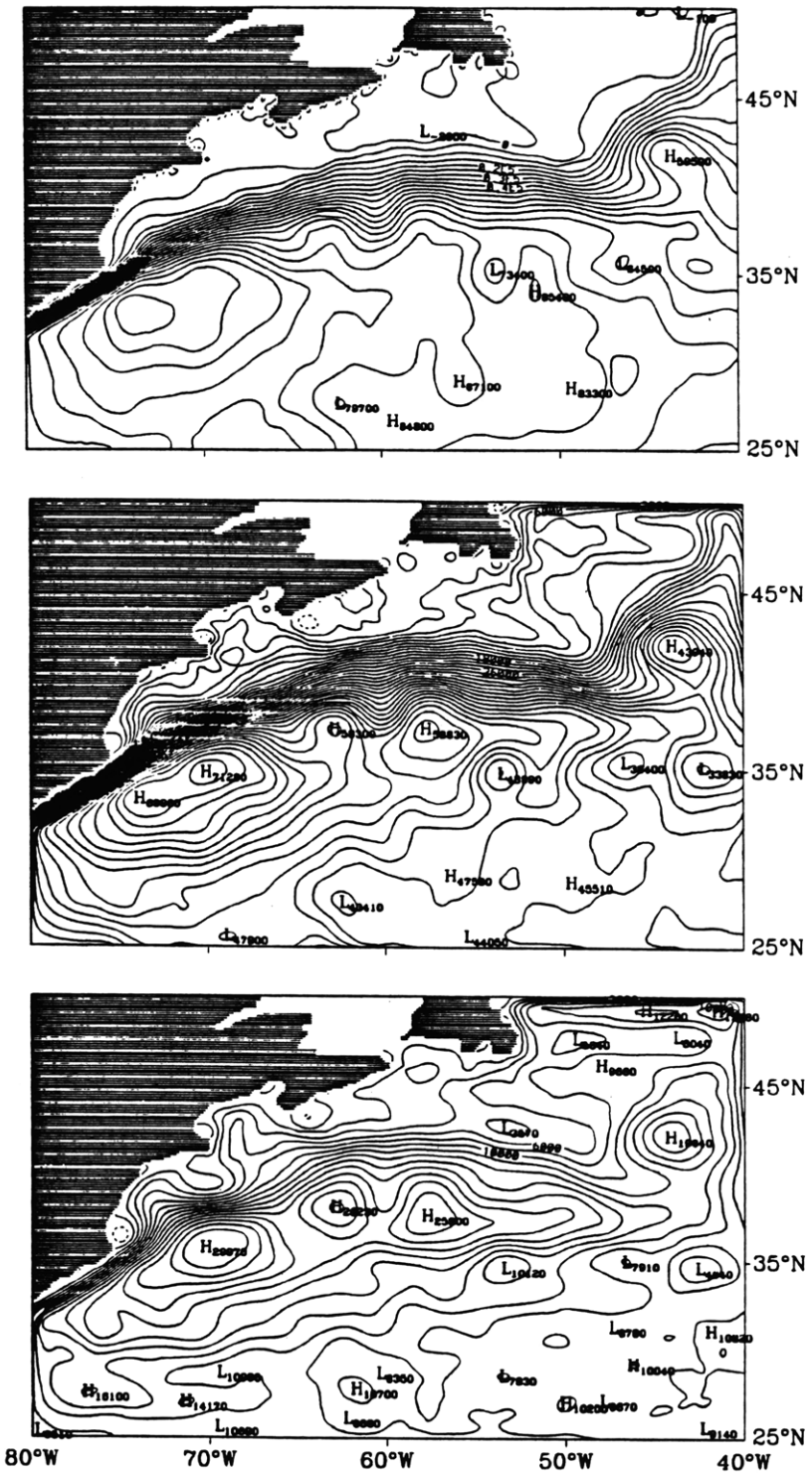

Fig. 5.11 Time average streamfunction field from the experiment in which the total streamfunction field ψ_{obs} is assimilated at the surface. (a) Layer 1. Contour interval is $5000\text{m}^2/\text{s}$. (b) Layer 2. Contour interval is $2000\text{m}^2/\text{s}$. (c) Layer 3. Contour interval is $2000\text{m}^2/\text{s}$.

d

e

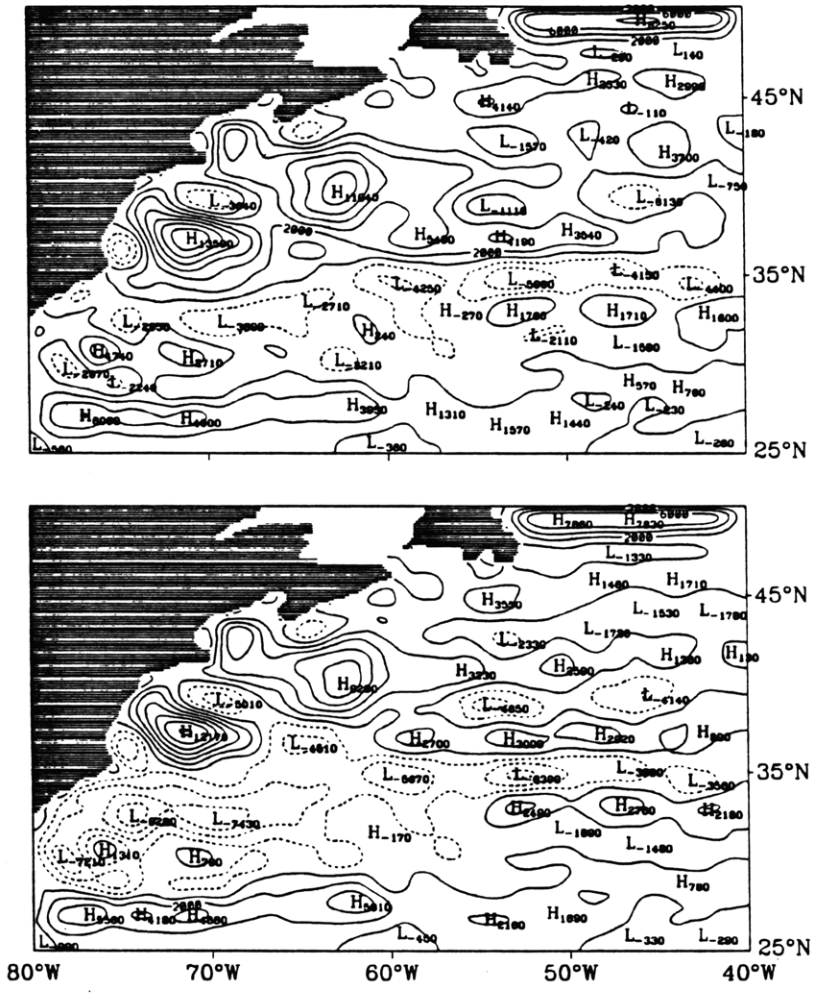

Fig. 5.11 (continued). (d) Layer 4. Contour interval is 2000m^2/s. (e) Layer 5. Contour interval is 2000m^2/s.

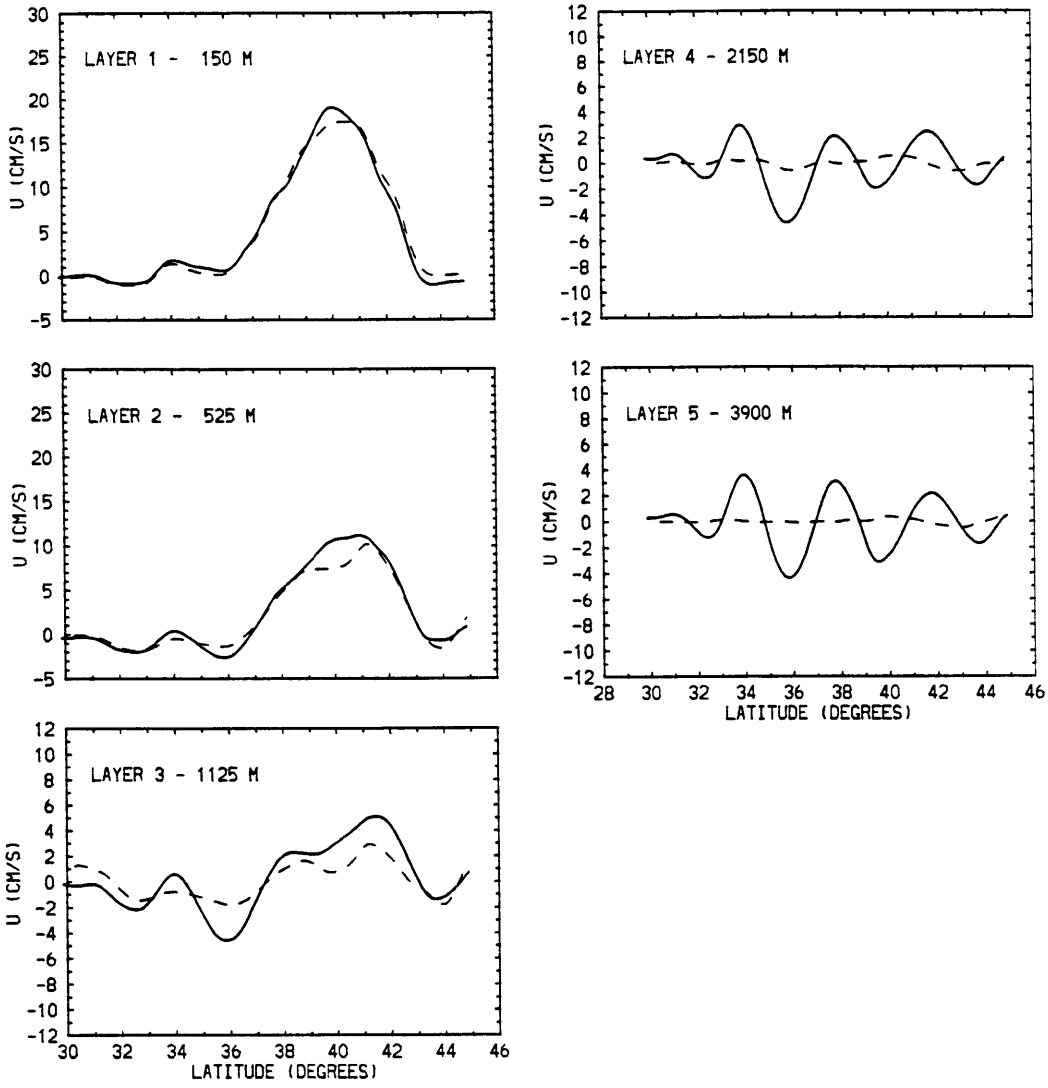

Fig. 5.12 Meridional profiles of mean zonal velocity at 55°W in the five model layers. The solid line corresponds to the experiment in which the total surface streamfunction is assimilated; the dashed line corresponds to the case in which only the mean field is assimilated.

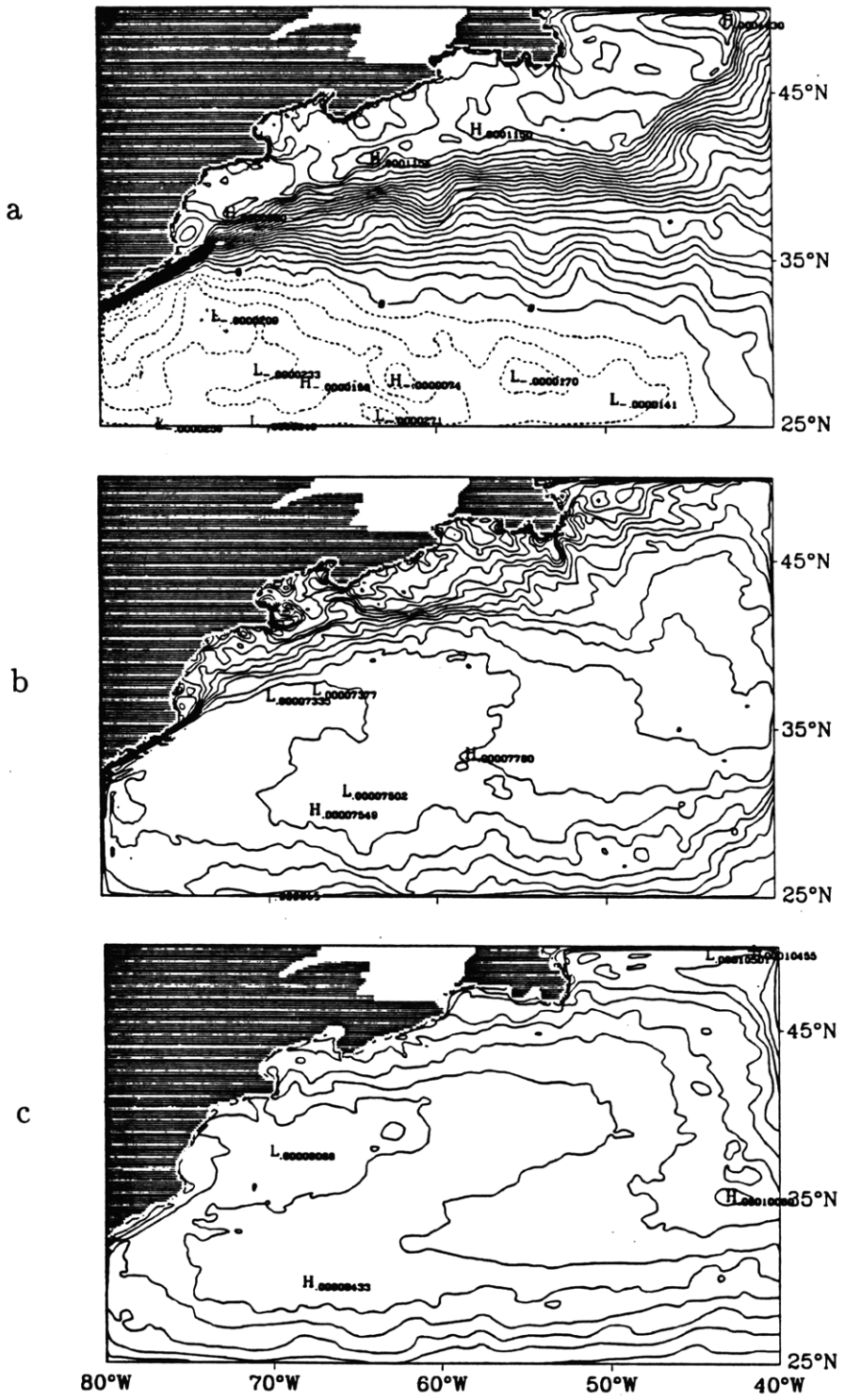

Fig. 5.13 Time average potential vorticity fields for the experiment in which the total ψ_{obs} is assimilated at the surface. (a) Layer 1. Contour interval is $5 \times 10^{-6}\text{s}^{-1}$. (b) Layer 2. Contour interval is $2.5 \times 10^{-6}\text{s}^{-1}$. (c) Layer 3. Contour interval is $2.5 \times 10^{-6}\text{s}^{-1}$.

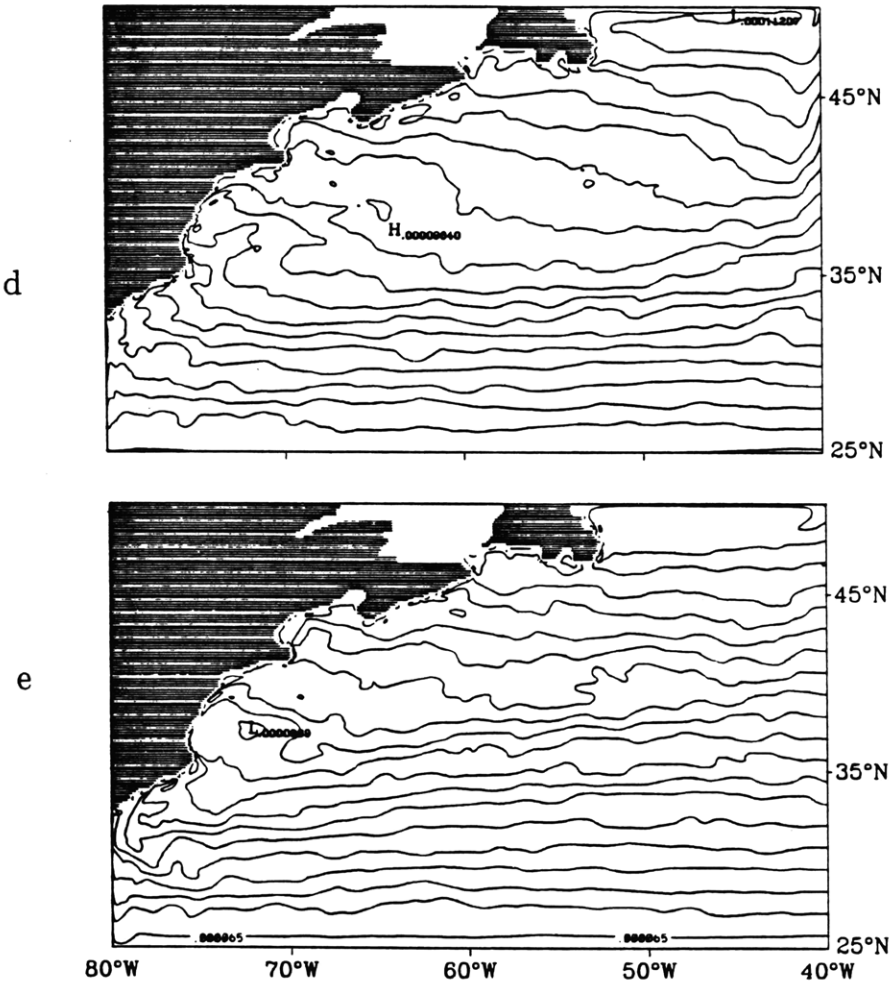

Fig. 5.13 (continued). (d) Layer 4. Contour interval is $2.5 \times 10^{-6}s^{-1}$. (e) Layer 5. Contour interval is $2.5 \times 10^{-6}s^{-1}$.

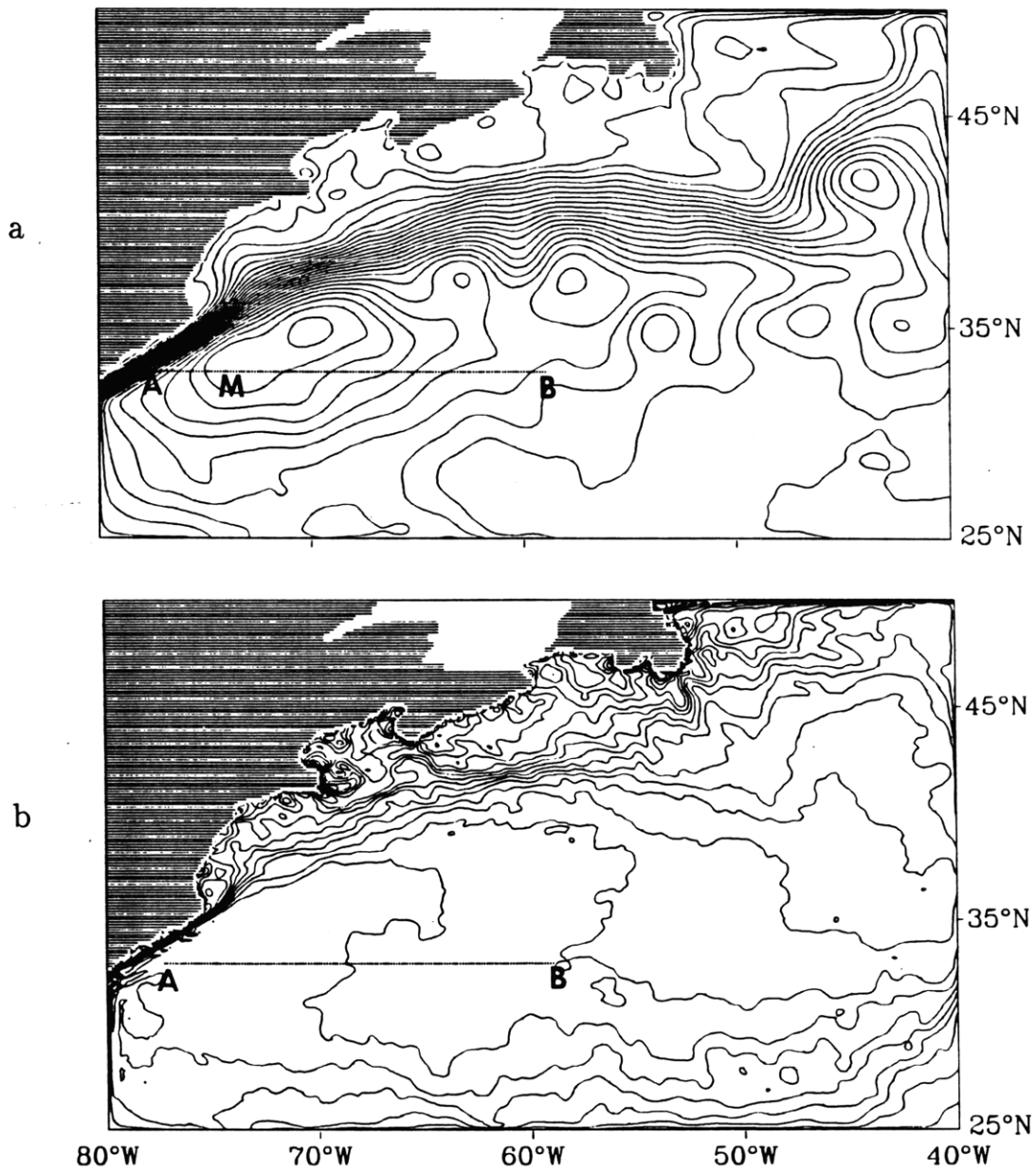

Fig. 5.14 Verification of the degree of agreement between streamfunction and potential vorticity contours in layer 2. (a) Streamfunction contours. Contour interval is $3000 m^2/s$. At the points A and B the streamfunction has the same value. Point M corresponds to the streamfunction maximum. The segment AB contains the points used for the scatter diagram. (b) Potential vorticity contours. Contour interval is $2.5 \times 10^{-6} s^{-1}$.

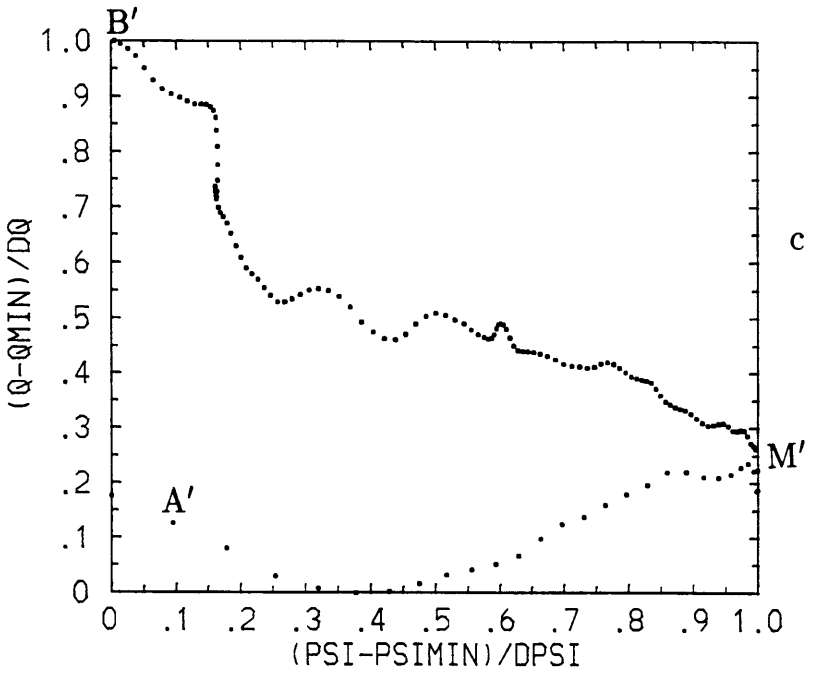

Fig. 5.14 (continued) (c) Scatter diagram for the points contained in the segment AB. The points A′, B′ and M′ are the representation in $(\bar{\psi}_2, \bar{q}_2)$ space of the points A, B and M in Fig. 5.14a.

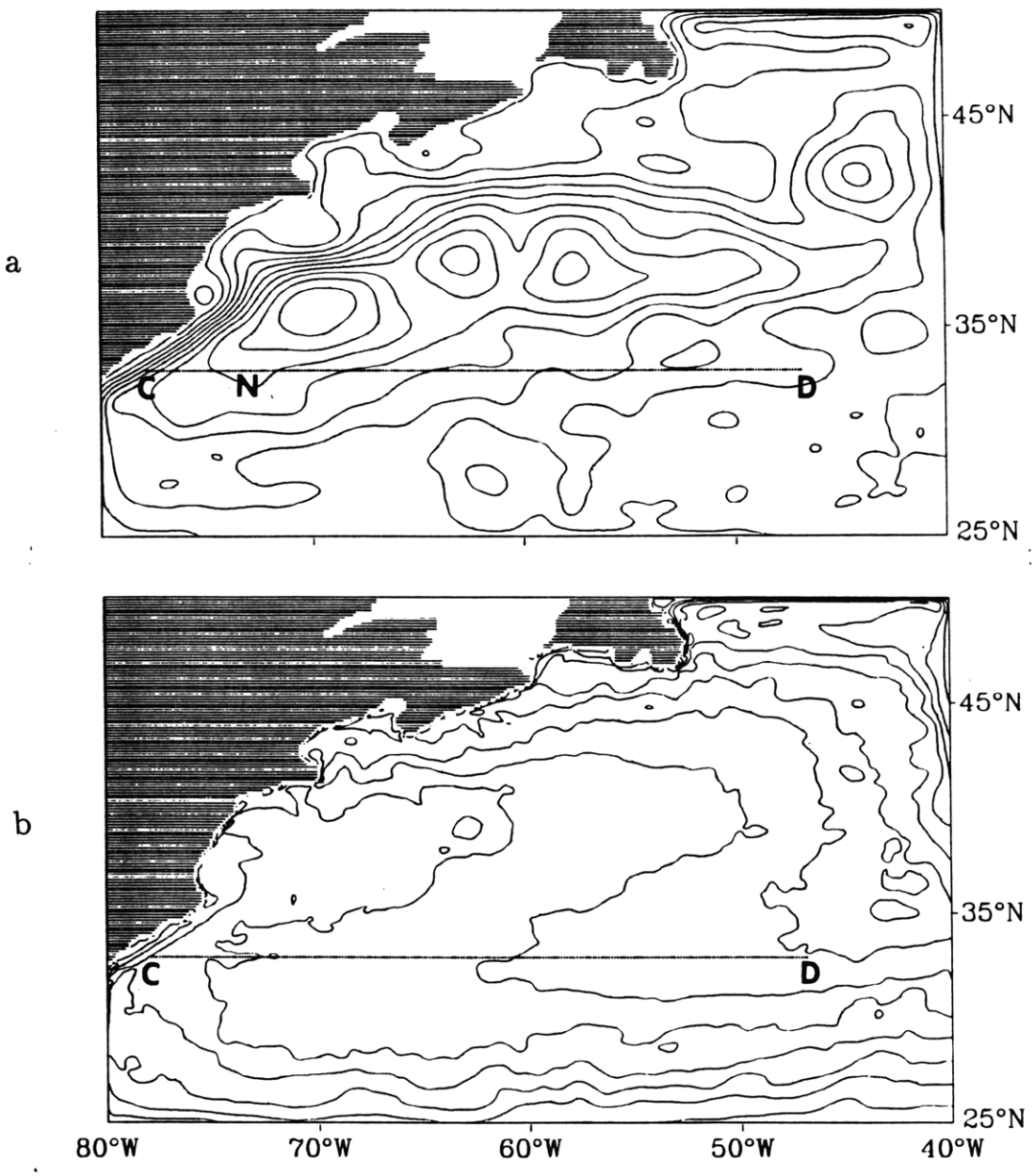

Fig. 5.15 Verification of the degree of agreement between streamfunction and potential vorticity contours in layer 3. (a)Streamfunction contours. Contour interval is $3000 m^2/s$. At the points C and D the streamfunction has the same value. Point N corresponds to the streamfunction maximum. The segment CD contains the points used for the scatter diagram. (b) Potential vorticity contours. Contour interval is $2.5 \times 10^{-6} s^{-1}$.

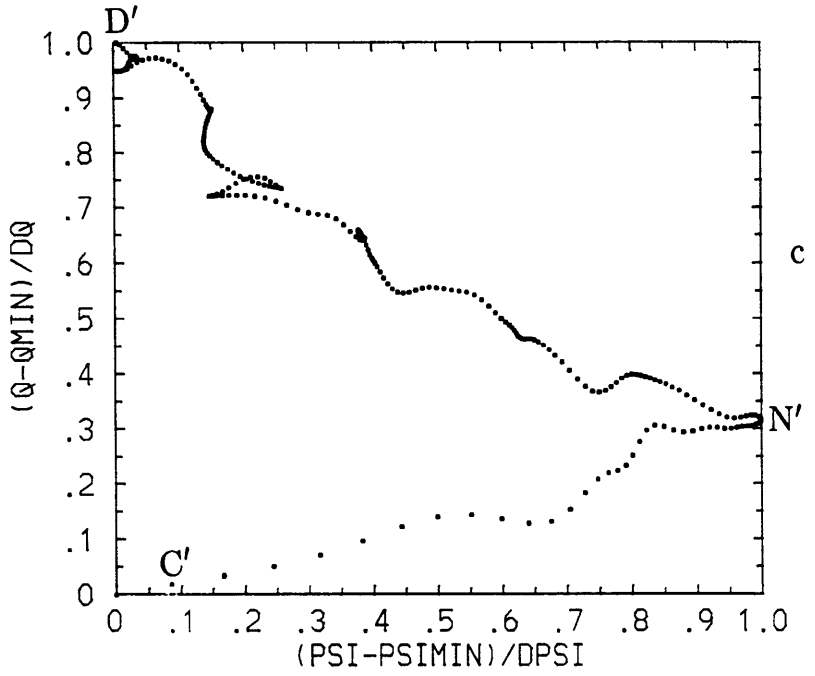

Fig. 5.15 (continued) (c) Scatter diagram for the points contained in the segment CD. The points C′, D′ and M′ are the representation in $(\bar{\psi}_2, \bar{q}_2)$ space of the points C, D and N in Fig. 5.15a.

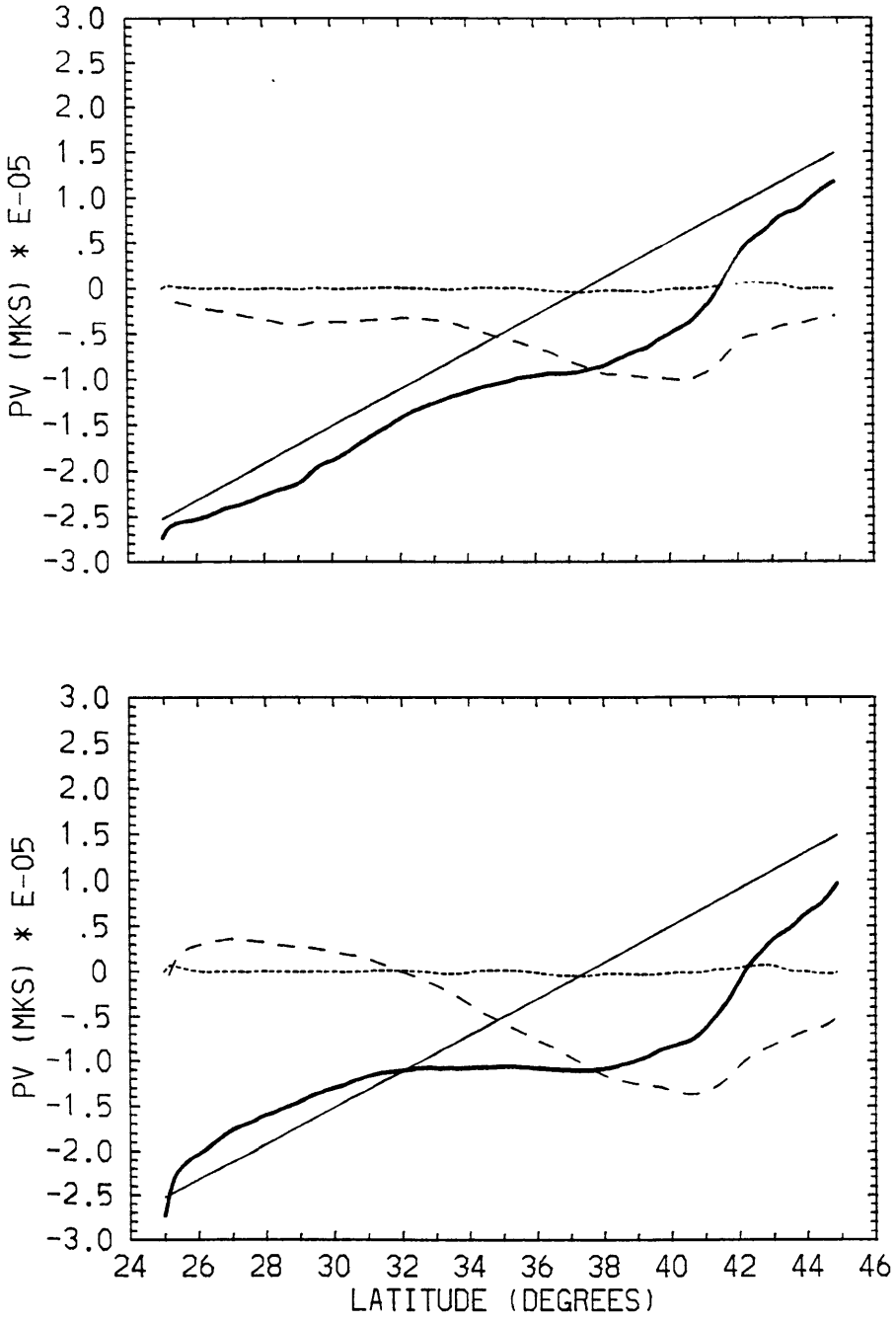

Fig. 5.16 Evolution of the different potential vorticity components in layer 2 during the experiment in which the total surface streamfunction is assimilated. (a) Meridional profiles of mean potential vorticity components around 55°W for the first 570 days of the assimilation experiment. (b) Meridional profiles of mean potential vorticity components around 55°W for the last 570 days of the assimilation experiment. The thin solid line represents the planetary vorticity; the dashed line the stretching term, the dotted line the relative vorticity and the thick solid line represents the total potential vorticity.

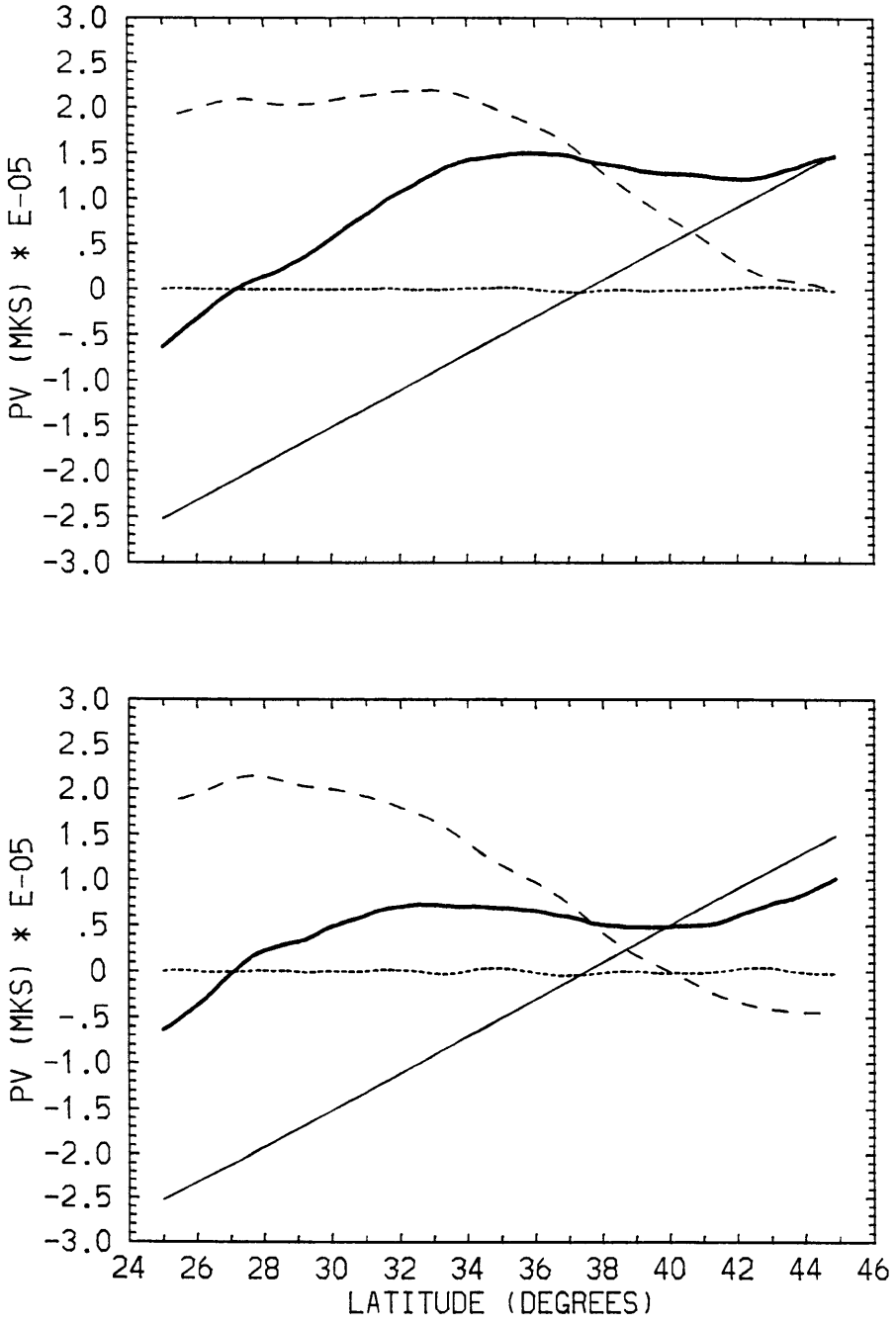

Fig. 5.17 Evolution of the different potential vorticity components in layer 3 during the experiment in which the total surface streamfunction is assimilated. (a) Meridional profiles of mean potential vorticity components around 55°W for the first 570 days of the assimilation experiment. (b) Meridional profiles of mean potential vorticity components around 55°W for the last 570 days of the assimilation experiment. The thin solid line represents the planetary vorticity; the dashed line

Chapter 6

Comparison of the assimilation results with observations

6.1 Introduction

In Chapter 4 we have analyzed the model behavior when no data assimilation is applied and the model is allowed to run freely. The circulation which develops in that case is the one consistent with the given parameter choices and with the specification of forcing and boundary conditions adopted. In that context we have identified aspects of the model climatology which are in partial disagreement with our current perception of the ocean circulation that is derived from the available observations. These aspects include both characteristics of the mean circulation (separation of the Gulf Stream from the coast, path of the separated stream, total transport etc.) and characteristics of the eddy climatology (geographical distribution of the eddy kinetic energy, space and time scales of the model variability). We would like to emphasize, once more, that no attempt has been made, in Chapter 4, to "tune" the model in order to make its behavior closer to the observed characteristics of the ocean circulation. Our major interest, there, was not to achieve the best possible model behavior, but to create a reference model run to compare with the results of the assimilation experiments.

In Chapter 5 we have studied the mechanisms of the model adjustment when the surface fields are constrained to follow some prescribed observations. We have shown that the surface data can constrain the flow in the subsurface layers: the mean component of the data tends to determine the structure of the subsurface fields, while the eddy component affects their intensity. For the given surface data, the way in which the modifications of the subsurface circulation occur and the "depth of influence" of the surface information are strongly dependent upon the model physics and vertical stratification.

Given this scenario, we now try to assess the degree of success of the assimilation procedure that we have implemented. The specific question that we address in this chapter is the following: how "realistic" are the subsurface fields that the model develops? That is, how effective are surface data in improving the global model behavior? In order to answer this question we present here the comparison between the results of the assimilation experiment and some of the available observations. In this regard we consider the experiment in which the total (mean + eddies) surface streamfunction is assimilated. The analysis described in the first part of this chapter is very similar to the one presented in Chapter 4, in order to highlight the modifications in the model behavior which are introduced by the data assimilation procedure. As in Chapter 4 we consider, here, aspects of the mean circulation as well as aspects of the eddy climatology, including position and intensity of the mean Gulf Stream and its southern recirculation, total transport, and distribution of eddy kinetic energy with depth.

A large part of the analysis described in this chapter is devoted to a comparison of the results of the assimilation experiment with the current meter data from the SYNOP East Array, which have been introduced in Chapter 2. As described in Chapter 2, these data were collected during a period of time partially

overlapping the Geosat mission. They are available at different locations within the Gulf Stream system (Fig. 1.2) and at different depths, the shallowest being about 250m and the deepest about 4000m. This data set thus offers a unique opportunity for investigating how the surface eddy signal is "projected" downward at different depths and how "realistic" the deep signature of the surface eddy information is.

We conclude this chapter with a dynamical interpretation of these comparisons and a discussion of the results.

6.2 The mean velocity field

In Chapter 4 (section 4.2) we have observed the tendency for the model mean streamfunction fields to drift away from the fields used as initial conditions, which are the ones derived from climatological data. The mean circulation that develops at statistical steady state (Fig. 4.1) shows a Gulf Stream which overshoots at Cape Hatteras, has a mean path displaced further south, and includes very intense recirculation gyres confined to the western half of the domain. No attempt has been made to correct these features with an appropriate tuning of the model parameters, so that the resulting mean circulation is not necessarily "the best possible" circulation achievable. However, the deficiencies that we have identified are, in different ways, common to all the numerical models of this area, so that the numerical experiment described in Chapter 4 can be considered as a typical one.

A comparison of the mean circulation obtained when no data assimilation is applied (Fig. 4.1) with the mean circulation obtained when a total surface streamfunction field is assimilated (Fig. 5.11) shows the effectiveness of surface data, when strongly nudged into the model, in modifying the global model behavior. A more direct comparison is presented in Fig. 6.1, where we show meridional profiles

of mean zonal velocity at 55°W in the five model layers. The solid line represents the results from the assimilation experiments, while the dashed line corresponds to the results from the control run. The dotted line in the panels for the three upper layers defines the mean velocity profiles derived from the climatological fields which have been used as initial conditions in both experiments.

The surface data constraint that is applied to the model during the assimilation experiment produces a substantial change in the mean velocity profiles in all five layers. In the upper layer the solid line and the dotted line are almost coincident, as a consequence of the strong nudging of the model upper layer mean streamfunction field toward the climatological streamfunction field. However, in layers 2 and 3, where the climatological fields are only used as initial conditions, the mean circulation which develops during the assimilation experiment shows enhanced maximum eastward velocity, between 40-42°N, with respect to the initial profiles (dotted line). Notice also the development, in these layers, of the westward return flow, at about 36°N, associated with the southern recirculation, which is practically absent in the corresponding climatological profiles. As described in Chapter 5, this component of the circulation is essentially eddy driven and is quite barotropic in character.

How do these results compare with observations? The Gulf Stream area is probably one of the most studied regions in the World Ocean, so that the observational basis is relatively large, including hydrographic data as well as current meter and float data. Two different representations of the mean velocity structure of the Gulf Stream have been developed from the available observations. The first one is the traditional Eulerian mean, in which the time average is performed with respect to a fixed coordinate system. The second representation, which can be defined as the "average synoptic Stream" (Hall and Bryden, 1985; Hogg, 1992)

describes the average structure of the flow as viewed in a coordinate frame whose origin is at the instantaneous axis of the meandering jet, as it moves as a whole. The surface data that we assimilate contain a mean component which is obtained as an Eulerian time average over a long term data set. Therefore the average Eulerian Stream seems to be the most appropriate description to be used for comparison with our assimilation results. In the following we consider comparisons with three different estimates of the average Eulerian Stream, estimates that have been derived from different data and with somewhat different criteria. In this way we hope to identify features of the mean circulation which can be considered robust and to assess their range of variation. The first comparison is with Richardson's section of mean zonal velocity at 55°W (Richardson, 1985), computed by using a combination of surface drifters, SOFAR floats and current meters. The second comparison is with the mean velocity profiles constructed by Owens (1991) from all the available SOFAR float data, at 70°W and at 55°W. Finally, the third comparison is with the mean velocity estimates computed from the current meter measurements at the SYNOP east array, near 55°W. The current meter data have been supplied by Hogg (Hogg, personal communication).

6.2.1 Comparison with Richardson's velocity section

The mean zonal velocity section computed by Richardson (1985) at 55°W represents a canonical description of the average Eulerian Stream at this longitude. The data sets used for this construction include surface drifter data, collected in the years 1977-1980, float data at the nominal depths of 700m and 2000m, covering the period 1980-1982, and current meter data at 4000m from the POLYMODE array II, which was operating from April 1975 to July 1977. The data from the surface buoys and the floats were averaged over geographical boxes 1° in latitude

and 10° in longitude. The comparison between the resulting estimates of mean zonal velocities and similar estimates from the assimilation results is shown in Fig. 6.2 at the middle depths of the model layers. The estimates computed by Richardson at the surface, 700m and 2000m have been interpolated linearly to the depths of the model layers 1, 2 and 3. The model results for layers 4 and 5 have been compared directly with Richardson's values at 2000 and 4000m. The estimates from the model have been averaged over 10 degrees of longitude centered at 55°W. In Fig. 6.2 the thick solid line describes the velocity profiles derived from the assimilation experiment, while the dots connected by the thin solid line are derived from Richardson's estimates. The vertical bars indicate the standard error of the mean. In the panels corresponding to layers 1, 2 and 3 the climatological zonal velocity profiles (dotted line) are also shown for reference. In the upper three layers the model profiles show an eastward jet with a reduced peak value. In layers 2 and 3 the jet defined by the solid line appears also broader than the observations. The maximum eastward velocities in layers 1, 2 and 3 which, in Richardson's profiles, are achieved around 39.5°N, appear displaced somewhat northward in the assimilation results. This can be noticed especially in layer 3 where the absolute maximum is found around 41.5°N. A northward displacement of about one degree in the maximum eastward velocity is already found in the upper layer climatological profile (dotted line) when compared with the profile from the surface drifters. However, we can also notice the correlation between the maxima around 38 and 41.5°N, in layer 3, with the corresponding maxima in layers 4 and 5. This suggests that the eddy-driven flow in layers 4 and 5 may be partially responsible for the characteristics of the eastward flowing jet in layer 3, and, to a smaller extent, in layer 2.

The position and intensity of the westward flow associated with the southern recirculation are in remarkably good agreement in all the five layers. An exception is found in the amplitude of the westward flow in layer 5, where the current meter

measurements, at 35.5°N, show a mean velocity more than twice that obtained in the model. The large amplitude of this westward flow, which appears to be bottom intensified, has been explained by Owens and Hogg (1980) as associated with the Taylor column that develops over a topographic bump. The absence of any topographic relief in the model does not allow bottom intensification in the westward flow at this latitude.

At 4000 m the sequence of zonal jets observed in the model profile is in remarkable agreement with the profile from the POLYMODE current meter measurements, over the range of latitude covered by the current meter array. Notice, in particular, in the solid profile, the presence of a westward flow around 39°N which represents the model expression of the northern recirculation. Even though no northern recirculation gyre is present in the surface climatological field that is assimilated, the deep flow, which is essentially eddy driven, does have this feature. However, the amplitudes of both the Gulf Stream and its countercurrents are underestimated in the model with respect to the current meter measurements.

In layer 4 the amplitude of the zonal currents is in better agreement with the observations. However, the sequence of alternating jets shown by the solid profile is not fully observed in the data. Only the southern countercurrent, the Gulf Stream and the northern countercurrent are present in the observation profile. The sequence of zonal jets in model layer 4 appears very similar to the one in layer 5. The flow in the two deeper model layers seems thus to have a barotropic character which is not found in Richardson's estimates at 2000 and 4000m. Whether this is a consequence of the different types of data sets used for his estimates (as well as different data processing and different time periods) or a consequence of a model deficiency cannot be determined from the information presently available.

The section of mean zonal velocity constructed by Richardson shows a mean Gulf Stream whose axis tilts southward with depth. This tilt, of about 2 degrees of latitude, seems too large on a theoretical basis (Hogg, personal communication), and it has not been observed in any other measurements. It may result from using, at different depths, data collected at different times (Owens, 1991). These considerations make the comparison with other observations especially necessary.

6.2.2 Comparison with Owens's velocity profiles

Profiles of mean zonal velocities have been computed by Owens (1991) from all the available SOFAR float data. The measurements have been averaged over 1° latitude by 5° longitude boxes centered at 70°W and at 55°W. At 70°W data are available at 700, 1500 and 2000m depth, while at 55°W only the profiles at 700 and 2000m are present.

The comparison at 70°W is shown in Fig. 6.3. The left panels correspond to the zonal velocities at the three available depths, while the right panels show the meridional velocities. In this case the assimilation results have been interpolated linearly to the data depths. The result is represented by the dashed line in Fig. 6.3. The dots correspond to the observational estimates. The standard errors of the mean, supplied by Owens, are indicated in the figure. At all three depths a mean Gulf Stream is observed both in the data and in the model results. The peak velocities, both zonal and meridional, are achieved between 37°N and 38°N. The Stream is oriented approximately east-northeast, so that a relatively large meridional velocity is present at this longitude. South of the Stream we see a weak westward return flow in both curves. The major discrepancies which emerge from this comparison are associated with the Stream width and intensity. At this longitude the data show, in fact, a relatively narrow jet, approximately 200-300km

wide, whereas the Gulf Stream from the model, at 700m, appears much broader (about 500km wide) and weaker. At this depth the maximum velocities estimated from the float data are about 25cm/s zonal and 13cm/s meridional. The peak velocities from the assimilation results, on the other hand, are only approximately 12 cm/s zonal and 6 cm/s meridional. These differences in width and intensity can be attributed to the characteristics of the surface mean field which is assimilated. Due to the much longer duration of the Bauer-Robinson data set with respect to the duration of the data set used by Owens, the surface and near surface Gulf Stream obtained from the assimilation experiment can be expected to be broader and weaker than in the data.

At 1500 and 2000m the velocity amplitudes from the model and from the observations are much more similar. Even if the mean field which is assimilated can constrain the structure of the flow in the subsurface layers, as explained in Chapter 5, the intensity of the flow in these layers is largely controlled by the eddy-flux processes, especially at depth.

Fig. 6.4 shows the comparison at 55°W. In this case the velocity estimates from the float data are available only at 700 and 2000m. At this longitude the jet is almost zonal. Meridional velocities are very weak, both in the model (dashed line) and in the data (dotted solid line), the differences being within the confidence interval of the observational estimates. The profiles from the data show a mean Gulf Stream which is much broader than the one at 70°W, a result consistent with the observed meandering of the separated jet. The Stream defined by the observations at 700m is, however, narrower than the one obtained from the model. Also, as in the comparison with Richardson's section, the maximum eastward velocity from the assimilation results is smaller, and its position is displaced about 2° north. The

westward return flow south of the Stream is found at the same latitude, in the model and in the data, also in this case.

At 2000m the maximum eastward velocity and the westward return flow derived from the assimilation results are in good agreement with the estimates from the float data. However, as in the comparison with Richardson's section, the dashed line in the lower-left panel shows a sequence of zonal jets which do not appear in the data profile at the same depth.

6.2.3 Comparison with the SYNOP east array data

As a final example of an observational perception of the mean circulation, we consider the mean velocities derived from the current meter measurements at the SYNOP east array. These estimates have been computed from the time series obtained at the moorings located at approximately 54.7°W (see Table 1.1 and Fig. 1.2). Most of the time series are about 2 years long, the only exceptions being the ones measured near 40°N at 500, 1000 and 1500m, whose duration is only 435 days. The standard errors of the mean have been evaluated by assuming a decorrelation time of 20 days (Owens, 1991). The results are shown in Fig. 6.5. The assimilation results have been interpolated linearly to the available current meter depths and are described by the dashed line. As before, the left panels refer to the zonal velocity and the right panels to the meridional velocity. The comparison in Fig. 6.5, even if limited to a narrower range of latitudes, shows characteristics similar to the ones observed in the previous two cases. The major discrepancies are associated with the width and the intensity of the eastward flowing jet, as described by the zonal velocity profiles. Also in this case these discrepancies are consistent with the duration of the current meter measurements (about 2 years), which is much shorter than the duration of the Bauer-Robinson climatology. The differences in velocity amplitude

are reduced considerably at 4000m. As previously discussed this is consistent with the fact that the deep flow in the model is essentially eddy-driven. Notice, however, the shift of approximately 1.5° in the two velocity profiles at 4000m. The velocity structure from the model at this depth is in relatively good agreement, in Fig. 6.2, with the POLYMODE array II current meter measurements. Hogg (1990) shows that the mean velocity pattern obtained from the SYNOP east array is qualitatively consistent with the pattern from the POLYMODE array II data. However, the velocity section at 55°W that Hogg has constructed by using both data sets simultaneously, shows that a northward shift of the POLYMODE data would yield a more consistent composite section. The reason for these differences in the position of the deep currents is not clear. A displacement of the mean deep Gulf Stream at the times of the two mooring deployments seems to be the most plausible explanation. However, in this case, we would expect a better agreement between the deep flow in the assimilation experiment and the measurements at the SYNOP east array than with the POLYMODE measurements. The time period of the Geosat data that have been assimilated is, in fact, partially overlapping with the time period of the measurements at the SYNOP east array. The Geosat data cover the period November 1986 - May 1988, while the SYNOP data are available approximately from September 1987 to August 1989, so that about 260 days of overlapping exist. Richardson (1985) discusses the variability in the position of the deep Gulf Stream over the whole period of the POLYMODE array II campaign, as revealed by its three nine-month period deployments. The deep eastward flow shifted approximately 200km southward over an 18 month period. A similar process might have occurred over the almost three year period covered by the combination of the Geosat and SYNOP data sets, thus providing a plausible explanation for the shift in the deep flow between the assimilation results and the SYNOP measurements.

6.2.4 Discussion

In this section we have tried to assess the degree of realism of the mean circulation obtained from the assimilation experiment in which a total (mean + eddy) upper layer streamfunction is assimilated. To that end we have considered three different descriptions of the Eulerian mean Gulf Stream, which have been derived from different data sets or different combinations of them. We find that the assimilation of the surface data appears to be very effective in constraining the characteristics of the flow in the different model layers. The position of the model Gulf Stream and its southern recirculation are in much better agreement with the observations when incorporating data assimilation. However, due to the characteristics of the climatological mean field which is assimilated, discrepancies are found in the width and in the amplitude of the eastward flowing jet. The Bauer-Robinson climatology covers, in fact, a period of time much longer than the duration of any of the other data sets. Therefore the streamfunction field which is computed from the Bauer-Robinson climatology has a Gulf Stream broader and weaker than the one estimated from the other authors. Because of the strong nudging applied, the mean streamfunction field in the model upper layer is constrained to agree with the climatological field. However, in the subsurface layers, the flow is not directly constrained by the surface data and its intensity is largely determined by the eddies. The discrepancies in flow amplitude are observed, in fact, to decrease with depth. At 2000 and 4000m the peak velocities in the model have amplitudes more similar to the ones seen in the observations. Exceptions are found in the comparison with the POLYMODE array II current meter data, in which both the Gulf Stream and its countercurrents appear more intense than in the model.

The velocity profiles in the model layers 4 and 5 show a series of zonal jets. This zonal velocity structure is not in disagreement with current meter

measurements at 4000m, in the range of latitudes covered by the measurements. However, the velocity profiles from the float data at 2000 m show a simpler velocity structure, where only the Gulf Stream and a weak westward flow south of the Stream are observed. The barotropic character of the flow in the two deeper model layers is thus not supported by the observations. Whether this is a consequence of the different data sets and different data processing at 2000 and 4000m or the result of a model deficiency is still unclear.

6.3 Total transport

Fig. 6.6 shows the time average barotropic streamfunction from the assimilation experiment we are considering. In this figure the Stream leaves the coast, at Cape Hatteras, with a transport of about 60 Sv (60×10^6 m^3/s), similar to the one prescribed at the inflow and also in agreement with the estimate of 65 Sv by Richardson and Knauss (1971). The model transport increases downstream and reaches a maximum around 70°W, where a local maximum in the intensity of the southern recirculation gyre occurs. East of this longitude the transport decreases to values of approximately 75 Sv. The maximum transport, of about 90 Sv, found in the model around 70°W agrees with some observational estimates. Halkin and Rossby (1985), for example, found a value of about 94 Sv for the average synoptic stream near 73°W, by using measurements from the freely falling velocity profiler Pegasus. A similar estimate was also obtained by Worthington (1976) at a hydrographic section near 70°W. However, the observed increase in total transport east of 70°W is not found in the model. The observational basis for the evolution of the transport downstream of 70°W has been presented by Hogg (1992) and we summarize it here.

At 68°W, at the GUSTO (*Gulf Stream Observations*) mooring, Hall and Bryden (1985) estimated a transport of 100 Sv. A further increase, of about 50 Sv, is observed between 68°W and 60°W (Hogg, 1992). Near 55°W, at the SYNOP east array, the transport remains as high as 147 Sv. The scenario that emerges from all these estimates is one in which the maximum values are achieved in the area between 60°W and 55°W. According to Hogg (1992) the increase in transport downstream of 68°W, seems to derive from both the northern and southern recirculation gyres, which would contribute a transport of 20-30 Sv each.

This analysis of transport distribution is for the synoptic Stream. The estimates for the average Eulerian Stream are much lower, because of the meandering of the jet. A simple conceptual model developed by Hogg (1992) shows that the transport reduction in the Eulerian average can be as high as 50%. Both the Stream and its recirculation gyres can be expected to be reduced by a similar factor. At 55°W Richardson (1985) estimated a value of 93 Sv for the transport carried by the average Eulerian stream. This value is about 30% smaller than the synoptic transport estimated by Hogg (1992) at the same longitude. However, a value of 93 Sv is larger than the transport found in the model at 55°W, which is about 75 Sv. In order to understand the reasons for this discrepancy we have compared the vertical distribution of zonal transport computed by Richardson with a similar distribution from the model. Richardson's estimates of transport per unit depth and surface to bottom transport are reproduced in Table 6.1. The estimates from the assimilation results are summarized in Table 6.2. The values for the Gulf Stream transport in the five model layers have been obtained, as in Richardson (1985), by integrating the eastward velocity bounded by countercurrents in the profiles shown in Fig. 6.2 (solid line). The values for the transports in the northern and southern recirculation gyres have been estimated by integrating the westward velocity areas flanking the Stream immediately to the north and to the south, respectively.

The vertical profiles derived from the assimilation results and from Richardson's estimates are shown in Fig. 6.7. The dots in the figure correspond to the model estimates, while the asterisks indicate Richardson's estimates, at the surface, 700m, 2000m and 4000m, with their associated uncertainty. The thick solid line indicates the profile obtained by using linear interpolation between the five model values and extrapolating a constant value to the bottom. The transport obtained by integrating this profile is about 82 Sv. The thick dotted line represents an alternative way of joining the points at 1125 and at 2150m. In this case the transport is about 75 Sv. An average estimate for the model transport is about 78-79 Sv. The thin dashed line is the profile obtained from Richardson's estimates at four depths, by using linear interpolation between them. This profile corresponds to a transport of about 99 Sv. If the thin dotted line is adopted between the values at 700 and 2000m the resulting transport is about 88 Sv. The value of 93 Sv, given by Richardson as the best estimate from the data he used, has been obtained by fitting a smooth curve between the values at 700 and 2000m.

The comparison between the thick profiles and the ones defined by the thin lines, in Fig. 6.7, shows, first, a reduced surface transport (linear extrapolation yields, in the model, a value of about 98 Sv instead of the 122 Sv estimated by Richardson) and, second, a much smaller depth independent transport. In Richardson's profile the barotropic transport is about 34 Sv, while in the model it is only about 18 Sv, almost 50% smaller than Richardson's estimate. The smaller surface value in the model can be attributed to the reduced maximum eastward velocity, near the surface, as discussed in the preceding section. The reduced barotropic transport can be understood by considering the comparison in Fig. 6.2. At 4000m the maximum velocity in the Gulf Stream is smaller than in the data. At 2000m the peak eastward velocity in the model is comparable to the observations,

but the Stream appears as a narrower jet. At both depths the Stream carries a smaller transport.

The transport in the model southern recirculation gyre is about 31 Sv (table 6.2). The value of 42 Sv reported by Richardson (Table 6.1) is obtained by considering, at 4000 m, the bottom intensified flow over topography. If the corresponding current meter estimate is halved to bring it in line with the velocity values at lesser depths, the transport in the southern recirculation gyre becomes about 29 Sv, statistically indistinguishable from the model estimate. The transport in the model northern recirculation gyre, on the other hand, is about 60% smaller than in the observations. Even if the deep flow shows a signature of westward velocities north of the Stream, this is insufficient to bring the transport values to the observed level. This underestimate of the northern recirculation gyre flow may be the consequence of inadequacies in the deep eddy field, perhaps associated with the lack of bottom topography. However, the lack of a northern recirculation gyre in the surface climatological field that is assimilated could also affect the eddy-mean flow interaction processes, leading to an inaccurate development of the deep flow in this area.

6.4 The eddy field

In this section we analyze the eddy field in the model subsurface layers when the Geosat data are assimilated at the surface. The degree of realism of the model eddy field depends both upon the accuracy of the assimilated data and upon the way the surface eddies are extrapolated at depth by the model. The characteristics of the Geosat data have been analyzed in Chapter 2. Although we have not supplied any precise estimate of the error distribution associated with the Geosat maps, we have discussed the capability of the Geosat data to measure a mesoscale eddy

field that compares well with in situ data at several specific locations. In that context we have found a relatively large coherence between geostrophic velocity time series derived from the Geosat maps and the current meter measurements at the SYNOP east array, in a broad frequency range. In this section we thus concentrate on the model aspect, and we analyze how the model extrapolation of the surface information compares with the observations. In particular we analyze how the coherence between model estimates and current meter measurements varies with depth. The vertical structure of the surface eddies, developed by the model, depends upon the model physics, upon the fixed vertical stratification, inherent in a QG model, and also upon the characteristics of the mean potential vorticity fields in the subsurface layers. We will discuss these issues in detail in the following.

In this section we consider, first, the comparison of the assimilation results with the current meter data at the SYNOP east array. We then analyze the distribution of the eddy kinetic energy as a function of depth. We will use estimates of eddy kinetic energy derived from observations at different depths (Schmitz, 1984; Owens, 1991) for assessing the success of the assimilation procedure in creating realistic eddy kinetic energy levels and distributions in the model subsurface layers.

6.4.1 Comparison with current meter data at the SYNOP east array

The SYNOP east array was operating during a period of time partially overlapping the Geosat mission, thus allowing the possibility of comparing time series from the assimilation results with time series measured in situ by the current meters. We thus start this analysis with a direct comparison of the time series covering the overlapping period. We will concentrate, in particular, on the measurements collected at the mooring near 54.7°W, 40.86°N. This mooring is

equipped with current meters at five different depths, which are, approximately, 250, 500, 1000, 1500 and 4000m (Table 2.1). The comparison is shown in Fig. 6.8. Fig. 6.8a describes the time evolution of the zonal velocities, while Fig. 6.8b describes the meridional velocity. The solid line indicates the current meter measurements, while the dashed line describes the model geostrophic velocities at the current meter depths. The latter have been computed by linear interpolation between the values at the five model layers. Day 0 on the abscissa corresponds to 1 September 1987. The current meter measurements at this mooring started on 23 September 1987.

The dashed and solid lines at 247m show characteristics similar to the ones observed in the comparison between the current meter measurements and the Geosat data, described in section 2.4. The most energetic, low-frequency events present in the current meter time series are captured also by the model time series, even if discrepancies in amplitude or in phase can sometimes be observed. The quality of the comparison near the surface is thus determined by the characteristics of the Geosat data. The degree of agreement between in situ data and model estimates appears to remain approximately the same at 500, 1000 and 1500m. At these depths the velocity signals are approximately equivalent barotropic, both in the model and in the data, i.e. their amplitudes decrease with depth, but their phase lines are almost vertical. Notice, in particular, the very energetic event which is observed in the zonal velocity record, between day 170 and day 220. Although the zonal velocity appears generally underestimated in the model results, the event can clearly be identified, in the model, down to 1500m depth. However, in the deep ocean, the comparison seems to degrade. The equivalent barotropic character appears to persist, in the data, also at 4000m, while the model signal is, at this depth, almost flat.

These statements can be better quantified by considering the variation of coherences and phases with depth. Coherences and phases between current meter time series and model time series, at the five available depths, are shown in Fig. 6.9. Coherences are presented in the left panels and phases in the right panels. The solid lines refer to the zonal velocity component, while the dotted lines correspond to the meridional velocity component. In Chapter 2 we have found that the Geosat time series are coherent with the current meter time series for periods longer than approximately 30 days. The results in Fig. 6.9 show that the coherence between model time series and current meter time series, in the same frequency band, remains above the significance level (dashed line) at 247, 500, 1008 and 1516m, even if it tends to decrease with depth. The phase differences, at these frequencies, appear very close to zero. At 4000m, however, the coherence drops below the significance level almost everywhere. Notice the presence, in the curves of zonal velocity coherence (solid line in Fig. 6.9), of a peak centered around 20-30 days. We recall, from the description of the model spectral characteristics, in Chapter 4, that there is the tendency, in the model, to develop barotropic basin modes in the same range of frequencies (20-30 days). It seems plausible, therefore, that a fraction of the energy contained in the Geosat eddy field at these frequencies excites the model basin modes.

In Fig. 6.10 we show the comparison between frequency spectra. The left panels are for the zonal velocity and the right panels for the meridional velocity. The solid lines refer to the current meters and the dashed lines to the model results. The spectra from the model are very similar to the spectra from the current meter measurements in the upper ocean, the differences being within the confidence interval at all periods longer than about 10 days. However, the discrepancies in the high frequency part of the spectra tend to increase with depth. At 4000m, in

particular, the energy level at periods shorter than 30-50 days drops, in the model spectra, much more rapidly than in the current meter spectra.

The conclusions that we can derive from this analysis is that the assimilation procedure that we have implemented can create in the model subsurface layers an eddy field with some realistic characteristics, depending upon the quality of the surface data. In the range of frequencies in which the Geosat data are coherent with the current meter data, the assimilation results are also coherent, down to a depth of approximately 1500m. This depth corresponds to the bottom of the third model layer. Coherence is lost in the deep ocean, which roughly corresponds to layers 4 and 5 in the model. How can we explain this loss of coherence at depth? We attempt some plausible explanations in the next section.

6.4.2 Vertical structure of the assimilated eddy field

The possible sources of error in the time dependent component of the assimilation results can be attributed to three causes: the surface data, the model physics (including vertical stratification) and the resulting model mean potential vorticity fields. In the following we analyze each of these aspects in detail:

1) **The surface data.** We have already discussed how the time dependence of the eddy field in the Geosat maps is coherent with in situ measurements over a broad frequency range. An additional aspect that needs to be considered is the frequency-wavenumber relationship. In fact, the spectral components that show a correct time dependence might be associated with incorrect wavenumbers, due to aliasing problems. The aliasing issue in the Geosat data set has been discussed in detail by Wunsch (1989b). A definitive answer is not yet available, due to the complex pattern of the

satellite measurements. However, we can anticipate, for example, that plane waves with crests parallel to the satellite arcs will be easily aliased to waves with zero wavenumber, if the cross-track sampling is too coarse. It can also be shown that waves whose wavenumber is correctly resolved by the spatial sampling, but whose frequency is not resolved by the temporal sampling will be aliased to waves with the same frequency, but with a wavenumber of opposite sign. A plane Rossby wave will thus appear as eastward propagating. An incorrect frequency-wavenumber relationship can be expected to introduce inaccuracies in the vertical structure associated with the surface signal, as will be described in the following.

2) **The model.** The model is based upon the quasi-geostrophic approximation. Therefore it cannot properly represent time dependent motions associated with ageostrophic processes. The verification of the geostrophic approximation in the Gulf Stream, performed by Johns, Watts and Rossby (1989), shows that the largest deviations from geostrophy are associated with high frequency meandering processes, and are found close to the surface. Therefore ageostrophic phenomena do not seem to be responsible for the discrepancies observed at depths. Another aspect that might affect the model response at depth is the lack of topographic relief. In the area around 40-41°N, 55°W, no significant bathymetric variation is present, so that this factor may or may not be a crucial one. Can topography at some distance from this site play a role? Probably. A final aspect is the model stratification, namely the vertical resolution and the discretization of the vertical density profile. Several experimental studies (see, for example, Davis, 1975; Richman, Wunsch and Hogg, 1977; Owens, 1985) have shown that the vertical structure of the mesoscale variability can be described in

terms of a few vertical modes, so that also the model vertical resolution does not seem to be a major issue.

3) **The mean potential vorticity fields.** The basic state potential vorticity distributions in the model subsurface layers affect the vertical profile of the time dependent motion. If, for example, the potential vorticity fields are dominated by the planetary term $(f_0 + \beta y)$, the assimilated eddies will be seen, by the model, as the surface signature of Rossby waves. The resulting vertical structure will be either oscillatory or exponentially decaying, depending on the frequency-wavenumber relationship of the surface signal. If, on the other hand, the basic state potential vorticity in the subsurface layers has very weak horizontal gradients, the vertical profile of a surface disturbance can be expected to be equivalent barotropic, with almost vertical phase lines. We will show this explicitly below. In this case the eddy amplitude decreases exponentially with depth, with an e-folding scale given by the ratio between the first Rossby deformation radius and the horizontal eddy length scale.

The current meter time series shown in Fig. 6.8 show a decreasing amplitude with depth, but no significant phase shift in time. The phase lines are almost vertical. This evidence of an equivalent barotropic character in the observations is consistent with having weak gradients in the mean potential vorticity fields. The current meter measurements in Fig. 6.8 were recorded at a location in the Gulf Stream where the eddy field is most intense. Therefore the possibility of a "well mixed" potential vorticity distribution appears plausible, at least on the basis of the potential vorticity dynamics observed in quasi-geostrophic models.

If the basic state potential vorticity is uniform and if dissipative processes represent a second order effect, conservation of potential vorticity implies that

potential vorticity anomalies are conserved following the water particles. Formally

$$\frac{dq'}{dt} = \frac{\partial q'}{\partial t} + J(\psi, q') = 0 \qquad (6.4.2.1)$$

where both the potential vorticity q and the streamfunction ψ have been decomposed into a time average part and a perturbation part according to the notation

$$q = \bar{q} + q' \qquad (6.4.2.2a)$$

$$\psi = \bar{\psi} + \psi' \qquad (6.4.2.2b)$$

Here we are considering the case in which $\bar{q}$ is uniform. If we assume a continuous stratification with a constant buoyancy frequency N the quasi-geostrophic perturbation potential vorticity is

$$q' = \frac{\partial^2 \psi'}{\partial x^2} + \frac{\partial^2 \psi'}{\partial y^2} + \frac{f_0^2}{N^2}\frac{\partial^2 \psi'}{\partial z^2} \qquad (6.4.2.3)$$

Suppose that the perturbation streamfunction is a plane wave with wavenumber $K = (\kappa, l)$ and frequency σ, namely

$$\psi' = F(z)e^{i\kappa x + ily - i\sigma t} \qquad (6.4.2.4)$$

where $F(z)$ represents the vertical structure. For a plane wave no self-advection is possible ($J(\psi', q') \sim 0$). If mean flow advection is also negligible ($J(\bar{\psi}, q') \sim 0$), equation (6.4.2.1) implies that q' must be locally constant, $\frac{\partial q'}{\partial t} \sim 0$. In this case the function $F(z)$ must satisfy the equation

$$F_{zz} - \frac{N^2 K^2}{f_0^2} F = 0 \qquad (6.4.2.5)$$

where the subscripts indicate double differentiation. In the assimilation context the surface amplitude of our plane wave solution can be considered as assigned. At the surface ($z = 0$) we have

$$\psi'(x, y, 0, t) = \psi'_{obs} = \psi_0 e^{i\kappa x + ily - i\sigma t} \qquad (6.4.2.6)$$

Therefore the boundary conditions for equation (6.4.2.5) in the case of a flat-bottomed ocean of depth D are:

$$F = \psi_0 \qquad \text{at} \quad z = 0 \tag{6.4.2.7a}$$

$$F_z = 0 \qquad \text{at} \quad z = -D \tag{6.4.2.7a}$$

The perturbation streamfunction solution is:

$$\psi' = \frac{\psi_0}{\cosh \lambda D} \cosh \lambda (z - D) e^{i\kappa x + ily - i\sigma t} \tag{6.4.2.8}$$

where

$$\lambda D = \frac{ND}{f_0} K \tag{6.4.2.9}$$

The amplitude of the perturbation streamfunction decreases exponentially with depth. The rate of vertical decay is determined by the quantity λD, which represents the ratio between the first Rossby deformation radius $L_R = \frac{ND}{f_0}$ and the horizontal scale of motion. The vertical profile does not depend on the frequency σ. Notice that a small Rossby deformation radius, corresponding to a weak stratification, allows a deeper vertical penetration. A typical value for the buoyancy frequency is $N \sim 10^{-3}\text{s}^{-1}$. Assuming $D \sim 5000\text{m}$ and $f_0 \sim 10^{-4}\text{s}^{-1}$ L_R will be approximately 50km (the Rossby deformation radius of the first baroclinic mode in the model is approximately 47 km). Given this value for the Rossby deformation radius the decay of the current meter velocities with depth that is observed in Fig. 6.8 is consistent with horizontal length scales of approximately 100 - 200km, which are reasonable values.

Consider now the case in which the basic state potential vorticity distribution is dominated by the planetary vorticity gradients. In this case a plane wave of the form given in (6.4.2.4) satisfies the equation (Pedlosky, 1979):

$$F_{zz} - \tilde{\lambda}^2 F = 0 \tag{6.4.2.10}$$

where

$$\tilde{\lambda}^2 = \frac{N^2}{f_0^2}\left(K^2 + \frac{\beta}{c}\right) \qquad (6.4.2.11)$$

c is the wave zonal phase speed, $c = \frac{\sigma}{\kappa}$. If $\tilde{\lambda}^2$ is positive the vertical structure will be exponentially decaying with depth, with an e-folding scale which is, in this case, frequency dependent. If, in particular, the phase speed is positive, the vertical decay rate is larger than in (6.4.2.8). If, on the other hand, $\tilde{\lambda}^2$ is negative, $F(z)$ will have an oscillatory behavior. The solution that satisfies the same boundary conditions (6.4.2.7) is, in this case:

$$\psi' = \frac{\psi_0}{\cos\tilde{\lambda}D}\cos\tilde{\lambda}(z-D)e^{i\kappa x + ily - i\sigma t} \qquad (6.4.2.12)$$

In our assimilation results the potential vorticity fields in layers 2 and 3 show areas in which the potential vorticity contours have been eroded by the turbulent eddy field, especially in the Gulf Stream and southern recirculation. In layers 4 and 5, on the other hand, the mean potential vorticity contours are dominated by the βy-term in a large part of the domain. At these depths the eddy field appears to be too weak to efficiently mix the potential vorticity. We will see in the next section, in fact, that the eddy kinetic energy level is generally underestimated in the deep model layers.

A possible interpretation of the time series comparison described in the previous section is that the assimilated eddy field is energetic enough, in the upper model layers, to effectively alter the mean potential vorticity distributions, in some areas. The corresponding vertical profile of the instantaneous surface signals will be equivalent barotropic, in agreement with the current meter measurements. In the two deeper layers, on the contrary, where the potential vorticity fields remain dominated by the planetary vorticity gradients, the eddy signals will disperse as Rossby waves, thus explaining the loss of coherence with the deep current meter data. In other words, eddies will effectively penetrate only to a depth at which

their associated currents are strong enough to mix the potential vorticity. Another possible reason for the loss of coherence in the deep ocean may be associated with the presence of eddy motion created by the model instabilities, motion that would not necessarily be correlated with the assimilated eddy field. Due to the strong nudging, this time dependent motion can only develop away from the surface where the restoring to the Geosat maps would damp any signal different from the data. The extent to which this mechanism is acting during the assimilation experiments and can represent a source of eddy motion in the deep ocean needs to be investigated in future studies.

If the surface data contain signals that appear to propagate eastward, because of aliasing problems, they can be expected to decay, in the deep ocean, with an e-folding scale given by $\tilde{\lambda}$ in (6.4.2.11). This effect may partially explain the drop in energy level that is observed in the model spectra (dashed line in Fig. 6.10) at periods shorter than 30-50 days, where the altimeter temporal sampling can be expected to be more critical.

6.4.3 Eddy kinetic energy

In Fig. 6.11 we show the eddy kinetic energy distribution obtained from the assimilation experiment. Only layers 1 (top), 3 (middle) and 5 (bottom) are shown for brevity. The eddy kinetic energy distribution in the first layer is very similar to the one derived from the interpolated Geosat data, shown in Fig. 2.10a. Maximum values are achieved along the mean Gulf Stream path. The eddy kinetic energy decreases away from the Stream to values of approximately $100 cm^2 s^{-2}$, which are found both in the gyre interior and in the area of the continental shelf, north of the Stream. The maximum values in Fig. 6.11 tend to be lower than the ones in Fig. 2.10a. The absolute maximum is observed around 65°W in both cases, but in Fig.

6.11 it is only $1500cm^2s^{-2}$ instead of $2000cm^2s^{-2}$, as observed in Fig. 2.10a. This effect is very likely caused by some degree of damping associated with the nudging term or with the other frictional terms present in the model.

In layer 3 (nominal depth 1125 m) maximum values are about $100cm^2s^{-2}$. Also in this case they occur following the mean Gulf Stream path. At this depth, however, the energy level appears to decay more slowly on either side of the maximum. In layer 5, only isolated maxima, of about $100cm^2s^{-2}$, can be observed within a large pool of almost uniform eddy kinetic energy, with values around $50cm^2s^{-2}$. The eddy kinetic energy appears to decay very slowly toward the border of the domain.

How do these results compare with observations? Several authors (Richardson, 1983; Schmitz, 1984) have observed and discussed the kinematical and dynamical links between the eddy kinetic energy distribution and the characteristics of the mean circulation. The observed eddy kinetic energy pattern shows a maximum near the Gulf Stream at all vertical levels. According to Schmitz (1984) the eddy kinetic energy decreases more abruptly into the gyre interior with increasing depth. In the map of surface eddy kinetic energy constructed by Richardson (1983b), and reproduced in Fig. 2.10b, the ratio between the Gulf Stream and the interior values is about 10. In the deep ocean, on the other hand, the eddy kinetic energy falls off from the Gulf Stream to the interior by two orders of magnitude, ranging from values around $100cm^2s^{-2}$ in the proximity of the Gulf Stream to values of only $1cm^2s^{-2}$ in the interior (Schmitz, 1984). An estimate of abyssal eddy kinetic energy, computed by Schmitz (1984), is reproduced in Fig. 6.12. This map was constructed by using measurements recorded at depths much below the main thermocline, typically around 4000m. Therefore the distribution in

Fig. 6.12 should be compared with the assimilation results in the model layer 5, whose middle depth is 3900m.

The comparison between the eddy kinetic energy distribution in the model upper layer (Fig. 6.11 (top)) with the surface eddy kinetic energy from the drifter data (Fig. 2.10b) shows a very similar pattern, but reduced maximum values in the assimilation results. The lower energy level observed in Fig. 6.11 can be partially attributed to the characteristics of the assimilated eddy maps. As discussed in section 2.5, the interpolation procedure used to construct the eddy maps smooths the sea surface height gradients and thus determines a reduction of the geostrophic eddy velocities. Some degree of damping associated with the nudging procedure might be responsible for a further reduction of the upper layer eddy kinetic energy in the assimilation results.

The eddy kinetic energy observed in the fifth model layer (Fig. 6.11(bottom)) has maximum values generally lower than in Fig. 6.12. Values of $100 cm^2 s^{-2}$ are found, in the model, as isolated patches, in contrast with the more extensive tongue of $100 cm^2 s^{-2}$ that is observed in Schmitz's map (Fig. 6.12). Moreover, the general eddy kinetic energy pattern in the model deepest layer does not show the abrupt decay from Gulf Stream values to interior values that appears in Schmitz's estimate. In the model the abyssal eddy kinetic energy tends to remain much more constant than in the data.

A more direct comparison between observations and assimilation results, at 55°W, is shown in Fig. 6.13. Meridional sections of eddy kinetic energy, computed by Owens (1991) from float data at 700 and 2000m, are compared with similar sections from the model. The dashed line indicates the model results, while the dots joined by the thin solid line represent the observational estimates. At both depths the peak values are smaller in the model than in the data. At 700m the

maximum eddy kinetic energy in the the assimilation results is about $370cm^2s^{-2}$, approximately 18% smaller than the observed maximum value of about $450cm^2s^{-2}$. Both the dashed curve and the solid curve peak around 39°N, and decay in a similar fashion toward the north. South of the maximum, on the other hand, the model result decreases much faster than the observed one. At 2000m the maximum eddy kinetic energy in the model is about $50cm^2s^{-2}$, which is 60% smaller than the observed maximum value of $150cm^2s^{-2}$. The energy level in the model is almost flat over the whole range of latitudes considered, while the observations show a relatively rapid decrease on either sides of the maximum.

The comparison at 700m is very similar, with a proper scaling, to the comparison in Fig. 2.13, where a meridional section of surface eddy kinetic energy from the drifter data is plotted together with an analogous section from the interpolated Geosat data. Therefore the discrepancies observed in Fig. 6.13 at 700m appear to be mainly associated with the characteristics of the surface data that have been assimilated. At depths, on the other hand, the large pool of almost constant eddy kinetic energy, which is in partial disagreement with the observations both at 2000 and 4000m, is probably associated with the model tendency to develop basin modes, as discussed in Chapter 4.

6.4.4 Discussion

The analysis presented in this section has shown that assimilation of surface eddy information can produce an eddy field with some realistic characteristics in the three upper model layers. In fact, time series of geostrophic velocities from the assimilation results are coherent with current meter measurements recorded at the same geographical location during the same period of time, in the frequency band in which the assimilated data are coherent, down to approximately 1500m

depth. A factor that seems to be very important in determining the vertical profile of the eddies is the horizontal distribution of potential vorticity in the different model layers. The eddy signals penetrate, as equivalent barotropic signals, down to a depth at which their currents are strong enough to efficiently mix the potential vorticity. In this range of depths the model time series appear to be coherent with the current meter time series. At greater depths, where the eddy field is too weak to erode the planetary vorticity gradients, the equivalent barotropic eddies will disperse as Rossby waves, leading to the observed loss of coherence with the deep current meter measurements. A fraction of the energy contained in the deep Rossby wave field appears to excite some of the model basin modes, thus producing, in the deep model layers, an eddy kinetic energy distribution that is slowly varying over scales comparable with the model domain.

Why is the eddy field weak in the model deep layers? Part of the reason can certainly be attributed to the reduced eddy amplitude in the assimilated data, as a consequence of the smoothing associated with the interpolation procedure. Another factor to be considered, however, is the spectral characterisics of the surface data. Incorrect frequency-wavenumber relationships in the surface data, due to aliasing problems, can give rise to an eddy field with an erroneous vertical structure in the assimilation results. An extreme case is represented by the surface signals that are aliased into eastward propagating disturbances. Such signals decay exponentially in the vertical and, therefore, they might be able to penetrate only to a limited depth.

6.5 Conclusions

In this chapter we have tried to assess how much closer to reality the model behavior becomes, when surface data are assimilated. To this end we have considered aspects of the mean circulation as well as characteristics of the eddy field.

Since the mean component of the surface data is a long term climatological mean, the representation of the mean circulation that we have adopted is the one derived from an Eulerian time average. The comparison between meridional profiles of mean zonal velocities computed from observations and similar profiles derived from the assimilation results shows a relatively good agreement in the position of both the Gulf Stream and the southern recirculation. The amplitude of the zonal velocity in the Gulf Stream is often underestimated, especially in the upper ocean, where the surface data constraint is most effective. The westward flow associated with the southern recirculation, on the other hand, has amplitudes remarkably similar to the observed ones, at almost all depths. This westward flow was not present in the climatological fields that have been used as initial conditions in layers 2 and 3. It appears to be an eddy driven feature.

The transport carried in the model southern recirculation at 55°W is very similar to the value estimated by Richardson (1985) when the bias in the deep measurements due to topographic effects is removed from the data. However, the overall transport pattern in the model does not capture the observed increase east of 70°W. At 55°W the top-to-bottom Eulerian transport obtained from the assimilation results is about 16% smaller than the one estimated by Richardson (1985) at the same longitude. This discrepancy can be attributed to the lack of a proper representation of the northern recirculation gyre. The latter is, in fact, missing from the surface climatological field that is assimilated. At depths, an eddy-driven westward flow develops north of the Stream, at approximately the correct latitude for the northern recirculation flow. However, the meridional extent of this westward flow appears too limited and its intensity too weak to produce a transport comparable with the observed.

The analysis of the eddy field in the assimilation results indicates the potential, for the assimilation procedure, to produce a realistic time dependent motion in the model subsurface layers. Comparison with in situ data measured during the same period of time shows, in fact, a relatively good agreement. A coherence above the significance level is obtained down to about 1500m depth, in a frequency band that is established by the spectral characteristics of the surface data. At periods longer than approximately 30 days, the model spectra are within the confidence interval from the current meter spectra at all depths. The eddy kinetic energy appears to be underestimated in the model results. This can partially be explained with the reduced energy level in the interpolated Geosat data that are assimilated, especially at high wavenumbers.

The main conclusion that can be drawn from the comparisons we have described is that nudging of a model with altimeter data appears to be a very promising tool for driving ocean models toward a more realistic behavior. This includes climatological aspects as well as aspects related to the time evolution of the model fields. We have seen that the imposition of a surface data constraint can radically alter the global model behavior. The deficiencies that we have detected in the assimilation results can be mainly attributed to limitations present in the data that have been used, in particular the mean climatological component. Most of the characteristics of the mean model circulation that appear in disagreement with the observations (width and intensity of the eastward flowing jet, limited development of the northern recirculation gyre, etc.) can in fact be attributed to inadequacies in this component. Further improvements in the assimilation results thus require a more adequate surface mean field. Future work must include the analysis of the performance of different mean fields, as well as the investigation of techniques that allow the assimilation of only the eddy component of the data. In the present analysis we have also identified a model limitation, the inadequate treatment of

the open boundary conditions; this limitation can be improved by implementing radiation boundary conditions at all the open boundaries. Some of the deficiencies in the present results may also be due to inadequacies in the quasi-geostrophic approximation. The extent to which this is true needs to be verified in the future by considering additional experiments with primitive equation models.

Table 6.1 Summary of the measured transport in the Gulf Stream, Northern Countercurrent and Southern Countercurrent along 55°W as given by Richardson (1985). The units are $10^3 m^2/s$ for the transport per unit depth, and $10^6 m^3/s$ for the surface to bottom values.

Depth	Northern Countercurrent	Gulf Stream	Southern Countercurrent
Surface	0±4	122±13	0±5
700m	7±4	28±8	7±4
2000m	9±2	8±3	5±2
4000m	9±2	7±1	12±1
Surface-Bottom	41±8	93±11	42±6

Table 6.2 Summary of the estimated transport in the Gulf Stream, Northern Countercurrent and Southern Countercurrent along 55°W from the assimilation results. The units are $10^3 m^2/s$ for the transport per unit depth, and $10^6 m^3/s$ for the surface to bottom values.

Depth	Northern Countercurrent	Gulf Stream	Southern Countercurrent
150m	1	84	0
525m	1	50	4
1125m	2	19	9
2150m	2	3	8
3900m	4	4	7
Surface-Bottom	15	78	31

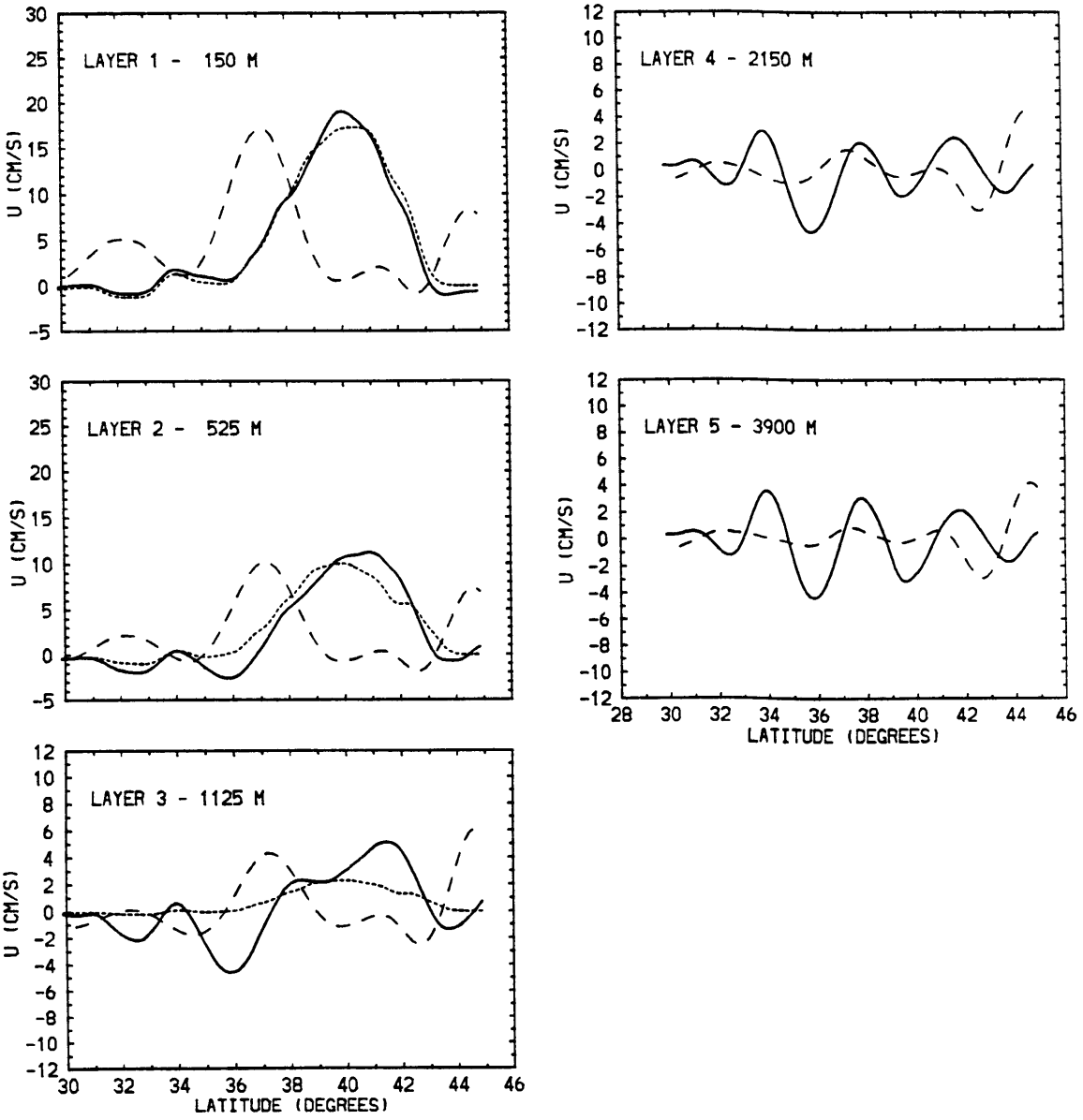

Fig. 6.1 Meridional profiles of mean zonal velocities around 55°W in the 5 model layers. The dashed line corresponds to the results from the numerical experiment in which no data are assimilated. The solid line corresponds to the assimilation experiment in which the total upper layer streamfunction field is assimilated. The profiles derived from the Bauer-Robinson climatology are also shown in layers 1, 2 and 3 (dotted line).

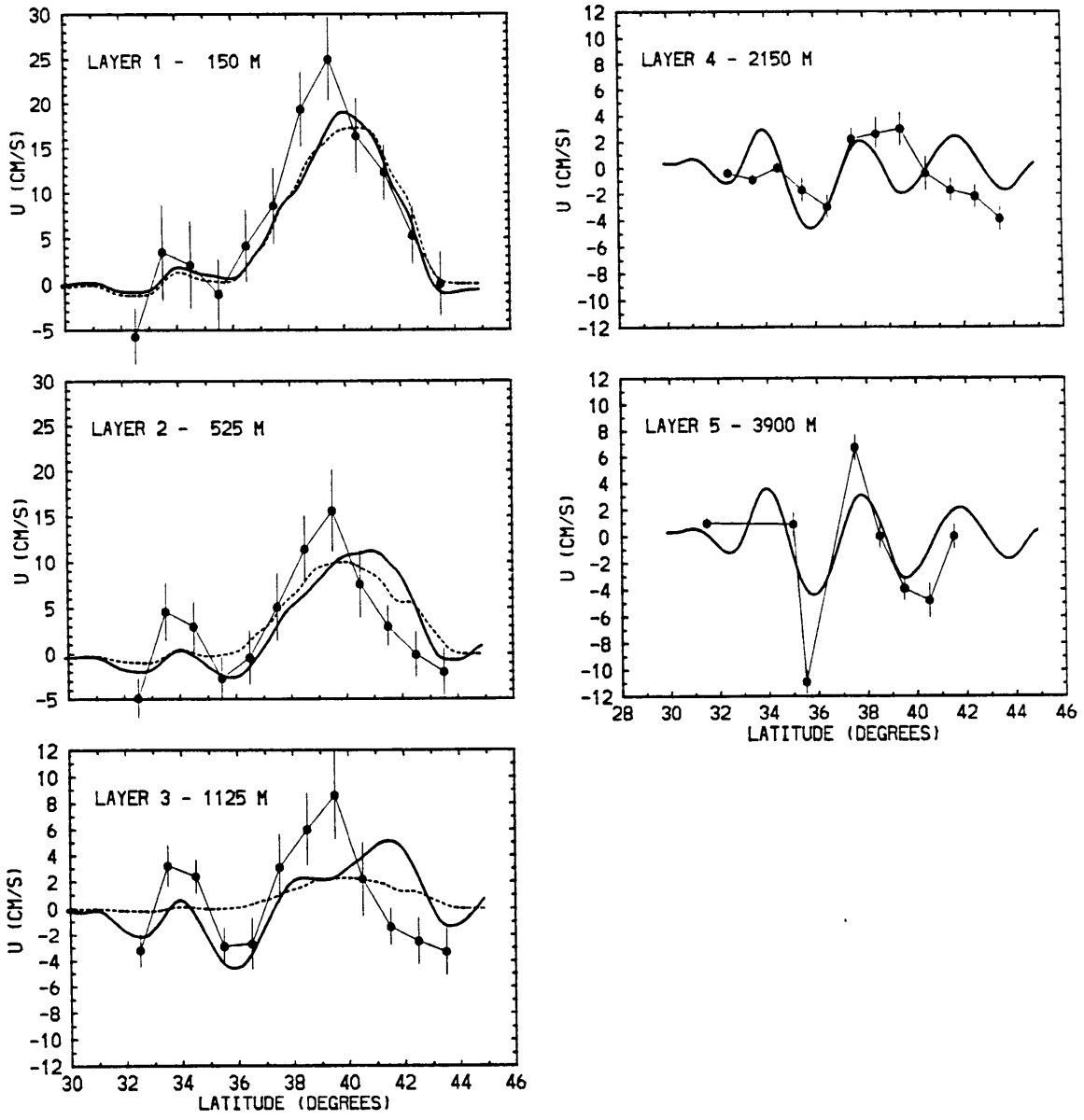

Fig. 6.2 Comparison between the meridional profiles of mean zonal velocities around 55°W from the assimilation results (thick solid line) and Richardson's estimates (dots connected by the thin solid line). In layers 1, 2 and 3 the values supplied by Richardson (1985) at the surface, 700m, and 2000m have been interpolated linearly to the layer depths. The model estimates in layers 4 and 5 have been compared directly with the float values at 2000m and the POLYMODE array II current meter data at 4000m. The vertical bars indicate the standard errors of the mean. In layers 1, 2 and 3 the profiles from the climatological fields are also shown for reference (dotted line).

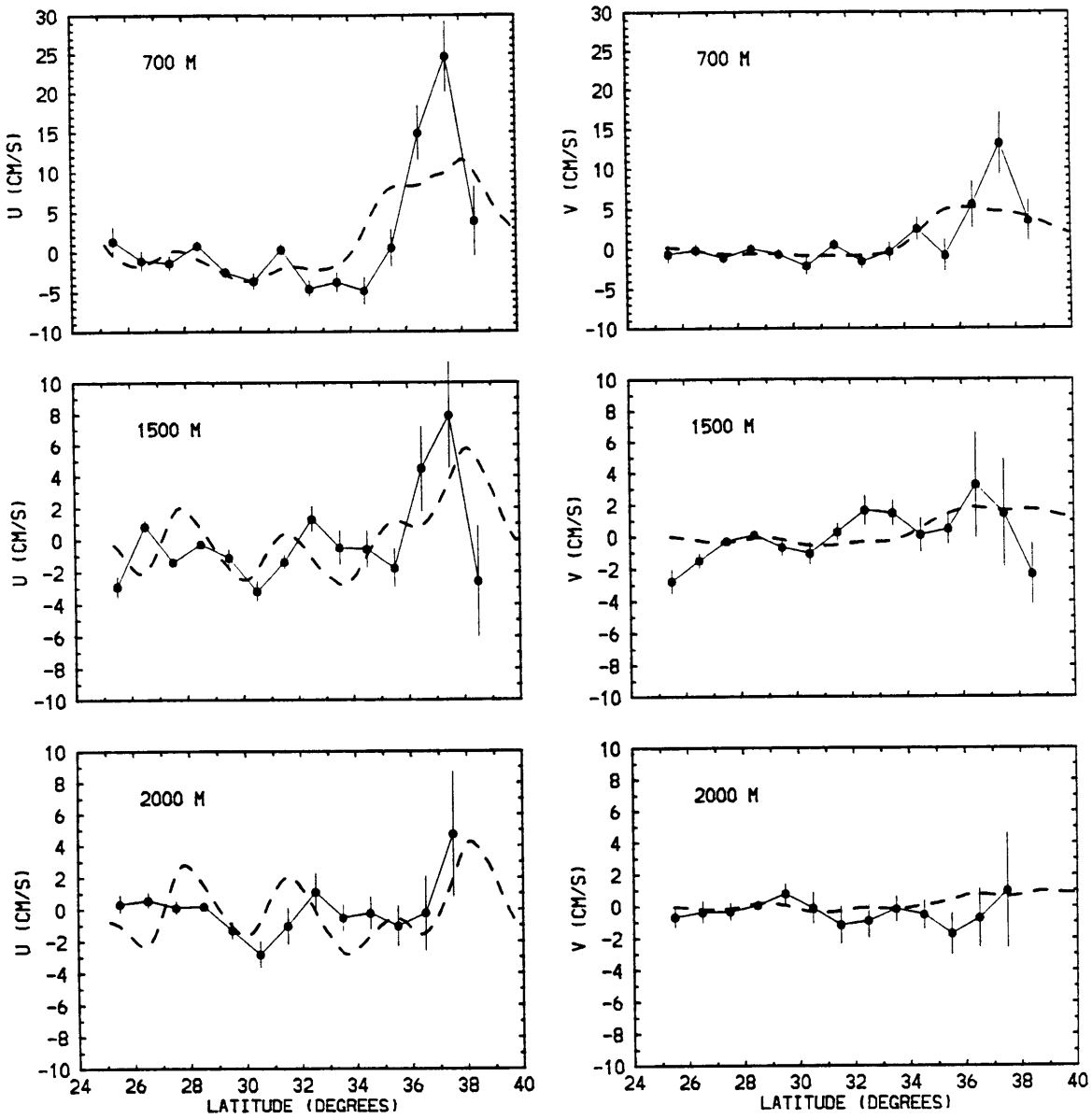

Fig. 6.3 Comparison between the meridional profiles of velocity components around 70°W from the assimilation results (dashed line) and estimates computed by Owens (1991) from SOFAR float data (dots connected by the thin solid line). The left panels show the zonal velocities at 700 (top), 1500 (center) and 2000m (bottom). The right panels show the meridional velocities at the same depths. Vertical bars indicate the standard error of the mean.

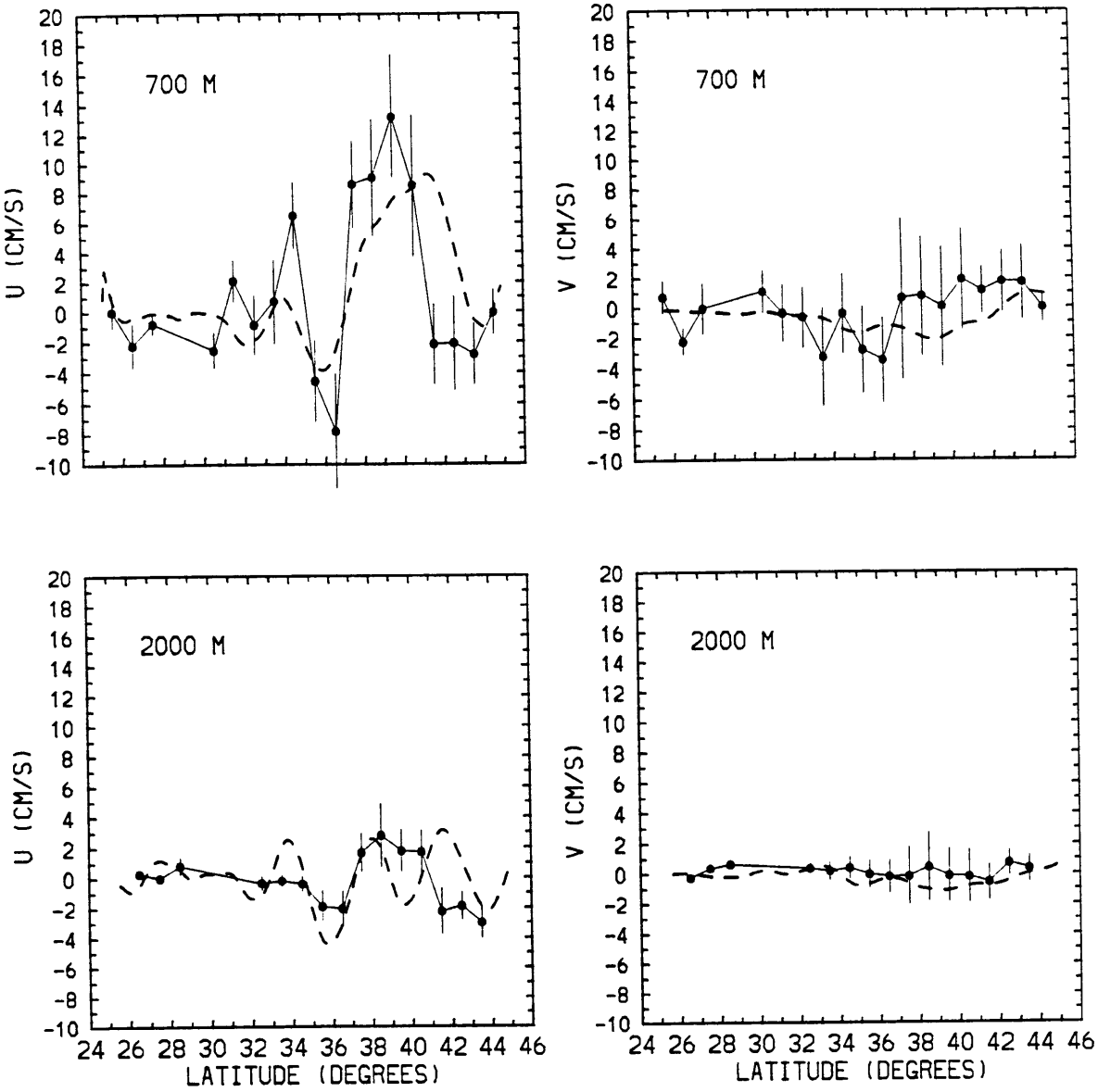

Fig. 6.4 Comparison between the meridional profiles of velocity components around 55°W from the assimilation results (dashed line) and estimates computed by Owens (1991) from SOFAR float data (dots connected by the thin solid line). The left panels show the zonal velocities at 700 (top) and 2000m (bottom). The right panels show the meridional velocities at the same depths. Vertical bars indicate the standard error of the mean.

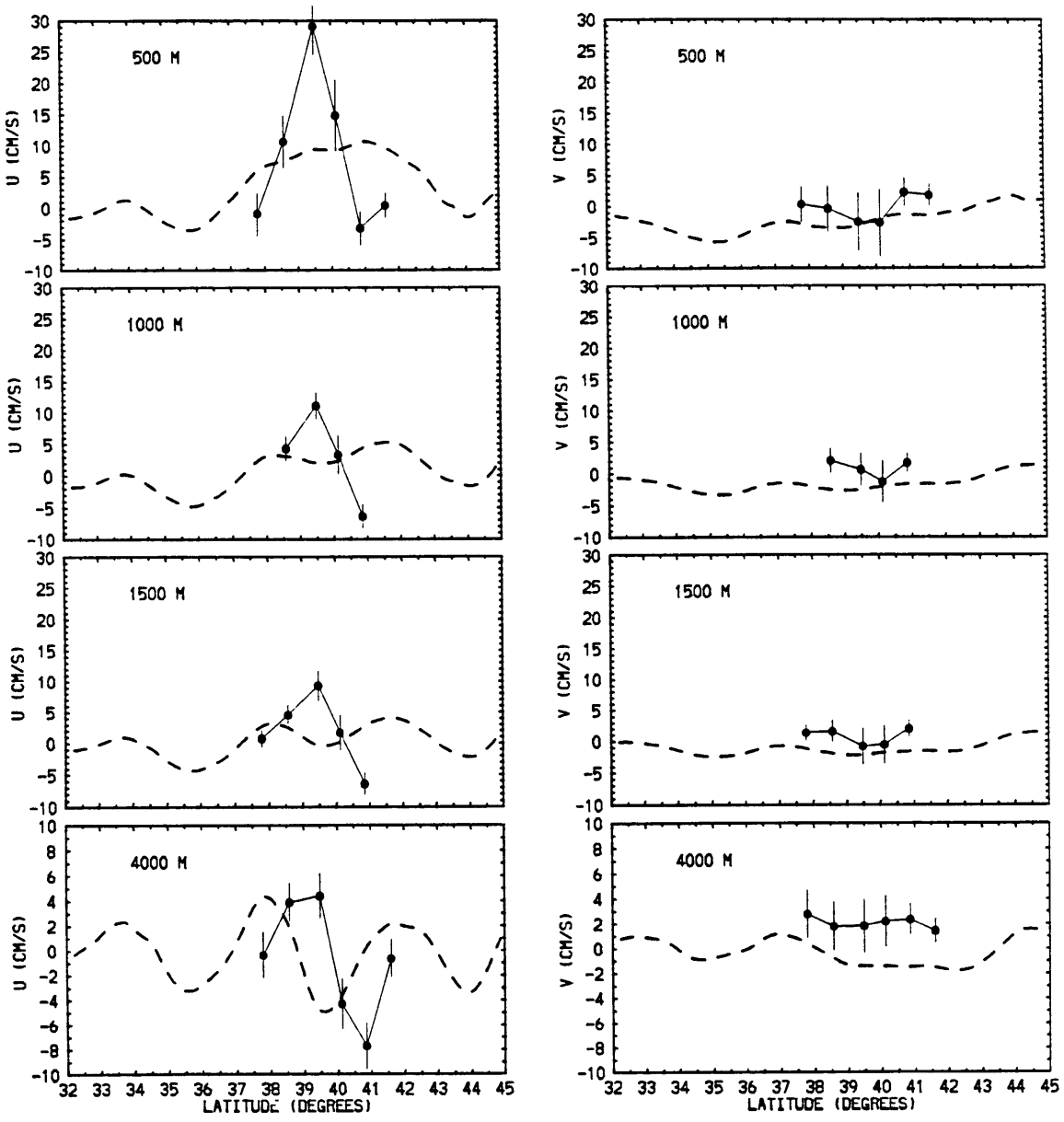

Fig. 6.5 Comparison between the meridional profiles of velocity components around 55°W from the assimilation results (dashed line) and estimates computed from the current meter measurements at the SYNOP east array (dots connected by the thin solid line). Vertical bars indicate the standard error of the mean.

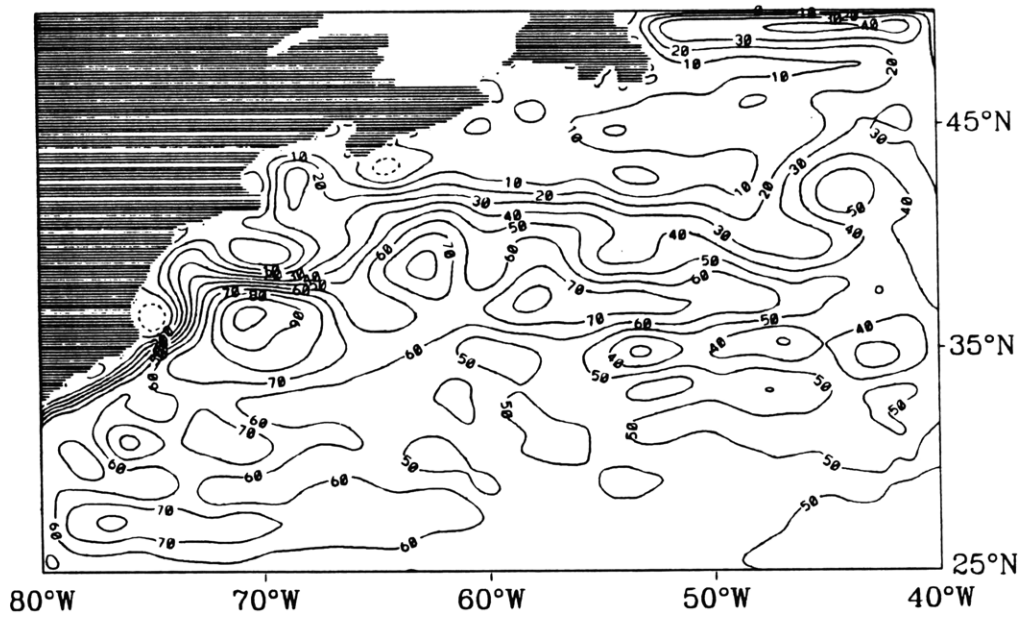

Fig. 6.6 Horizontal distribution of the model time average barotropic streamfunction $\psi_B = \sum_{i=1}^{i=5} H_i \psi_i$. Contour interval is $10 \times 10^6 \mathrm{m}^3\mathrm{s}^{-1}$ (10 Sv).

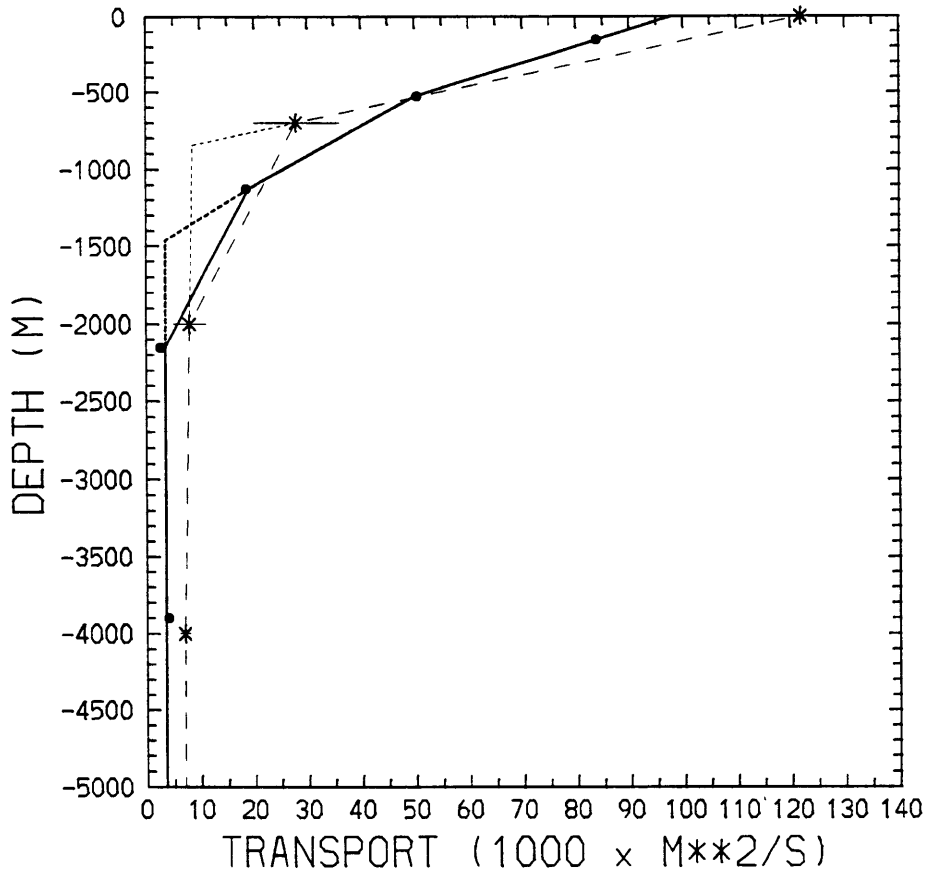

Fig. 6.7 Vertical profile of mean zonal transport around 55°W. The dots represent the transport per unit depth in the five model layers. The asterisks represent estimates computed by Richardson (1985). The total surface-to-bottom transport obtained in the model by using linear interpolation (thick solid line) is about 82Sv. If two straight lines are used between the second and fourth model layers (thick dotted line) the transport estimate is about 75Sv. Richardson estimated a total surface-to-bottom transport of 99Sv by using linear interpolation (thin dashed line) and 88Sv by using two straight lines (thin dotted line). The best estimate, obtained by using a smooth curve between 700 and 2000m (not shown) was 93Sv.

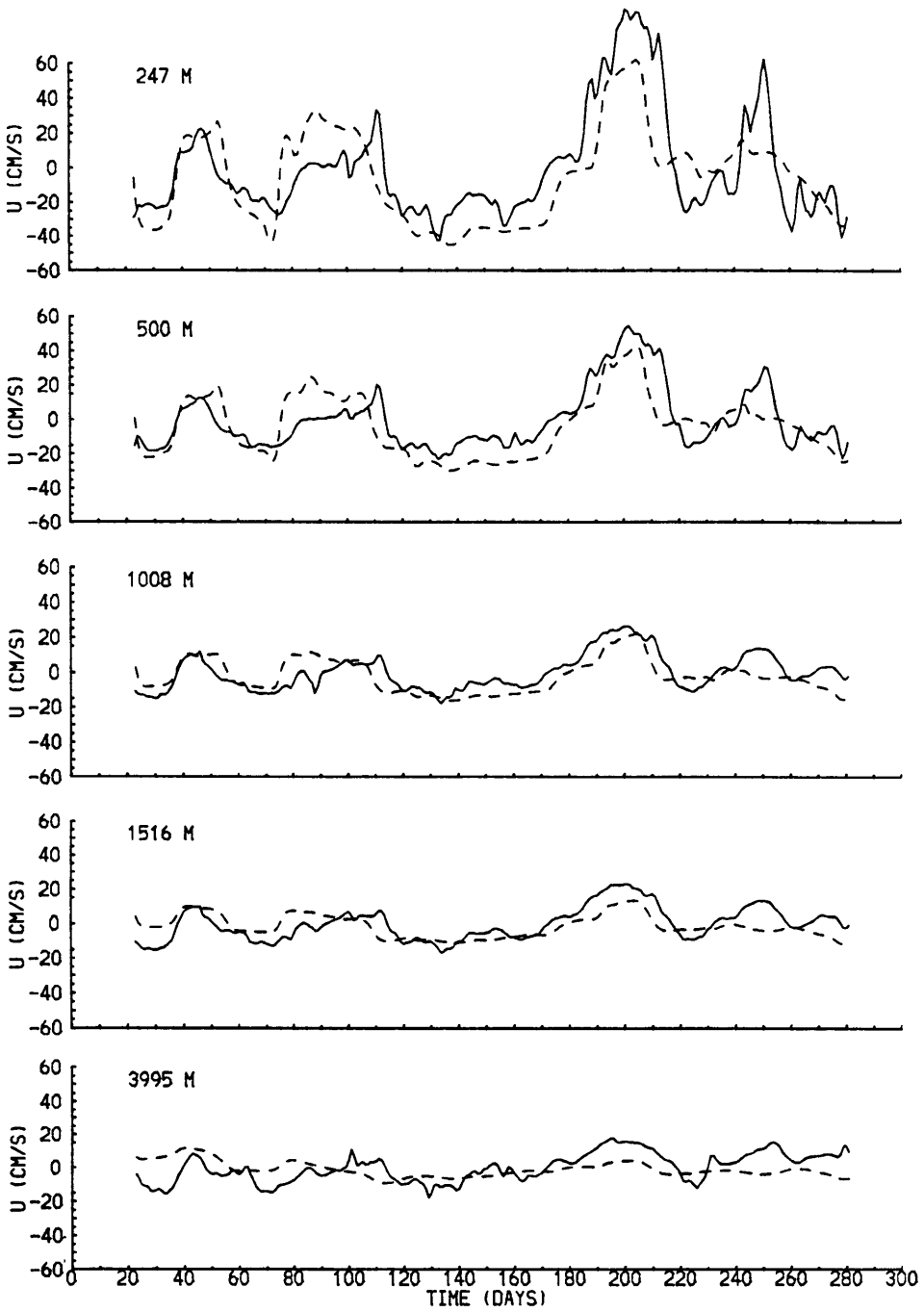

Fig. 6.8a Comparison between zonal velocity time series measured at 54.67°W, 40.86°N (solid line) and geostrophic zonal velocity time series derived from the assimilation results (dashed line) as a function of depth. The time average velocity has been subtracted from all time series. Day 0 in abscissa corresponds to 1 September 1987. The current meter measurements started on 23 September 1987. The model results have been interpolated linearly to the current meter depths.

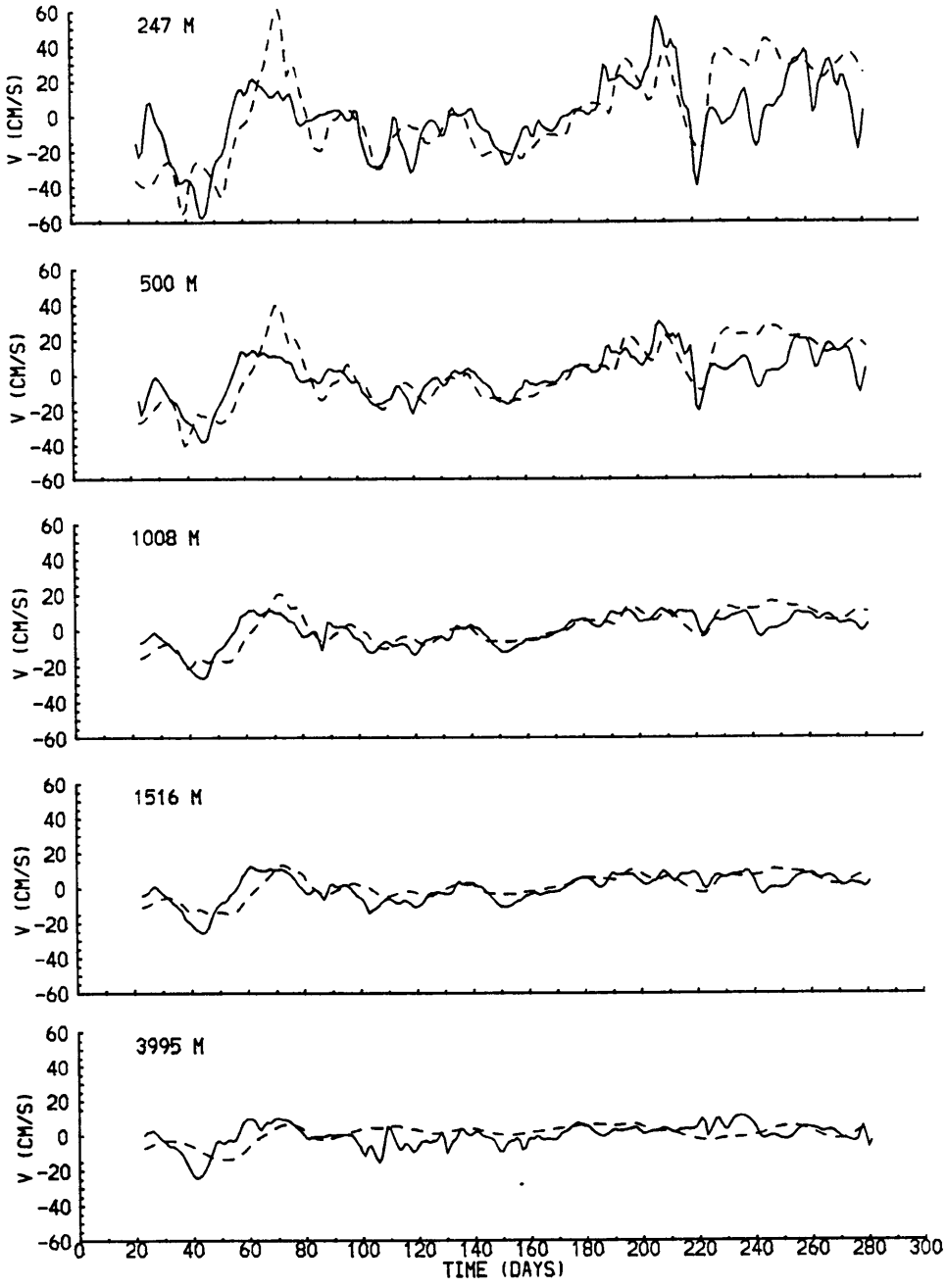

Fig. 6.8b As in Fig. 6.8a but for the meridional eddy velocity component.

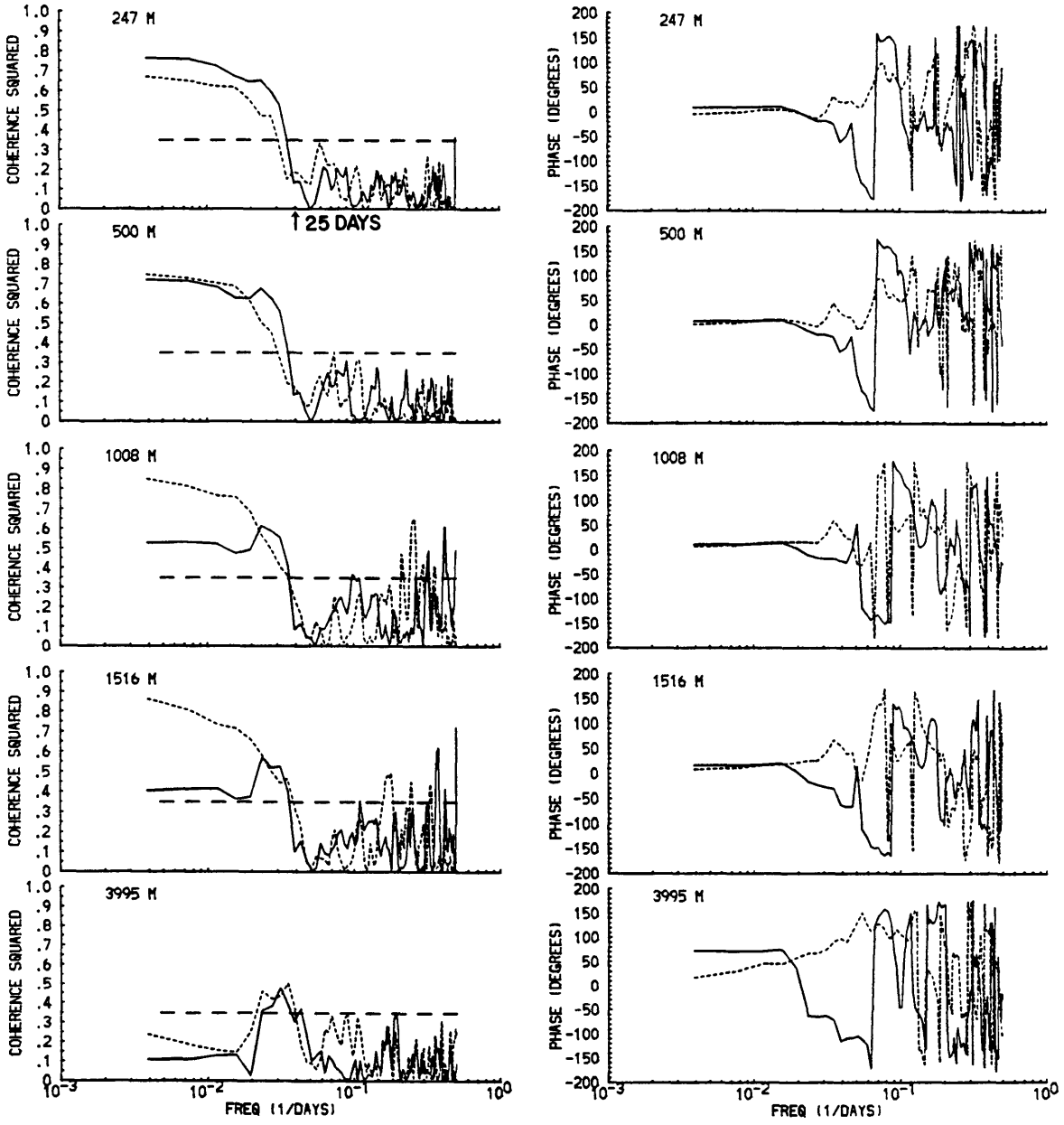

Fig. 6.9 The left panels show the coherence between eddy velocity time series measured by current meters at 54.67°W, 40.86°N and geostrophic eddy velocities computed from the assimilation results at the same location, as a function of depth. The solid line indicates the zonal velocity, the dotted line the meridional velocity. The long dashed line represents the significance level. The right panels show the corresponding phases as a function of depth.

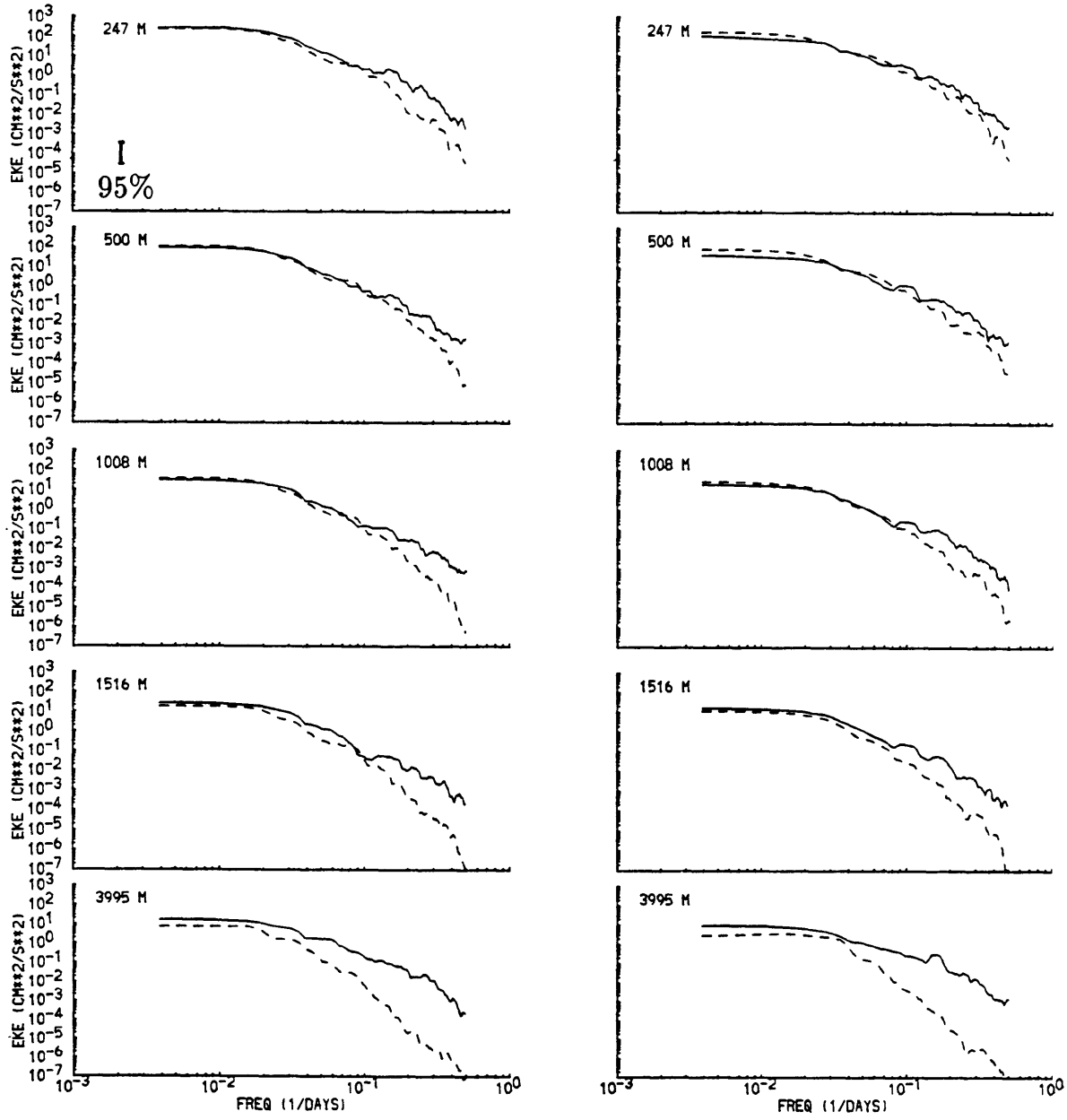

Fig. 6.10 Frequency spectra computed from the time series shown in Fig. 6.8. Left panels show spectra of zonal velocities, right panels spectra of meridional velocities. The solid line indicates the spectra from the current meter time series, while the dashed line refers to the spectra from the assimilation results. The 95% confidence interval is shown in the figure.

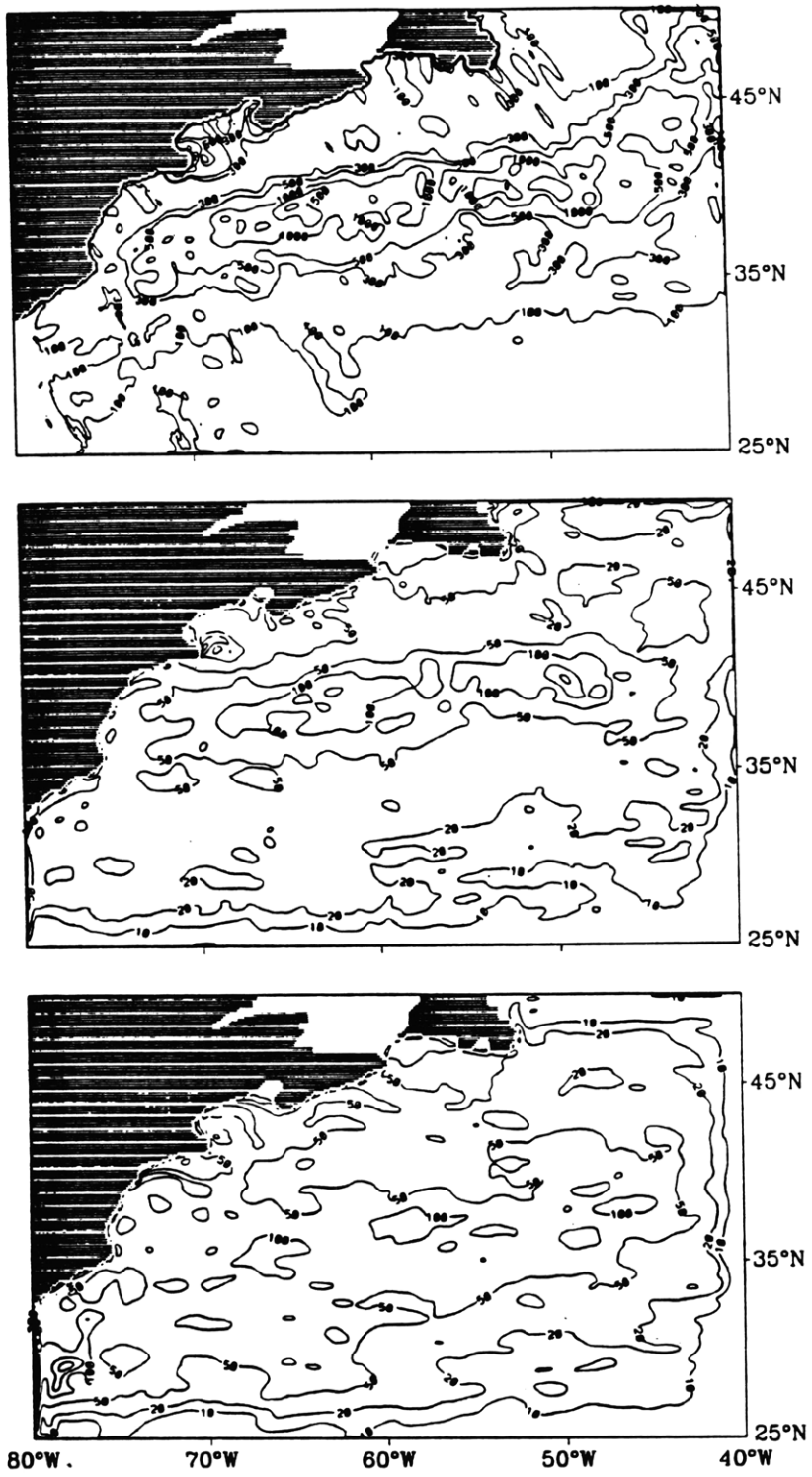

Fig. 6.11 Eddy kinetic energy distribution in model layers 1 (top), 3 (middle) and 5 (bottom) resulting from the assimilation experiment. Units are cm^2/s^2.

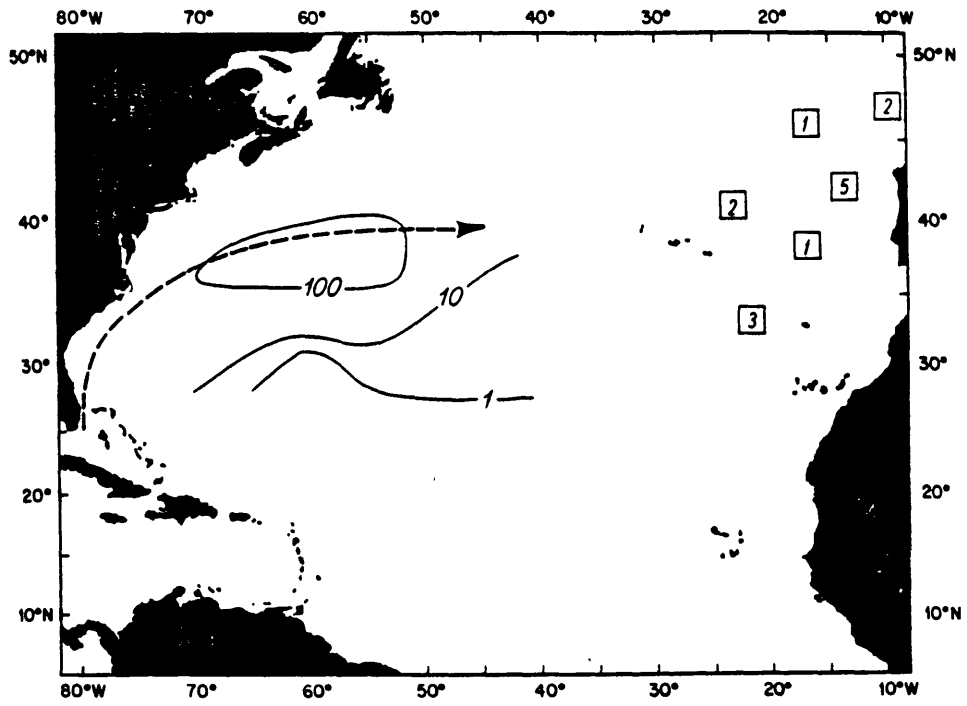

Fig. 6.12 Distribution of abyssal eddy kinetic energy (in cm^2/s^2) computed by Schmitz (1984) from current meter measurements much below the main thermocline, typically at 4000m depth. The heavy dashed line is the locus of maximum kinetic energy for the surface layer mean flow, as estimated by Wyrtky et al. (1976)

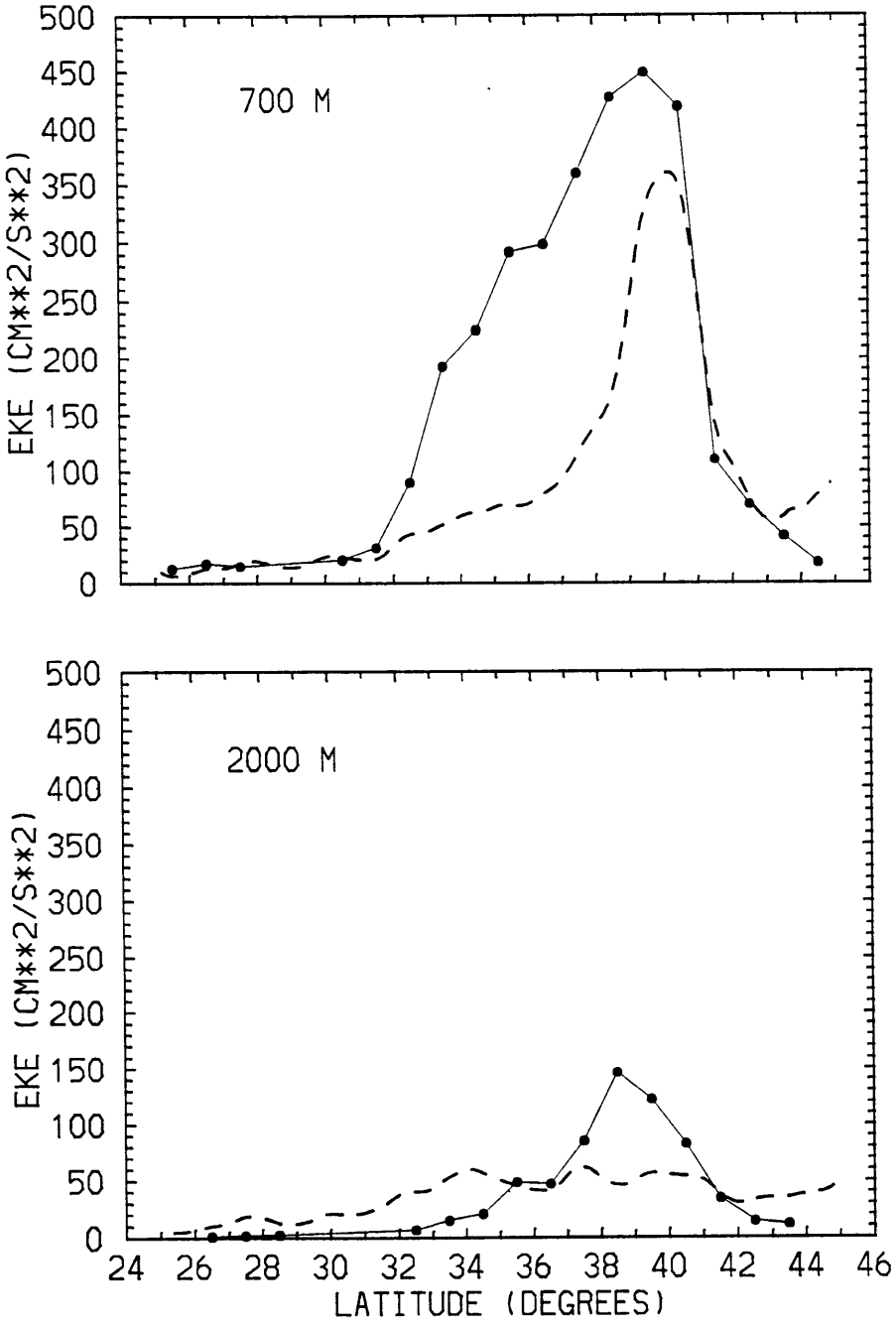

Fig. 6.13 Comparison of meridional profiles of eddy kinetic energy at 55°W. The dashed line indicates the profiles derived from the model, the dots connected by the thin solid line are estimates computed by Owens (1991) from float data at 700 and 2000m.

Chapter 7

Conclusions

Data sets that cover a large area over synoptic time scales have become available since the advent of the satellite missions. These data sets offer oceanographers the possibility of effectively constraining numerical models of the ocean circulation. Although numerical models have proved very useful for analyzing some of the physical processes occurring in the ocean, they still show limitations in accurately reproducing basic climatological aspects of the ocean circulation. Data assimilation can thus be a very powerful tool for improving the model realism. The optimal way of combining data with model predictions has been known, from a theoretical viewpoint, for a long time and it has led to the development of algorithms such as the Kalman filter and the Kalman smoother. However, the practical implementation of these optimal methods presents several problems. They include both a computational load which is presently unaffordable when considering data assimilation in large scale high resolution models, and also the need to supply a priori information about the model error which is not readily known.

Because of these reasons one needs to consider the feasibility of suboptimal methods. The nudging technique is one of the most popular, due to its easy implementation and very low computational costs. Nudging has already been used in several studies of assimilation of altimeter data. Some of these studies have addressed technical issues, such as the performance of different implementations of the method and the dependence of the assimilation results upon the data sampling

characteristics. These studies have therefore been performed in the context of identical twin experiments, in which the assimilated data are model produced, so that the success of the assimilation procedure can be easily verified. Assimilation of real data introduces new issues that cannot be properly accounted for with twin experiments. In particular the differences between some aspects of the model climatology and the observed ocean climatology require a dynamical understanding of the assimilation procedure, in which model and data are blended together. A physical grasp of the assimilation results is necessary in order to identify the reasons for the success or failure of the assimilation procedure. It is also necessary for developing an educated intuition about the best way of implementing the nudging method or other similar suboptimal methods.

In this study we have started addressing these issues by using a QG model of the Gulf Stream region. The data that we have assimilated are maps of sea surface height which have been obtained as the superposition of sea surface height variability deduced from the Geosat altimeter measurements and a mean field constructed from historical hydrographic data. Although these surface maps cannot be expected to be perfectly accurate, they do supply a description of the surface geostrophic circulation which appears closer to reality than the one derived from the model with no assimilation. The path of the mean Gulf Stream, the distribution of the eddy field as well as the eddy space and time scales are some of the climatological features which appear much more realistic in these surface fields than in the model. Therefore the perspective that we have adopted in this study is to consider these data as a "perfect" representation of the surface ocean circulation and impose them as a strong constraint to the model. The goal is then to understand, from a dynamical viewpoint, the effect of this constraint on the global model behavior.

The specific questions that we have asked are: first, "What are the physical mechanisms responsible for the model adjustment and for the final statistical equilibrium when the surface data constraint is imposed to the model?", and second "How much more realistic is the global model behavior when the surface data are assimilated?"

The first question has been addressed in Chapter 5. We have first developed a dynamical framework, with the aid of an analytical example, in order to identify the relevant mechanisms responsible for the model adjustment during the assimilation experiments. In particular we have tried to understand the relative role of the mean and eddy components of the surface data in determining the model evolution and final statistical equilibrium characteristics. Due to the model nonlinearities, the surface mean field that is assimilated alters the geostrophic contours in the model subsurface layers. The resultant pattern of geostrophic contours represents, at first order, the structure of the mean circulation in these layers. The intensity of the flow along the open contours is determined by the boundary values. Inside the closed geostrophic contours, on the other hand, the amplitude of the flow is the result of a balance between forcing and dissipation. The forcing mechanism is supplied by the eddy flux divergence of interface height, corresponding to vertical propagation of horizontal momentum. Therefore, if the eddy field is vanishingly weak, only a very weak flow can develop inside closed geostrophic contours. If, in addition, no inflow/outflow conditions are specified at the open boundaries in some of the subsurface layers, no flow is possible in those layers. From these theoretical considerations we have learned that the surface mean field can constrain the flow structure in the subsurface layers. The depth of influence of the surface information is strongly dependent on stratification. The intensity of the flow is determined by eddy forcing, dissipation and boundary conditions.

These theoretical ideas are supported by the results of the assimilation experiments. We have compared the results of two different experiments: in the first one only the surface mean field has been assimilated, while in the second experiment the total surface streamfunction field (mean + eddies) has been used. In the first experiment the eddy field that the model develops as a consequence of instability processes is strongly damped at the surface by the relaxation toward a steady field. The resulting eddy field is therefore very weak. As expected from our theoretical considerations the flow in the two deeper layers, which are not forced with any inflow/outflow at the open boundaries, is also vanishingly weak. The flow pattern in layers 2 and 3 is consistent with our conceptual model, when the climatological mean field that is assimilated is considered. In the second experiment the presence of the eddies in the assimilated surface data does not affect the basic characteristics of the mean circulation pattern in these two intermediate layers. This tells us that the structure of the mean circulation is still controlled, to a large extent, by the geometry of the geostrophic contours associated with the climatological surface mean field. However, the efficient vertical transfer of horizontal momentum achieved by the eddies leads, in this case, to the development of a relatively significant component of the flow in the two deeper layers. The enhancement of the flow in the deep model ocean is communicated to the upper layers, where the mean circulation becomes also more energetic. This barotropic tendency in the eddy induced mean circulation is limited by the constraint imposed on the surface model fields, whose amplitude is bound to remain close to the data.

Another difference introduced by the presence of an energetic eddy field is associated with the evolution of the potential vorticity fields. If eddies are weak, as in the case of our first experiment, the potential vorticity evolution is controlled, at first order, by the mean flow advection, which establishes constant values of potential vorticity along mean streamlines. Eddy advection represents a second

order effect which determines the erosion of the potential vorticity gradients among adjacent streamlines. This process leads to the development of uniform distributions of potential vorticity inside closed geostrophic contours. If, on the other hand, the eddy field is relatively energetic, so that eddy advection is comparable with mean flow advection, the distribution of the mean potential vorticity contours differs from the mean streamline distribution.

The second question considered in this study, "How much more realistic is the global model behavior when surface data are assimilated?" has been addressed in Chapter 6. We have tried to answer this question by comparing the assimilation results with some available observations. The aspects of the model behavior which we have focused upon are the mean circulation, the eddy kinetic energy level and distribution as well as eddy time scales as a function of depth. The availability of current meter measurements during a period of time partially overlapping the Geosat mission has also allowed a direct comparison of velocity time series as a function of depth. The "mean circulation" that we have adopted for these comparisons is the one computed as an Eulerian time average. Different representations of the Eulerian mean flow, derived from different data sets, have been considered in order to identify the robust features of the mean circulation. Most of the observations are from the area around 55°W. The comparison of meridional profiles of mean velocities along 55°W reveals a striking similarity between the model profiles and the observation profiles at this longitude. The most remarkable aspect that has emerged from this comparison is the model development of eddy driven recirculations on either side of the Stream, at approximately the right positions. The southern recirculation has also the "correct" amplitude at almost all depths, while the northern recirculation is somewhat underestimated. The lack of a northern recirculation in the surface mean field that is assimilated may be in part responsible for the limited development of this feature also in the deep

model layers. The undergoing processes of eddy-mean flow interaction during the assimilation experiment as well as the way they are related to the characteristics of the surface data need to be analyzed in more detail in future studies.

The time series of eddy geostrophic velocities derived from the assimilation results are coherent with the current meter time series at periods longer than about 30 days, down to a depth of approximately 1500m. Coherence is lost in the deep ocean. A definite explanation of this loss of coherence is not readily obtained from the present results and further work is necessary to address this issue more directly. However, one can supply some possible explanations. The vertical structure of the current meter time series appears to be equivalent barotropic: the amplitude of the eddy signals decreases with depth, but without any appreciable phase change. These characteristics can be explained with the presence of a uniform mean potential vorticity distribution. The same equivalent barotropic character is found in the model results in the upper 1500m. Below this depth the eddy signal in the model is generally weaker than in the observations. The first possible explanation is that the surface eddies can penetrate, as equivalent barotropic signals, to a depth where they are energetic enough to mix potential vorticity. Below this depth they tend to disperse as Rossby waves and coherence with the current meter measurements is lost. However, we cannot exclude the possibility of eddy generation due to model instabilities. Although the surface model eddy field is strongly relaxed toward the observations, instability disturbances with a small amplitude close to the surface may not be damped by nudging. In this case they would supply a time dependent motion, especially at depth, that is not necessarily correlated with the assimilated eddy field.

The eddy kinetic energy level in the different model layers is generally lower than the observed one. This is partially a consequence of the underestimated energy

level in the Geosat maps that are assimilated, due to the smoothing effect of the interpolation procedure. In the deeper layers the way the eddy kinetic energy level drops away from the Stream is much slower in the model than in the observations. We have explained these characteristics in terms of the model tendency to develop barotropic basin modes. In the model simulation with no assimilation this type of oscillation represents, in fact, the dominant signal in the far field. We have thus identified a model deficiency that needs to be improved by a more appropriate treatment of the open boundary conditions. Radiation boundary conditions need to be implemented at all open boundaries. Some characteristics of the observed deep circulation appear related to the presence of bottom relief. Therefore future studies should consider the inclusion of bottom topography in the model geometry. The present results can represent a reference case for identifying the bathymetric influence on the model behavior when surface data are assimilated.

The main conclusion of this study is that assimilation of surface data with the nudging method represents a very promising tool for driving ocean models toward a more realistic behavior. In particular the possibility of building into the model a "realistic" eddy field by assimilating surface eddy information, seems to have important consequences on the development of realistic features of the model mean circulation, such as the recirculation. Several questions remain unanswered and represent stimulating topics for future studies. First of all what do we mean by "realistic" eddy field? Are there specific aspects of the surface eddy fields that are essential for driving a correct mean flow? Is it simply the geographical distribution of the eddy intensity that is important or does the presence of some particular spatial and temporal scales also play a role? These issues need to be addressed by performing a more detailed analysis of the distribution of the divergent component of the eddy fluxes. Future work also includes additional experiments with different mean fields in order to identify additional aspects of the eddy-mean flow interaction

processes. The inclusion of a northern recirculation gyre in the surface mean field that is assimilated should be considered. We have seen that the lack of any flow in the area north of the Stream leads to the development of a westward flow in the model subsurface layers. This feature of the circulation can be understood theoretically, but it still represents an unrealistic feature that needs to be corrected.

In this study we have made the choice of interpolating the data onto the model grid at time intervals short enough that a continuous assimilation in time has been possible. We have also assumed that the data are uniformly accurate and we have neglected the inclusion of data errors in this study. The reason for these choices has been to understand the process of the model adjustment when complete surface information is used to constrain the surface model fields. In this regard this study can be considered as a reference case. In future studies the effect of an irregular space-time distribution of the surface data on the assimilation results as well as the influence of an inhomogeneous data error distribution should be considered. Finally, further work is necessary in order to establish more precise connections, from a dynamical viewpoint, between nudging and related optimal methods, such as the Kalman filter and the Kalman smoother. On one hand, this would supply a more rigorous basis for the choices involved in the implementation of nudging. On the other hand, the dynamical understanding of the model response to the surface data constraint, obtained in experiments using the nudging method, can offer useful insights for the "educated guesses" required in the implementation of the Kalman filter and smoother.

REFERENCES

Anthes, R. A., 1974: Data assimilation and initialization of hurricanes prediction models, *J. Atmos. Sci.*, **31**, 701 - 719.

Bauer, R.A., M.K. Robinson, 1985: Description of the Bauer-Robinson Numerical Atlas, Version VIII, Compass Systems, Inc., San Diego, Calif.

Berry, P. and J. Marshall, 1989: Ocean modelling studies in support of altimetry, *Dyn. Atmos. Oceans*, **13**, 269-300.

Bratseth, A.M., 1986: Statistical interpolation by means of successive corrections, *Tellus*, **38A**, 439-447.

Bryan, K., 1963: A numerical investigation of a nonlinear model of a wind-driven ocean, *J.Atmos.Sci*, 20, 594-606.

Bretherton, F. P., R. E. Davis, and C. Fandry, 1976: A technique for objective analysis and design of oceanographic instruments applied to MODE-73, *Deep-Sea Res.*, **23**, 559-582.

Bretherton, F.P. and D.B. Haidvogel, 1976: Two-dimensional turbulence above topography, *J. Fluid Mech.*, **78**, 129-154.

Budgell, N.P., 1986: Nonlinear data assimilation for shallow water equations in branched channels, *J. Geophys. Res.*, **91**, 10633-10644.

Cessi, P. 1990: Recirculation and separation of boundary currents, *J. Mar. Res.*, **48**, 1-35.

Chapman, D.C., 1985: Numerical treatment of cross-shelf open boundaries in a barotropic coastal ocean model, *J.Phys.Oceanogr.*, **15**, 1060-1075.

Cheney, R.E., B.C. Douglas, R.W. Agreen, L. Miller, D.L. Porter, and N.S. Doyle, 1987: Geosat altimeter geophysical data record user handbook, *NOAA Tech. Memo NOS NGS-46*, 20 pp., Natl. Geod. Surv., Rockville, MD.

Clarke, R.A., H.W. Hill, R.F. Reiniger and B. Warren, 1980: Current system south and east of the Grand Banks of Newfoundland, *J.Phys.Oceanogr.*, **10**, 25-65.

Cressman, G.P., 1959: An operational objective analysis system, *Mon. Wea. Rev.*, **87**, 367-374.

Davis, R.E., 1975: Statistical methods, in *Dynamics and the analysis of MODE-I: Report of the MODE-I Dynamics Group*, Massachussets Institute of Technology, Cambridge, MA, 1-26 (unpublished document).

Fofonoff, N. P., 1954: Steady flow in a frictionless homogeneous ocean, *J. Mar. Res.*, **13**, 254-262.

Fu, L. and J. Vasquez, 1988: On correcting radial orbit errors for altimetric satellites using crossover analysis, *J. Atm. and Oc. Tech.*, **5**,466-471.

Fukumori, I. and C. Wunsch, 1991: Efficient representation of North Atlantic hydrographic and chemical distributions, *Prog. Oceanog.*, **27**, 111-195.

Fukumori, I., F. Martel and C. Wunsch, 1991: The hydrography of the North Atlantic in the early 1980s. An Atlas, *Prog. Oceanog.*, **27**, 1-110.

Fukumori, I., J. Benveniste, C. Wunsch and D.B. Haidvogel, 1992: Assimilation of sea surface topography into an ocean circulation model using a steady-state smoother, submitted.

Gaspar, P. and C. Wunsch, 1989: Estimates from altimeter data of barotropic Rossby waves in the northwestern Atlantic ocean, *J.Phys.Oceanogr.*, **19**, 1821-1844.

Gelb, A., 1974: *Applied Optimal Estimation*, M.I.T. Press, Cambridge, MA, 374 pp.

Ghil, M., and P. Malanotte-Rizzoli, 1991: Data assimilation in meteorology and oceanography, *Advances in Geophysics*, **33**, 141-266.

Haines, K., 1991: A direct method of assimilating sea surface height data into ocean models with adjustments to the deep circulation, *J.Phys.Oceanogr.*, **21**, 843-868.

Haines, K., P. Malanotte-Rizzoli, R.E. Young and W.R. Holland, 1992: A comparison of two methods for the assimilation of altimeter data into a shallow water model, *Dyn. Atmos. Oceans*, in press.

Halkin D. and T. Rossby, 1985: The structure and transport of the Gulf Stream at 73°W, *J.Phys.Oceanogr.*, **15**, 1439-1452.

Hall, M.M., 1986: Horizontal and vertical structure of the Gulf Stream velocity at 68°W, *J.Phys.Oceanogr.*, **16**, 1814-1818.

Hall, M.M. and H.L.Bryden, 1985: Profiling the Gulf Stream with a current meter mooring, *Geophysical Research Letters* **12**, 203-206.

Hellerman, S. and M. Rosenstein, 1983: Normal monthly wind stress over the world ocean with error estimates, *J.Phys.Oceanogr.*, **13**, 1093-1104.

Hogg, N.G., 1990: Some early impressions from SYNOP East, *The SYNOPticians*, **1** (2).

Hogg, N.G., 1992: On the transport of the Gulf Stream between Cape Hatteras and the Grand Banks, *Deep Sea Res.*, **39**, 1231-1246.

Holland, W.R., 1967: On the wind-driven circulation in an ocean with bottom topography, *Tellus*, **19**, 582-599.

Holland, W.R., 1973: Baroclinic and topographic influences on the transport in western boundary currents, *Geophysical Fluid Dynamics*, **4**, 187-210.

Holland, W.R. and L.B.Lin, 1975a: On the origin of mesoscale eddies and their contribution to the general circulation of the ocean.I.A preliminary numerical experiment., *J.Phys.Oceanogr.*, **5**, 642-65.

Holland, W.R. and L.B.Lin, 1975b: On the origin of mesoscale eddies and their contribution to the general circulation of the ocean.II. A parameter study., *J.Phys.Oceanogr.*, **5**, 658-669.

Holland, W.R., 1978: The role of mesoscale eddies in the general circulation of the ocean–numerical experiments using a wind-driven quasi-geostrophic model., *J.Phys.Oceanogr.*, **8**, 363-392.

Holland, W.R. and P.B.Rhines, 1980: An example of eddy-induced ocean circulation, *J.Phys.Oceanogr.*, **10**, 1010-1031.

Holland, W.R. and W.J.Schmitz, Jr., 1985: Zonal Penetration scale of model mid-latitude jets, *J.Phys.Oceanogr.*, **15**, 1859-1875.

Holland, W.R., 1986: Quasigeostrophic modeling of eddy-resolving ocean circulation, in *Advanced Physical Oceanographic Numerical Modeling*, edited by J.O'Brien, 608 pp.

Holland, W.R. and P. Malanotte Rizzoli, 1989: Assimilation of altimeter data into an ocean circulation model: space versus time resolution studies, *J.Phys.Oceanogr.*, **19**, 1507-1534.

Holland, W.R., V. Zlotnicki and L.-L. Fu, 1991: Modelled time-dependent flow in the Agulhas Retroflection region as deduced from altimer data assimilation, *S.Afr.J.mar.Sci.*, **10**, 407-427.

Illari, L. and J. Marshall, 1983: On the interpretation of eddy fluxes during a blocking episode, *J. Atmos. Sci.*, **40**, 2232-2242.

Johns, E., D. R. Watts and H. T. Rossby, 1989: A test of geostrophy in the Gulf Stream, *J. Geophys. Res.*, **94**, C3, 3211-3222.

Keffer, T., 1985: The ventilation of the world's oceans: maps of the potential vorticity field, *J.Phys.Oceanogr.*,**15**, 509-523.

Krisnamurti, T.N., X. Jishan, H.S. Bedi, K. Ingles and D. Oosterhof, 1991: Physical initialization for numerical weather prediction over the tropics, *Tellus*, **43 A**, 53-81.

Large, W.G., W.R. Holland and J.C. Evans, 1991: Quasi-geostrophic ocean response to real wind forcing: the effects of temporal smoothing, *J.Phys.Oceanogr.*, **21**, 998-1017.

Leaman, K.D., E. Johns and T. Rossby, 1989: The average distribution of volume transport and potential vorticity with temperature at three sections across the Gulf Stream, *J.Phys.Oceanogr.*, **19**, 36-51.

Le Traon, P.Y., M.C. Rouquet and C. Boissier, 1990: Spatial scales of mesoscale variability in the North Atlantic as deduced from Geosat data, *J. Geophys. Res.*, **95**, C11, 20,267-20,285.

Levitus, S., 1982: Climatological atlas of the world ocean, *NOAA Prof.Pap.*, **13**, 173 pp.

Malanotte-Rizzoli, P. and R.E. Young, 1992: Can localized clusters of velocity data be useful for data assimilation?, *Dyn. Atmos. Oceans*, **17**, 1, 23-62.

Mann, C. R., 1967: The termination of the Gulf Stream and the beginning of the North Atlantic Current, *Deep-Sea Res.*, **14**, 337-359.

Marshall, J.C., 1984: Eddy-mean-flow interaction in a barotropic ocean model, *Quart.J.R.Met.Soc.*, **110**, 573-590.

Marshall, J. and G. Nurser, 1986: Steady, free circulation in a stratified quasi-geostrophic ocean, *J.Phys.Oceanogr.*, **16**, 1799-1813.

Marshall, D. and J.C. Marshall, 1992: Zonal penetration scale of midlatitude oceanic jets, *J.Phys.Oceanogr.*, **22**, 1018-1032.

McDowell, S., P. Rhines and T. Keffer, 1982: North Atlantic potential vorticity and its relation to the general circulation, *J.Phys.Oceanogr.*, **12**, 1417-1436.

McWilliams, J.C. and N.J.Zabusky, 1982: Interaction of isolated vortices. I: modons colliding with modons, *Geophys. Astrophys. Fluid Dyn.*, **19**, 207-227.

Miller, A.J., W.R. Holland and M.C.Hendershott, 1987: Open-ocean response and normal mode excitation in an eddy-resolving General circulation model, *Geophys. Astrophys. Fluid Dynamics* **37**, 253-278.

Owens, B.W. and N.G. Hogg, 1980: Oceanic observations of stratified Taylor columns near a bump, *Deep-Sea Res.*, **27**, 1029-1045.

Owens, B.W., 1985: A statistical description of the vertical and horizontal structure of eddy variability on the edge of the Gulf Stream recirculation, *J.Phys.Oceanogr.*, **15**, 195-205.

Owens, B.W., 1991: A statistical description of the mean circulation and eddy variability in the northwestern Atlantic using SOFAR floats, *Prog. Oceanog.*, **28**, 257-303.

Pedlosky, J., 1979: *Geophysical Fluid Dynamics.* Springer-Verlag, 624 pp.

Perigaud, C., 1990: Sea level oscillations observed with Geosat along the two shear fronts of the Pacific North Equatorial Countercurrent, *J. Geophys. Res.*, **95**, C5, 7239-7248.

Read, P.L., P.B. Rhines and A.A. White, 1986: Geostrophic scatter diagrams and potential vorticity dynamics, *J. Atmos. Sci.*, **43**, 3226-3240.

Rhines, P.B., 1979: Geostrophic turbolence. *Ann. Rev. Fluid Mech.*, **11**, 401-441

Rhines, P.B. and W. Young, 1982: A theory of wind driven circulation. I: Midocean gyres. *J. Mar. Res.*, **40**(3), 559-596.

Rhines, P.B. and R. Schopp, 1991: The wind-driven circulation: Quasi-Geostrophic simulations and theory for nonsymmetric winds, *J. Phys. Oceanogr.*, **21**, 1438-1469.

Richardson, P.L. and J.A. Knauss, 1971: Gulf Stream and Western Boundary Undercurrent observations at Cape Hatteras, *Deep-Sea Res.*,**18**, 1089-1109.

Richardson, P.L., 1983a: A vertical section of eddy kinetic energy through the Gulf Stream system, *J.Geophys.Res.*, 88, C4, 2705-2709.

Richardson, P.L., 1983b: Eddy kinetic energy in the North Atlantic from surface drifters, *J.Geophys.Res.*, 88, C7, 4355-4367.

Richardson, P.L., 1985: Average velocity and transport of the Gulf Stream near 55°W, *J.Mar.Res.*, **43**, 83-111.

Richardson, W.S., W.J. Schmitz, Jr., and P.P. Niiler, 1969: The velocity structure of the Florida Current from the Straits of Florida to Cape Fear, *Frederick C. Fuglister Sixtieth Anniversary Volume, Deep Sea Research*, 16 (Supplement), 225-231.

Richman, J.G., C. Wunsch and N.G. Hogg, 1977: Space and time scales of mesoscale motion in the western North Atlantic, *Reviews of Geophysics and Space Physics*, **15**, 385-420.

Robinson, M.K., R.A.Bauer and E.H.Schroeder, 1979: Atlas of North Atlantic-Indian Ocean monthly mean temperatures and salinities of the surface layer, *Ref.Publ.*, **18**, 213 pp., U.S.Naval Oceanogr.Office, Washington, D.C.

Roemmich, D., 1983: Optimal estimation of hydrographic station data and derived fields, *J. Phys. Oceanogr.*, **13**, 1544-1549.

Schmitz, W.J., Jr. and W.R.Holland, 1982: A preliminary comparison of selected numerical eddy-resolving general circulation experiments with observations, *J.Mar.Res.*, **40**, 75-117.

Schmitz, W.J., Jr., 1984: Abyssal eddy kinetic energy in the North Atlantic, *J.Mar.Res.*, **42**, 509-536.

Schmitz, W.J., Jr. and W.R.Holland, 1986: Observed and modeled mesoscale variability near the Gulf Stream and Kuroshio extension, *J.Geophys.Res.*, **91**, C8, 9624-9638.

Schmitz, W.J., Jr., and J.D. Thompson, 1992: A note on the effects of horizontal resolution in a limited area model of the Gulf Stream System, *J. Phys. Oceanogr.*, in press.

Schwiderski, E.W., 1980: On charting global tides, *Rev. Geophys. Space Phys.*, **18**, 243-268.

Stammer, D., and C.W. Böning, 1992: Mesoscale variability in the Atlantic ocean from Geosat altimetry and WOCE high-resolution numerical modeling, *J. Phys. Oceanogr.*, **22**, 732-752.

Tai, C.K., 1988: Geosat crossover analysis in the tropical Pacific, 1, Constrained sinusoidal crossover adjustment, *J. Geophys. Res.*, **93**, 10621-10629.

Teague, W.J., M.J.Carron and P.J.Hogan, 1990: A comparison between the Generalized Digital Environmental Model and Levitus climatologies, *J. Geophys. Res.*, **95**, 7167-7183.

Thompson, J.D. and W.J. Schmitz, Jr., 1989: A limited-area model of the Gulf Stream: design, initial experiments, and model-data intercomparison, *J. Phys. Oceanogr.*, **19**, 791-814.

Tripoli, G.J. and T.N. Krishnamurti, 1975: Low-level flows over the GATE area during summer 1972, *Mon. Wea. Rev.*, **103**, 197-216.

Vasquez, J., V. Zlotnicki, and L.-L. Fu, 1990: Sea level variability in the Gulf Stream between Cape Hatteras and 50°W: a Geosat study, *J. Geophys. Res.*, **95**,C10, 17,957-17,964.

Veronis, G., 1966: Wind-driven ocean circulation.Part 2.Numerical solution of the nonlinar problem, *Deep-Sea Res.*, **13**, 31-55.

Verron, J. and W.R. Holland, 1989: Impacts de donnees d'altimetrie satellitaire sur les simulations numeriques des circulations generales oceaniques aux latitudes moyennes, *Annls. Geophys.*, **7**, 31-46.

Verron, J., 1992: Nudging altimeter data into quasigeostrophic ocean models, *J. Geophys. Res.*, **97**, C5, 7479-7491.

Willebrand, J., R.H. Käse, D. Stammer, H.-H. Hinrichsen and W. Krauss, 1990: Verification of Geosat surface topography in the Gulf Stream extension with surface drifting buoys and hydrographic measurements, *J. Geophys. Res.*, **95**, 3007-3014.

Worthington, L.V., 1976: On the North Atlantic Circulation. The Johns Opkins Oceanographic studies, **6**, 110 pp.

Wunsch, C., 1989a: Tracer inverse problems, *Oceanic Circulation Models: Combining Data and Dynamics*, D.L.T. Anderson and J. Willebrand, Eds., 605 pp.

Wunsch, C., 1989b: Sampling characteristics of satellite orbits, *J. Atm. and Oc. Tech.*, **6**, 891-907.

Wyrtky, K., L. Magaard and J. Hager, 1976: Eddy energy in the oceans, *J. Geophys. Res.*, **81**, 2641-2646.

Zlotnicki, V., A. Hayashi and L.-L. Fu, 1989: The JPL-Oceans 8902 version of Geosat Altimetry data, JPL Internal Document D-6939, 17 pp. [available from Jet Propulsion Lab., California Institute of Technology, Pasadena, CA 91109.]

Zlotnicki, V., 1990: Sea level differences across the Gulf Stream and Kuroshio extension, *J. Phys. Oceanogr.*, **21**, 599-609.